Temporal evolution of crystal mush reservoirs beneath the Bárðarbunga-Veiðivötn volcanic system, Iceland

Alberto Caracciolo

Faculty of Earth Sciences
University of Iceland
2021

Temporal evolution of crystal mush reservoirs beneath the Bárðarbunga-Veiðivötn volcanic system, Iceland

Alberto Caracciolo

Dissertation submitted in partial fulfillment of a
Philosophiae Doctor degree in Geology

PhD Committee
Enikő Bali
Guðmundur H. Guðfinnsson
Maren Kahl
Margaret E. Hartley

Opponents
Maxim Portnyagin
Chiara Maria Petrone

Faculty of Earth Sciences
School of Engineering and Natural Sciences
University of Iceland
Reykjavik, February 2021

Temporal evolution crystal mush reservoirs beneath the Bárðarbunga-Veiðivötn volcanic system, Iceland
Crystal mush reservoirs beneath central Iceland
Dissertation submitted in partial fulfillment of a *Philosophiae Doctor* degree in Geology

Faculty of Earth Sciences
School of Engineering and Natural Sciences
University of Iceland
Sturlugata 7
102, Reykjavik
Iceland

Telephone: 525 4000

Bibliographic information:
Alberto Caracciolo, 2021, Temporal evolution of crystal mush reservoirs beneath the Bárðarbunga-Veiðivötn volcanic system, Iceland. PhD dissertation, Faculty of Earth Sciences, University of Iceland, 140 pp.

Author ORCID: https://orcid.org/0000-0003-1416-9301
ISBN: 978-9935-9555-2-4

Printing: Háskólaprent
Reykjavik, Iceland, February 2021

Abstract

The physico-chemical properties of magma storage reservoirs in multi-level magmatic systems may change with time, along with the timescales at which crystals and melts are processed throughout the crust.

In this thesis, I use an integrated approach of quantitative petrological and geochemical analysis combined with diffusion chronometry to evaluate temporal variations of magma storage and transfer conditions through crystal mush reservoirs beneath the Bárðarbunga-Veiðivötn volcanic system in Central Iceland. To do this, I targeted five eruptive units of different age, namely Ljósufjöll (subglacial), Brandur, Fontur and Saxi (early-Holocene), Þjórsárdalshraun and Drekahraun (middle-Holocene) and Veiðivötn 1477 AD (historical).

The composition of macrocrysts indicates that they are not in chemical equilibrium with the liquid that carried them to the surface. Plagioclase, olivine and clinopyroxene core compositions are too primitive to be in equilibrium with the carrier liquid, which indicates that storage and disaggregation of crystal mushes played an important role in these eruptions. Macrocryst compositions vary with time, with subglacial and early-Holocene magmatic units being characterized by more primitive and less variegate compositions (An_{85-92}, Fo_{81-87}) compared to middle-Holocene and historical units (An_{80-92}, Fo_{77-87}). Application of different geobarometers suggests that, regardless of time, underneath the Bárðarbunga-Veiðivötn system there is a multi-tiered, compositionally layered plumbing system in which crystals and melts are gradually transferred to shallower levels. In particular, I argue for a temporally invariant reservoir(s) in the middle crust, located at about 7-8 km depth, in which melts last equilibrate with the crystal cargo prior to eruptions. The largest contribution from deep-seated, lower crustal reservoir(s) occurs during subglacial and early-Holocene times. Trace elements and oxygen isotopes ($\delta^{18}O$) are consistent with the supply of primary mixtures of melts that contain depleted and enriched mantle signatures. As primary mixtures migrate towards upper crustal levels, they become more evolved and their $\delta^{18}O$ values become lower as a result of crustal contamination processes. Fe-Mg diffusion chronometry shows that macrocrysts were mobilized and entrained into the final carrier liquid over timescales of 5-12 months in the early-Holocene, whereas middle-Holocene and historical macrocrysts were disaggregated within timescales of about 2 months. The presence of crystalline gabbroic nodules in the early-Holocene samples, and their larger crystal content relative to recent samples, likely indicates that during the early-Holocene the mush required more time to be loosened, mobilised and converted into an eruptible magma. These temporal changes may be attributed to an increase in magma production rates in the early-Holocene associated with glacio-isostasy effects.

Útdráttur

Eðlisefnafræðilegir eiginleikar kvikugeyma í kvikukerfum sem dreifast á mörg dýptarbil í jarðskorpunni geta breyst með tímanum, sem og tímakvarði ferla sem hafa áhrif á kristalla og bráðir í skorpunni.

Í þessari ritgerð beiti ég aðferð þar sem saman eru nýttar magnbundnar bergfræðilegar og jarðefnafræðilegar greiningar ásamt ákvörðunum á tíma með efnasveimismælingum. Tilgangurinn er að meta breytingar með tíma á geymslu og hreyfingar kviku í kristalríkum kvikugeymum undir Bárðarbungu-Veiðivatnakerfinu. Með þetta að markmiði beini ég sjónum mínum að fimm gosmyndunum af mismunandi aldri, þ.e. Ljósufjöllum (gos undir jökli), Brandi, Fonti og Saxa (frá snemm-Nútíma), Þjórsárdalshrauni og Drekahrauni (frá mið- Nútíma) og frá sögulegu gosi í Veiðivötnum árið 1477.

Efnasamsetning díla gefur til kynna að þeir hafi ekki verið í jafnvægi við bráðina sem bar þá til yfirborðs. Samsetning kjarna í plagíóklasi, ólivíni og klínópýroxeni er of frumstæð til að hafa verið í efnajafnvægi við bráðina, sem þýðir að geymsla og uppbrot á kristalríkri kviku höfðu mikilvægu hlutverki að gegna í þessum eldgosum. Samsetning díla er breytileg með tíma og eru gosmyndanir frá síðasta jökulskeiði og myndanir frá því snemma á Nútíma frumstæðari og hafa minni breytileika í samsetningu (An_{85-92}, Fo_{81-87}) en myndanir frá mið-Nútíma og sögulegum tíma (An_{80-92}, Fo_{77-87}). Mismunandi þrýstimælar gefa til kynna að óháð tíma hafi verið undir Bárðarbungu-Veiðivatnakerfinu lagskipt kvikukerfi hvað varðar samsetningu, dreift yfir dýptarbil, þar sem kristallar og bráð flytjast smám saman upp á við. Ég færi sérstaklega rök fyrir því að í miðskorpunni á um 7-8 km dýpi hafi til lengri tíma verið geymir þar sem bráðir og kristallar ná jafnvægi fyrir eldgos. Mest kom úr geymi eða geymum djúpt í neðri skorpunni á ísöld og snemma á Nútíma. Snefilefni og súrefnissamsætur ($\delta^{18}O$) benda til aðstreymis frumstæðra bráðarblandna sem bera merki um bæði sneidda og auðgaða möttulþætti. Við það að frumstæðar bráðarblöndur færast upp í efra hluta skorpunnar þróast þær og $\delta^{18}O$-gildi þeirra lækka vegna skorpumengunar. Tímamælingar með Fe-Mg-sveimi sýna að dílar fóru síðast á hreyfingu og voru hrifsaðir upp af kviku 5-12 mánuðum fyrir gos, meðan það losnaði um díla í mið-Nútíma og sögulegum gosmyndunum um 2 mánuðum fyrir gos. Tilvist gabbróhnyðlinga í sýnum frá því snemma á Nútíma og það að þeir hafa meira af kristöllum en hnyðlingar í yngri sýnum bendir til að á þeim tíma hafi að kristalrík kvika þurft lengri tíma til brotna upp, fara af stað og breytast í kviku sem gat komið upp í gosum. Þessar breytingar með tíma má tengja aukinni kvikuframleiðni á snemm-Nútíma sem aftur má rekja til áhrifa frá breyttu jökulfargi.

Preface

This thesis is the outcome of the research carried out at the University of Iceland from October 2017 to October 2020. This study was financed by the University of Iceland Research Fund (Nr: HI17060092) and the EIMSKIP PhD fund of the University of Iceland. I have also benefitted from the Landsvirkjun Energy Research Fund (NÝR-18 – 2018) and from the Icelandic Research Fund (Rannis). The work includes three research articles of which two are published and one is ready to be submitted to a scientific journal at the time of submission of this thesis:

I. **Caracciolo, A**., Bali, E., Guðfinnsson, G.H., Kahl, M., Halldórsson, S.A., Hartley, M.E., Gunnarsson, H., 2020. *Temporal evolution of magma and crystal mush storage conditions in the Bárðarbunga-Veiðivötn volcanic system, Iceland*. Lithos 352–353. https://doi.org/10.1016/j.lithos.2019.105234

II. **Caracciolo, A**., Kahl, M., Bali, E., Guðfinnsson, G.H., Halldórsson, S.A., Hartley, M.E., 2021. *Timescales of crystal mush mobilization in the Bárðarbunga-Veiðivötn volcanic system based on olivine diffusion chronometry*. Am. Mineral (In press). https://doi.org/doi.org/10.2138/am-2021-7670

III. **Caracciolo. A.**, Halldórsson, S.A., Bali, E., Marshall E.W., Jeon H., Whitehouse M.J., Barnes J.D., Guðfinnsson, G.H., Kahl, M., Hartley, M.E. (in prep). *Oxygen isotope evidence for progressively assimilating trans-crustal magma plumbing systems in Iceland*. To be submitted to *Geology*.

Table of contents

List of Figures

Abbreviations

P – Pressure

T – Temperature

X – Composition

fO_2 – Oxygen Fugacity

t - Time

MI – Melt inclusion

SVZ – Snæfellsnes Volcanic Zone

RPRZ – Reykjanes Peninsula Rift Zone

WVZ – Western Rift Zone

SIVZ – South Iceland Volcanic Zone

ERZ – Eastern Rift Zone

NRZ – Northern Rift Zone

OPAM – Olivine-Plagioclase-Augite-Melt

An – Anorthite

Fo – Forsterite

$\delta^{18}O$ – Oxygen isotope ratio

Mg# - Mg number

MORB – Mid-Ocean Ridge Basalt

DM – Depleted mantle

EM – Enriched mantle

Acknowledgements

First and foremost, I would like to thank my PhD supervisors Enikő Bali, Guðmundur Heiðar Guðfinnsson and Maren Kahl, from whom I learned a lot during the last three years. I accepted the PhD position without knowing them in person and could not have asked for better supervisors. Enikő has always been very generous with her time for me and available for discussions. She never put pressure on me but rather, her most common daily comment before heading home was 'don't work too late!' Guðmundur has always been very helpful and open for chats. I am also grateful to him for his help with microprobe analyses. I really enjoyed the evenings at your home with delicious Hungarian food and Pálinka. Thanks, Maren, for introducing me to the diffusion modelling world. I deeply appreciated your help and constructive advice during these years. I am also grateful to Margaret Hartley, who is the external member of my PhD committee. Thank you for your help and for the time you devoted to improving my manuscripts.

Secondly, I would like to thank Sæmundur Ari Hálldórsson. Although he is not officially on my PhD committee, he has always been extremely supportive and interested in my work, he supplied me with most of the samples and I am very grateful to him for his help and enthusiasm and his door was always open for a chat.

Thank you to Martin Whitehouse, Heejin Jeon, Kerstin Lindén (Nordsim lab, Swedish Museum of Natural History), Duncan Hedges, Richard Walshaw and Geoffrey E. Lloyd (University of Leeds) for their aid with sample preparation and data acquisition.

These three years would not have been the same without the people and friends I have worked with at the University, with a special mention to Cécile, Siqi, Andrea and Gotje, who have been fully supportive and available for a chat. Thanks to the people I have met in Iceland during the last three years and a big thank to a special person I recently met, without whom this final PhD period would not have been the same. I feel really lucky of having you in my life!

I want to thank my friends back in Italy. It is not simple to make friendships endure from overseas, but moving abroad has made me appreciate your friendship even more. A special thanks goes to Riccardo and Valentina, my expatriated friends in Canada, who have virtually shared with me most of my time and daily life in Iceland.

To my family in Italy – I thank you for your support and hope you will have the chance to visit Iceland soon!

1 Introduction

'A magma chamber is a large pool of liquid rock beneath the surface of the Earth'. This is how Wikipedia defines a magma chamber, which reflects the classic concept of a shallow, long-lived, liquid-dominated reservoir that eventually solidifies into plutons. However, geophysical studies have failed to detect large, liquid-rich magma chambers underneath active volcanoes. Observations are more consistent with the presence of hot igneous rocks containing small amounts of liquid, with magma storage taking place at variable depths in the crust (e.g. Farrell et al., 2014; Lowenstern et al., 2017; Magee et al., 2018; Sinton and Detrick, 1992). Similarly, petrological studies show that magmas may be processed over a large range of depths, in so-called transcrustal magmatic systems (e.g. Cashman et al., 2017; Edmonds et al., 2019; Maclennan, 2019). Magma reservoirs building up transcrustal systems are dominated by crystal mushes, defined as dynamic domains made up of a crystalline framework through which the melt is distributed (Cashman et al., 2017; Maclennan, 2019; Marsh, 2006, 1995). Also, liquid-rich bodies may exist in magma reservoirs, mostly formed by expulsion of liquid from a mush (Bachmann and Bergantz, 2004; Pistone et al., 2015).

Numerous petrological and geochemical studies demonstrate the transcrustal nature of Icelandic volcanism, in which magmas are stored and transferred throughout the entire crustal section (e.g. Caracciolo et al., 2020; Greenfield et al., 2016; Halldórsson et al., 2008; Hansen and Grönvold, 2000; Hartley et al., 2018; Neave and Putirka, 2017; Sigmundsson et al., 2010). During their journey towards the surface, magmas traverse and interact with different storage reservoirs, ultimately affecting their physico-chemical properties like pressure, temperature and chemical composition. At present, there is no consolidated view of how magma properties may change throughout the crustal section. In addition, there are no systematic studies about how the architecture of magmatic systems and the timescales of magmatic processes may change in the temporal domain, which is key information for future eruption forecasting and their related hazards.

In this doctoral thesis I use an approach of quantitative geochemical analyses and geothermobarometry methods, coupled with multi-element diffusion chronometry in olivine crystals, to unravel changes of the physico-chemical properties (e.g. P, T, X) of melts and crystals as they cross magma storage reservoirs, and to reconstruct temporal changes of magma plumbing architecture in central Iceland. By using trace elements and oxygen isotopes, I follow the extent of crustal contamination throughout magma processing from mantle to upper crust, and its variation with time. I targeted temporally diverse eruptive units from the Bárðarbunga-Veiðivötn volcanic system, one of the most active volcanic systems of Iceland (Larsen, 2002), with the goal of assessing millennial-scale variations of magma plumbing in Iceland. To my knowledge, this is the first study to examine the temporal evolution of a specific magmatic system.

1.1 Geology of Iceland

Sitting on a divergent plate boundary between the North American and Eurasian plates, Iceland is a volcanic island situated in the North Atlantic Ocean, and one of the most profuse producers of basaltic magmas on Earth (Thordarson and Larsen, 2007).

Iceland is the only place in the world where a mid-ocean ridge expresses itself above sea level. This is due to the intersection of the Mid-Atlantic Ridge with a mantle plume, which causes excessive mantle melting and the formation of anomalous crustal thicknesses across Iceland. The oceanic crustal thickness varies from about 20 km along the coasts up to a maximum of 45 km underneath Vatnajökull ice cap in central Iceland (Darbyshire et al., 2000; Jenkins et al., 2018), where the inferred centre of the plume is located (Harðardóttir et al., 2018).

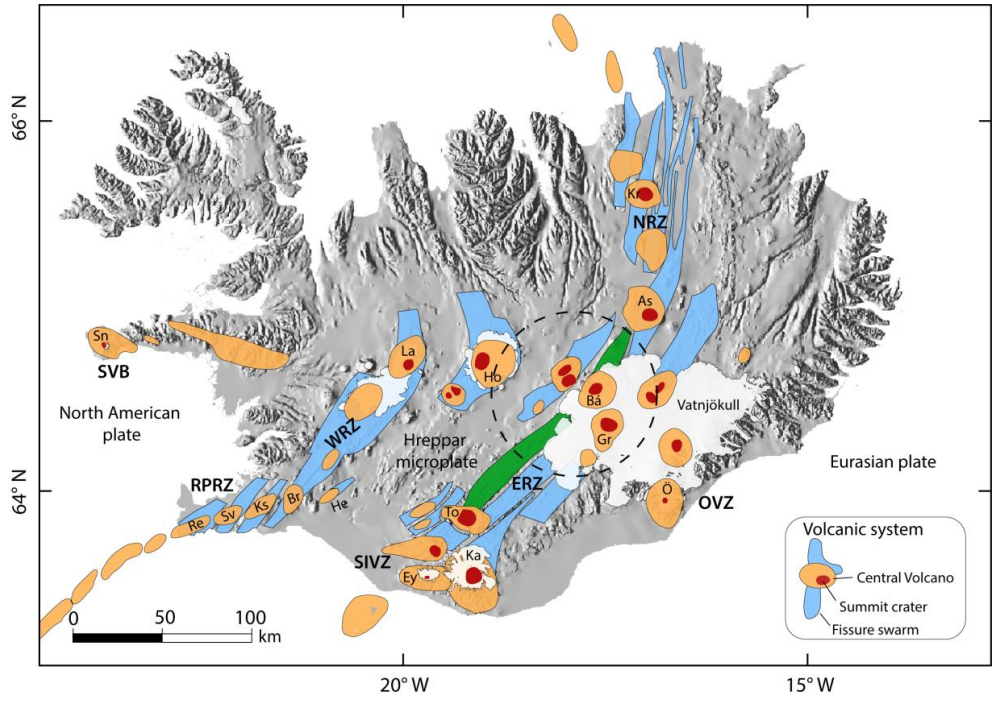

Fig. 1.1. *Map of Iceland showing the location of active volcanic systems and central volcanoes. The Bárðarbunga volcanic system is shown in green. The dotted line indicates the inferred current location of the mantle plume. SVB: Snæfellnes Volcanic Belt, Sn: Snæfellsjökull. RPRZ: Reykjanes Peninsula Rift Zone, Re: Reykjanes, Sv: Svartsengi, Ks: Krýsuvík, Br: Brennisteinsfjöll. WRZ: Western Rift Zone, He: Hengill, La: Langjökull, Ho: Hofsjökull. SIVZ: South Iceland Volcanic Zone, Ey: Eyjafjallajökull, Ka: Katla, To: Torfajökull. ERZ: Eastern Rift Zone, Ba: Bárðarbunga, Gr: Grímsvötn. OVZ: Öræfajökull Volcanic Zone, Ö: Öræfajökull. NRZ: Northern Rift Zone, As: Askja, Kr: Krafla. Modified after Einarsson (2018).*

The North American and Eurasian plates are drifting apart at a rate of 18-19 mm/year (Sigmundsson et al., 2020) and the plate boundary intersects Iceland from southwest to

northeast segmenting the island into 20-100 km wide neovolcanic zones (Fig. 1.1) (Einarsson, 2008; Sigmundsson et al., 2020). In Southern Iceland, the plate boundary splits in two branches, with an aseismic microplate between the two branches called the Hreppar microplate. The neovolcanic rift zones are divided into 30 volcanic systems, each with specific geochemical and tectonic features (Thordarson and Höskuldsson, 2008; Thordarson and Larsen, 2007).

The volcanic systems are the principal geological structures of Iceland. They are characterized by a fissure swarm which is usually associated with a central volcano (Thordarson and Larsen, 2007). The neovolcanic zones are further divided into rift zones (RPRZ, WRZ, ERZ, NRZ) and flank zones (SVB, SIVZ, OVZ), based on extensive crustal spreading or the lack thereof, respectively (Sigmundsson et al., 2020). An additional difference between flank and rift zones comes from the compositions of the eruptive products. Along the rift zones, the magmatism is tholeiitic, whereas mildly alkalic magmas and transitional magmas erupt in the flank zones (Jakobsson et al., 2008).

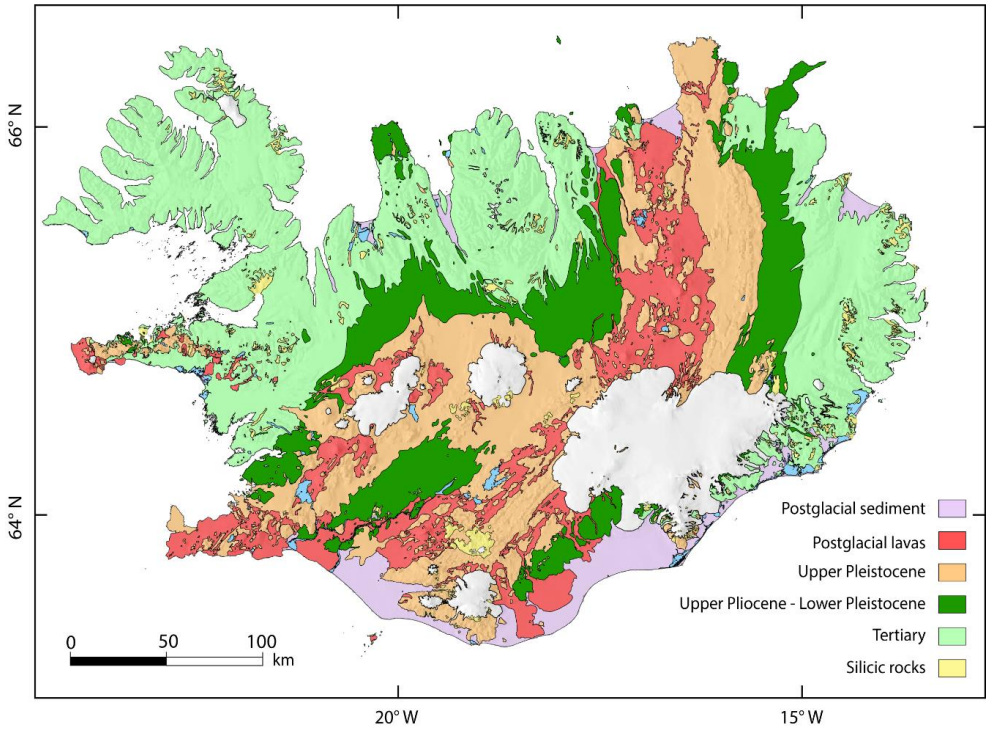

Fig. 1.2. *Simplified geological map of Iceland, showing the different geological formations with a colour scheme depending on age. Upper Pleistocene: <0.8 Ma; Upper Pliocene – Lower Pleistocene: 0.3-3.3 Ma. Glaciers are shown in white and water bodies in light blue. Geological map by the Icelandic Museum of Natural History and Iceland Geodetic Survey.*

The majority of the rocks on Iceland's surface are basalts, with intermediate and silicic rocks having an abundance of less than 10% (Fig. 1.2) (Jónasson, 2007). The onset of glaciation cycles around 3.3 million years ago marked an important environmental change, also affecting volcanic products (e.g. Maclennan et al., 2002; Sigvaldason et al., 1992). Extensive subglacial volcanics developed between 3.3 Ma and the end of the last glacial period (Weichselian glaciation), around 12.000-10.000 years ago.

Geological maps of Iceland usually divide rocks into primary epochs, being Tertiary (>3.3 Ma), Plio-Pleistocene (3.3-0.8 Ma) and Upper Pleistocene (<0.8 Ma). Rocks formed after the last glacial period are referred to as postglacial, and are younger than 12.000-10.000 years (Fig. 1.2). Postglacial lavas are mostly located along the neovolcanic zones, along with Upper Pleistocene rocks, which were produced by subglacial volcanism.

1.2 The Bárðarbunga-Veiðivötn volcanic system

The Bárðarbunga volcanic system, situated underneath the Vatnajökull ice cap in the ERZ, with a total length of 190 km and an area of about 2500 km^2, is the largest volcanic system of Iceland (Thordarson and Höskuldsson, 2008). With at least 27 eruptions in the last 11 centuries, it is one of the most active volcanic systems in Iceland (Larsen and Guðmundsson, 2014), with the last eruption occurring in 2014-15 (Halldórsson et al., 2018; Sigmundsson et al., 2015). The central edifice consists of two subglacial volcanoes: the 2009 m high Bárðarbunga central volcano, with up to 700 m deep, ice-filled caldera, and Hamarinn, a potential smaller second central volcano located 20 km SW of Bárðarbunga. The Bárðarbunga volcanic system is associated with a fissure swarm, which is divided in two segments: the 55 km long Dyngjuháls fissure swarm extends towards the north, and the 115 km long Veiðivötn fissure swarm propagates southwest from Bárðarbunga (Larsen and Guðmundsson, 2014).

The southwest part of the Bárðarbunga volcanic system is commonly referred to as the Bárðarbunga-Veiðivötn volcanic system (Fig. 1.3). While the ice-covered part of the volcanic system is dominated by phreatomagmatic basaltic eruptions, in the ice-free part of the fissure swarm, effusive basaltic eruptions are more common. However, in areas with high groundwater levels and/or abundant surface water, phreatomagmatic explosive basaltic eruptions may occur. This was the case with some postglacial tephra cones and the recent Vatnaöldur (~870 AD) and Veiðivötn (~1477) eruptions, in which highly fragmented basaltic tephra was produced (Larsen and Guðmundsson, 2014). In the extreme southwest, the Veiðivötn fissure swarm propagates into the Torfajökull volcanic system, in which silicic and mixed magmas may erupt (Zellmer et al., 2008).

The persistent and temporally well-constrained eruptive activity during the Holocene (Larsen and Guðmundsson, 2014), the large spatial extent of the system, and the availability of phyric to ultrphyric (e.g. Hansen and Grönvold, 2000) glassy tephra and lava samples means that the Bárðarbunga-Veiðivötn volcanic system is an ideal location to investigate the temporal and compositional evolution of magma storage reservoirs on the scale of a single volcanic system. To do this, I have selected five geologically well-characterized eruptive units (Fig. 1.3) that span a full glacial cycle, from a <100 ka subglacial eruption to a historical eruption in 1477 AD.

Eruptive units (Fig. 1.3) have been divided in four temporally diverse groups based on their inferred ages:

- ***Subglacial unit***. Ljósufjöll, a previously unstudied subglacial magmatic ridge, is the oldest magmatic unit covered by my sample suite. Ljósufjöll is composed of phyric basalts that transition from pillow lavas to hyaloclastites, suggesting a subglacial origin. Ljósufjöll is thought to have erupted during the last glacial period (Vilmundardóttir et al., 2000) and therefore its age is constrained to be between 100 ka and 12 ka.

- ***Early-Holocene units***. Early-Holocene refers to magmatic units erupted early in postglacial times (~12 to ~7 ka). In particular, here I studied the tephra cones Brandur, Fontur and Saxi (Halldórsson et al., 2008; Hansen and Grönvold, 2000; Holness et al., 2019, 2007), which were built up by postglacial explosive phreatomagmatic eruptions. Saxi and Fontur are aligned along a ~2.5 km long fissure, whereas Brandur is located 3 km west of Saxi, on the edge of Þórisvatn lake (Fig. 1.3). Each cone consists of unconsolidated, crystal-rich tephra along with abundant gabbroic nodules up to 10-15 cm in diameter. Furthermore, numerous individual plagioclase macrocrysts, up to 4 cm long, are found around the tephra craters. It has been suggested that these craters were the source of the 8600-year-old Þjórsárhraun lava (Hansen and Grönvold, 2000; Hjartarson, 1988; Jakobsson, 1979), but this remains unproven and their precise age is not known.

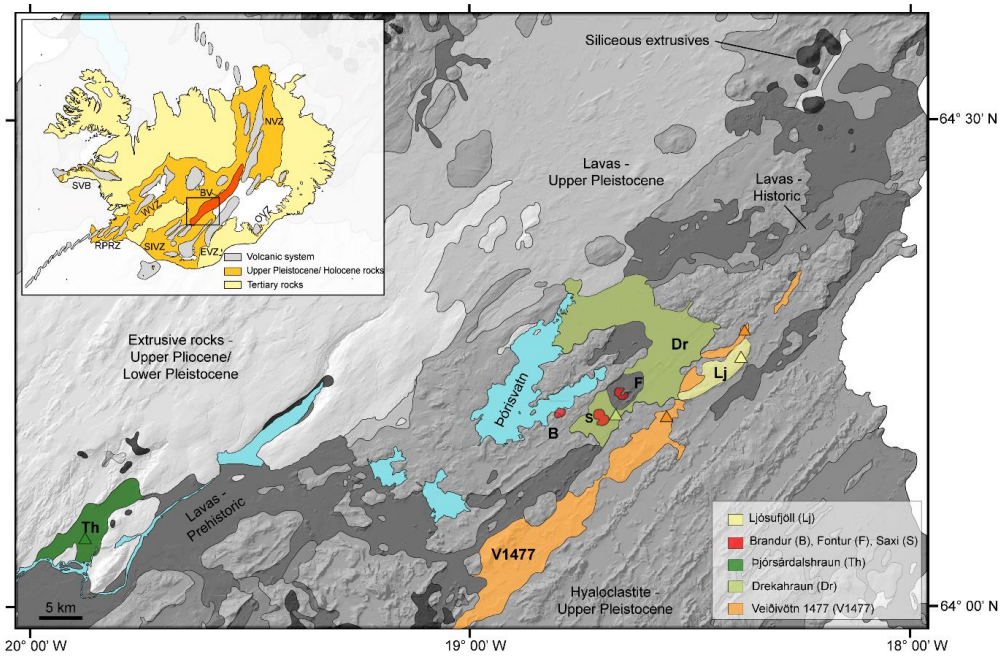

Fig. 1.3. *Geological map of the southernmost part of the Bárðarbunga-Veiðivötn volcanic system (from Caracciolo et al., 2020). The general geology of the area is indicated with greyscale colours. Eruptive units studied in this work are marked in colours. Historic lavas are younger than 1100 BP; prehistoric lavas are older than 1100 BP. Triangles show the exact sampling location within each unit.*

- ***Middle-Holocene units.*** Middle-Holocene eruptive units studied in this thesis are Þjórsárdalshraun and Drekahraun lavas, dated by tephrochronology to between 3000-4000 years BP. They belong to the Tungnaá lava sequence, a group of prehistorical basaltic eruptions produced in the Veiðivötn area over the last 9000 years (Pinton et al., 2018). Þjórsárdalshraun followed the course of Þjórsá River, creating a field of rootless cones in Þjórsárdalur valley (Fig. 1.3) close to Hekla volcano. Samples consist of fragmented lavas. Drekahraun was emplaced in the Veiðivötn area and I collected fresh scoria samples from the source vents.

- ***Historical.*** The term 'historical' refers to eruptive units produced after the settlement of Iceland in 874 AD. In this work, I include the historical Veiðivötn ~1477 eruption, which produced ~10 km^3 of highly fragmented, crystal-poor basaltic tephra and some lava flows (Larsen and Guðmundsson, 2014). This volume includes tephra and lavas ranging from basalt to rhyolite, which erupted simultaneously as the Veiðivötn magmas entered into the Torfajökull volcanic system (McGarvie, 1984; Zellmer et al., 2008). Here I have studied basaltic tephra samples from the central and southern parts of the Veiðivötn fissure (Fig. 1.3).

1.3 Magma storage reservoirs underneath Iceland

Many petrological barometers are associated with a pressure uncertainty of about ±1.5 kbar (4.5 km), nearly as much as the equivalent thickness of typical oceanic crust in mid-ocean ridge settings. However, in Iceland, the occurrence of a much thicker crust up to 45 km (Darbyshire et al., 2000) allows the use of petrological barometers to constrain melt and mineral crystallization depths. Petrological estimates of crystallization depths are obtained using barometers based on the composition of three-phase saturated melts (Yang et al., 1996), mineral-melt equilibria (Neave and Putirka, 2017; Putirka, 2008) and on the volatile content of melt inclusions (e.g., Newman and Lowenstern, 2002). Studies carried out on different volcanic systems of Iceland highlight that crystallization occurs at a range of depths in the crust (Haddadi et al., 2017; Halldórsson et al., 2018; Hansen and Grönvold, 2000; Hartley et al., 2018; Neave et al., 2013; Neave and Putirka, 2017), suggesting a mechanism of crustal accretion involving injection of melts at different depths, in accordance with the so-called stacked-sills model (Greenfield and White, 2015; Kelemen et al., 1997). This is also supported by persistent seismicity observed throughout the crustal section underneath the Askja (Greenfield et al., 2016) and the Bárðarbunga (Hudson et al., 2017) volcanic systems.

The multi-level nature of Icelandic magmatism is associated with mushy layes within the Icelandic crust. Microanalytical studies of the crystal cargo of Icelandic eruptions show that the compositions of crystal cores are usually more primitive than the liquid that brought them to the surface (Holness et al., 2007; Neave et al., 2014; Thomson and Maclennan, 2013). The trace element composition of mineral-hosted melt inclusions (MIs) suggests that as crystallization proceeds, the MI compositional variability collapses to a value close to that of the carrier liquid (Maclennan, 2008), revealing a strong relationship between macrocrysts and their carrier liquid. This genetic relationship suggests that macrocrysts are likely to derive from disaggregation and mobilization of crystal mushes that formed within magma bodies where storage and evolution of the carrier liquid took place. Crystal mush fragments can be eruped as glomerocrysts or cumulate nodules (Hansen and Grönvold, 2000). Mush piles can be compositionally stratified (Thomson and Maclennan, 2013), with more evolved compositions forming at the top of the mush pile. If the crystallinity of the mush exceeds ~60 vol. % (Cashman et al., 2017), the mush in considered to be non-eruptible and it may crystallize and form a plutonic rock in the crust.

Two endmember models are currently frequently used to describe magma movement during Icelandic eruptions: the lateral flow hypothesis and the magma reservoir hypothesis (Hartley and Thordarson, 2013). The lateral flow hypothesis suggests that magma supply is focused underneath the central volcano and replenishment of the magma chamber causes lateral transfer of magma in dykes in the shallow crust. The magma reservoir hypothesis envisions large, elongated reservoirs at the base of the crust and tensile stresses causes the emplacement of subvertical dykes in the crust. Based on geophysical data registered prior to recent Icelandic eruptions (Ágústsdóttir et al., 2016; Hollingsworth et al., 2012; Sigmundsson et al., 2015), both models seem to be applicable to Icelandic eruptions.

2 Methodology

A total of 25 thin sections of representative whole-rock samples were prepared for the different magmatic units. Additionally, individual crystals and glass grains were hand-picked from crushed material and mounted in epoxy. Olivine and plagioclase crystals containing glassy MIs were individually hand-polished to expose the melt inclusions at the surface. More details on melt inclusion preparation are reported in the supplementary material of Paper I (see section 9.1).

Major element compositions of macrocrysts (olivine, plagioclase and clinopyroxene), groundmass glasses and melt inclusions were carried out using the JEOL JXA-8230 electron probe microanalysis (EPMA) at the Institute of Earth Science, University of Iceland. Details on electron microprobe set-up and calibration are included in the supplementary material of Paper I (see section 9.1). Olivine concentration profiles of major and minor elements were also acquired by EPMA and details are reported in Paper II (see section 10.1).

Crystallographic orientation maps of olivine crystals were obtained by electron backscatter diffraction (EBSD) using the FEI Quanta 650 FEG-SEM at the University of Leeds Electron Microscopy and Spectroscopy Centre (LEMAS). A total of six mounts containing olivine crystals were prepared for diffusion modelling-related analyses (EPMA, EBSD). Details on EBSD analyses are included in Paper II (see section 10.1).

Trace element and oxygen isotope compositions of groundmass glasses and melt inclusions were acquired by secondary ion mass spectrometry (SIMS) at the NordSim laboratory located in the Department of Geosciences at the Swedish Museum of Natural History in Stockholm, Sweden. I made a total of four epoxy mounts (AC1-4 mounts) with MI-bearing crystals and glass chips. Oxygen isotope compositions of groundmass glass chips were also measured by the laser fluorination (LF) method at the University of Texas at Austin. Details on SIMS and LF techniques are reported in the supplementary material of paper III (see section 11.1).

I calculated magma storage pressures based on: (1) Olivine–plagioclase–augite–melt (OPAM) barometer (Hartley et al., 2018; Yang et al., 1996); and (2) clinopyroxene-melt barometer (Neave and Putirka, 2017). The OPAM barometer was applied to both groundmass glasses and melt inclusions and it has a standard error of the estimate (SEE) of ±1.3 kbar (Hartley et al., 2018). The new clinopyroxene-melt barometer of Neave and Putirka (2017) is calibrated for ultramafic to intermediate compositions and it reproduces the calibration data with a SEE of ±1.4 kbar. Magma storage temperatures were calculated following the liquid-only and mineral-melt equations reported in Putirka (2008). More details about thermobarometry calculations and associated uncertainties are reported in the supplementary material of paper I (see section 9.1).

2.1 Diffusion chronometry

Diffusion chronometry is a method based on the extent to which ion exchange reactions respond to changes in environmental conditions, such as temperature, pressure, composition and/or oxygen fugacity (Dohmen et al., 2017). Minerals crystallizing from magmas respond texturally and compositionally to those changes by growing zones with different compositions which contain information about past events (Costa et al., 2008; Kahl et al., 2011, 2013, 2015, 2017; Shea et al., 2015; Dohmen et al., 2017). Chemical potential gradients across compositional zones are smoothed out with time as a result of diffusion processes. Therefore, diffusion chronometry involves modelling the diffusive relaxation process from specific initial conditions, which reflect the composition of the crystal at the time the perturbation was introduced, to the point at which diffusion stopped to play a role (e.g. eruption) (Fig. 2.1). Relaxation of chemical gradients in crystals is similar to relaxation of gradients in topography, due to erosion processes. In the case of zoning in crystals, the gradients are chemical potentials, while in case of topography they are potential energy (Costa and Morgan, 2010).

Diffusion can be described as the movements of particles relative to other particles in a region of many particles (Onsager, 1945). At the microscopic scale, it is the relative movement of ions within the crystal lattice, which requires defects in the crystal structure, such as dislocation or vacancies (Costa and Morgan, 2010). The rate at which diffusion happens is a complex function of the diffusion mechanism, the point defect chemistry of the crystal, the temperature and the geometry of the interface across which diffusion occurs (Dohmen et al., 2017).

Fick's second law (diffusion equation) expresses the concentration variation as a function of time:

$$\frac{\partial C_i(x,t)}{\partial t} = \frac{\partial}{\partial x}\left(D_i \frac{\partial C_i(x,t)}{\partial x}\right)$$

where C_i is the concentration of element i, x denotes the distance, D_i is the compositionally dependent diffusion coefficient of element i, and t is time. The rate at which chemical elements diffuse is expressed by the diffusion coefficient. The Fe-Mg diffusion coefficient in olivine is a function of T, P, X, fO_2 (Dohmen et al., 2007) and its expression in $\mu m^2/s$ along crystal sections parallel to [001] is:

$$X_{Fe-Mg} = 6.21 \cdot 10^2 \cdot \left(\frac{f_{O2}}{10^{-7}}\right)^{\frac{1}{6}} \cdot 10^{3(0.9-Fo)} \cdot \exp\left(-\frac{201000 + (P - 10^5) \cdot 7 \cdot 10^{-6}}{RT}\right)$$

where T is in Kelvin, P and fO_2 in Pascal, Fo the mole fraction of the forsterite component and R is the gas constant in $J \cdot mol^{-1} \cdot K^{-1}$. In this thesis, I focus on Fe-Mg, Mn and Ni diffusion in olivine crystals, using experimentally determined diffusion coefficients (Fe-Mg, Mn, Dohmen and Chakraborty, 2007; Dohmen et al., 2007; Ni, Petry et al., 2004; Holzapfel et al., 2007).

The crystallographic orientation has an important effect on the diffusion coefficient, because diffusion in non-cubic crystals is anisotropic, in the same way that optical properties are. The diffusion coefficient along an arbitrary direction can be calculated if the diffusion coefficients along the three principal axes are known (Costa et al., 2008). For example, Fe-Mg diffusion in olivine is about six times faster along the [001] axis than along the [100] and [010] axes (Chakraborty, 1997; Dohmen et al., 2007).

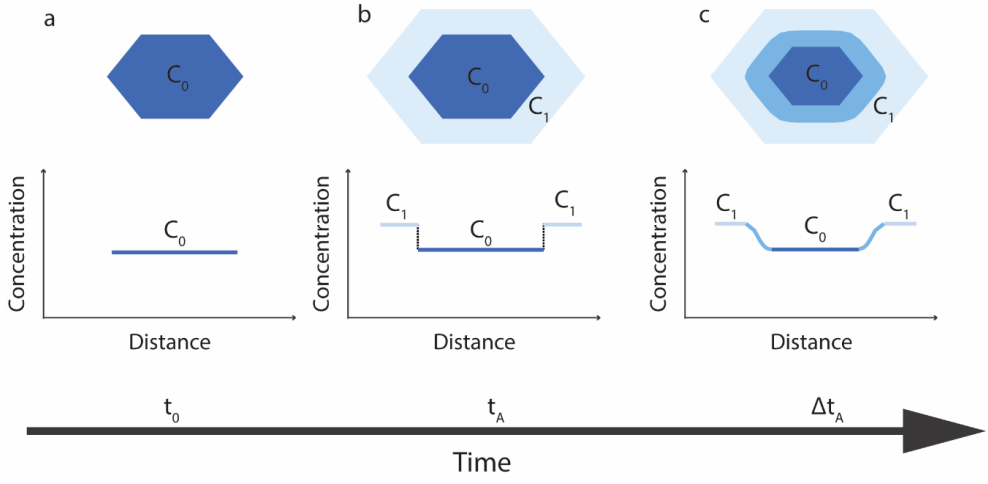

Fig. 2.1. *Schematic illustration, modified after Kahl et al. (2011), showing the main concept behind diffusion chronometry methods. a) An initially homogeneous crystal, with concentration C_0 at time t_0. b) Crystallization of a new compositional plateau (C_1) as a result of a change in one or more environmental variables (X, P, T, fO_2) and formation of a concentration gradient. This results in a stepped initial profile (dotted black line). c) Diffusion acts to relax the gradient between the two compositional plateaux and the initial concentration profile is smoothed within a timescale Δt_a, after which diffusion effectively stops (e.g. as a result of a temperature drop upon eruption).*

The progressive evolution of the concentration profile (Fig. 2.1) is tracked assuming appropriate initial and boundary conditions. Initial conditions refer to the initial shape of the profile, before diffusive modification started (Fig. 2.1b). The reconstruction of the initial profile can be complex and different strategies have been proposed (Kahl et al., 2011). In most of the crystals studied in this thesis, I assumed homogenous initial profiles, guided by the occurrence of extended compositional plateaux at the cores, which are unaffected by diffusion. Boundary conditions reflect the type of boundary between the crystal and the surrounding medium at the crystal rim. In my models, I considered crystal boundaries to be open and in contact with a melt of fixed composition.

The evolution of the concentration with time is then obtained numerically using an explicit one dimensional finite difference method (Costa et al., 2008). For my modelling, I created my own Matlab code which models diffusion of Fe-Mg, Mn and Ni in olivine crystals, using the form of the diffusion equation (expression A2) reported in Costa et al. (2008). The space and time coordinates are discretized into small and finite increments to build a

grid, with a step size Δx along the space coordinate and Δt along the time coordinate. With this method, one can calculate the concentration at any given grid point at a certain number of time steps. Numerical implementations usually require a trade-off between spatial and temporal resolutions, which is assessed based on the Courant-Friedrichs-Lewy (CFL) condition. The stability of the numerical solution is expressed by:

$$r = \frac{D\Delta t}{\Delta x^2} < 0.5$$

where Δx was set to 5 µm, which is a good compromise between calculation speed and the resolution of the analysed diffusion profiles (3-6 µm). In my modelling, I set a specific value of r=0.3 to have the CFL condition fulfilled. Having defined r, Δx and the diffusion coefficient, I could calculate the time increments Δt at any given time step. I therefore manually changed the number of time steps until a best-fit curve for a given Fe-Mg diffusion profile was observed (Fig. 2.2). Subsequently, I used the same time step and the identical initial and boundary conditions to model diffusion of Mn and Ni. If the calculated curves fit the measured profile shapes, I assumed that zoning profiles were controlled by diffusion. The whole time was then obtained multiplying the time increments by the number of timesteps.

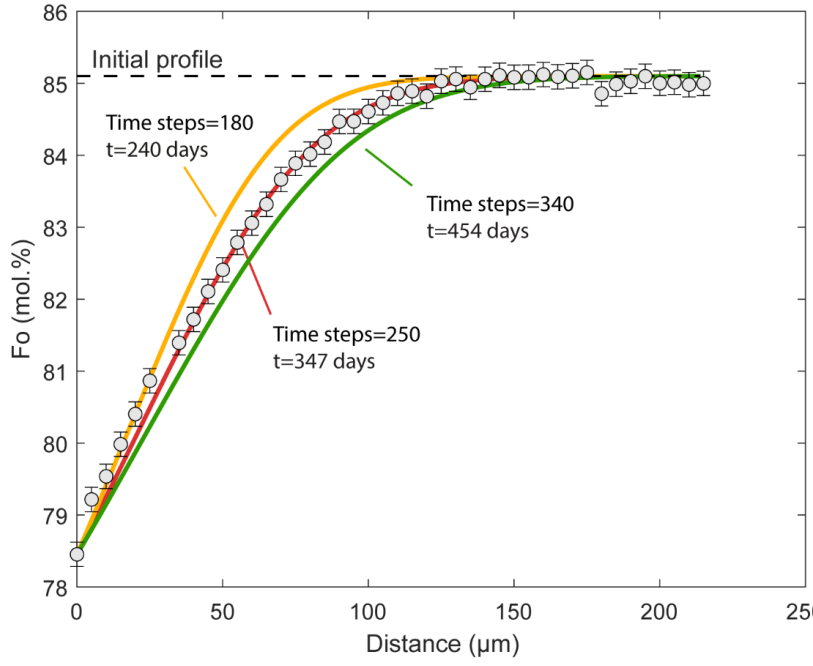

Fig. 2.2. *An example illustrating how the compositional zoning patterns were modelled. For this specific crystal from Brandur locality, the yellow, red and green line indicate the concentration after 180, 250 and 340 time steps, respectively, starting from the inferred initial profile (black dotted line). By manually changing the number of time steps, one could observe the evolution of the diffusion profile with respect to the measured EMPA profile (grey circles), until the best match (red line) with the measured profile was observed*

3 Paper I : Temporal evolution of magma and crystal mush storage conditions in the Bárðarbunga-Veiðivötn volcanic system, Iceland

3.1 Summary and main results

Unravelling the depth of magma storage beneath active volcanoes is essential for interpreting geodetic and geophysical signals of volcanic unrest. However, the location of eruption-feeding magma storage reservoirs within the crust may change with time, with important implication for time-integrated models of crustal formation mechanism and future eruption mitigation.

Nowadays, magma plumbing systems are envisioned as composed of multi-level magma storage horizons embedded in crystal mush zones, which are dynamic levels in which the melt is distributed through a continuous framework of crystals (Cashman et al., 2017; Maclennan, 2019). Therefore, crystal mushes contain vital information on the pressure, temperature, composition and processes occurring underneath active volcanoes. In this study I examined and characterized unstudied crystal mush-bearing samples erupted in the period from the Weichselian glaciation until historical time in the Bárðarbunga-Veiðivötn volcanic system to unravel temporal snapshots of magma storage conditions underneath Central Iceland.

To examine the temporal changes of magma storage reservoirs, I studied the composition of macrocrysts, groundmass glasses and melt inclusions and I merged those data with geothermobarometry calculations. I calculated magma storage depths using the olivine-plagioclase-augite-melt (OPAM) barometer (Hartley et al., 2018; Yang et al., 1996) on glasses and melt inclusions along with the clinopyroxene-melt barometer described by Neave and Putirka (2017).

The major results and conclusions of this work are as follows:

- Samples from all eruptive units contain evidence of entrainment of crystal mush fragments. The composition of the cores of plagioclase, olivine and clinopyroxene crystrals is too primitive to be in equilibrium with the liquid that carried them to the surface. In addition, the composition of the rims is in chemical equilibrium with the carrier liquid. This suggests that macrocrysts were stored in crystal mushes and later incorporated in the carrier liquid.
- The chemical composition and the major element compositional variability of the carrier liquid changes with time. The most primitive carrier liquid is erupted in the time of glaciation (MgO 8.0-8.5 wt%), whereas the MgO content of the carrier liquid decreases from the middle-Holocene (7.0-7.5 wt%) to historical time (6.3-6.8 wt%), with the largest variability observed in early-Holocene time (5.5-7.5 wt%).
- Primitive melt inclusions, which are thought to provide chemical information about early stages of magma history, record large chemical variability which tends to decrease as melt evolution proceeds. This suggests that compositionally diverse

primary melts were supplied to the Bárðarbunga-Veiðivötn volcanic system. However, during their journey towards the surface, the melts underwent concurrent mixing and crystallization processes (Maclennan, 2008) that masked their original fingerprints.

- The composition of plagioclase and olivine macrocrysts varies with time. Macrocryst compositions become more evolved and more variable with time. Particularly, primitive compositions (An_{90-92}, Fo_{85-87}) become less abundant and/or completely lack in middle-Holocene and historical magmatic units. Similarly, evolved macrocrysts compositions (An<86, Fo<81) are exclusively found in middle-Holocene and historical samples.
- Barometry calculations on groundmass glasses and clinopyroxenes highlight temporally invariant mid-crustal crystallization conditions in a reservoir(s) located at around 7.3 ± 2.7 (1σ) depth, in good agreement with petrological and geophysical results obtained for the 2014-15 Holuhraun eruption. In addition, OPAM equilibration pressures of melt inclusions hosted in primitive crystals from the oldest magmatic units strongly suggest that in glacial and early-Holocene time macrocrysts crystallized in deep-seated reservoir(s) located down to 25 km depth. This deep crystallization record is not observed in middle-Holocene and historical samples (Fig. 3.1), pointing out the lack of contribution of deep-seated, lower crustal, storage reservoir(s).
- Isostatic adjustments and glacial rebound effects that affected the Icelandic crust during the postglacial time, along with the increase in magma production rates (Le Breton et al., 2016; Maclennan et al., 2002; Slater et al., 1998), may be responsible for the tapping of lower-crustal reservoir in the early-Holocene. In contrast, the dominance of mid-crustal reservoir during the middle-Holocene and historical time may be associated with the establishment of a long-term, presently observed, crustal pressure equilibrium.

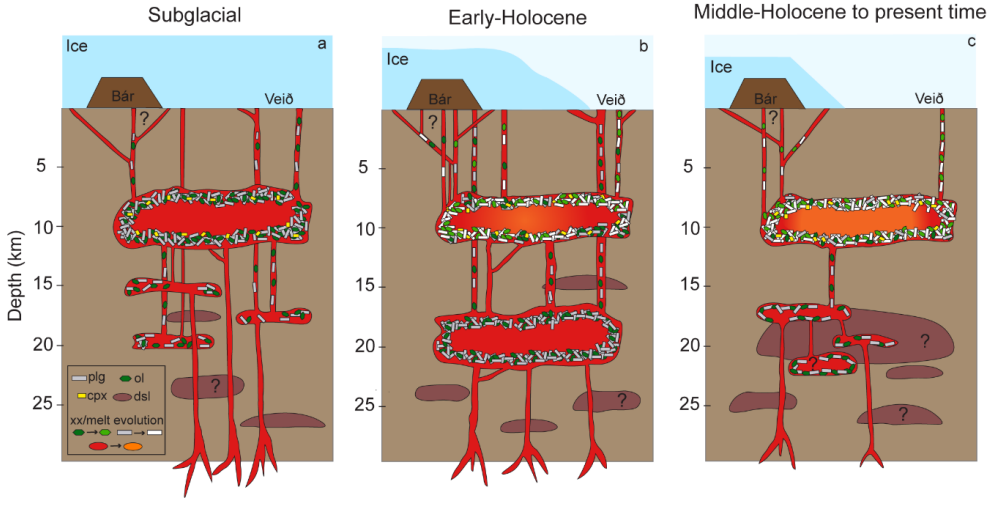

Fig. 3.1. *Schematic cartoon showing the plumbing architecture of the Bárðarbunga-Veiðivötn volcanic system during the (a) subglacial, (b) early-Holocene and (c) middle-Holocene to historical time.*

4 Paper II: Timescales of crystal mush mobilization in the Bárðarbunga-Veiðivötn volcanic system based on olivine diffusion chronometry

4.1 Summary and main results

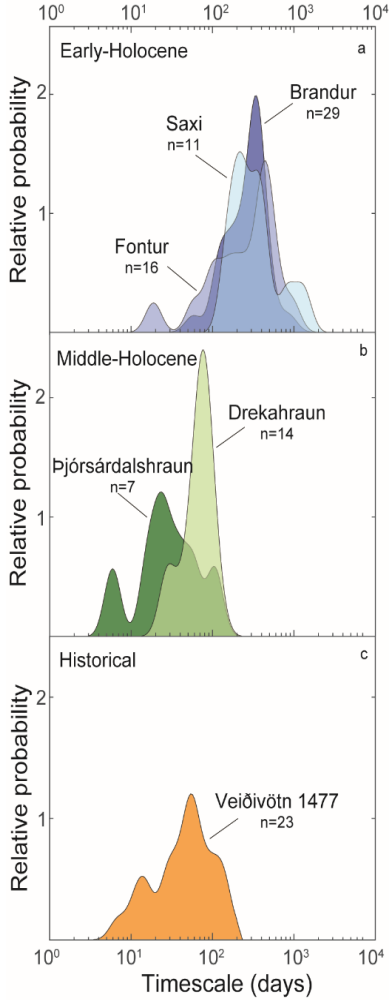

The timescales of magmatic processes within a volcanic system may be variable over a volcano's geological history. The chemical zoning observed in crystals reflects changes in the physical and/or chemical conditions of the reservoir under which they grew and compositional pattern may record the timescales of magmatic processes. By modelling the relaxation of crystal zoning patterns with diffusion chronometry, it is possible to calculate the timescales over which the process that caused the zonation occurred.

Textural and chemical evidence indicates that macrocrysts found in the Holocene sample suite from the Bárðarbunga-Veiðivötn magmatic system were stored and later disaggregated and/or mobilised from crystal mush horizons. Macrocrysts were mobilised by the carrier melt which is responsible for the outermost zoning observed in olivine crystals. Therefore, I used multi-element (Fe-Mg, Mn and Ni) diffusion chronometry in olivine crystals to calculate the time that elapsed between the disaggregation/mobilisation of crystal mush following melt injection, when chemical re-equilibration with the carrier liquid started, and the eruption, when diffusion stopped to play a role. In this study, I determined how crystal mush disaggregation timescales have changed over time within the Bárðarbunga-Veiðivötn volcanic system, with direct implications for future eruption forecasting. In addition, I merged diffusion modelling results with prior geobarometry constraints (Caracciolo et al. 2020) to reconstruct the depth at which these processes occurred.

Fig. 4.1. *Probability distribution of calculated timescales for (a) early-Holocene units, (b) middle-Holocene units and (c) historical unit. n=number of olivine macrocrysts modelled for each locality.*

The major results and conclusions of this work are as follows:

- Macrocryst contents vary between studied samples, with early-Holocene units being highly porphyritic (10-45 vol%) and containing gabbroic nodules, whereas middle-Holocene and historical units are less phyric (5-15 vol%).
- Olivine macrocrysts analysed for diffusion modelling show primitive core compositions in the early-Holocene time (Fo_{84-87}), but become more evolved and variable ($Fo_{80-86.5}$) in the middle-Holcoene and historical time.
- Most of the olivine macrocrysts show normal zoning. Namely, the forsterite content decreases towards the rims.
- The groundmass glass, which is assumed to represent the composition of the carrier liquid, is in chemical equilibrium with olivine macrocryst rims. This suggests that the outermost zoning was produced by interaction with a melt which was more evolved than the one that crystallized the cores. I believe that this process caused disaggregation of crystal mush clots and the onset of the diffusion clock.
- Crystal mush disaggregation timescales are found to change over time (Fig. 4.1). Early-Holcoene olivine macrocrysts record long and variable timescales, with most being in the range 200-400 days. Oppositely, middle-Holocene and historical macrocrysts typically re-equilibrated within timescales of about 70 and 60 days respectively.

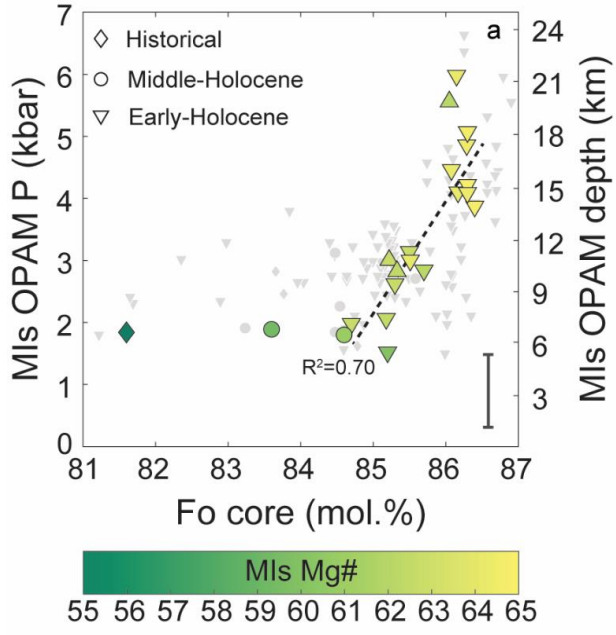

Fig. 4.2. *Olivine core compositions plotted versus MI OPAM pressures. Grey symbols are olivine-hosted MIs from Caracciolo et al. (2020). Symbols are coloured according to their Mg#. A positive correlation is observed between pressure and olivine and MI compositions.*

- I link the variation in disaggregation timescales to the occurrence of a more densely-packed mush fabric in the early-Holocene compared to recent time, as evidenced by the large macrocryst contents and the presence of gabbroic nodules in the early-Holocene samples. Since the middle-Holocene, the mush system is likely characterized by a large melt-mineral ratio, such that melts would rapidly mobilise mush clots within a couple of months.
- I observe a positive correlation between olivine compositions, MI equilibration pressures and MI compositions (Fig. 4.2). As olivine crystallization depth decreases, the composition of MIs and olivines gets more evolved.
- I propose that within the Bárðarbunga-Veiðivötn magmatic system, melts and crystals are gradually transported upwards throughout a multi-tiered system that culminates in a mid-crustal reservoir(s) at about 7-11 km depth, where final disaggregation by the carrier liquid takes place.

5 Paper III: Oxygen isotope evidence for progressively assimilating trans-crustal magma plumbing systems in Iceland

5.1 Summary and main results

The Bárðarbunga-Veiðivötn volcanic system is envisioned as a multi-tiered system of interconnected stacked sills in which magmas are processed over a large range of depths. Once primary melts are supplied into the plumbing system, they start their journey towards the surface and are likely to experience several processes that modify the original mantle-like signatures. For example, concurrent mixing and crystallization throughout the crust has been held responsible for masking compositional diversity of primary melts supplied underneath Icelandic volcanoes (Maclennan, 2008). Also, it has been recognised that crustal rocks are able to modify the oxygen isotope composition of primary melts, with important implication for basalt petrogenesis. Oxygen isotope values of Iceland's crustal rocks differ significantly from mantle values. This is because Iceland is located at high latitudes and receives strongly ^{18}O-depleted precipitations which penetrate into the Icelandic crust and causes upper crustal rocks to become ^{18}O-depleted relative to the mantle (Gautason and Muehlenbachs, 1998). Models of crustal accretions along axial rift zones suggest that the altered basaltic pile is typically ~7-10 km thick (Foulger et al., 2003; Jenkins et al., 2018; Pálmason, 1986). However, at present, our understanding of how and where Icelandic melts are affected by crustal contamination across trans-crustal magmatic systems is limited.

With the intent of quantifying the extent of oxygen isotope exchange as melts ascend through the crust, I present new determinations of trace element contents and oxygen isotope ratios ($\delta^{18}O$) in melt inclusions and groundmass glasses from the Bárðarbunga volcanic system. Furthermore, I combine trace element and $\delta^{18}O$ data with geobarometry calculations, to unravel at which depth in the Icelandic crust assimilation processes modify the $\delta^{18}O$ values of Icelandic basalts.

The major results and conclusions of this work are as follows:

- As commonly observed in Iceland, primitive melts from the Bárðarbunga volcanic system are typically ^{18}O-depleted compared to MORB, which has $\delta^{18}O$ =5.7±0.2 ‰. Melt inclusion $\delta^{18}O$ values vary between +3.2‰ and +6.4‰. Groundmass glasses have $\delta^{18}O$ values between +2.6‰ and +5.5‰, on average lower than $\delta^{18}O$ valyes of melt inclusion (Fig. 5.1).
- $\delta^{18}O$ values decrease with decreasing MgO content. This correlation is usually linked to assimilation of hydrothermally altered crustal rocks. Similarly, the trace element variability (e.g. Zr/Nb) collapses as a function of melt evolution. This suggests that as melts become more evolved, they go through concurrent mixing and crystallization (Maclennan et al. 2008).

- The existence of a geochemically enriched, isotopically light domain in the Icelandic mantle has been demonstrated by several studies (e.g. Macpherson et al., 2005; Thirlwall et al., 2006). Therefore, I carried out the modelling (Fig. 5.1) assuming that, in addition to the crustal endmember, the variation of $\delta^{18}O$ values is controlled by the existence of depleted (DM) and enriched (EM) mantle domains underneath Bárðarbunga volcano, as observed elsewhere in Iceland.

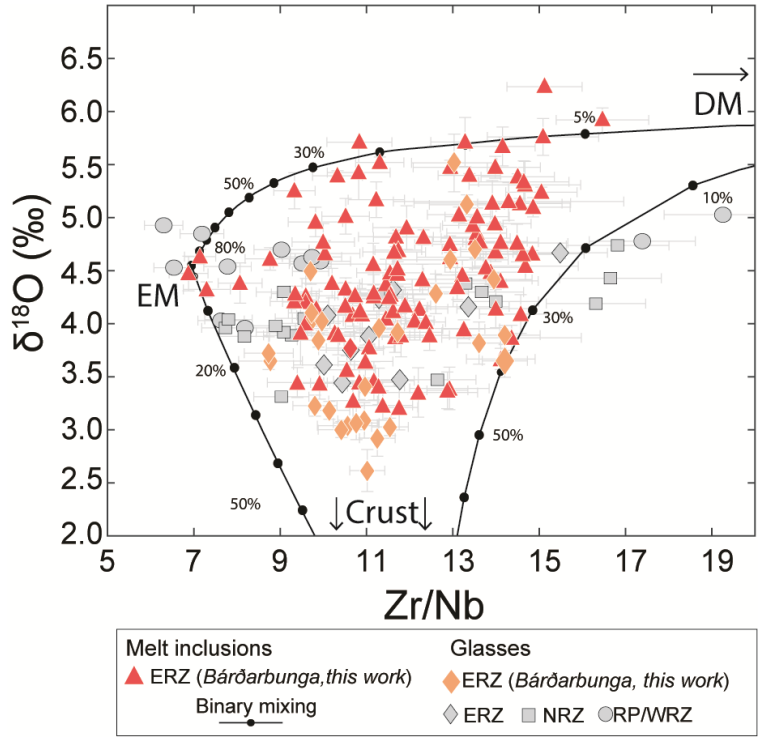

Fig. 5.1*. MI and groundmass glass variations of $\delta^{18}O$ values as a function of Zr/Nb for the Bárðarbunga dataset (red and orange symbols) and for published and unpublished subglacial glasses from Iceland's neovolcanic zones (see section 11.1). Black lines indicate binary mixing between DM, EM and the crust.*

- I carefully estimated the trace element and oxygen isotope compositions of the crust and the mantle endmembers and I modelled binary mixing processes between the different pairs of the endmembers. Any datapoint is the result of at least three-step process: (1) Melting of DM and EM domains at different degree of partial melting; (2) Melts originating from DM and EM domains mix together in different proportions; (3) Supply of primary mixtures and their contamination as they acent in the Icelandic crust.
- Assuming a crust with $\delta^{18}O$ = 0‰, I estimated that up to 55% of oxygen isotope exchange is required to explain the lowest $\delta^{18}O$ values recorded by groundmass glasses, with most of the extent of oxygen isotope exchange being in the range 20-30%. The extent of oxygen isotope exchange is commonly used as a proxy of crustal assimilation.

- The positive correlation between MI equilibration pressure, oxygen isotope exchange and melt composition (MgO content) (Fig. 5.2) indicates that as melts move towards the surface, they become more contaminated by the crust. In particular, most of the contamination occurs in the upper and middle crust between 3.5 and 10 km depth, where the shallowest reservoir(s) is inferred to be located.
- Based on my data, I envision the Bárðarbunga plumbing system as a progressively assimilating multi-tiered plumbing system where, as melts move shallower in the crust, they get more evolved and they assimilate more crustal material.

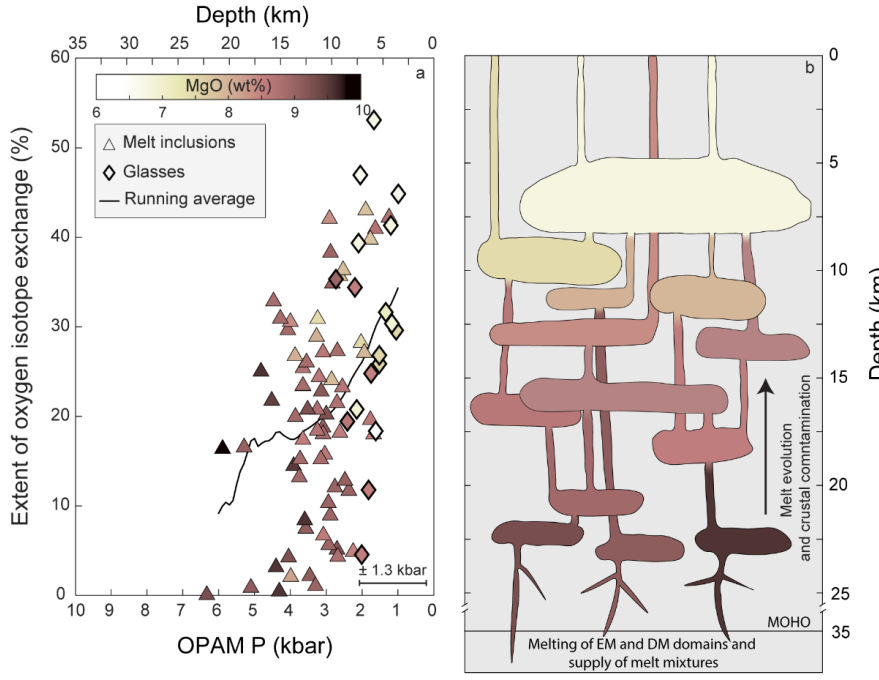

Fig. 5.2*. (a) The relationship between MI and glass equilibration pressures, extent of oxygen isotope exchange and melt composition (b) Cartoon illustrating the plumbing architecture of the Bárðarbunga volcanic system based on oxygen isotope data.*

6 The Ljósufjöll paradox

In the first paper I describe the petrography and mineral chemistry of the extrusives from Ljósufjöll, the subglacial unit of my sample set. However, this magmatic unit is not taken into consideration in the diffusion paper (paper II), the reason being the lack of zonation in the original olivine cargo. Nonetheless, I find it important to explain in more detail the case of the Ljósufjöll magmatic unit.

The Ljósufjöll samples consist of pillow lava with glassy rinds. On a thin section scale, samples display a coarse-grained groundmass (Fig. 6.1b-d) composed of plagioclase, clinopyroxene, olivine and oxide crystals, which fade into a cryptocrystalline and glassy matrix (Fig. 6.1 a-c) towards the margins of the pillows. The composition of plagioclase and olivine rims appears to be related to the groundmass texture. Plagioclase rims in contact with the coarse-grained groundmass are thicker (30-70 µm) and their composition is in the range An_{65-71}, while rims in contact with the glassy matrix are thinner (10-40 µm) and more primitive, in the range An_{79-86}. Plagioclase macrocryst cores record a narrow compositional range ($An_{86-90.5}$). Olivine crystals adjacent to glassy groundmass are unzoned (Fig. 6.1a) and their composition is in the range Fo_{84-87}. Zoned olivines from Ljósufjöll (Fig. 6.1b) are exclusively found next to the coarse-grained groundmass and the rims have a composition of $Fo_{71-77.5}$.

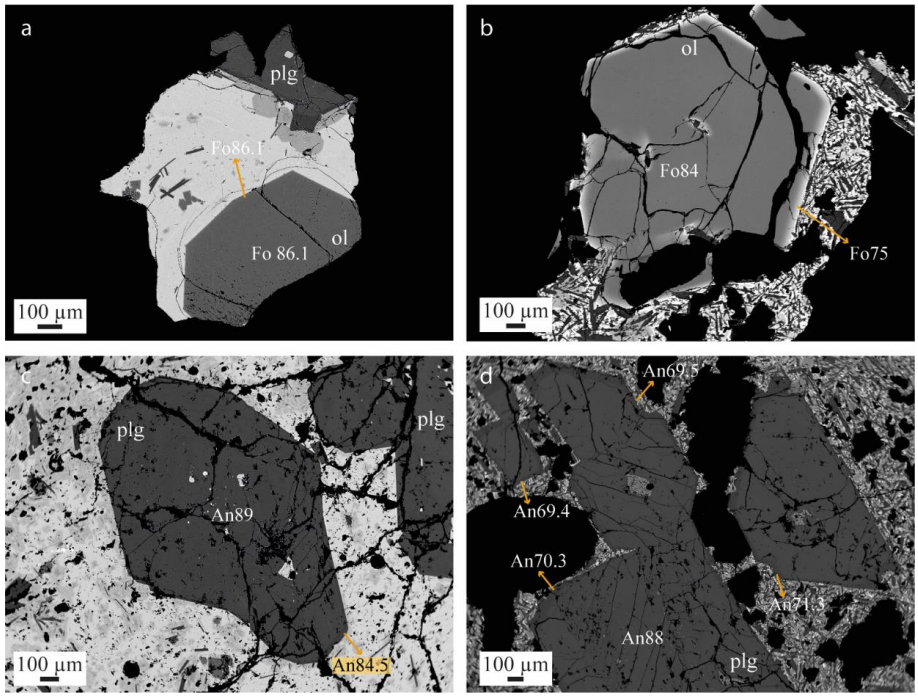

Fig. 6.1 *Backscatter electron (BSE) images showing the petrographic features of olivine (a-b) and plagioclase (c-d) crystals from Ljósufjöll. Note the different texture of the groundmass and the different zoning patterns. Orange arrows indicate the composition of crystal rims. Fo:forsterite; An:anorthite; plg:plagioclase; ol:olivine.*

These differences in texture and composition may be related to the fact that Ljósufjöll samples come from a pillow lava, whose interior had longer time to cool and crystallize. I propose that the macrocrysts incorporated within the glassy groundmass are representative of the original cargo, while the ones scattered in the coarse-grained groundmass have experienced post-emplacement processes (e.g. crystallization of the groundmass and growth of thicker crystal rims during pillow cooling).

The liquid that carried Ljósufjöll macrocrysts to the surface is the most primitive of the studied eruptive units, with MgO in the range 8.0-8.5 wt%. This liquid is found to be close to chemical equilibrium only with some of the plagioclase rims (Fig. 6.1c) formed in the glassy matrix. All other magmatic units studied in this thesis have more evolved carrier liquid compositions (MgO 6.2–7.5 wt%) which are found to be in equilibrium with olivine and plagioclase rims in the respective units. In the case of Ljósufjöll, it is not straightforward to explain the simultaneous presence of equilibrium plagioclase rims and the lack of analogous rims around the olivines. I propose two possible scenarios:

1. *Olivine rims have been reset by diffusion processes.* It is possible that rims grew on olivine macrocrysts but have been reset by diffusion processes due to a prolonged interaction with the carrier liquid. Oppositely, plagioclase rims were preserved due to the very sluggish coupled inter-diffusion rates of NaSi and CaAl in plagioclase. Indeed, the Fe-Mg diffusion coefficient in olivines is much faster than the NaSi-CaAl diffusion coefficient of plagioclase (e.g. Grove et al., 1984). This enhances the ability of plagioclase to conserve major element zonation patterns. However, if this were the case, I would expect to see chemical zonation in olivines with respect to slowly diffusing elements (e.g. Ca, Cr, P), whereas three chemical maps acquired of unzoned olivines do show either completely homogeneous olivines or a slight enrichment in Fe at the rims, and I do not see any chemical variation in the slowly diffusing elements.

2. *Short timescales of crystal transport*. The second scenario envisions that macrocrysts were disaggregated from the mush pile within a very short time before the eruption, impeding olivine-melt diffusion re-equilibration. This would explain the lack of zonation of olivine crystals, suggesting a brief melt-crystal interaction. This scenario is also consistent with the primitive composition of Ljósufjöll carrier liquid, which suggests that it did not have time to evolve and/or interact with more evolved melts. Crystallization of plagioclases is more affected by other parameters than just melt composition, like water content. In this scenario, the occurrence of plagioclase rims could be related to degassing inducing crystallization (e.g. Applegarth et al., 2013).

A further argument for a fast ascent comes from $\delta^{18}O$ values of Ljósufjöll groundmass glasses. $\delta^{18}O$ values are found to be highly variable, in the range 3.9-5.5 ‰, with many of them being close to mantle-like values. Assuming an isotopically light crust in the subglacial period, this observation suggests that the Ljósufjöll carrier liquid did not reside for a long time in the shallow part of the crust and did not experience large amounts of crustal contamination. However, this is not consistent with final equilibration depths calculated for Ljósufjöll carrier liquid. OPAM equilibration pressures of Ljósufjöll groundmass glasses are in the range 1.4-2.7 kbar, with a mean of 2.1±0.4 kbar. This result suggests that olivine, plagioclase and clinopyroxene have crystallized in equilibrium with the carrier liquid in upper to mid-crustal reservoir(s).

7 Concluding remarks

Magma batches underneath Icelandic volcanoes are thought to be processed at different depths across the entire crustal section and these depths may change over the geological history of a volcano. This study is the first to assess temporal changes of magma storage depths, magmatic processes, crystal and melt compositions within the scale of a single volcanic system. I carried out a petrological-geochemical study, coupled with diffusion modelling and oxygen isotope analyses, on a unique sample suite from the Bárðarbunga-Veiðivötn volcanic system in central Iceland to unravel temporal changes that occurred underneath that volcanic system from the Weichselian glaciation to historical time.

I envision the Bárðarbunga-Veiðivötn volcanic system as a multi-tiered system of interconnected stacked sills in which magmas gradually move upwards to higher levels, until they accumulate in mid-crustal reservoirs located at around 7-11 km depth. These sills are dominated by crystal mushes, where storage and later disaggregation plays an important role in the petrogenesis of the studied eruptive products. Crystals and melts indicate that the plumbing system is compositionally layered. Their compositions become more evolved as they move upwards in the crustal section, with primitive, deep-seated crystal phases being mostly sampled in the subglacial and early-Holocene eruptive products. However, relatively evolved crystals are exclusively found in the middle-Holocene and historical eruption products and they crystallized in the middle crust. Therefore, I believe that, as historical time was approached, mid-crustal storage reservoirs came to dominate the plumbing architecture, while in the early-Holocene, the plumbing system was distributed throughout the entire crustal section.

The occurrence of a multi-level system also influences the depth and the extent to which melts are contaminated by crustal rock. Most of the contamination that affects oxygen isotope values occurs in the middle crust, with a correlation between oxygen isotope values and melt equilibration depths suggesting a progressively assimilating magmatic column. The Bárðarbunga plumbing system culminates in a shallow (7-11 km) reservoir(s) from where magmas are withdrawn during eruptions. Rifting events may be responsible for the remobilization of melt pockets that intrude the shallow reservoir, causing the destabilization of the crystal mush pile and triggering eruptions. My kinetic modelling shows that crystal mush fragments were disaggregated within timescales of 4-12 months in the early-Holocene, while only about 2 months passed during historical time.

One of the most important implications of my study is that in the Bárðarbunga-Veiðivötn volcanic system the time between disaggregation of mush piles and eruption has decreased considerably over the geological time, indicating that the modern volcanic system is responding faster to melt injection with shorter warning time prior to eruptions. Application of a similar multidisciplinary approach to volcanoes where the last known eruption occurred long before the installation of state-of-the-art monitoring techniques is the sole option to unravel the potential impact of future eruptions (Hartley et al., 2016).

8 References

Ágústsdóttir, T., Woods, J., Greenfiel, T., Green, R.G., White, R.S., Winder, T., Brandsdóttir, B., Steinthórsson, S., Soosalu, H., 2016. Strike-slip faulting during the 2014 Bárðarbunga- Holuhraun dike intrusion, central Iceland. Geophys. Res. Lett. 43, 1–10. https://doi.org/10.1002/2014GL059364.Received

Applegarth, L.J., Tuffen, H., James, M.R., Pinkerton, H., Cashman, K. V., 2013. Direct observations of degassing-induced crystallization in basalts. Geology 41, 243–246. https://doi.org/10.1130/G33641.1

Bachmann, O., Bergantz, G.W., 2004. On the origin of crystal-poor rhyolites: Extracted from batholithic crystal mushes. J. Petrol. 45, 1565–1582. https://doi.org/10.1093/petrology/egh019

Caracciolo, A., Bali, E., Guðfinnsson, G.H., Kahl, M., Halldórsson, S.A., Hartley, M.E., Gunnarsson, H., 2020. Temporal evolution of magma and crystal mush storage conditions in the Bárðarbunga-Veiðivötn volcanic system, Iceland. Lithos 352–353. https://doi.org/10.1016/j.lithos.2019.105234

Cashman, K. V., Sparks, R.S.J., Blundy, J.D., 2017. Vertically extensive and unstable magmatic systems: A unified view of igneous processes. Science (80-.). 355, 1–9. https://doi.org/10.1126/science.aag3055

Chakraborty, S., 1997. Rates and mechanisms of Fe-Mg interdiffusion in olivine at 980°–1300°C. J. Geophys. Res. 102, 12317. https://doi.org/10.1029/97jb00208

Costa, F., Dohmen, R., Chakraborty, S., 2008. Time Scales of Magmatic Processes from Modeling the Zoning Patterns of Crystals. Rev. Mineral. Geochemistry 69, 545–594. https://doi.org/10.2138/rmg.2008.69.14

Costa, F., Morgan, D., 2010. Time Constraints from Chemical Equilibration in Magmatic Crystals, Timescales of Magmatic Processes: From Core to Atmosphere. https://doi.org/10.1002/9781444328509.ch7

Darbyshire, F.A., White, R.S., Priestley, K.F., 2000. Structure of the crust and uppermost mantle of Iceland from a combined seismic and gravity study. Earth Planet. Sci. Lett. 181, 409–428. https://doi.org/10.1016/S0012-821X(00)00206-5

Dohmen, R., Becker, H.W., Chakraborty, S., 2007. Fe-Mg diffusion in olivine I: Experimental determination between 700 and 1,200°C as a function of composition, crystal orientation and oxygen fugacity. Phys. Chem. Miner. 34, 389–407. https://doi.org/10.1007/s00269-007-0157-7

Dohmen, R., Chakraborty, S., 2007. Fe – Mg diffusion in olivine II : point defect chemistry , change of diffusion mechanisms and a model for calculation of diffusion coefficients in natural olivine. Phys. Chem. Miner. 34, 409–430. https://doi.org/10.1007/s00269-007-0158-6

Dohmen, R., Faak, K., Blundy, J.D., 2017. Chronometry and Speedometry of Magmatic Processes using Chemical Diffusion in Olivine, Plagioclase and Pyroxenes. Rev. Mineral. Geochemistry 83, 535–575. https://doi.org/10.2138/rmg.2017.83.16

Edmonds, M., Cashman, K. V, Holness, M., Jackson, M., 2019. Architecture and dynamics of magma reservoirs. Philos. Trans. R. Soc. A Math. Phys. Eng. Sci. 377, 1–29.

Einarsson, P., 2018. Short-term seismic precursors to icelandic eruptions 1973–2014. Front. Earth Sci. 6, 3–8. https://doi.org/10.3389/feart.2018.00045

Einarsson, P., 2008. Plate boundaries , rifts and transforms in Iceland. Jokull 58, 35–58.

Farrell, J., Smith, B.R., Husen, S., Diehl, T., 2014. beyond the Yellowstone caldera. AGU Publ. Geophys. Res. Lett. 41, 3068–3073. https://doi.org/10.1002/2014GL059588.Received

Foulger, G.R., Du, Z., Julian, B.R., 2003. Icelandic-type crust 567–590.

Gautason, B., Muehlenbachs, K., 1998. Oxygen isotopic fluxes associated with high-temperature processes in the rift zones of Iceland. Chem. Geol. 145, 275–286. https://doi.org/10.1016/S0009-2541(97)00148-4

Greenfield, T., White, R.S., 2015. Building icelandic igneous crust by repeated melt injections. J. Geophys. Res. Solid Earth 120, 7771–7788. https://doi.org/10.1002/2015JB012009

Greenfield, T., White, R.S., Roecker, S., 2016. The magmatic plumbing system of the Askja central volcano, Iceland, as imaged by seismic tomography. J. Geophys. Res. Solid Earth 121, 7211–7229. https://doi.org/10.1002/2016JB013163

Grove, T.L., Baker, M.B., Kinzler, R.J., 1984. Coupled CaAl-NaSi diffusion in plagioclase feldspar: Experiments and applications to cooling rate speedometry. Geochim. Cosmochim. Acta 48, 2113–2121. https://doi.org/10.1016/0016-7037(84)90391-0

Haddadi, B., Sigmarsson, O., Larsen, G., 2017. Magma storage beneath Grímsvötn volcano, Iceland, constrained by clinopyroxene-melt thermobarometry and volatiles in melt inclusions and groundmass glass. J. Geophys. Res. Solid Earth 122, 6984–6997. https://doi.org/10.1002/2017JB014067

Halldórsson, S.A., Bali, E., Hartley, M.E., Neave, D.A., Peate, D.W., Guðfinnsson, G.H., Bindeman, I., Whitehouse, M.J., Riishuus, M.S., Pedersen, G.B.M., Jakobsson, S., Askew, R., Gallagher, C.R., Guðmundsdóttir, E.R., Gudnason, J., Moreland, W.M., Óskarsson, B. V, Nikkola, P., Reynolds, H.I., Schmith, J., Thordarson, T., 2018. Petrology and geochemistry of the 2014–2015 Holuhraun eruption, central Iceland: compositional and mineralogical characteristics, temporal variability and magma storage. Contrib. to Mineral. Petrol. 173, 1–25. https://doi.org/10.1007/s00410-018-1487-9

Halldórsson, S.A., Oskarsson, N., Gronvold, K., Sverrisdottir, G., Steinthorsson, S., 2008. Isotopic-heterogeneity of the Thjorsa lava — Implications for mantle sources and crustal processes within the Eastern Rift Zone , Iceland. Chem. Geol. 255, 305–316. https://doi.org/10.1016/j.chemgeo.2008.06.050

Hansen, H., Grönvold, K., 2000. Plagioclase ultraphyric basalts in Iceland : the mush of the rift. J. Volcanol. Geotherm. Res. 98, 1–32.

Harðardóttir, S., Halldórsson, S.A., Hilton, D.R., 2018. Spatial distribution of helium isotopes in Icelandic geothermal fluids and volcanic materials with implications for location, upwelling and evolution of the Icelandic mantle plume. Chem. Geol. 480, 12–27. https://doi.org/10.1016/j.chemgeo.2017.05.012

Hartley, M.E., Bali, E., Maclennan, J., Neave, D.A., Halldórsson, S.A., 2018. Melt inclusion constraints on petrogenesis of the 2014–2015 Holuhraun eruption, Iceland. Contrib. to Mineral. Petrol. 173, 1–23. https://doi.org/10.1007/s00410-017-1435-0

Hartley, M.E., Thordarson, T., 2013. The 1874-1876 volcano-tectonic episode at Askja, North Iceland: Lateral flow revisited. Geochemistry, Geophys. Geosystems 14, 2286–2309. https://doi.org/10.1002/ggge.20151

Hjartarson, A., 1988. Þjórsárhraunið mikla - stærsta nútímahraun jarðar. Náttúrufræöingurinn 58, 1–16.

Hollingsworth, J., Leprince, S., Ayoub, F., Avouac, J.P., 2012. Deformation during the 1975-1984 Krafla rifting crisis, NE Iceland, measured from historical optical imagery. J. Geophys. Res. B Solid Earth 117, 1–24. https://doi.org/10.1029/2012JB009140

Holness, M.B., Anderson, A.T., Martin, V.M., Maclennan, J., Passmore, E., Schwindinger, K., 2007. Textures in partially solidified crystalline nodules: a window into the pore structure of slowly cooled mafic intrusions. J. Petrol. 48, 1243–1264. https://doi.org/10.1093/petrology/egm016

Holness, M.B., Stock, M.J., Geist, D., 2019. Magma chambers versus mush zones: constraining the architecture of sub-volcanic plumbing systems from microstructural analysis of crystalline enclaves. Philos. Trans. R. Soc. A Math. Phys. Eng. Sci. 377, 1–28. https://doi.org/10.1098/rsta.2018.0006

Holzapfel, C., Chakraborty, S., Rubie, D.C., Frost, D.J., 2007. Effect of pressure on Fe-Mg, Ni and Mn diffusion in (FexMg1-x)2SiO4olivine. Phys. Earth Planet. Inter. 162, 186–198. https://doi.org/10.1016/j.pepi.2007.04.009

Hudson, T.S., White, R.S., Greenfield, T., Ágústsdóttir, T., Brisbourne, A., Green, R.G., 2017. Deep crustal melt plumbing of Bárðarbunga volcano, Iceland. Geophys. Res. Lett. 44, 8785–8794. https://doi.org/10.1002/2017GL074749

Jakobsson, S.P., 1979. Petrology of Recent basalts of the Eastern Volcanic Zone, Iceland. Acta Nat. Islandica 26, 1–103.

Jakobsson, S.P., Jònasson, K., Sigurdsson, A., 2008. The three igneous rock series of Iceland. Jökull 58, 117–138.

Jenkins, J., Maclennan, J., Green, R.G., Cottaar, S., Deuss, A.F., White, R.S., 2018. Crustal Formation on a Spreading Ridge Above a Mantle Plume: Receiver Function Imaging of the Icelandic Crust. J. Geophys. Res. Solid Earth 123, 5190–5208. https://doi.org/10.1029/2017JB015121

Jónasson, K., 2007. Silicic volcanism in Iceland: Composition and distribution within the active volcanic zones. J. Geodyn. 43, 101–117. https://doi.org/10.1016/j.jog.2006.09.004

Kahl, M., Chakraborty, S., Costa, F., Pompilio, M., 2011. Dynamic plumbing system beneath volcanoes revealed by kinetic modeling, and the connection to monitoring data: An example from Mt. Etna. Earth Planet. Sci. Lett. 308, 11–22. https://doi.org/10.1016/j.epsl.2011.05.008

Kahl, M., Chakraborty, S., Costa, F., Pompilio, M., Liuzzo, M., Viccaro, M., 2013. Compositionally zoned crystals and real-time degassing data reveal changes in magma transfer dynamics during the 2006 summit eruptive episodes of Mt. Etna. Bull. Volcanol. 75, 1–14. https://doi.org/10.1007/s00445-013-0692-7

Kahl, M., Chakraborty, S., Pompilio, M., Costa, F., 2015. Constraints on the nature and evolution of the magma plumbing system of Mt. Etna volcano (1991-2008) from a combined thermodynamic and kinetic modelling of the compositional record of minerals. J. Petrol. 56, 2025–2068. https://doi.org/10.1093/petrology/egv063

Kahl, M., Viccaro, M., Ubide, T., Morgan, D.J., Dingwell, D.B., 2017. A branched magma feeder system during the 1669 eruption of Mt Etna: Evidence from a time-integrated study of zoned olivine phenocryst populations. J. Petrol. 58, 443–472. https://doi.org/10.1093/petrology/egx022

Kelemen, P.B., Koga, K., Shimizu, N., 1997. Geochemistry of gabbro sills in the crust–mantle transition zone of the Oman ophiolite: implications for the origin of the oceanic lower crust. Earth Planet. Sci. Lett. 146, 1–31. https://doi.org/https://doi.org/10.1016/S0012-821X(96)00235-X

Larsen, G., 2002. A brief overview of eruptions from ice-covered and ice-capped volcanic systems in Iceland during the past 11 centuries: frequency, periodicity and implications. Geol. Soc. London, Spec. Publ. 202, 81–90. https://doi.org/10.1144/GSL.SP.2002.202.01.05

Larsen, G., Guðmundsson, M.T., 2014. Volcanic system : Bárðarbunga system. Cat. Icelandic Volcanoes 1–11.

Le Breton, E., Dauteuil, O., Biessy, G., 2016. Post-glacial rebound of Iceland during the Holocene. J. Geol. Soc. London 167, 417–432. https://doi.org/10.1144/0016-76492008-126.Post-glacial

Lowenstern, J., Sisson, T., Hurwitz, S., 2017. Probing Magma Reservoirs to Improve Volcano Forecasts. Eos (Washington. DC). 98. https://doi.org/10.1029/2017eo085189

Maclennan, J., 2019. Mafic tiers and transient mushes: evidence from Iceland. Philos. Trans. R. Soc. A 377, 1–20. https://doi.org/10.1098/rsta.2018.0021

Maclennan, J., 2008. Concurrent mixing and cooling of melts under Iceland. J. Petrol. 49, 1931–1953. https://doi.org/10.1093/petrology/egn052

Maclennan, J., Jull, M., McKenzie, D., Slater, L., Grönvold, K., 2002. The link between volcanism and deglaciation in Iceland. Geochemistry, Geophys. Geosystems 3, 1–25. https://doi.org/10.1029/2001GC000282

Macpherson, C.G., Hilton, D.R., Day, J.M.D., Lowry, D., Grönvold, K., 2005. High-3He/4He, depleted mantle and low-δ 18O, recycled oceanic lithosphere in the source of central Iceland magmatism. Earth Planet. Sci. Lett. 233, 411–427. https://doi.org/10.1016/j.epsl.2005.02.037

Magee, C., Stevenson, C.T.E., Ebmeier, S.K., Keir, D., Hammond, J.O.S., Gottsmann, J.H., Whaler, K.A., Schofield, N., Jackson, C.A.-L., Petronis, M.S., O'Driscoll, B., Morgan, J., Cruden, A., Vollgger, S.A., Dering, G., Micklethwaite, S., Jackson, M.D., 2018. Magma Plumbing Systems: A Geophysical Perspective. J. Petrol. 59, 1217–1251. https://doi.org/10.1093/petrology/egy064

Marsh, B.D., 2006. Dynamics of Magmatic systems. Elements 2, 287–292. https://doi.org/10.1016/S0074-6142(09)60100-5

Marsh, B.D., 1995. Solidification fronts and magmatic evolution. Mineral. Mag. 60, 5–40. https://doi.org/10.1180/minmag.1996.060.398.03

McGarvie, D.W., 1984. Torfajokull: a volcano dominated by magma mixing. Geology 12, 685–688. https://doi.org/10.1130/0091-7613(1984)12<685:TAVDBM>2.0.CO;2

Neave, D.A., Maclennan, J., Hartley, M.E., Edmonds, M., Thordarson, T., 2014. Crystal storage and transfer in basaltic systems: The skuggafjoll eruption, Iceland. J. Petrol. 55, 2311_2346. https://doi.org/10.1093/petrology/egu058

Neave, D.A., Passmore, E., Maclennan, J., Fitton, G., Thordarson, T., 2013. Crystal-melt relationships and the record of deep mixing and crystallization in the AD 1783 Laki eruption, Iceland. J. Petrol. 54, 1661–1690. https://doi.org/10.1093/petrology/egt027

Neave, D.A., Putirka, K.D., 2017. A new clinopyroxene-liquid barometer , and implications for magma storage pressures under Icelandic rift zones. Am. Mineral. 102, 777–794. https://doi.org/http://dx.doi.org/10.2138/am-2017-5968

Newman, S., Lowenstern, J.B., 2002. Volatile Calc : a silicate melt – H2O – CO2 solution model written in Visual Basic for excel. Comput. Geosci. 28, 597–604. https://doi.org/doi:10.1016/S0098-3004(01)00081-4

Onsager, L., 1945. Theories and Problems of Liquid Diffusion. Ann. N. Y. Acad. Sci. 46, 241–265. https://doi.org/10.1111/j.1749-6632.1945.tb36170.x

Pálmason, G., 1986. Model of crustal formation in Iceland, and application to submarine mid-ocean ridges. West. North Atl. Reg. https://doi.org/10.1130/DNAG-GNA-M.87

Petry, C., Chakraborty, S., Palme, H., 2004. Experimental determination of Ni diffusion coefficients in olivine and their dependence on temperature, composition, oxygen fugacity, and crystallographic orientation. Geochim. Cosmochim. Acta 68, 4179–4188. https://doi.org/10.1016/j.gca.2004.02.024

Pinton, A., Giordano, G., Speranza, F., Thordarson, T., 2018. Paleomagnetism of Holocene lava flows from the Reykjanes Peninsula and the Tungnaá lava sequence (Iceland): implications for flow correlation and ages. Bull. Volcanol. 80, 1–19. https://doi.org/10.1007/s00445-017-1187-8

Pistone, M., Arzilli, F., Dobson, K.J., Cordonnier, B., Reusser, E., Ulmer, P., Marone, F., Whittington, A.G., Mancini, L., Fife, J.L., Blundy, J.D., 2015. Gas-driven filter pressing in magmas: Insights into in-situ melt segregation from crystal mushes. Geology 43, 699–702. https://doi.org/10.1130/G36766.1

Putirka, K.D., 2008. Thermometers and barometers for volcanic systems. Rev. Mineral. Geochemistry 69, 61–120. https://doi.org/10.2138/rmg.2008.69.3

Shea, T., Costa, F., D. Krimer, Hammer, J.E., 2015. Accuracy of timescales retrieved from diffusion modeling in olivine : A 3D perspective † 100, 2026–2042.

Sigmundsson, F., Einarsson, P., Hjartardóttir, Á.R., Drouin, V., Jónsdóttir, K., Árnadóttir, T., Geirsson, H., Hreinsdóttir, S., Li, S., Ófeigsson, B.G., 2020. Geodynamics of Iceland and the signatures of plate spreading. J. Volcanol. Geotherm. Res. 391, 106436. https://doi.org/10.1016/j.jvolgeores.2018.08.014

Sigmundsson, F., Hooper, A., Hreinsdóttir, S., Vogfjörd, K.S., Ófeigsson, B.G., Heimisson, E.R., Dumont, S., Parks, M., Spaans, K., Gudmundsson, G.B., Drouin, V., Árnadóttir, T., Jónsdóttir, K., Gudmundsson, M.T., Högnadóttir, T., Fridriksdóttir, H.M., Hensch, M., Einarsson, P., Magnússon, E., Samsonov, S., Brandsdóttir, B., White, R.S., Ágústsdóttir, T., Greenfield, T., Green, R.G., Hjartardóttir, Á.R., Pedersen, R., Bennett, R.A., Geirsson, H., la Femina, P.C., Björnsson, H., Pálsson, F., Sturkell, E., Bean, C.J., Möllhoff, M., Braiden, A.K., Eibl, E.P.S., 2015. Segmented lateral dyke growth in a rifting event at Bárðarbunga volcanic system, Iceland. Nature 517, 191–195. https://doi.org/10.1038/nature14111

Sigmundsson, F., Hreinsdóttir, S., Hooper, A., Árnadóttir, T., Pedersen, R., Roberts, M.J., Óskarsson, N., Auriac, A., Decriem, J., Einarsson, P., Geirsson, H., Hensch, M., Ófeigsson, B.G., Sturkell, E., Sveinbjörnsson, H., Feigl, K.L., 2010. Intrusion triggering of the 2010 Eyjafjallajökull explosive eruption. Nature 468, 426–432. https://doi.org/10.1038/nature09558

Sigvaldason, G.E., Annertz, K., Nilsson, M., 1992. Effect of glacier loading/deloading on volcanism: postglacial volcanic production rate of the Dyngjufjöll area, central Iceland. Bull. Volcanol. 54, 385–392. https://doi.org/10.1007/BF00312320

Sinton, J.M., Detrick, R.S., 1992. Mid-ocean ridge magma chambers. J. Geophys. Res. Solid Earth 97, 197–216. https://doi.org/10.1029/91JB02508

Slater, L., Jull, M., McKenzie, D., Gronvöld, K., 1998. Deglaciation effects on mantle melting under Iceland: Results from the northern volcanic zone. Earth Planet. Sci. Lett. 164, 151–164. https://doi.org/10.1016/S0012-821X(98)00200-3

Thirlwall, M.F., Gee, M.A.M., Lowry, D., Mattey, D.P., Murton, B.J., Taylor, R.N., 2006. Low δ 18 O in the Icelandic mantle and its origins: Evidence from Reykjanes Ridge and Icelandic lavas. Geochim. Cosmochim. Acta 70, 993–1019. https://doi.org/10.1016/j.gca.2005.09.008

Thomson, A., Maclennan, J., 2013. The distribution of olivine compositions in icelandic basalts and picrites. J. Petrol. 54, 745–768. https://doi.org/10.1093/petrology/egs083

Thordarson, T., Höskuldsson, Á., 2008. Postglacial volcanism in Iceland. Jokull 197–228.

Thordarson, T., Larsen, G., 2007. Volcanism in Iceland in historical time: Volcano types, eruption styles and eruptive history. J. Geodyn. 43, 118–152. https://doi.org/10.1016/j.jog.2006.09.005

Vilmundardóttir, E.G., Snorrason, S.P., Larsen, G., 2000. Geological map of subglacial volcanic area southwest of Vatnajökull icecap, Iceland, 1: 50.000. Natl. Energy Auth. Natl. Power Company, Reykjavík, Icel.

Yang, H.-J., Kinzler, R.J., Grove, T.L., 1996. Experiments and models of anhydrous, basaltic olivine-plagioclase-augite saturated melts from 0.001 to 10 kbar. Contrib. to Mineral. Petrol. 124, 1–18. https://doi.org/10.1007/s004100050169

Zellmer, G.F., Rubin, K.H., Gronvöld, K., Jurado-Chichay, Z., 2008. On the recent bimodal magmatic processes and their rates in the Torfajökull–Veidivötn area, Iceland. Earth Planet. Sci. Lett. 269, 388–398. https://doi.org/10.1016/j.epsl.2008.02.026

9 Paper I

Temporal evolution of magma and crystal mush storage conditions in the Bárðarbunga-Veiðivötn volcanic system, Iceland

Alberto Caracciolo, Enikő Bali, Guðmundur H. Guðfinnsson, Maren Kahl, Sæmundur A. Halldórsson, Margaret E. Hartley, Haraldur Gunnarsson

Manuscript published in Lithos, Elsevier. https://doi.org/10.1016/j.lithos.2019.105234

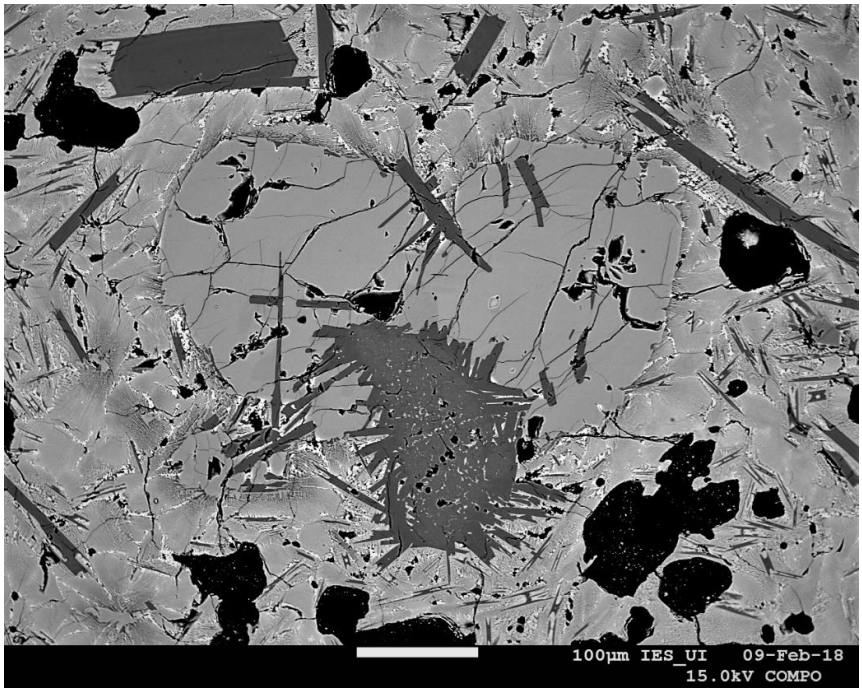

Temporal evolution of magma and crystal mush storage conditions in the Bárðarbunga-Veiðivötn volcanic system, Iceland

Alberto Caracciolo[a], Enikő Bali[a,b], Guðmundur H. Guðfinnsson[a], Maren Kahl[c], Sæmundur A. Halldórsson[a], Margaret E. Hartley[d], Haraldur Gunnarsson[a]
https://doi.org/10.1016/j.lithos.2019.105234

[a] *Nordic Volcanological Center, Institute of Earth Sciences, University of Iceland, Sturlugata 7, 101 Reykjavík, Iceland*
[b] *Faculty of Earth Sciences, University of Iceland, Sturlugata 7, 101 Reykjavík, Iceland*
[c] *Institut für Geowissenschaften, Universität Heidelberg, Heidelberg, Germany*
[d] *School of Earth and Environmental Sciences, University of Manchester, Manchester, UK*

Abstract

The depth(s) of magma storage reservoirs beneath active volcanic regions may change with time. Determining the rates and causes of millennial-scale changes in magmatic system architecture is critical for the development of realistic time-integrated models of crustal evolution. Here we examine a suite of samples from the exceptionally well-exposed Bárðarbunga-Veiðivötn volcanic system in central Iceland in order to resolve the temporal evolution of magma storage conditions within one of Iceland's most productive volcanic systems. We have measured the major and minor elemental composition of glass, mineral and melt inclusion from five erupted units that span a full glacial cycle, from a <100 ka subglacial eruption to a historical eruption in 1477 AD. All samples contain macrocrysts (>500 μm), polymineralic clots and high-crystallinity nodules, consistent with derivation from crystal mush bodies. Macrocryst rims are in chemical equilibrium with their respective carrier melts, while macrocrysts cores are too primitive to have crystallized from these melts. Each sample records a distinct range of macrocryst compositions, indicating that the composition and/or eruptibility of stored crystal mush has changed with time. Macrocrysts from the oldest units are the most primitive, and the macrocryst compositional range becomes wider and, on average, more evolved, with time. Clinopyroxene-melt and melt-based (OPAM) geobarometers reveal temporally invariant crystallization conditions of 1.9-2.2 ± 0.7 (1σ) kbar pressure, corresponding to depths around 6.8-7.8 ± 2.5 km. All the samples also contain melt inclusions trapped at mid-crustal pressures of ~2.6 kbar (9.6 km). In addition, melt inclusions hosted in most primitive olivines and plagioclases from subglacial and early Holocene eruptions preserve evidence of crystallization in a lower-crustal storage level(s) located at 17.5 km (4.9 kbar). This petrological record of deep crystallization may be linked to a surge in eruption rates, tapping of lower-crustal magma reservoirs, consistent with a crustal response associated with postglacial isostatic rebound. In contrast, the absence of a deep crystallization signature in the younger eruptive units may reflect lower magma production rates under steady-state conditions of the crust, and new magma pathways favouring melt storage in the mid-crust.

1. Introduction

For more than 100 years, the concept of a melt-dominated and long-lived magma chamber has been a commonly accepted paradigm in volcanology. However, our understanding of volcanic plumbing systems and processes has improved in the last few decades due to new geophysical, petrological and geological evidence (e.g., Ryan, 2018; Sinton and Detrick, 1992; West et al., 2001). Magma plumbing systems beneath active volcanoes are now envisaged to be characterized by sets of crustal reservoirs that are dominated by relatively liquid-poor crystal mushes (Edmonds et al., 2019; Marsh, 2006). Crystal mushes are dynamic horizons made of a semi-rigid framework of crystals within which the melt is distributed (Cashman et al., 2017; Maclennan, 2019). These bodies cannot be erupted in their entirety due to their rheological properties, but mush fragments can be disaggregated from the system by an ascending melt, and carried to the surface as glomerocrysts, nodules or macrocrysts (Cashman et al., 2017). Evidence from mush fragments is essential to constrain pressure (P), temperature (T), composition (X) and processes operating within a plumbing system.

Magmas in Iceland commonly carry disaggregated fragments of crystal mushes (Cooper et al., 2016; Halldórsson et al., 2018; Hansen and Grönvold, 2000; Neave et al., 2013, 2014, 2017; Óskarsson et al., 2017; Passmore et al., 2012; Svavarsdóttir et al., 2017). Petrological investigations of the geochemical relationship between macrocrysts and their carrier liquids have revealed that some mush fragments are related to their carrier liquid (Neave et al., 2013), while others cannot be cogenetic (Halldórsson et al., 2008). Identifying the location of a magma storage reservoir(s) within a plumbing system and tracking its evolution with time is important for clarifying the functioning of a volcanic system and for future eruption mitigation.

The Bárðarbunga-Veiðivötn volcanic system, located in the Eastern Volcanic Zone (EVZ), is ideal for investigating the temporal and compositional evolution of a basaltic magma storage reservoir(s) on the scale of a single volcanic system. This is because (1) it is one of the most active volcanic systems in Iceland during the Holocene; (2) extrusives consist of phyric and ultra-phyric rocks containing disaggregated crystal mush fragments (e.g., Halldórsson et al., 2018, 2008; Hansen and Grönvold, 2000; Holness et al., 2019); and (3) Holocene tephras from the Bárðarbunga system (Óladóttir et al., 2011) exhibit distinctive compositional variations as a function of time (Fig. 1). Furthermore, a fundamental observation from the Icelandic rift system is the apparent effect of deglaciation on magma plumbing dynamics. This is well documented in the Reykjanes Peninsula (Gee et al., 1998; Jakobsson et al., 1978), in the Western Volcanic Zone (Eason et al., 2015; Sinton et al., 2005) and in the Northern Volcanic Zone (Maclennan et al., 2002; Slater et al., 1998), although it remains unclear if and how magmatic plumbing systems were affected in the EVZ.

In this work, we present mineral, groundmass glass and melt inclusion major and minor elemental compositions from a temporally diverse (fully subglacial to historical) sample set from the Bárðarbunga-Veiðivötn volcanic system in central Iceland. Each sample provides a snapshot of the physical and chemical state of the volcanic system at the time of eruption. By linking geochemical and petrological data with geothermobarometry calculations, we explore the temporal evolution of magma storage conditions in the Bárðarbunga-Veiðivötn system. We first chemically characterize a sample suite comprising fresh nodules, macrocrysts and glass. Secondly, we employ a range of mineral-melt and melt-based thermobarometers (Hartley et al., 2018; Neave et al., 2017; Putirka, 2008; Yang et al., 1996) to evaluate magma storage conditions for each eruptive unit. On

the basis of these observations, we make an attempt to reconstruct the architecture of the Bárðarbunga-Veiðivötn magmatic system and the changes occurring within it from the last glacial period to recent times.

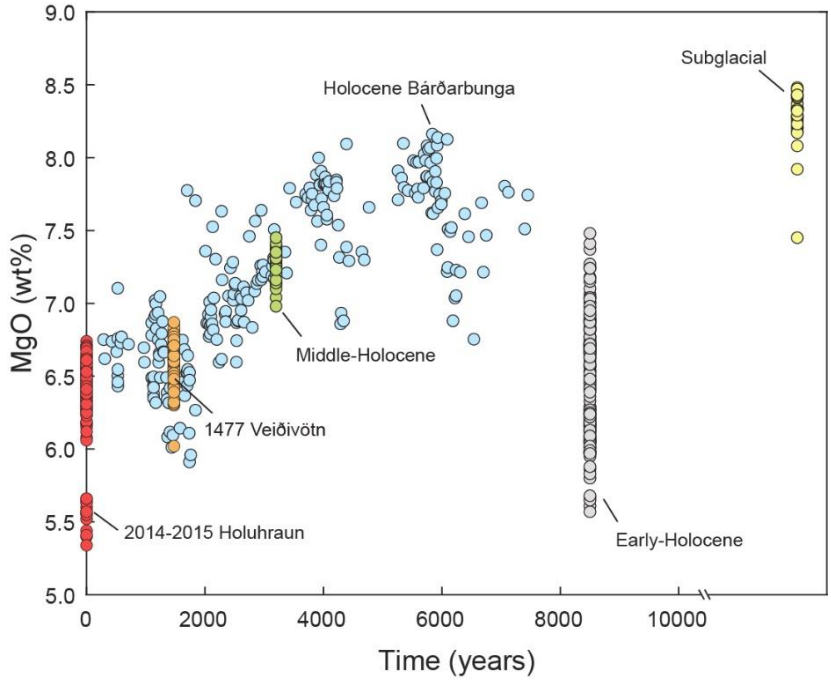

Fig. 1. *Temporal variation of MgO content in glasses from the Bárðarbunga-Veiðivötn volcanic system. Subglacial (Ljósufjöll), early-Holocene (Brandur, Fontur and Saxi tephra cones), middle-Holocene (Drekahraun) and Veiðivötn 1477 data are presented in this study. 'Holocene Bárðarbunga' glass compilation from Óladóttir et al. (2011). 2014-2015 Holuhraun eruption glass composition from Halldórsson et al. (2018). Temporal evolution trends are also observed in CaO, FeO and TiO_2 contents (not shown).*

2. GEOLOGICAL SETTING AND SAMPLING

2.1 The Bárðarbunga-Veiðivötn volcanic system

The Bárðarbunga volcanic system (Fig. 2) is the most extensive volcanic system in Iceland with a total length of 190 km and an area of about 2500 km2 (Thordarson and Höskuldsson, 2008). With one eruption every 50 years in the last 1100 years, the Bárðarbunga volcanic system is one of the most active system in Iceland (Larsen and Guðmundsson, 2014). The central edifice is split into two subglacial volcanoes: Bárðarbunga, a ~2009 m-high caldera-bearing volcano situated under the Vatnajökull ice cap, and Hamarinn, a smaller second central volcano located 20 km SW of Bárðarbunga. The associated fissure swarm is commonly subdivided into two segments: the Dyngjuháls fissure swarm extends 55 km north-northeast from Bárðarbunga into the Northern Volcanic Zone, while the Veiðivötn fissure swarm extends 115 km southwest from Bárðarbunga into the Eastern Volcanic Zone.

The southwest part of the Bárðarbunga volcanic system is commonly referred to as the Bárðarbunga-Veiðivötn volcanic system. The Veiðivötn part consists of numerous well-developed volcanic fissures orientated N45° (Larsen, 1984; Larsen and Guðmundsson, 2014; Thordarson and Larsen, 2007). In the extreme southwest, the Veiðivötn fissure swarm propagates into the Torfajökull volcanic system with production of both silicic and mixed products (Larsen, 1984; Mørk, 1984; Zellmer et al., 2008). The latest eruption took place on the northern fissure swarm, producing the 2014-15 Holuhraun lava (Pedersen et al., 2017).

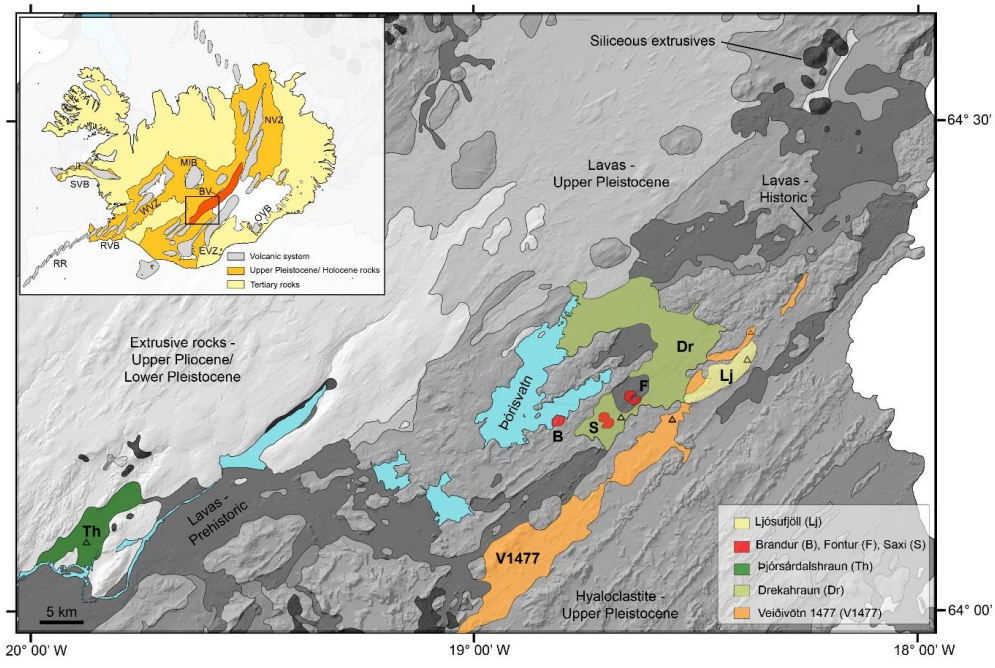

Fig. 2. *Geological map of the southernmost part of the Bárðarbunga-Veiðivötn system. The general geology of the area is indicated with greyscale colours. Eruptive units studied in this work are marked in colours. Historic lavas are younger than 1100 BP; prehistoric lavas are older than 1100 BP. Triangles show the exact sampling location within each unit. The insert map in the upper left corner shows the outline of the active neovolcanic zones (in grey) and the Bárðarbunga-Veiðivötn system (BV) in red. RR: Reykjanes Ridge; RVB: Reykjanes Volcanic Belt; SVB: Snæfellsnes Volcanic Belt; WVZ: Western Volcanic Zone; MIB: Mid-Iceland Belt; BV: Bárðarbunga-Veiðivötn system; EVZ: Eastern Volcanic Zone; OVB: Öraefajökull Volcanic Belt; NVZ: Northern Volcanic Zone. Geological map compiled by Haukur Jóhannesson and Kristján Sæmundsson published by the Icelandic Museum of Natural History and Iceland Geodetic Survey.*

Table 1. Sample list, description and location.

Sample name	Age	Coordinates		Description	Previous work
		Latitude (N)	Longitude (W)		
Ljósufjöll	Subglacial	64° 16' 51.2''	18° 23' 40.8''	pillow lava	-
Brandur	Early Holocene	64° 13' 55.6''	18° 48' 8.6''	lava, tephra, nodules	Hansen and Grönvold (2000), Holness et al. (2007)
Fontur	Early Holocene	64° 15' 17.9''	18° 38' 0.2''	lava, tephra, nodules	Hansen and Grönvold (2000), Halldorsson et al. (2008), Holness et al. (2007)
Saxi	Early Holocene	64° 13' 49.2''	18° 42' 15.7''	lava, tephra, nodules	Hansen and Grönvold (2000), Halldorsson et al. (2008), Holness et al. (2007)
Þjórsárdalshraun	Middle-Holocene	64° 08' 43.2''	19° 49' 26.8''	lava with nodules	-
Drekahraun	Middle-Holocene	64° 14' 0.4''	18° 39' 57.2''	fresh scoria	-
Veiðivötn 1477	Historical (1477 AD)	64° 14' 29.2''	18° 31' 50.7''	fresh scoria	-

2.2 Sample description

We have selected a suite of geologically well-characterised eruptive units from volcanic formations situated in the Bárðarbunga-Veiðivötn volcanic system (Fig. 2 and Table 1).

Ljósufjöll (Lj)

Ljósufjöll, a subglacial volcanic ridge located within the Veiðivötn fissure system (Lj, Fig. 2). Studied samples are from a glassy pillow lava, corresponding to Ljósufjöll formations b and c (lja and ljb) described by Vilmundardóttir et al. (2000). Ljósufjöll is thought to have erupted early during the last glacial period (Weichselian) and is therefore likely to be younger than 100 ka (Jóhannesson et al., 1982). No prior petrochemical studies have been carried out on Ljósufjöll.

Brandur (B), Fontur (F) and Saxi (S)

Brandur, Fontur and Saxi are three early-Holocene tephra cones located to the east of Þórisvatn lake (B, F, S, Fig. 2). Fontur and Saxi are aligned along a ~2.5 km-long linear fissure, while Brandur is located 3 km west of the fissure on the edge of Þórisvatn lake. The craters consist of unconsolidated, crystal-rich, fine-grained glassy material with plagioclase macrocrysts up to 4 cm long, and abundant nodules of plagioclase, olivine and clinopyroxene (Halldórsson et al., 2008; Hansen and Grönvold, 2000; Holness et al., 2007, 2019; Vilmundardóttir, 1977). These craters have been suggested to be the source of the Þjórsárhraun lava (8.6 ka, e.g. Halldórsson et al., 2008; Hansen and Grönvold, 2000; Hjartarson, 1988; Jakobsson, 1979). In addition to samples collected for this study, we also collected data from samples previously studied by Hansen and Grönvold (2000).

Þjórsárdalshraun (Th) and Drekahraun (Dr) (Tungnaá lava)

Lava flows produced in the Veiðivötn fissure over the last 9 ka, but before the settlement of Iceland in 874 AD, are collectively referred to as the Tungnaá lava sequence. At 45 km^3, this is one of the most voluminous lava sequences in Iceland (Vilmundardóttir, 1977). The source vents of the Tungnaá lavas are now mostly buried by younger formations but were probably located in the southern part of the Veiðivötn fissure swarm (Pinton et al., 2018). Þjórsárdalshraun and Drekahraun (Th and Dr, Fig. 2) are mid-Holocene lavas belonging to the Tungnaá sequence. They are dated to between 3-4 ka BP by tephrochronology (Pinton et al. 2018). Drekahraun samples consist of fresh and vesicular scoria collected west of Drekavatn, near the lava source vents (Dr, Fig. 2). The Þjórsárdalshraun lava was largely emplaced to the north of Hekla volcano, flowing westward following the Þjórsá river and ultimately forming a field of rootless cones in Þjórsárdalur valley (Th, Fig. 2).

Veiðivötn 1477 (V)

The 1477 AD Veiðivötn eruption is the most recent eruption covered by our sample suite. The eruption is considered to be the largest basaltic explosive eruption that has occurred in Iceland in the last 1200 years (Thordarson and Larsen, 2007). It took place on a 65 km long fissure and produced 5-10 km3 of highly fragmented basaltic tephra and small lava flows. This volume includes both tephras and lavas ranging from basalt to rhyolite which erupted simultaneously as the Veiðivötn magmas entered the Torfajökull silicic center to southwest (McGarvie, 1984; Mørk, 1984; Zellmer et al., 2008). Tephra from this eruption covered an area of 53 km2 on land and has been found as far afield as Ireland and Sweden (Larsen, 1984; Larsen and Guðmundsson, 2014). Here we study fresh and glassy basaltic scoria from the central and southern part of the main fissure specifically avoiding the mixed magmas near Torfajökull (V1477, Fig. 2).

3. METHODS

3.1 Sample preparation, analytical and thermobarometry methods

Thin sections of well-preserved and representative whole rock samples were made from each unit. Plagioclase, olivine and clinopyroxene crystals (0.5-2.4 mm) were hand-picked from crushed samples, mounted in epoxy resin and polished to expose glassy melt inclusions (MIs). Crystals containing devitrified MIs were heated in a high-temperature furnace at 1210 ± 5 °C, which was expected to exceed the crystallization temperature. The re-homogenized MIs were later exposed at the surface. Major element compositions of macrocrysts (n = 1530), their host glass (n = 328) and olivine- and plagioclase-hosted MIs (n= 436) were determined by electron microprobe (EPMA) using a JEOL JXA-8230 SuperProbe at the University of Iceland. 1σ errors reported in this work are based on multiple standard analyses collected during different analytical sessions. All melt inclusion compositions have been corrected for the effect of post-entrapment crystallization (PEC) on the inclusion walls.

We calculated magma storage temperatures based on glass compositions (Yang et al., 1996) and mineral-glass pairs (Putirka, 2008). Crystallization pressures were calculated based on clinopyroxene-melt pairs, following the method described by Neave and Putirka (2017), which has a standard error of estimate (SEE) of ±1.4 kbar, whereas the olivine-plagioclase-augite-melt (OPAM) barometer (Hartley et al., 2018; Yang et al., 1996) was applied to estimate groundmass glass and MI equilibration pressures (SEE=±1.3 kbar). Full details of analytical methods, homogenization experiments, PEC corrections and thermobarometry calculations are provided as supplementary material (S1).

4. Results

4.1 Petrography

All our samples contain three main macrocryst (>500 μm) phases: olivine, clinopyroxene and plagioclase. Minerals are present either as single grains scattered in the groundmass or in polymineralic glomerocrysts (Fig. 3). Plagioclase is the most common mineral phase in all samples (Fig. 3a). Plagioclase macrocrysts are generally euhedral and range from 500-6000 μm in size, although crystals up to 3-4 cm are found in Brandur, Fontur and Saxi samples. Clinopyroxene macrocrysts range between 500-1600 μm and often occur in glomerocrysts (Fig. 3b), although large euhedral clinopyroxene is occasionally found (Fig. 3c). Olivine macrocrysts are typically 500-2000 μm in size and are either euhedral or show rounded and resorbed habits (Fig. 3d-e). Cr-rich spinel is sporadically found in the groundmass glass and is also widespread as inclusions in olivine and plagioclase macrocrysts.

Naturally quenched melt inclusions are abundant in olivines and plagioclases from Ljósufjöll, Brandur, Fontur, Saxi and Veiðivötn 1477. The melt inclusions range in size from 10-150 μm (Fig. 3d-e). Plagioclase and olivine crystals from Þjórsárdalshraun and Drekahraun contain MIs that are partially crystallized. Crystals in the tephra cones Brandur, Fontur and Saxi are surrounded by a glassy to fine-grained matrix. Ljósufjöll samples display a coarse-grained groundmass (Fig. 3g) composed of plagioclase,

clinopyroxene, olivine and oxides, changing to a cryptocrystalline and glassy matrix towards the pillow margins (Fig. 3h). Drekahraun and Veiðivötn 1477 samples contain a fine-grained matrix with glassy portions at the tephra clast rims. Þjórsárdalshraun samples have a holocrystalline groundmass.

Samples from all localities have plagioclase macrocrysts with cores exhibiting complex internal textures. The inner part is either oscillatory or patchy zoned and always wrapped by euhedral to subhedral rims. The thickness of Ljósufjöll plagioclase rims appears to be correlated with the matrix texture (Fig. 3g-h). Plagioclase rims in contact with coarse-grained groundmass are thicker (~30-70 μm) (Fig. 3g), while plagioclase rims scattered in cryptocrystalline to glassy matrix are thinner (~10-40 μm) (Fig. 3h). Þjórsárdalshraun plagioclase macrocrysts are normally zoned.

In backscattered electron (BSE) images, clinopyroxenes display bright and dark sectors (Fig. 3b). The clinopyroxenes are found either as glomerophyric clots or as fine to coarse intergrowths of clinopyroxene and plagioclase forming next to plagioclase macrocrysts. In Veiðivötn 1477, Ljósufjöll and the tephra cone samples, clinopyroxene also occurs as scattered single grains (Fig. 3c). Olivine crystals are often resorbed, especially in Brandur, Fontur and Saxi samples, although euhedral crystals are found in all localities.

Abundant cm-size (up to 10 cm) olivine gabbro xenoliths are found in the Brandur, Fontur and Saxi cones (Fig. 3e). The five studied nodules all contain 70-80 vol.% plagioclase in a subophitic texture with some resorbed interstitial olivine and clinopyroxene. The framework is sustained by transparent, light brown interstitial glass, which is locally crystallized to a fine intergrowth of plagioclase, clinopyroxene ± olivine (see also Hansen and Grönvold, 2000 and Holness et al., 2007). Two xenoliths, 0.5-0.9 cm in size, were also found in the Þjórsárdalshraun lava samples (Fig. 3f). They consist of olivine-free gabbro, with plagioclase and clinopyroxene forming an ophitic texture, and contain localized pockets of coarse- to fine-grained interstitial material (Fig. 3f).

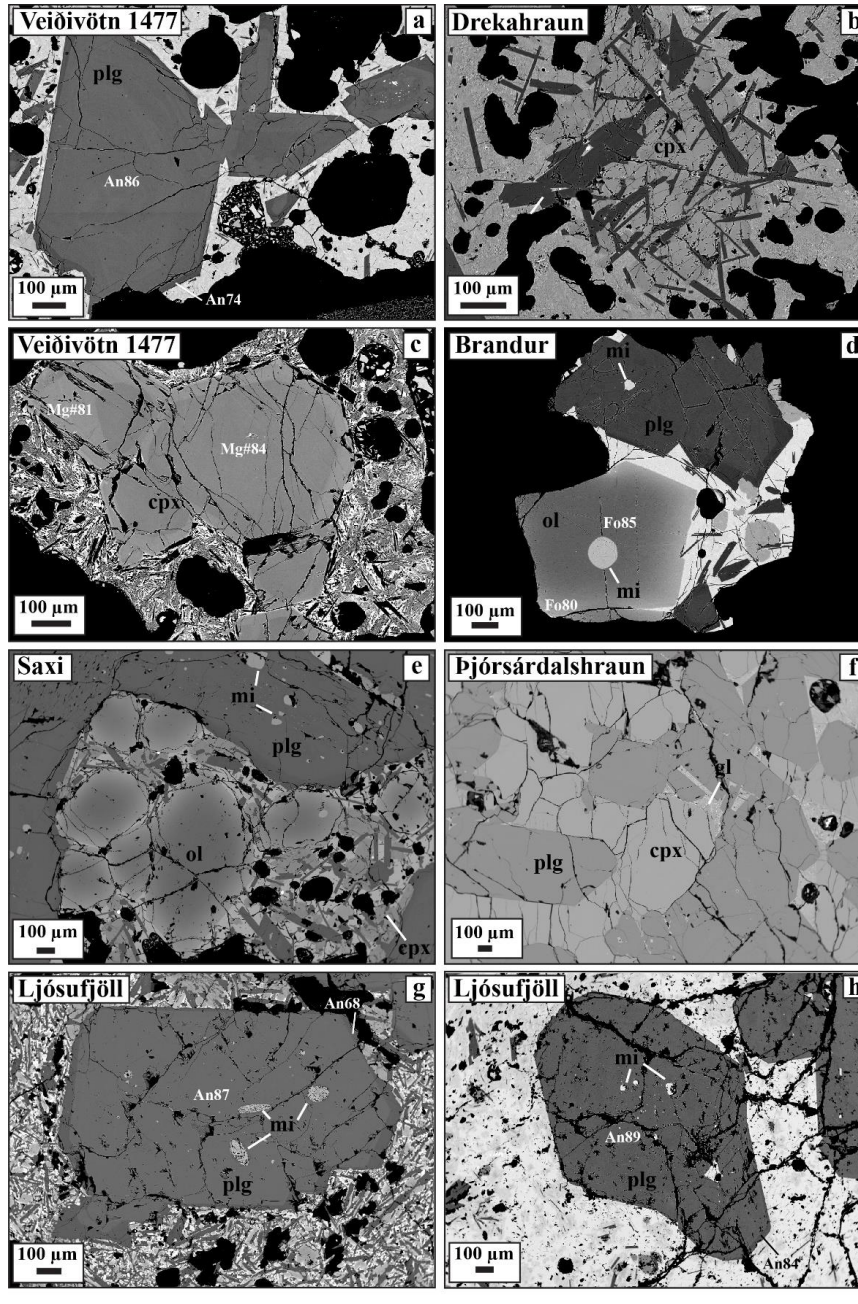

Fig. 3. *Backscattered electron (BSE) images showing the main petrographic and chemical features of the studied samples. A) Plagioclase macrocryst from the Veiðivötn 1477 eruption with an oscillatory zoned interior surrounded by a darker rim. B) Glomerophyric clot from Drekahraun. Sector zoned clinopyroxene crystals that have grown with plagioclases. C) Clinopyroxene macrocryst from Veiðivötn 1477 showing resorbed dark*

cores enclosed by less primitive rims. d) Normally zoned olivine with a large melt inclusion from Brandur. E) Saxi tephra cone nodule with olivine and plagioclase macrocrysts and clinopyroxene in glomerophyric clots. f) Nodule from Þjórsárdalshraun: plagioclase crystals surrounded by homogeneous clinopyroxene; interstitial glass pockets are also observed. g) Plagioclase crystal from Ljósufjöll with crystalline melt inclusions, surrounded by a coarse-grained groundmass. h) Plagioclase crystal from Ljósufjöll within a glassy groundmass. plg= plagioclase; ol= olivine; cpx= clinopyroxene; mi= melt inclusion; gl= interstitial glass; Fo=olivine fosterite content; An=plagioclase anorthite content; Mg#= clinopyroxene Mg#.

4.2 Mineral and glass chemistry

Macrocryst compositions are summarized in Fig. 4a-c. For each mineral phase, variation diagrams are also shown in Fig. 4d-f and in the supplementary material (Fig. S1.2-S1.4). Groundmass glass and melt inclusion compositions are reported in Fig. 1 and Fig. 5. The full EPMA dataset is provided as supplementary material (S2).

4.1 Plagioclase

Plagioclase macrocrysts commonly have bytownitic to anorthitic compositions. Ljósufjöll plagioclase macrocryst cores display a narrow compositional range of $An_{86\text{-}90.5}$, whereas the composition of the rims depends on the groundmass glass texture (Fig. 3g-h). Plagioclase rims in contact with coarse-grained groundmass have more evolved compositions within the range $An_{65\text{-}71}$, while plagioclase rims adjacent to cryptocrystalline to glassy groundmass record compositions within the range $An_{79\text{-}86}$ (Fig. 4a and 3d). Plagioclase macrocryst cores from Brandur, Fontur and Saxi samples are in the range $An_{83\text{-}91.5,}$ with Fontur plagioclase cores having slightly less compositional variation of $An_{86\text{-}90.5}$ (Fig. 4a). All plagioclase macrocrysts are surrounded by $An_{71\text{-}81}$ rims. Þjórsárdalshraun and Drekahraun plagioclase macrocryst core and rim compositions are between $An_{84\text{-}91}$ and $An_{71\text{-}86}$, respectively (Fig. 4a and 4d), while plagioclases found in Þjórsárdalshraun nodules are more homogeneous ($An_{85\text{-}89.5}$). Macrocryst cores and rims from Veiðivötn 1477 display the largest compositional variation of all studied localities. Plagioclase core compositions are $An_{78\text{-}91}$, while rims are $An_{66\text{-}77}$.

4.2 Clinopyroxene

Clinopyroxenes have augititic compositions. Ljósufjöll clinopyroxene cores and dark sectors in BSE images have compositions of Mg# 84-87 ($Mg\#=[(MgO_{mol})/(MgO_{mol}+FeO^{tot}_{mol})]*100$), while rims and bright sectors have Mg# 76-86 (Fig. 4b and 3e). Brandur, Fontur and Saxi cones contain clinopyroxene with cores and dark sectors in the range Mg# 78-87 and rims and bright sectors in the range Mg# 75-84 (Fig. 4b). Þjórsárdalshraun clinopyroxenes have Mg# 76.6-84.7, while clinopyroxenes found in the nodules are more homogeneous, being in the range Mg# 83-85. Drekahraun clinopyroxene cores and dark sectors range between Mg# 81.7-85, while rims and bright sectors are in the range Mg# 79-84. Here, many reversely zoned clinopyroxenes occur with Fe-rich cores (Mg# 70-72) surrounded by Fe-poor sectors (Mg# 82-84) (Fig. 4b and 3e). Clinopyroxene dark sectors found in Veiðivötn 1477 samples vary in the range Mg# 79-85 and bright sectors in the range Mg# 75.7-82. A few clinopyroxene crystals, occurring as

large single grains, are normally zoned with large Mg-rich cores of Mg# 84-85 overgrown by rims with Mg# 81-82. Reversely zoned clinopyroxenes contain Fe-rich cores (Mg# 67-75.4) followed by oscillatory zoning.

Clinopyroxene crystals can be strongly sector zoned, which is mostly reflected in their Ca, Al and Ti contents (e.g.: Nakamura, 1973; Ubide et al., 2019). In order to minimise this compositional effect, we plotted the Al_2O_3/TiO_2 vs Mg# for all clinopyroxene analyses (Fig. 4e). In general, the Al_2O_3/TiO_2 increases with increasing Mg# and the Al_2O_3/TiO_2 variation is greater for clinopyroxene with Mg# >83. Crystals with Mg# >83 show an Al_2O_3/TiO_2 span of 1.73 (1σ), in contrast to clinopyroxenes with Mg# <83 where this span is only 0.97 (1σ). Ljósufjöll and tephra cone clinopyroxenes record the largest dispersion, while recent samples have a narrower range. In fact, middle-Holocene units and historical units do sample primitive clinopyroxene in terms of Mg# and they register relatively low Al_2O_3/TiO_2 ratios and Cr_2O_3 contents. Indeed, Cr-rich (Cr_2O_3 >0.8 wt%) clinopyroxenes are exclusively sampled by the old units (Fig. S1.3c).

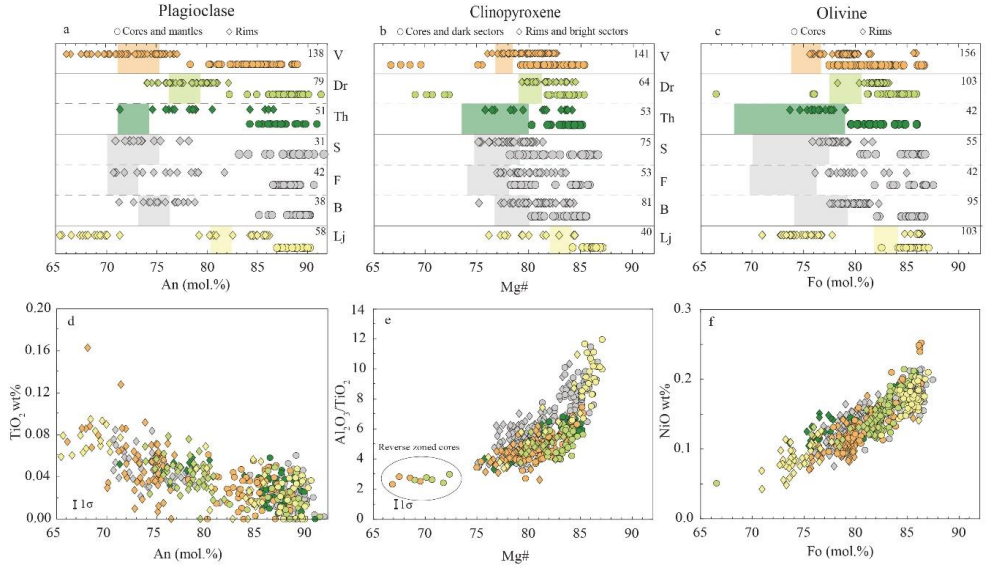

Fig. 4. *The range in (a) An content of plagioclase, (b) Mg# of clinopyroxene, and (c) Fo content of olivine for each locality. Core and rim compositions are depicted as circles and diamonds, respectively. Clinopyroxene dark and bright sectors refer to sector zones in BSE images. Coloured bands represent the mineral compositions calculated to be in equilibrium with the carrier liquid for each sample, where the glass composition is taken as representative of the carrier melt. Numbers in each corner state the number of point analyses in minerals for that specific locality and mineral phase. In general, macrocryst cores are more primitive than the equilibrium compositions whilst rims are more evolved and tend to overlie the equilibrium bands. Lj: Ljósufjöll; B: Brandur; F: Fontur; S: Saxi; Th: Þjórsárdalshraun; Dr: Drekahraun; V: Veiðivötn 1477. (d)-(f) Variation diagrams showing the TiO_2 content vs An content of plagioclase (d), Al_2O_3/TiO_2 vs Mg# clinopyroxene (e), and NiO content vs Fo content of olivine (f) macrocrysts. 1σ error is smaller than the symbol sizes unless otherwise shown.*

4.3 Olivine

In Ljósufjöll samples, unzoned olivine macrocrysts vary in composition from Fo_{84} to Fo_{87}. Zoned olivines, on the other hand, have core and rim compositions of $Fo_{82.5\text{-}87}$ and $Fo_{71\text{-}77.5}$, respectively (Fig. 4c and 3f). Olivine macrocrysts from Brandur, Fontur and Saxi have homogeneous core compositions of $Fo_{82\text{-}87.5}$ and rims between $Fo_{76\text{-}82}$ (Fig. 4c). Olivine cores from Þjórsárdalshraun and Drekahraun vary in the range $Fo_{79.5\text{-}86}$ and $Fo_{82.4\text{-}86}$, respectively. Þjórsárdalshraun olivine rims have compositions within the range $Fo_{73.6\text{-}79}$, while Drekahraun olivine rims have compositions of $Fo_{78\text{-}83}$. Reversely zoned olivines, mostly occurring in Drekahraun samples, have cores of $Fo_{66.5\text{-}82}$ encased by more primitive $Fo_{80\text{-}82}$ rims (Fig. 4c and 3f). Sparse olivines in Veiðivötn 1477 samples show a wide compositional range of cores and rims, between $Fo_{77\text{-}87}$ and $Fo_{75.4\text{-}85.5}$, respectively.

Olivine variation diagrams for all locations are shown in Fig. 4f and Fig. S1.4. Olivine cores have NiO contents between 0.1 and 0.25 wt.% that decrease to 0.05 wt.% in the rims (Fig. 4f). Fe/Mn ratio, diagnostic of parental magma compositional differences (e.g., Sobolev et al., 2007), varies between 51 and 86 (Fig. S1.4a), with more variation observed in the most primitive crystals (Fo >85, 1σ=5.2) compared to olivines with Fo <85 (1σ=4.3).

4.4 Groundmass glass

Groundmass glass composition varies as a function of time (Fig. 1). From early-Holocene till present, carrier melts become more evolved. Indeed, Ljósufjöll groundmass glass is the most primitive (Fig. 1 and 5) with Mg# 57-60, MgO 7.5-9.3 wt% and TiO_2 0.95-1.1 wt%, being one of the most primitive tholeiite glass compositions known from the EVZ (see Hansen and Grönvold, 2000; Neave et al., 2014, 2017; Óladóttir et al., 2011; Passmore et al., 2012). Drekahraun and Veiðivötn 1477 groundmass glasses show a tight compositional range (Fig. 1 and 5). Drekahraun glass (Mg# 50.5-55) has MgO 7-7.5 wt% and TiO_2 1.6-1.8 wt%, whereas Veiðivötn 1477 groundmass glass (Mg# 45.7-49.8) contains MgO 6-6.9 wt% and TiO_2 1.7-2 wt%. The groundmass of samples from Þjórsárdalshraun, assumed to represent melt compositions, refer to fine-grained pockets found in the nodules. Þjórsárdalshraun nodule glass (Fig. 2f) displays a large chemical variability (Fig. 5) (MgO 5.7-7.5 wt% and TiO_2 1.9-2.3 wt%), perhaps due to microcrystals. The compositional variation of groundmass glass from the tephra cones (B-F-S) is relatively large in comparison to other localities (Fig. 1 and 5) and our data are in good agreement with previously published data (Hansen and Grönvold, 2000). We note that Brandur generally has more primitive glass (Mg# 46-53, MgO 6.1-7.5 wt.%) than Fontur and Saxi (Mg# 40-49 and 41.5-50.5, MgO 5.5-7.5 wt% and 5.5-7 wt%, respectively).

4.5 Melt inclusions

The majority of MIs from all localities, corrected for post-entrapment processes (S1), form a group with Mg# 58-68 (Fig. 5a-d). The only locality where MI and interstitial glass compositions overlap is Ljósufjöll. Ljósufjöll MIs have MgO between 8.0-9.7 wt%, while other localities record a wider range (MgO 6.2-10.0 wt%). Among the most primitive melt inclusions (Mg# >65, MgO 8.5-10.0 wt%, n=24), two are hosted in plagioclases ($An_{86\text{-}89}$) from Drekahraun and Þjórsárdalshraun (MgO of MIs 8.5-8.7 wt%), one is a plagioclase-hosted (An_{90}) MI from Brandur (MgO 10.0 wt%), and the other 21 MIs are hosted in olivines ($Fo_{86.5\text{-}88}$) from the tephra cones (MgO 9.3-10.0 wt%).

Evolved MIs (Mg# <55, n=56,) are widespread in all eruptive units except Ljósufjöll. They are hosted in both plagioclase (An_{83-88}) and olivine (Fo_{76-80}). The groundmass glass and MI variations of our dataset are found to be in excellent agreement with published whole rock and glass compositions (Halldórsson et al., 2008, 2018; Hartley et al., 2018; Jakobsson, 1979; Óladóttir et al., 2011; Svavarsdóttir et al., 2017) from Bárðarbunga volcanic system (pale blue fields in Fig. 5), although our samples do not include primitive MIs with Mg# as high as 71 as found in Holuhraun samples (Bali et al., 2018; Hartley et al., 2018).

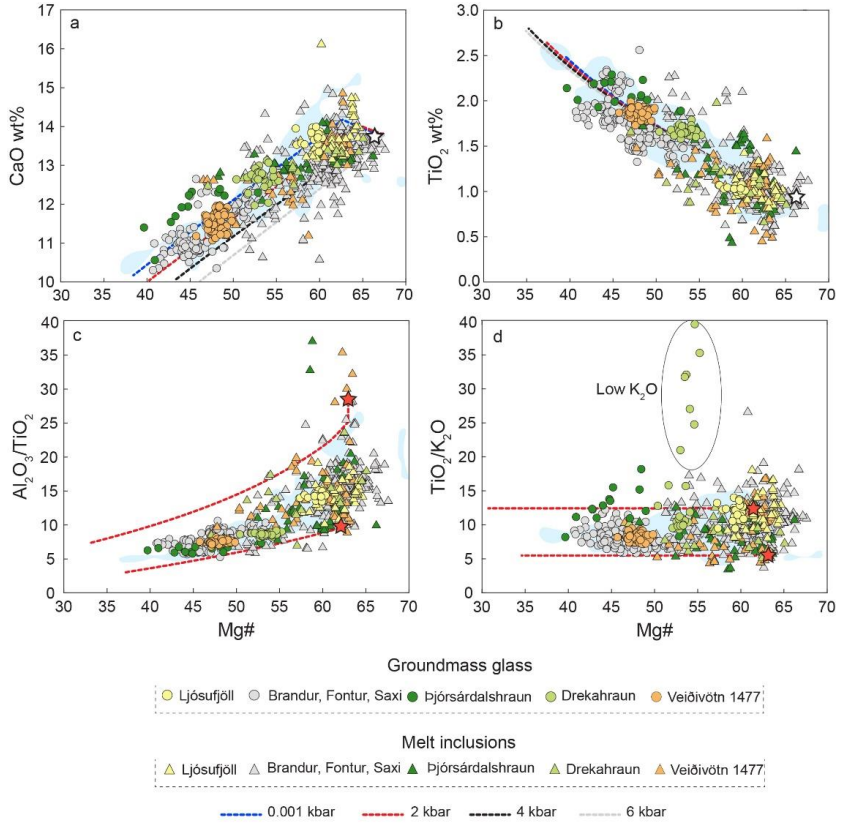

Fig. 5. *Variation diagrams showing (a) CaO content, (b) TiO_2 content, (c) Al_2O_3/TiO_2, and (d) TiO_2/K_2O vs Mg# of groundmass glasses (circles) and melt inclusions (triangles) from the studied samples. Liquid lines of descent (LLD) in (a) and (b) are calculated starting from the same melt composition (white stars) at different pressures. LLDs in (c) and (d) are calculated at 2 kbar, using two different starting compositions (red stars). See main text for details. All LLDs were calculated using Petrolog3 (Danyushevsky and Plechov, 2011). Blue fields denote published data from Bárðarbunga-Veiðivötn system (Halldórsson et al., 2008, 2018; Hartley et al., 2018; Jakobsson, 1979; Óladóttir et al., 2011; Svavarsdóttir et al., 2017). Low K_2O data within the ellipse were acquired from glassy to cryptocrystalline areas which could be affected by quench modifications. 1σ error is smaller than the symbols.*

4.6 Macrocryst compositions and mineral-melt equilibrium

Figure 4a-c shows macrocryst compositional ranges, along with mineral compositions calculated to be in equilibrium with the observed groundmass glass compositions, shown with coloured bands. Equilibrium olivine compositions were calculated using a fixed $Kd^{ol-melt}_{Fe-Mg}$ of 0.3, following Roeder and Emslie (1970), and equilibrium clinopyroxene compositions following the model of Wood and Blundy (1997). Equilibrium plagioclase compositions were calculated using equation 33 from the model of Namur et al. (2011).

Plagioclase, olivine and clinopyroxene macrocryst rims are generally found to be close to the compositions predicted to be in equilibrium with the groundmass glass, with the exception of Ljósufjöll macrocryst rims. Macrocryst cores are always too primitive to be in equilibrium with groundmass glass compositions. This feature is fairly common in mush-bearing magmas and has been observed in other eruptive units from the EVZ (Halldórsson et al., 2008, 2018; Neave et al., 2013, 2014, 2015).

5. Geothermobarometry results

5.1 Clinopyroxene storage pressures and groundmass equilibration pressures

The relative probability of clinopyroxene crystallization pressures are shown as kernel density estimates (KDE) in Fig. 6 a-d. Clinopyroxenes from all eruptive units give comparable crystallization pressure ranges of 0.5-4.5 kbar (Table 2 and Fig. 6). Each locality returns a well-defined peak in the KDE (Fig. 6a-d), located at ~2 kbar. The mean calculated pressure across all units is 2.2 ± 0.7 (1σ) kbar. Only a few clinopyroxenes (n=14, Mg#78-85) – the majority of which are from Drekahraun and the tephra cone localities – return pressures higher than 3.5 kbar. Assuming an average Icelandic crustal density of 2.86 g/cm3 (Carlson and Herrick, 1990), our data indicate a mid-crustal magma storage zone located at 7.8 ± 2.5 (1σ) km (Fig. 6 a-d).

In Fig. 6a-d, we plot KDEs of equilibration pressures calculated for both groundmass glasses and melt inclusions. Groundmass glasses return a mean of 1.9 ± 0.8 (1σ) kbar, which is statistically indistinguishable from our calculated clinopyroxene-liquid pressures (Table 2). The majority of groundmass glasses are within the range 0.4–3.0 kbar. Similar equilibrium pressures are obtained for the Bárðarbunga Holocene tephras (Óladóttir et al., 2011a), with a mean pressure of 2.6 ± 0.4 (1σ) kbar (Fig. 6). Therefore, although the studied carrier melts have distinct and variable chemical compositions, they all last equilibrated with olivine, plagioclase and augite at essentially the same depth (Fig. 6a-d), in a mid-crustal reservoir located at 6.8 ± 2.8 (1σ) km. Barometry calculations carried out on 2014-15 Holuhraun samples reveal a magma storage zone located at about 7-8 km depths, consistent with geophysical observations (Halldórsson et al., 2018; Hartley et al., 2018).

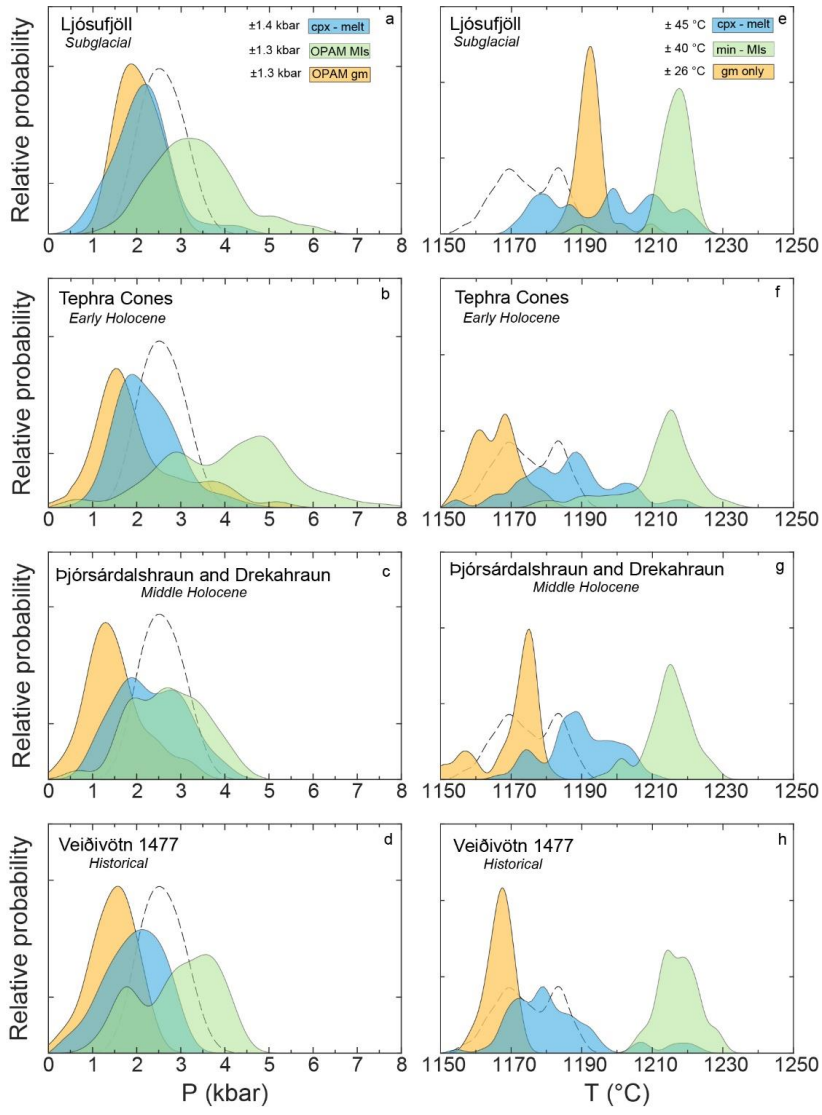

Fig. 6. *Kernel density estimate plots, with bandwidth 0.3, of calculated pressures (a)-(d) and temperatures (e)-(h) for all studied units. Clinopyroxene-melt pressures are calculated using the Neave and Putirka (2017) barometer; OPAM barometry (Hartley et al., 2018; Yang et al., 1996) was applied both to glasses and PEC-corrected melt inclusions. Reported MI pressures represent compositions with a returned probability of fit higher than 80%. Temperatures are calculated using a glass-only thermometer and cpx, ol and plag-melt thermometers from Putirka (2008). See the main text for more details. The dotted curve in each plot shows the pressure and temperature distribution for Holocene Bárðarbunga glasses from Óladóttir et al. (2011). Errors (± next to the legend) indicate the standard error of estimate of the thermometers and barometers used. Table 2 lists the numbers of processed cpx, glass and MIs for each locality.*

5.2 OPAM melt inclusion equilibration pressures

Out of 436 olivine and plagioclase-hosted MIs, 299 inclusions return probability fits >0.8 (table 2 and Fig. 6a-d). The oldest, subglacial unit Ljósufjöll, records a fairly large range of MI trapping pressures, with broad peak at 3.3 kbar and a tail up to 6 kbar. Inclusions from the tephra cones display a bimodal distribution with one peak at 3.0 kbar and another at 4.9 kbar. The high-pressure peak is well defined for Brandur, Fontur and Saxi samples, with 108 MIs recording pressures higher than 4.0 kbar, but not statistically significant for Ljósufjöll inclusions due to the low number of samples (11 MIs show pressures between 4.0-6.0 kbar). Þjórsárdalshraun and Drekahraun return MI equilibration pressures in the range 0.6-4.5 kbar, with a main peak at 2.7 kbar and a minor peak at 1.9 kbar. MI in Veiðivötn 1477 samples show a bimodal distribution but the probability distribution is not well defined due to the small number of inclusions (n=28). The calculated pressures range between 1.2-4.2 kbar with a most common equilibration pressure at 3.6 kbar and a second peak at 1.8 kbar.

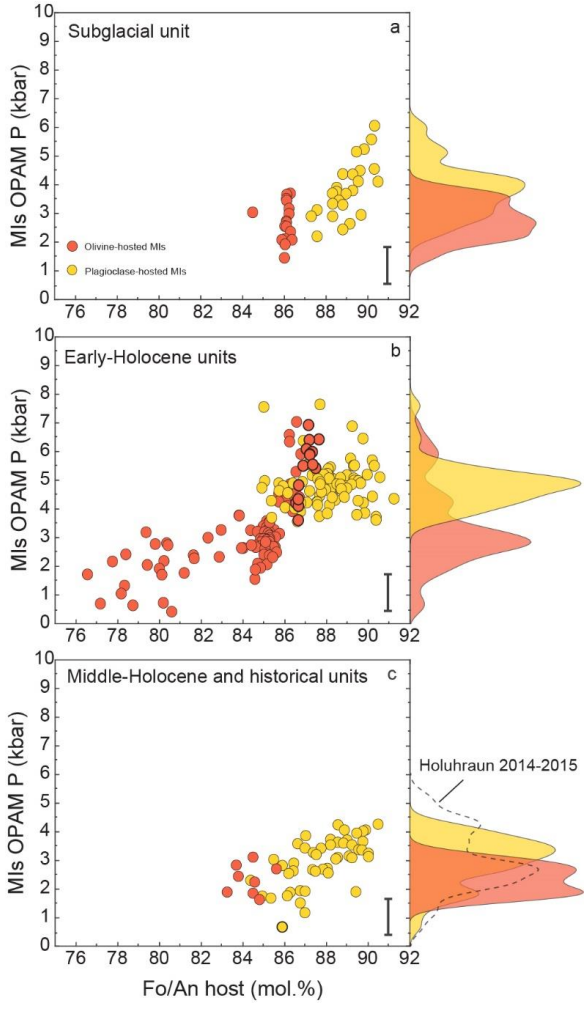

Fig. 7. *Relationship between host mineral composition and melt inclusion equilibration pressure, for (a) subglacial unit (Ljósufjöll) (b) early-Holocene units (Brandur, Fontur and Saxi cones) and (c) middle-Holocene/historical units (Tungnaá lavas and Veiðivötn 1477). Kernel density estimates to the right of the plots show the relative probability of equilibration pressures for olivine- and plagioclase-hosted melt inclusions. MI pressure distributions for Holohraun eruption is reported as dotted curve. Error bars refer to the OPAM standard error of estimate (SEE=1.3 kbar). MIs outlined with thicker lines have Mg#>65 and are the least likely to be three-phase saturated.*

We have explored the relationship between MI pressures and the composition of the host crystals in all units (). In the subglacial unit (Fig. 7a), MIs hosted in Fo~86 olivine crystals record a most probable peak at around 2.6 kbar (9.3 km), while plagioclase-hosted

MIs show a main peak at 3.9 kbar (13.9 km) and multiple secondary peaks, with the equilibration pressures up to a maximum of 6.0 kbar (21.4 km). Brandur, Fontur and Saxi cones record an even larger range of MI equilibration pressures (0.4-7.6 kbar) (Fig. 7b). Plagioclase-hosted MIs were entrapped within the pressure range 3.5-7.6 kbar (12.5-27 km) at a most probable pressure of 4.9 kbar (17.5 km). Olivine-hosted MIs were trapped at pressures within the range 0.4-7.0 kbar (1.5-25 km). MI equilibration pressures increase with the forsterite content of the host olivine, which is mainly noticeable in Fig. 7b, where we distinguish two different MI populations: (1) MIs trapped in Fo76-86 crystals, with a most probable pressure of 2.8 kbar (10 km) and (2) MIs hosted in Fo86-88 crystals, which produce the high-pressure tail of the distribution, with secondary peaks at 4.3 kbar (15.3 km) and 6 kbar (21.4 km). Macrocrysts from Brandur, Fontur and Saxi were previously studied by Hansen and Grönvold (2000). They concluded that macrophenocrysts crystallized between 7 and 40 km depth (2-11 kbar). Finally, middle-Holocene and historical units have a narrow range of MI trapping pressures (Fig. 7c), of 0.7-4.3 kbar (2.5-15 km). Olivine-hosted MIs crystallized at a most probable pressure range of 1.9-2.6 kbar (6.8-9.2 km), while plagioclase-hosted MI equilibration pressures are more variable, with a main peak at 3.3 kbar (11.7 km).

One might argue that the highest pressures calculated for the primitive melt inclusions are potentially not valid as, despite the numerical filtering, these melts might not be saturated in clinopyroxene. Using Eq. 35 of Putirka (2008), we have calculated equilibrium melt compositions for the most primitive clinopyroxene macrocrysts observed in our crystal cargo (i.e. Mg#85-87). We find that silicate melts with Mg#melt = 61-65 are in equilibrium with Mg# 85-87 clinopyroxenes, suggesting that only inclusions with Mg#>65 should be treated with caution (n=17, circles with black thick outline in Fig. 7b and 7c). Furthermore, model calculations with Petrolog (discussed in detail later) suggest that clinopyroxene with Mg# ~88 will be on the liquidus of Mg# ~65 melts at pressures of 2-6 kbar.

5.3 Geothermometry

KDEs for calculated temperatures are illustrated in Fig. 6e-h and mean temperature values are reported in Table 3. There is little variation in melt temperature between the samples, although there is some indication that the Ljósufjöll carrier melt was hotter than the carrier liquids in the other eruptions. Calculated temperatures for Ljósufjöll groundmass glass range between 1185 and 1210 °C (mean at 1193 ± 4 (1σ) °C), while samples from tephra cones, Tungnaá lava and Veiðivötn 1477 give similarly lower temperatures, with a mean at 1165 ± 7 (1σ) °C, 1170 ± 8 (1σ) °C and 1167 ± 3 (1σ) °C, respectively. Furthermore, Ljósufjöll groundmass glass temperatures are statistically indistinguishable from those derived from its melt inclusions. Across all samples, the recovered carrier melt temperatures are within the ± 26°C SEE of the thermometer (Eq. 16, Putirka, 2008), but are sufficiently different to suggest that during the last glacial period, melts erupted in the Bárðarbunga system were hotter than recent carrier magmas.

The clinopyroxene-melt thermometer returns wider temperature variations within individual samples (Fig. 6e-h), but the sample average crystallization temperatures are remarkably consistent with an overall mean crystallization temperature of 1188 ± 17 °C. We find no significant temporal variation in crystallization temperature. Finally, the plagioclase-melt and olivine-melt thermometers applied to MIs return temperatures with a narrowly focused peak at 1214 ± 10 (1σ) °C, regardless of age.

Table 2. Number of clinopyroxenes, groundmass glasses and MIs processed for geobarometry estimates along with pressure results. Pressures are in kbar.

	cpx-melt barometry				OPAM barometry									
	Clinopyroxenes				Groundmass glasses				Melt inclusions					
	n. analysis	n. cpx-melt	P		n. analysis	P_f>80%	P		n. analysis		P_f>80%		P	
			Mean	σ			Mean	σ	ol-hosted	plg-hosted	ol-hosted	plg-hosted	Mean	σ
Ljósufjöll	43	40	2.1	0.6	29	26	2.0	0.4	18	30	17	24	3.3	0.9
Brandur	59	45	2.2	0.7	69	42	1.6	0.6	86	37	73	22	3.6	1.5
Fontur	34	24	2.2	0.6	33	6	3.5	0.9	24	54	20	31	4.4	1.1
Saxi	47	35	2.3	0.7	63	5	3.2	1.5	39	37	17	33	4.4	1.3
Þjórsárdalshraun	41	35	1.9	0.7	13	11	1.5	0.8	5	33	5	23	2.7	0.9
Drekahraun	63	45	2.6	0.8	30	6	1.5	0.2	0	17	0	6	2.9	1.0
Veiðivötn 1477	144	90	1.9	0.6	91	15	1.5	0.5	4	52	3	25	2.9	0.9
Total	431	314			328	111			176	260	135	164		

P_f = probability of fit ; σ= standard deviation

6. Discussion

6.1 Modelling fractional crystallization

The glass compositional trends in Fig. 5a-b could, to a first order, be largely controlled by fractional crystallization, although the complete variation in groundmass glass and MI major element compositions is difficult to explain solely with fractional crystallization along a single liquid line of descent. Results from our thermobarometric calculations suggest polybaric crystallisation (Fig. 6). Therefore, we calculated liquid lines of descent (LLDs) from the average composition of the most primitive melt inclusions for the whole dataset (n=24, Mg# >65) at different pressures of 0.001, 2, 4 and 6 kbar. The starting composition has Mg# of ~66, TiO_2 0.97 wt%, MgO 9.5 wt% and CaO 13.4 wt% (white stars, Fig. 5a, b). Models were run using the Petrolog3 software (Danyushevsky and Plechov, 2011), applying the pressure-sensitive mineral-melt model of Ariskin et al. (1993). Oxygen fugacity was set at the QFM buffer, assuming similar oxidation conditions to those measured in the most recent eruption of the Bárðarbunga volcano (Bali et al., 2018; Halldórsson et al., 2018).

A similar approach was used for LLDs in Fig. 5 c-d, which show Al_2O_3/TiO_2 and TiO_2/K_2O as a function of Mg#. Both diagrams show that the variability in these oxide ratios decreases with decreasing Mg#. Al_2O_3/TiO_2 in melt inclusions varies between 6 and 37 (1σ= 4.3) (Fig. 5c), while in groundmass glasses, it is between 5 and 15 (1σ= 2.1), with the Ljósufjöll carrier liquid having the highest Al_2O_3/TiO_2 (~15). A similar diversity is also observed in TiO_2/K_2O (Fig. 5d), with primitive melts recording the largest spread. Therefore, we modelled fractional crystallization at 2 kbar considering different starting compositions to encompass the observed diversity in primitive melt compositions (red stars in Fig. 5c, d). Out of the most primitive MIs (Mg# >60), we averaged MIs with high and low Al_2O_3/TiO_2, ending up with (1) a melt composition with high Al_2O_3/TiO_2 (28.1 ± 3.3 (1σ)) and (2) a melt with low Al_2O_3/TiO_2 (9.5 ± 0.4 (1σ)).

Although the trend of CaO vs. Mg# (Fig. 5a) in the glasses is roughly covered by polybaric fractional crystallisation, variation in TiO_2 (Fig. 5b) and oxide ratios such as TiO_2/K_2O (Fig. 5 c, d) cannot be explained by simple fractional crystallization of a single parental melt composition. Thus, regardless of the model and the starting composition adopted, a single LLD cannot reproduce the observed chemical variability. Therefore, we suggest that neither isobaric nor polybaric fractional crystallization alone is sufficient to describe the observed glass composition variability.

6.2 Evidence for concurrent mixing and crystallization

Element ratio variability in olivine and clinopyroxene macrocrysts and MIs provides evidence for the occurrence of diverse primary melts in the Bárðarbunga-Veiðivötn plumbing system. Clinopyroxene records a notable decrease in the variability of Al_2O_3/TiO_2 (Fig. 4e) and Cr_2O_3 (Fig. S1.3c) as clinopyroxene Mg# decreases. A similar behaviour is observed for olivine, where there is a much greater spread in Fe/Mn among Fo-rich crystals than Fo-poor crystals (Fig. S1.4a). Furthermore, we observe comparable trends in the oxide ratios of groundmass glasses and melt inclusions (e.g., Al_2O_3/TiO_2 and TiO_2/K_2O in Fig. 5c and Fig. 5d, respectively), with melt compositions at an early stage of magmatic evolution showing the greatest variability. This behaviour has been observed in

samples from several Icelandic eruptions with regards to trace elements (e.g., Hartley et al., 2018; Maclennan et al., 2003; Maclennan, 2008; Neave et al., 2013).

In order to explain such variability at an early stage of magma history, we must invoke heterogeneities in the mantle source or in the melting process. As primary melts form, they start their history of magmatic evolution and progress through storage, crystallization and mixing (Maclennan, 2008). The compositional variation of primitive crystals (Fig. 4e and Fig. S1.3c) and their melt inclusions (Fig. 5c) has not been preserved with melt evolution, testifying that mixing and compositional homogenization has occurred between MI entrapment and eruption. In our samples, the most primitive MIs, hosted in olivine crystals of Fo~88, have Mg# ~67 and we do not observe olivine crystals of Fo >88. We propose that our samples do not preserve near-primary mantle-derived melts and most likely we are missing the earliest stages of the crystallization story. The most primitive melts are therefore likely to have had even more variable compositions than those preserved in our samples.

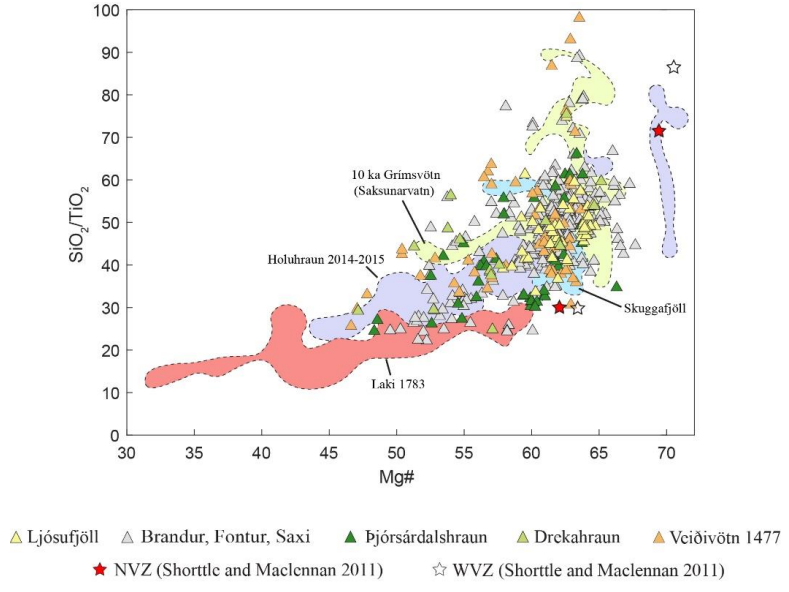

Fig. 8. *SiO_2/TiO_2 vs Mg# of melt inclusions from this work along with published data from the subglacial Skuggafjöll eruption (Neave et al., 2014), the 10 ka early-Holocene Grímsvötn eruption (Neave et al., 2015), the historical 1783 Laki eruption (Neave et al., 2013) and the 2014-15 Holuhraun eruption (Bali et al., 2018). Our melt inclusions span the compositional variability recorded by other eruptions form the EVZ. Also indicated are depleted and enriched end-member melt compositions for the Northern Volcanic Zone (NVZ, red stars) and the Western Volcanic Zone (WVZ, white stars) (Shorttle and Maclennan, 2011). 1σ error is within the symbol sizes.*

We compared our data with melt inclusion compositions from elsewhere in Iceland's EVZ. Figure 8 shows melt inclusion compositions from the 1783 AD Laki eruption (Neave et al., 2013), Skuggafjöll subglacial eruption (Neave et al., 2014), the 10 ka Grímsvötn tephra series (Neave et al., 2015) and the recent 2014-15 Holuhraun eruption

(Bali et al., 2018). Naturally quenched MIs from Laki are fairly evolved with Mg# extending to much lower values (Mg# 32-60) and a very narrow range of SiO_2/TiO_2 (Fig. 8), and seem to follow a slightly different trend from our data. Conversely, melt inclusions from the 10 ka Grímsvötn (MgO up to 10.5 wt%) and Skuggafjöll (MgO up to 10.3 wt%) samples show large variations in SiO_2/TiO_2, closely matching the most primitive compositions reported in this work. Finally, melt inclusions from Holuhraun span the compositional variation recorded by our data (Fig. 8), although more primitive melts (Mg#~71), relative to our dataset, are captured by the Holuhraun melt inclusion record.

In summary, major and minor elements of macrocrysts, as well as melt inclusions, preserve evidence for compositionally diverse parental melts that might reflect heterogeneities in the mantle source or different degrees of partial melting (Maclennan, 2008). This needs to be further investigated by trace elements and stable and radiogenic isotopes. However, the compositional variability decreases as mixing and fractional crystallization progresses, producing the magma composition documented by the carrier melt.

6.3 Characteristics of the crystal cargo

In the case of Ljósufjöll macrocrysts, equilibrium with the carrier liquid is exclusively registered by plagioclase with intermediate compositions (An_{79-86}), although olivine cores are close to equilibrium (Fig. 4). We suggest that macrocrysts incorporated within the glassy groundmass are representative of the original cargo and that the macrocrysts scattered within the coarse-grained groundmass would have experienced post-emplacement crystallization of the outermost rims (An_{65-71}). The fact that Ljósufjöll samples come from a pillow lava, whose interior had longer time to cool and evolve, supports the chemical evidence for the two macrocrysts types.

In all units, macrocryst cores could not have crystallized from the respective carrier melts (Fig. 4a-c). In Fig. 9a-b, we show KDEs (coloured areas) for plagioclase and olivine macrocryst core compositions against time. We also report the most primitive mineral compositions (vertical bars), which are calculated to crystallize from the most primitive melt inclusions from each magmatic unit. Finally, we show a comparison of olivine and plagioclase macrocryst core compositions (dotted curves) in samples of subglacial (Skuggafjöll; Neave et al. 2014), early Holocene (10 ka Grímsvötn; Neave et al. 2015) and historical (1783 Laki and 2014-2015 Holuhraun eruptions; Neave et al. 2013, Halldórsson et al., 2018) eruptions that all took place in central Iceland.

Macrocryst cores are close to the predicted equilibrium compositions with melt inclusions (Fig. 9a-b), and MIs appear to be in equilibrium with plagioclase, clinopyroxene and olivine with maximum values of An ~86-87, Mg# ~85-86 (not shown) and Fo ~86-87, respectively. As a result, high-MgO melts represented by the most primitive melt inclusions could have crystallized the majority of clinopyroxene and olivine core compositions acquired in this work, although this does not apply to plagioclases with the highest An. Plagioclase macrocrysts with An>87 are widespread at all localities, and must have crystallized from melts that are not preserved in our petrological record.

Ljósufjöll has a very restricted range of plagioclase macrocryst compositions (An_{87-91}). The range of plagioclase compositions expands with time: for younger eruptive units the plagioclases are skewed towards more evolved compositions (Fig. 9a), and high-An cores are rare in the middle-Holocene and historical units. Similar relationships are observed for olivine, with the range of core compositions extending to lower Fo with time (Fig. 9b). Comparing our results with crystal compositions from the 2014-2015 Holuhraun

eruption (Halldórsson et al., 2018), we find that the Holuhraun cargo records a wider distribution of plagioclase macrocryst compositions (An_{69-92}) compared to Veiðivötn 1477, but a similar distribution of olivine macrocryst compositions (Fo_{76-88}).

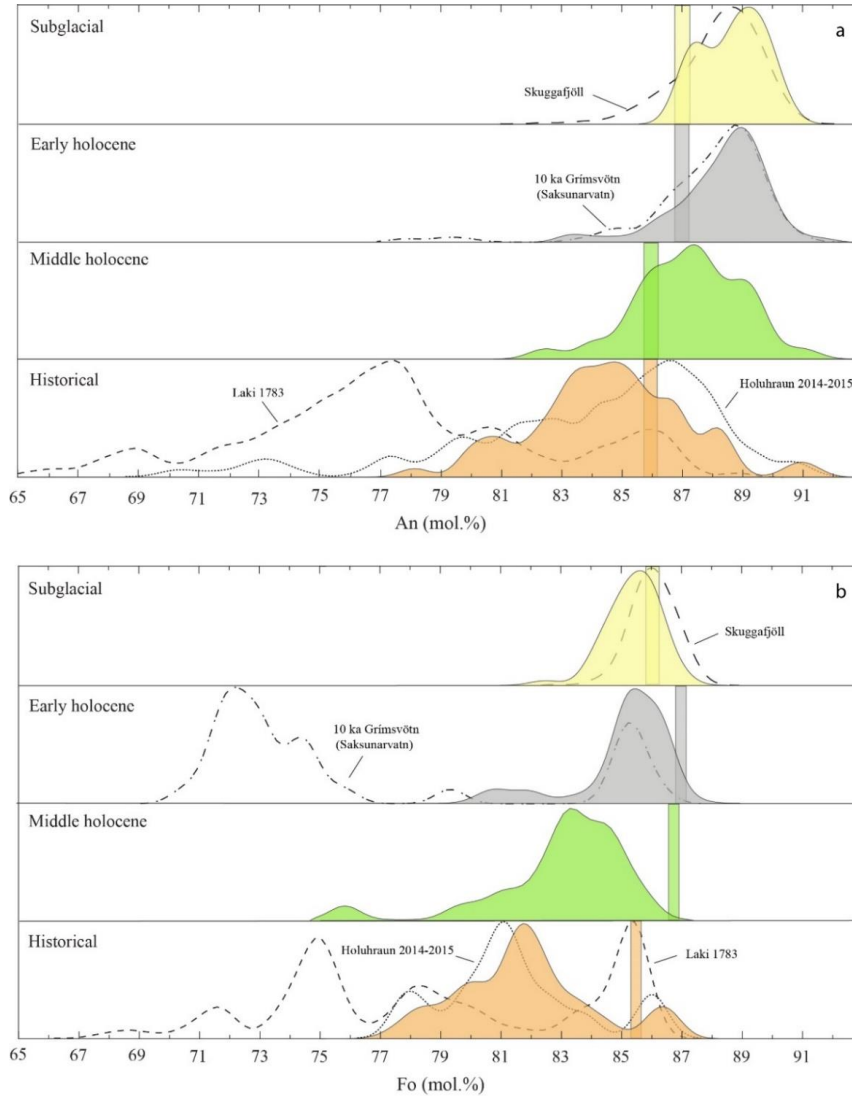

Fig. 9. *Kernel density estimate (KDE) curves showing the relative probability of plagioclase and olivine compositions and how the probability has changed with time (a) An content of plagioclase macrocryst cores (b) Fo content of olivine macrocryst cores. Coloured bars indicate the mineral composition in equilibrium with the most primitive MIs within each magmatic unit. Dotted and dashed lines show KDE for published subglacial and Holocene eruption data for the EVZ. Skuggafjöll (Neave et al., 2014); 10ka Grímsvötn (Neave et al., 2015); 1783 Laki (Neave et al., 2013); 2014-2015 Holuhraun (Halldórsson et al., 2018).*

A similar variation of macrocryst compositions is observed when we compare available samples within the EVZ of similar age (Fig. 9a-b). We find that the subglacial Skuggafjöll (Neave et al., 2014) and 10 ka Grímsvötn (Neave et al., 2015) samples record a narrow range in plagioclase core compositions (An_{83-92}), while historical eruptions such as Laki have much more variable plagioclase compositions (An_{65-90}) (Neave et al., 2013). Interestingly, this partially also applies to olivine macrocrysts. The subglacial Skuggafjöll eruption products have a restricted olivine compositional range (Fo_{84-87}), but olivines from the 10 ka Grímsvötn show a broader and bimodal (Fo_{69-77} and Fo_{83-87}) compositional distribution. The 1783 Laki eruption has several olivine populations in the range Fo_{67-87}. However, the compositional range in Laki crystal cargo might be affected by availability of a much larger dataset compared to the other eruptions. Taken together, these data suggest that more evolved crystals have been erupted with time, both within the scale of a single volcanic system and, potentially, on the scale of the EVZ and central Iceland.

6.4 Assessing the temporal variability of the Bárðarbunga-Veiðivötn volcanic system

In the case of Iceland in the postglacial period (<12 ka), the crust has been affected by isostatic adjustments (Sigmundsson, 1991) due to ice removal and glacial rebound effects (Le Breton et al., 2016), with magma eruption rates 20-30 times higher than at present day (Maclennan et al., 2002; Sigvaldason et al., 1992). Modelling studies (Eksinchol et al., 2019; Jull and McKenzie, 1996) and chemical constraints (Eason et al., 2015; Gee et al., 1998; Hardarson and Fitton, 1991; Maclennan et al., 2002; Sinton et al., 2005; Slater et al., 1998) have provided evidence to link this eruption pulse either to the release of pooled magma enhanced by a change of the stress field in the crust (Gudmundsson, 1986; Sigvaldason et al., 1992) or to an increase in the decompression melting rate of the mantle (Jull and McKenzie, 1996; Maclennan et al., 2002) caused by the unloading of the ice cap above Iceland.
The evolution of the Bárðarbunga-Veiðivötn volcanic system in the late Pleistocene and Holocene can likely be explained within this framework and we propose three different stages (Fig. 10):

(1) A steady-state glacial stage when a 2000 m-thick ice cap (Sigmundsson, 1991) pressed down the crust, sampled by the subglacial unit (Fig. 10a). In this period the magmatic system was characterized by magma storage regions distributed over a large crustal interval of ~5-21 km (Fig. 10a). The accuracy of the OPAM barometer does not allow us to resolve the vertical arrangement of the deeper storage zones (i.e., multiple stacked sills) in the mid- to lower crust (Kelemen et al., 1997). In this period, the crystal-mush system was characterized by highly primitive macrocrysts that were picked up by a primitive and homogeneous carrier liquid.
(2) A changing state of the magmatic system, when decompression and glacial rebound effects associated with ice unloading occurred (Jull and McKenzie, 1996; Le Breton et al., 2016; Maclennan et al., 2002; Slater et al., 1998), represented by the early-Holocene tephra cones (Fig. 10b). Our results (Fig. 7) on Brandur, Fontur and Saxi samples can be interpreted as a result of an increase in magma production rates (Jull and McKenzie, 1996; Maclennan et al., 2002) that promoted the input of primitive melts from the mantle and crystallization of

primitive macrocrysts in a deep-seated storage zone(s). We find that crystallization of primitive olivine (Fo>85-86) and plagioclase (An>85) macrocryst cores took place at a mid- to lower-crustal depths of 15-22 km (Fig. 10b). Some of these macrocrysts were transported upwards into mid-crustal reservoir(s) (7-11 km), where more evolved phases also crystallized. Furthermore, although it is still unresolved how deglaciation might have affected the chemistry of erupted melts, it is clear that early postglacial products record a greater variability in MgO contents, and are depleted in incompatible elements compared with lavas erupted when the ice load was thought to be relatively stable or absent (Eason et al., 2015; Gee et al., 1998; Jull and McKenzie, 1996; Maclennan et al., 2002; Sinton et al., 2005; Slater et al., 1998). This is consistent with our observation of a larger spread in the MgO contents of carrier liquids erupted in the early Holocene (Fig. 1).

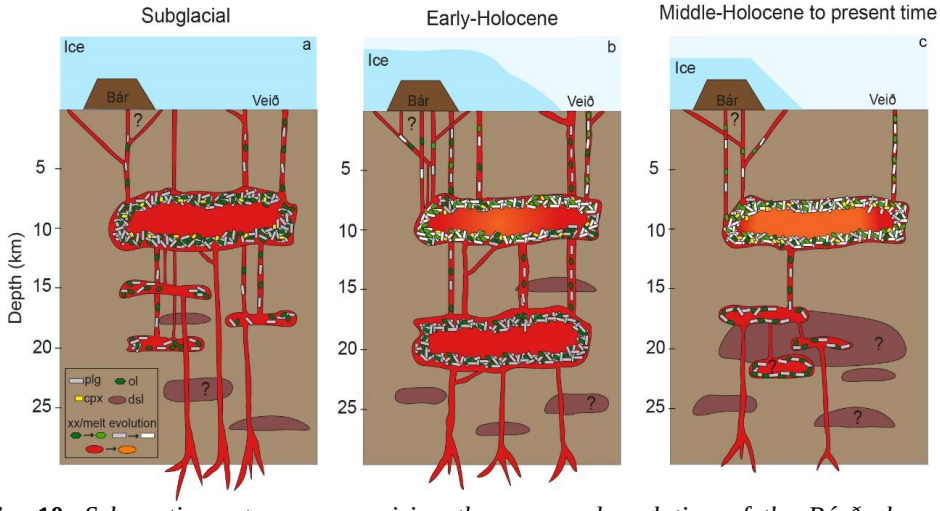

Fig. 10. *Schematic cartoon summarizing the proposed evolution of the Bárðarbunga-Veiðivötn magmatic system over time, based on barometry, thermometry and chemical data. a) Subglacial time. The magmatic system is distributed over a wide range of depths, with a main storage zone in the middle crust. At that time, crystal mush bodies were mostly composed of primitive macrocrysts. b) Early-Holocene time when the magmatic system underwent glacial rebound effects. The magmatic system is characterized by (1) a storage zone in the mid-crust at around 10 km depth, mostly made up of evolved macrocrysts and (2) a deep-crustal zone(s) at 17 km depth, where more primitive macrocrysts crystallize. The increase in magma productivity facilitated movement of magma from deep regions to the surface. c) The magmatic system configuration since the middle-Holocene. The magmatic system is most likely dominated by a mid-crustal reservoir, with crystal mush horizon(s) made up of evolved macrocrysts. Once crustal pressure equilibrium has been established, mid-crustal storage zone(s) dominate the magmatic system configuration, with new magma passageways being established and melts being homogenized in the middle crust. Primitive plagioclase and olivine crystals are coloured in grey and dark green respectively; evolved plagioclase and olivine crystals are coloured in white and light green respectively. Bár: Bárðarbunga edifice; Veið: Veiðivötn area; plg: plagioclase; ol: olivine; cpx: clinopyroxene; dsl: deactivated/disconnected storage levels; xx=crystal.*

(3) A steady-state stage, which we observe at the present, with the magmatic system being unaffected by short-term ice unloading effects, sampled by middle-Holocene and historical units (Fig. 10c). MI pressures likely indicate comparable crystallization depths of olivine and plagioclase macrocrysts in a storage zone(s) in the mid-crust. MI equilibration pressures estimated for the 2014-2015 Holuhraun eruption (Hartley et al., 2018) are all below 5 kbar (dotted KDE in Fig. 7c), with the most probable pressure at 3.2 kbar (11.4 km), which is consistent with our data. We infer that since the middle-Holocene, magmas erupted in the Bárðarbunga-Veiðivötn system have mainly carried evolved olivine and plagioclase macrocrysts (Fig. 9) that were stored at mid-crustal depths around 7-13 km (Fig. 10c).

All these clues rule out the involvement of a deep reservoir during historical eruptions, at least as a direct source for extrusives. The absence of a deep signature can be interpreted as a result of the re-establishment of a new pressure equilibrium. Shallow storage region(s) may then dominate the plumbing architecture. As seen at Etna volcano, passageways of melts in a magmatic system can change with time (Kahl et al., 2013). From this perspective, the deep reservoir(s) might be bypassed by melts coming from the mantle in historical time, most likely because new and stable magma pathway has been established. Deep earthquake swarms (~22 km) beneath the Bárðarbunga system, which have been associated with deep melt injections and melt movement (Hudson et al., 2017) are also of importance here. However, the 2014-15 Holuhraun eruption products preserve no petrologic record of crystals or melt inclusions from this depth. Our combined data suggest that since the middle-Holocene, crystals and melts from the deep storage zone have not been directly transferred to the surface. This is perhaps due to a more effective homogenisation within the mid-crustal storage zone(s). In contrast, the deep reservoir(s) was clearly sampled in the early Holocene and during subglacial eruptions, indicating that during this period the magmatic system had a different architecture that permitted direct ascent of magma from deeper storage regions to the surface.

7. Conclusions

1. Studied samples contain evidence of interaction with a crystal mush reservoir(s) and entrainment of crystal mush fragments.

2. Olivine and plagioclase macrocryst compositions vary with time. The older formations are dominated by primitive crystals, whereas in the mid-Holocene to historic formations their chemistry is skewed towards more evolved compositions.

3. Macrocryst cores and primitive melt inclusions exhibit a great chemical variability, which is likely linked to compositionally heterogeneous primary melts. The decrease of this variability, highlighted by the carrier liquid and macrocryst compositions, provides evidence for concurrent mixing and crystallization of compositionally diverse melts within the system.

4. Clinopyroxene-melt and OPAM barometries return a temporally consistent crystallization pressure of 2.2 ± 0.7 (1σ) kbar and 1.9 ± 0.8 (1σ) kbar, corresponding to a depth of 7.3 ± 2.7 (1σ) km, which are consistent with a

relatively shallow reservoir located in the middle crust. These estimates are in perfect agreement with petrological and geophysical results obtained for 2014-15 Holuhraun eruption.

5. The subglacial and early-Holocene formations preserve a crystal cargo that originated from a deep reservoir with An- and Fo-rich macrocrysts crystallized at about 17.5 km (4.9 kbar) depth. In contrast, mid-Holocene to historical samples record only shallower crystallization pressures of 2-4 kbar (7-13 km). It appears that since the middle-Holocene no crystals from the deep storage zone are transferred directly to the surface, which could indicate the establishment of new magma pathways and more complete homogenization of melts in the shallow storage zone during this period.

6. At the end of the last glacial maximum, the isostatic rebound caused a significant change in the stress field of the crust and an increase in the melting rate in the upper mantle, triggering a large pulse in magmatic activity (Le Breton et al., 2016; Maclennan et al., 2002; Slater et al., 1998). Following this, during the early-Holocene, the lower crust was continuously supplied with fresh batches of melt that allowed magma from deep regions to erupt at the surface. Once crustal pressure equilibrium has been re-established following the early-Holocene, shallower storage levels dominated the system architecture with more efficient mixing and homogenisation of melts prior to eruption.

Acknowledgments

This research work was financially supported by the University of Iceland Research Fund (Nr: HI17060092) and the EIMSKIP PhD fund of the University of Iceland. We are thankful to Karl Grönvold and Maja Bar Rasmussen for collecting some of the samples. Rósa Ólafsdóttir is thanked for providing the GIS shapefiles for the geological map. We thank Matt Pankhurst and an anonymous reviewer for their valuable comments and suggestions that improved the manuscript. M. E. Hartley acknowledges support from NERC grant NE/P002331/1. The involvement of S. A. Halldórsson was partly in relation to H2020 project EUROVOLC, funded by the European Commission (Grant 731070). M. Kahl acknowledges support from IRF postdoctoral fellowship grant 152726-051.

References

Ariskin, A.A., Frenkel, M.Y., Barmina, G.S., Nielsen, R.L., 1993. Comagmat: a Fortran program to model magma differentiation processes. Comput. Geosci. 19, 1155–1170. https://doi.org/10.1016/0098-3004(93)90020-6

Bali, E., Hartley, M.E., Halldórsson, S.A., Gudfinnsson, G.H., Jakobsson, S., 2018. Melt inclusion constraints on volatile systematics and degassing history of the 2014–2015 Holuhraun eruption, Iceland. Contrib. Mineral. Petrol. 173, 9. https://doi.org/10.1007/s00410-017-1435-0

Carlson, R.L., Herrick, C.N., 1990. Densities and porosities in the oceanic crust and their variations with depth and age. J. Geophys. Res. 95, 9153–9170. https://doi.org/10.1029/JB095iB06p09153

Cashman, K. V., Sparks, R.S.J., Blundy, J.D., 2017. Vertically extensive and unstable magmatic systems: A unified view of igneous processes. Science. 355, 1–9. https://doi.org/10.1126/science.aag3055

Cooper, K.M., Sims, K.W.W., Eiler, J.M., Banerjee, N., 2016. Timescales of storage and recycling of crystal mush at Krafla Volcano, Iceland. Contrib. Mineral. Petrol. 171, 1–19. https://doi.org/10.1007/s00410-016-1267-3

Danyushevsky, L. V., Plechov, P., 2011. Petrolog3: Integrated software for modeling crystallization processes. Geochem. Geophys. Geosyst. 12, 1-32. https://doi.org/10.1029/2011GC003516

Eason, D.E., Sinton, J.M., Grönvold, K., Kurz, M.D., 2015. Effects of deglaciation on the petrology and eruptive history of the Western Volcanic Zone, Iceland. Bull. Volcanol. 77, 1-27. https://doi.org/10.1007/s00445-015-0916-0

Edmonds, M., Cashman, K. V, Holness, M., Jackson, M., 2019. Architecture and dynamics of magma reservoirs. Philos. Trans. R. Soc. A. 377, 1-29

Eksinchol, I., Rudge, J.F., Maclennan, J. 2019. Rate of melt ascent beneath Iceland from the magmatic response to deglaciation. Physics.geo-ph. 1–33.

Gee, M.A.M., Taylor, R.N., Thirlwall, M.F., Murton, B.J., 1998. Glacioisostacy controls chemical and isotopic characteristics of tholeiites from the Reykjanes Peninsula, SW Iceland. Earth Planet. Sci. Lett. 164, 1–5. https://doi.org/https://doi.org/10.1016/S0012-821X(98)00246-5

Gudmundsson, A., 1986. Mechanical aspect of postglacial volcanism and tectonics of the Reykjanes Peninsula, southwest Iceland. J. Geophys. Res. 91, 12,711-12,721.

Halldórsson, S.A., Bali, E., Hartley, M.E., Neave, D.A., Peate, D.W., Guðfinnsson, G.H., Bindeman, I., Whitehouse, M.J., Riishuus, M.S., Pedersen, G.B.M., Jakobsson, S., Askew, R., Gallagher, C.R., Guðmundsdóttir, E.R., Gudnason, J., Moreland, W.M., Óskarsson, B. V, Nikkola, P., Reynolds, H.I., Schmith, J., Thordarson, T., 2018. Petrology and geochemistry of the 2014–2015 Holuhraun eruption, central Iceland: compositional and

mineralogical characteristics, temporal variability and magma storage. Contrib. Mineral. Petrol. 173, 1-25. https://doi.org/10.1007/s00410-018-1487-9

Halldórsson, S.A., Oskarsson, N., Gronvold, K., Sverrisdottir, G., Steinthorsson, S., 2008. Isotopic-heterogeneity of the Thjorsa lava — Implications for mantle sources and crustal processes within the Eastern Rift Zone, Iceland. Chem. Geol. 255, 305–316. https://doi.org/10.1016/j.chemgeo.2008.06.050

Hansen, H., Grönvold, K., 2000. Plagioclase ultraphyric basalts in Iceland : the mush of the rift. J. Volcanol. Geotherm. Res. 98, 1–32.

Hardarson, B.S., Fitton, J.G., 1991. Increased mantle melting beneath Snaefellsjökull volcano during Late Pleistocene deglaciation. Nature 353, 62–64. https://doi.org/https://doi.org/10.1038/353062a0

Hartley, M.E., Bali, E., Maclennan, J., Neave, D.A., Halldórsson, S.A., 2018. Melt inclusion constraints on petrogenesis of the 2014–2015 Holuhraun eruption, Iceland. Contrib. Mineral. Petrol. 173, 1-23. https://doi.org/10.1007/s00410-017-1435-0

Hjartarson, A., 1988. Þjórsárhraunið mikla - stærsta nútímahraun jarðar (The great Þjórsá lava - The largest Holocene lava on Earth). Náttúrufræöingurinn 58, 1–16.

Holness, M.B., Anderson, A.T., Martin, V.M., Maclennan, J., Passmore, E., Schwindinger, K., 2007. Textures in partially solidified crystalline nodules: a window into the pore structure of slowly cooled mafic intrusions. J. Petrol. 48, 1243–1264. https://doi.org/10.1093/petrology/egm016

Holness, M.B., Stock, M.J., Geist, D., 2019. Magma chambers versus mush zones: constraining the architecture of sub-volcanic plumbing systems from microstructural analysis of crystalline enclaves. Philos. Trans. R. Soc. A. 377, 1-28. https://doi.org/10.1098/rsta.2018.0006

Hudson, T.S., White, R.S., Greenfield, T., Ágústsdóttir, T., Brisbourne, A., Green, R.G., 2017. Deep crustal melt plumbing of Bárðarbunga volcano, Iceland. Geophys. Res. Lett. 44, 8785–8794. https://doi.org/10.1002/2017GL074749

Jakobsson, S.P., 1979. Petrology of Recent basalts of the Eastern Volcanic Zone, Iceland. Acta Nat. Islandica 26, 1–103.

Jakobsson, S.P., Jónsson, J., Shido, F., 1978. Petrology of the western Reykjanes Peninsula, Iceland. J. Petrol. 19, 669–705. https://doi.org/10.1093/petrology/19.4.669Jull, M., McKenzie, D., 1996. The effect of deglaciation on mantle melting beneath IcelandJ. Geophys. Res. 101, 21,815-21,828.

Kahl, M., Chakraborty, S., Costa, F., Pompilio, M., Liuzzo, M., Viccaro, M., 2013. Compositionally zoned crystals and real-time degassing data reveal changes in magma transfer dynamics during the 2006 summit eruptive episodes of Mt. Etna. Bull. Volcanol. 75, 1–14. https://doi.org/10.1007/s00445-013-0692-7

Kelemen, P.B., Koga, K., Shimizu, N., 1997. Geochemistry of gabbro sills in the crust–mantle transition zone of the Oman ophiolite: implications for the origin of the

oceanic lower crust. Earth Planet. Sci. Lett. 146, 1–31. https://doi.org/https://doi.org/10.1016/S0012-821X(96)00235-X

Larsen, G., 1984. Recent volcanic history of the Veidivötn fissure swarm, southern Iceland - an approach to volcanic risk assessment. J. Volcanol. Geotherm. Res. 22, 33–58. https://doi.org/10.1016/0377-0273(84)90034-9

Larsen, G., Guðmundsson, M.T., 2014. Volcanic system : Bárðarbunga system. Cat. Icelandic Volcanoes 1–11.

Le Breton, E., Dauteuil, O., Biessy, G., 2016. Post-glacial rebound of Iceland during the Holocene. J. Geol. Soc. London 167, 417–432. https://doi.org/10.1144/0016-76492008-126.Post-glacial

Maclennan, J., 2019. Mafic tiers and transient mushes: evidence from Iceland. Philos. Trans. R. Soc. A 377, 1-20. https://doi.org/10.1098/rsta.2018.0021

Maclennan, J., 2008. Concurrent mixing and cooling of melts under Iceland. J. Petrol. 49, 1931–1953. https://doi.org/10.1093/petrology/egn052

Maclennan, J., Jull, M., McKenzie, D., Slater, L., Grönvold, K., 2002. The link between volcanism and deglaciation in Iceland. Geochem. Geophys. Geosyst. 3, 1–25. https://doi.org/10.1029/2001GC000282

Maclennan, J., McKenzie, D., Grönvold, K., Shimizu, N., Eiler, J.M., Kitchen, N., 2003. Melt mixing and crystallization under Theistareykir, northeast Iceland. Geochem. Geophys. Geosyst. 4, 1-40. https://doi.org/10.1029/2003GC000558

Marsh, B.D., 2006. Dynamics of magmatic systems. Elements. 2, 287–292. https://doi.org/10.1016/S0074-6142(09)60100-5

McGarvie, D.W., 1984. Torfajokull: a volcano dominated by magma mixing. Geology 12, 685–688. https://doi.org/10.1130/0091-7613(1984)12<685:TAVDBM>2.0.CO;2

Mørk, M.B.E., 1984. Magma mixing in the post-glacial veidivötn fissure eruption, southeast Iceland: a microprobe study of mineral and glass variations. Lithos 17, 55–75. https://doi.org/10.1016/0024-4937(84)90006-9

Nakamura, Y., 1973. Origin of sector-zoning of igneous clinopyroxenes. Am. Mineral. 58, 986–990.

Namur, O., Charlier, B., Toplis, M.J., Vander Auwera, J., 2011. Prediction of plagioclase-melt equilibria in anhydrous silicate melts at 1-atm. Contrib. Mineral. Petrol. 163, 133–150. https://doi.org/10.1007/s00410-011-0662-z

Neave, D.A., Buisman, I., MacLennan, J., 2017a. Continuous mush disaggregation during the long-lasting Laki fissure eruption, Iceland. Am. Mineral. 102, 2007–2021. https://doi.org/10.2138/am-2017-6015CCBY

Neave, D.A., Hartley, M.E., Maclennan, J., Edmonds, M., Thordarson, T., 2017b. Volatile and light lithophile elements in high-anorthite plagioclase-hosted melt inclusions from Iceland. Geochim. Cosmochim. Acta 205, 100–118. https://doi.org/10.1016/j.gca.2017.02.009

Neave, D.A., Maclennan, J., Hartley, M.E., Edmonds, M., Thordarson, T., 2014. Crystal storage and transfer in basaltic systems: The Skuggafjoll eruption, Iceland. J. Petrol. 55, 2311_2346. https://doi.org/10.1093/petrology/egu058

Neave, D.A., Maclennan, J., Thordarson, T., Hartley, M.E., 2015. The evolution and storage of primitive melts in the Eastern Volcanic Zone of Iceland: the 10 ka Grímsvötn tephra series (i.e. the Saksunarvatn ash). Contrib. Mineral. Petrol. 170, 1–23. https://doi.org/10.1007/s00410-015-1170-3

Neave, D.A., Passmore, E., Maclennan, J., Fitton, G., Thordarson, T., 2013. Crystal-melt relationships and the record of deep mixing and crystallization in the AD 1783 Laki eruption, Iceland. J. Petrol. 54, 1661–1690. https://doi.org/10.1093/petrology/egt027

Neave, D.A., Putirka, K.D., 2017. A new clinopyroxene-liquid barometer, and implications for magma storage pressures under Icelandic rift zones. Am. Mineral. 102, 777–794. https://doi.org/http://dx.doi.org/10.2138/am-2017-5968

Óladóttir, B.A., Larsen, G., Sigmarsson, O., 2011. Holocene volcanic activity at Grímsvötn, Bárdarbunga and Kverkfjöll subglacial centres beneath Vatnajökull, Iceland. Bull. Volcanol. 73, 1187–1208. https://doi.org/10.1007/s00445-011-0461-4

Óskarsson, B. V., Andersen, C.B., Riishuus, M.S., Sørensen, E.V., Tegner, C., 2017. The mode of emplacement of Neogene flood basalts in eastern Iceland: the plagioclase ultraphyric basalts in the Grænavatn group. J. Volcanol. Geotherm. Res. 332, 26–50. https://doi.org/10.1016/j.jvolgeores.2017.01.006

Passmore, E., Maclennan, J., Fitton, G., Thordarson, T., 2012. Mush disaggregation in basaltic magma chambers: Evidence from the AD 1783 Laki eruption. J. Petrol. 53, 2593–2623. https://doi.org/10.1093/petrology/egs061

Pedersen, G.B.M., Gudmundsson, M.T., Reynolds, H.I., Höskuldsson, A., Jónsdóttir, I., Dürig, T., Gallagher, C., Gudnason, J., Askew, R., Magnusson, E., Nikkola, P., Moreland, W.M., Drouin, V.J.P.B., Thordarson, T., Dumont, S., Óskarsson, B.V., Riishuus, M.S., Sigmundsson, F., Schmith, J., 2017. Lava field evolution and emplacement dynamics of the 2014–2015 basaltic fissure eruption at Holuhraun, Iceland. J. Volcanol. Geotherm. Res. 340, 155–169. https://doi.org/10.1016/j.jvolgeores.2017.02.027

Pinton, A., Giordano, G., Speranza, F., Thordarson, T., 2018. Paleomagnetism of Holocene lava flows from the Reykjanes Peninsula and the Tungnaá lava sequence (Iceland): implications for flow correlation and ages. Bull. Volcanol. 80, 1-19. https://doi.org/10.1007/s00445-017-1187-8

Putirka, K.D., 2008. Thermometers and Barometers for Volcanic Systems. Rev. Mineral. Geochem. 69, 61–120. https://doi.org/10.2138/rmg.2008.69.3

Roeder, P.L., Emslie, R.F., 1970. Olivine-liquid equilibrium. Contrib. Mineral. Petrol. 29, 275–289. https://doi.org/10.1007/BF00371276

Ryan, M.P., 2018. The mechanics and three-dimensional internal structure of active magmatic systems: Kilauea volcano, Hawaii. J. Geophys. Res. Solid Earth. 93, 4213–4248. https://doi.org/10.1029/JB093iB05p04213

Shorttle, O., Maclennan, J., 2011. Compositional trends of Icelandic basalts: Implications for short-length scale lithological heterogeneity in mantle plumes. Geochem. Geophys. Geosyst. 12, 1-32. https://doi.org/10.1029/2011GC003748

Sigmundsson, F., 1991. Post-glacial rebound and asthenosphere viscosity in Iceland. Geophys. Res. Lett. 18, 1131-1134.

Sigvaldason, G.E., Annertz, K., Nilsson, M., 1992. Effect of glacier loading/deloading on volcanism: postglacial volcanic production rate of the Dyngjufjöll area, central Iceland. Bull. Volcanol. 54, 385–392. https://doi.org/10.1007/BF00312320

Sinton, J., Grönvold, K., Sæmundsson, K., 2005. Postglacial eruptive history of the Western Volcanic Zone, Iceland. Geochem. Geophys. Geosyst. 6, 1-34. https://doi.org/10.1029/2005GC001021

Sinton, J.M., Detrick, R.S., 1992. Mid-ocean ridge magma chambers. J. Geophys. Res. Solid Earth 97, 197–216. https://doi.org/10.1029/91JB02508

Slater, L., Jull, M., McKenzie, D., Gronvöld, K., 1998. Deglaciation effects on mantle melting under Iceland: results from the Northern Volcanic Zone. Earth Planet. Sci. Lett. 164, 151–164. https://doi.org/10.1016/S0012-821X(98)00200-3

Sobolev, A. V, Hofmann, A.W., Kuzmin, D. V, Yaxley, G.M., Arndt, N.T., Chung, S., Danyushevsky, L. V, Elliott, T., Frey, F. A., Garcia, M.O., Gurenko, A.A., Kamenetsky, V.S., Kerr, A.C., Krivolutskaya, N.A., Matvienkov, V. V, Nikogosian, Rocholl A., I.K., Sigurdsson, I.A., Sushchevskaya, N.M., Teklay, M., 2007. The amount of recycled crust in sources of mantle-derived melts. Science 316, 412–418. https://doi.org/10.1126/science.1138113

Svavarsdóttir, S.I., Halldórsson, S.A., Guðfinnsson, G.H., 2017. Geochemistry and petrology of Holocene lavas in the Bárðardalur region, N-Iceland. Part I: geochemical constraints on source provenance. Jökull 67, 17–42.

Thordarson, T., Höskuldsson, Á., 2008. Postglacial volcanism in Iceland. Jokull. 58, 197–228.

Thordarson, T., Larsen, G., 2007. Volcanism in Iceland in historical time: volcano types, eruption styles and eruptive history. J. Geodyn. 43, 118–152. https://doi.org/10.1016/j.jog.2006.09.005

Ubide, T., Mollo, S., Zhao, J., Nazzari, M., Scarlato, P., 2019. Sector-zoned clinopyroxene as a recorder of magma history, eruption triggers, and ascent rates. Geochim. Cosmochim. Acta. 251, 265-283. https://doi.org/10.1016/j.gca.2019.02.021

Vilmundardóttir, E.G., 1977. Tungnarhraun, jardhfraedhiskyrsla (Tungnáhraun lavas, geological report). Orkustofnun Raforkudeild 7702, 1–166.

Vilmundardóttir, E.G., Snorrason, S.P., Larsen, G., 2000. Geological map of subglacial volcanic area southwest of Vatnajökull icecap, Iceland, 1: 50.000. Natl. Energy Auth. Natl. Power Company, Reykjavík, Iceland.

West, M., Menke, W., Tolstoy, M., Webb, S., Sohn, R., 2001. Magma storage beneath axial volcano on the Juan de Fuca mid-ocean ridge. Nature 413, 833-836.

Wood, B.J., Blundy, J.D., 1997. A predictive model for rare earth element partitioning between clinopyroxene and anhydrous silicate melt. Contrib. Mineral. Petrol. 129, 166–181. https://doi.org/10.1007/s004100050330

Yang, H.-J., Kinzler, R.J., Grove, T.L., 1996. Experiments and models of anhydrous, basaltic olivine-plagioclase-augite saturated melts from 0.001 to 10 kbar. Contrib. Mineral. Petrol. 124, 1–18. https://doi.org/10.1007/s004100050169

Zellmer, G.F., Rubin, K.H., Gronvöld, K., Jurado-Chichay, Z., 2008. On the recent bimodal magmatic processes and their rates in the Torfajökull–Veidivötn area, Iceland. Earth Planet. Sci. Lett. 269, 388–398. https://doi.org/10.1016/j.epsl.2008.02.026

9.1 Supplementary information and figures attached to Paper I

1. Electron microprobe analysis

Major element compositions of macrocrysts (olivine, plagioclase and clinopyroxene), glass and melt inclusions (MIs) were determined in thin sections and grain mounts by electron probe microanalysis (EPMA) using a JEOL JXA-8230 SuperProbe at the Institute of Earth Science, University of Iceland. The microprobe is equipped with five wavelength-dispersive spectometers (WDS) and an energy-dispersive spectrometer. Analyses were acquired using a 15 keV accelerating voltage and a probe current of 10-20 nA. Glass and MIs were analysed with a defocused electron beam of 5-15 µm, except small melt inclusions where a point beam was used. In order to avoid Na loss in glasses, Na was always analysed first on its spectrometer with a relatively short counting time (20 s on the peak, 10 s on the background). For all other elements, counting time are 30-40 s on the peak and 15-20 s on the background. All mineral phases were analysed with a beam size of 1-5 µm. Counting times for olivines and clinopyroxenes were 30 s on peaks and 15-30 s on backgrounds, while for plagioclase crystals 40 s and 20-40 s on peaks and backgrounds, respectively.

Natural and synthetic standards were used to check the accuracy and reproducibility of the measurements. Secondary standards of plagioclase (Astimex Standards Ltd), Cr-augite (NMNH 164905), Springwater meteorite olivine (USNM 2566), and basaltic glass A-99 from Makaopuhi Lava Lake (NMNH 113498-1) were analysed prior each session. The CITZAF correction program (Armstrong, 1991) was used for all analyses, except for oxides where ZAF correction was applied. 1σ errors reported in the diagrams are based on the standard deviation of multiple standard analyses collected during different analytical sessions.

2. Melt inclusions

2.1 Melt inclusions homogenization

Lava and tephra samples were crushed at the University of Iceland using the tungsten carbide, manganese steel Jaw Crusher BB 100. The crushed material was then sieved and melt inclusion-bearing macrocysts ranging from 0.5-2.4 mm in size were hand-picked under a binocular microscope. Olivine and plagioclase crystals were individually hand-polished to expose glassy melt inclusions at the surface. Even though naturally quenched MIs occur in abundance, samples from Þjórsárdalshraun, Drekahraun and Veiðivötn units preserve only crystallized MIs, which require re-homogenization prior to geochemical analysis. Crystals containing crystalline melt inclusions were put into a graphite crucible, mixed with graphite powder, heated in a high-temperature furnace at 1210 ± 5 °C for 5 min and quenched in cold water immediately after. Heated crystals were then examined by optical microscope to check for the complete homogenization and the lack of oxidation. All analysed MIs (n=17) from Drekahraun samples were homogenized, along with 33 MIs from Þjórsárdalshraun and 24 MIs from Veiðivötn. All homogenized MIs were hosted in plagioclase.

2.2 Post-entrapment crystallization correction

The chemical compositions of melt inclusions can be significantly modified by post entrapment processes, including crystallization of the host mineral on the inclusion walls (post-entrapment crystallization, PEC), and Fe-Mg diffusion in olivine-hosted MIs (Danyushevsky et al., 2000). Olivine-hosted inclusion compositions were corrected using the "Olivine MI" tool in Petrolog3 (Danyushevsky and Plechov, 2011), which takes into account both host olivine crystallization and Fe-Mg diffusion processes. This process results in decreasing FeOtot and increasing MgO contents within the inclusion (Danyushevsky et al., 2000). One of the input parameters of this procedure is the original iron content of the melt before diffusive Fe-loss, referred as FeO*. The original iron content was estimated starting from the groundmass glass composition variations. We calculated the equilibrium Fo content for each glass analysis and plotted it against the FeO content of the melt. Using the equation derived from the linear regression (R^2=0.95), the original FeO* can be estimated at any given Fo value. The host olivine composition was measured adjacent to each melt inclusion.

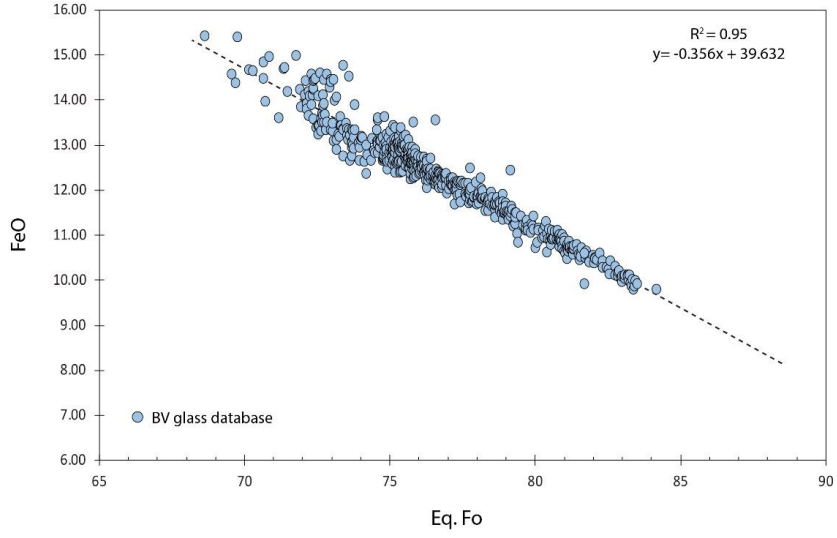

Fig. S1. *Equilibrium Fo content vs FeO_{tot} of glasses from the Bárðarbunga-Veiðivötn volcanic system (groundmass glasses analysed during this work and Holocene tephra analyses from Óladóttir et al. (2011a). Fo calculated considering a Kd_{Fe-Mg}^{ol-liq} of 0.3±0.03 (Roeder and Emslie, 1970). The regression equation derived from that diagram can be used to estimate the original FeO* at a given Fo value for samples from the Bárðarbunga-Veiðivötn system.*

For plagioclase-hosted melt inclusions, we employed a similar procedure to that of Neave et al. (2017). Given that Al_2O_3 is the most modified element during PEC in plagioclase-hosted MIs and TiO_2 is incompatible during crystallization, we plotted the Al_2O_3 contents of olivine-hosted MIs (previously corrected for post entrapment processes) as a function of TiO_2 contents. Using the regression equation derived from olivine-hosted MIs, we estimated the unmodified Al_2O_3 content at the time of the entrapment. Consequently, the

composition of the melt at the time of the entrapment has been calculated by adding the host plagioclase composition (measured next to the MI) back into the inclusion. Finally, the plagioclase equilibrium constant, $Kd_{An-Ab}^{plg-liq}$ of 0.27±0.11 (Putirka, 2008) was used as an additional parameter to check the correction procedure. Following this procedure, 12% of the plagioclase-hosted melt inclusions fell outside the accepted Kd range and were than rejected for any further consideration.

3. Thermobarometry methods

3.1 Clinopyroxene – melt barometer and geothermometers

In order to apply clinopyroxene melt barometry, it is important that equilibrium conditions between clinopyroxene crystals and melt are satisfied. In our dataset, only clinopyroxene rims are found to be in equilibrium with the carrier melts (Fig. 4b) and therefore we calculated clinopyroxene crystallization pressures following the method described by Neave and Putirka (2017). This barometer reproduces the calibration data with a standard error of estimate (SEE) of ±1.4 kbar. We matched putative equilibrium liquids with clinopyroxene compositions based on strict equilibrium criteria. Liquids were selected from a large database (n=845) of glass and melt inclusion compositions (Mg# 39.6-67.6) collected during this work, along with Holocene glassy tephra units from Bárðarbunga volcano (n=236) (Óladóttir et al. 2011a). The equilibrium criteria were the following: 1) We checked the Fe-Mg partitioning between clinopyroxene and melt, and excluded any pairs that did not satisfy the criterion $Kd_{Fe-Mg}^{cpx-melt}$=0.27± 0.03 (Grove et al., 1992; Putirka et al., 2003); 2) We considered Ti partitioning (D_{Ti}) between clinopyroxene and melt using the lattice strain model of Hill et al. (2011), and selected clinopyroxene-melt pairs that are within 40% of the predicted Ti equilibrium; 3) We compared predicted and observed DiHd, EnFs and CaTs clinopyroxene components (Putirka, 1999) and selected only equilibrium clinopyroxene-melt pairs with DiHd, EnFs and CaTs errors lower than 5%, 12% and 6% respectively. Pressure and temperature were then determined by solving equations 33 and 1 from Putirka (2008) and Neave and Putirka (2017), respectively. Of 431 clinopyroxene compositions from all units, a total of 314 analyses were successfully matched (Table 2) to putative equilibrium melt compositions. No matches were found for 117 clinopyroxene compositions, mainly consisting of clinopyroxene cores and dark sectors in which the predicted DTi was too low to be in equilibrium with available melt compositions.

Groundmass glass and melt inclusion temperatures were estimated with a melt-only thermometer (SEE= ±26 °C) (Yang et al., 1996), and clinopyroxene-melt, olivine-melt and plagioclase-melt thermometers (SEE= ±45, ±42, ±36 °C, respectively) (Putirka, 2008).

3.2 Melt equilibration pressures (OPAM barometry)

The equilibrium pressure of groundmass glasses and melt inclusions can be estimated from the effect of pressure on the olivine-plagioclase-augite-melt (OPAM) boundary in composition space, provided that the magma was saturated in these mineral phases (Grove et al., 1992; Yang et al., 1996). Consequently, it is possible to derive the pressure at which the melt last equilibrated with olivine, plagioclase and augite. Here we use the approach described by Hartley et al. (2018) to calculate OPAM equilibration pressures. This implementation uses equations 1-3 of the Yang et al. (1996) barometer to iteratively calculate three phase-saturated melt compositions at a range of crustal pressures

and compares these with the measured melt composition. The best-fitting pressure between measured and predicted melt compositions is then assessed against a significance threshold: if the probability of fit is >0.8, then the measured melt composition is expected to be three phase-saturated, and hence return a robust pressure estimate. The standard error of this implementation is ±1.3 kbar. We processed 328 groundmass glass analyses and 436 PEC-corrected MI analyses from all eruptive units through the OPAM barometer (Table 2) and filtered our results according to the probability of fit >0.8 criterion. We also applied this calculation to Holocene tephra glass compositions from Bárðarbunga eruptions (Óladóttir et al., 2011a).

Additional supplementary figures

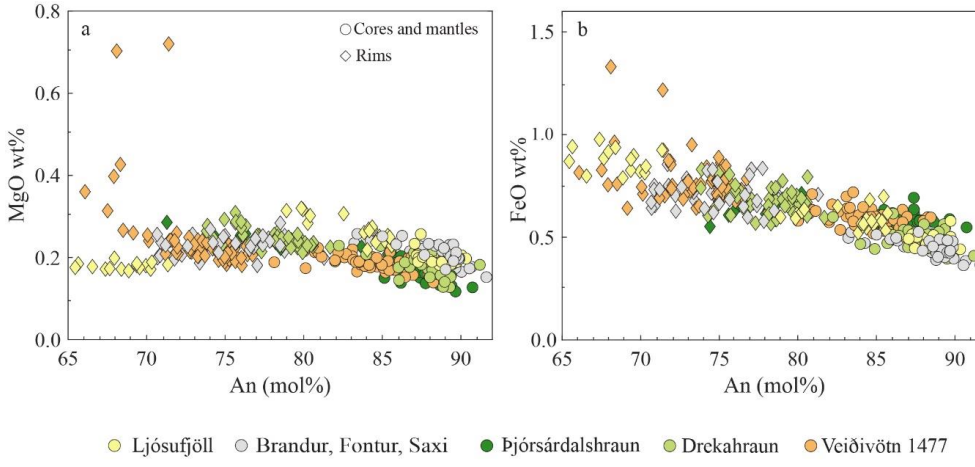

Fig. S2. *a-b) Compositional variation of plagioclase macrocrysts as a function of An (mol%). Selected elements are MgO and FeO. 1σ error is within the symbol size.*

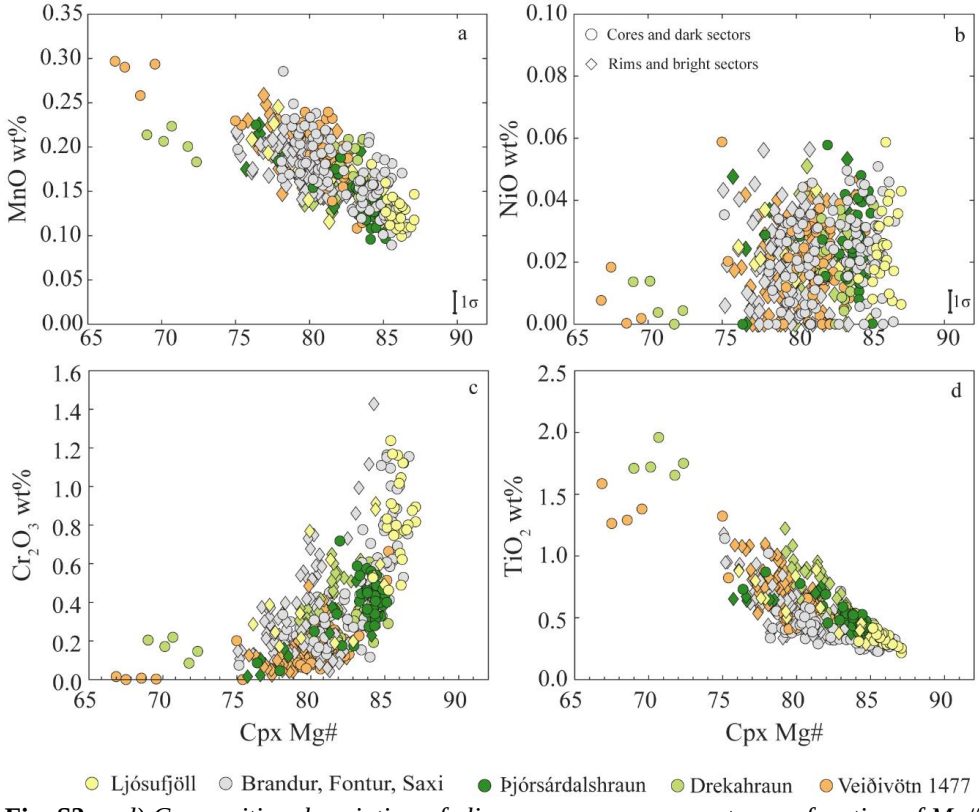

Fig. S3. *a-d) Compositional variation of clinopyroxene macrocrysts as a function of Mg#. Selected elements are MnO, NiO, Cr_2O_3 and TiO_2. 1σ error is within the symbol size unless otherwise indicated.*

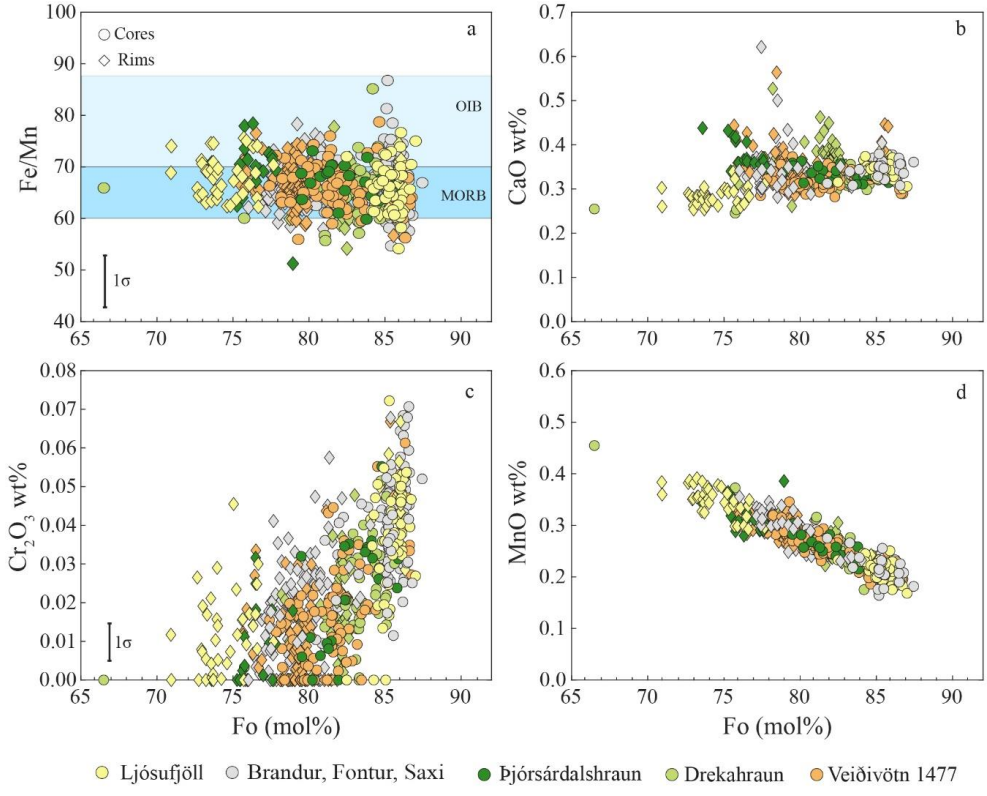

Fig. S4. *a-d) Compositional variation of olivine macrocrysts as a function of Fo (mol%). Selected elements are Fe/Mn ratio, CaO, Cr_2O_3 and MnO. MORB and OIB fields from Sobolev et al. (2007). 1σ error is within the symbol size unless otherwise indicated.*

Supplementary references

Armstrong, J.T., 1991. Quantitative Elemental Analysis of Individual Microparticles with Electron Beam Instruments, in: Heinrich, K.F.J., Newbury, D.E. (Eds.), Electron Probe Quantitation. Springer US, Boston, MA, pp. 261–315. https://doi.org/10.1007/978-1-4899-2617-3_15

Danyushevsky, L. V., Della-Pasqua, F.N., Sokolov, S., 2000. Re-equilibration of melt inclusions trapped by magnesian olivine phenocrysts from subduction-related magmas: petrological implications. Contrib. to Mineral. Petrol. 138, 68–83. https://doi.org/10.1007/PL00007664

Danyushevsky, L. V., Plechov, P., 2011. Petrolog3: Integrated software for modeling crystallization processes. Geochemistry, Geophys. Geosystems 12. https://doi.org/10.1029/2011GC003516

Grove, T.L., Kinzler, R.J., Bryan, W.., 1992. Fractionation of mid-ocean ridge basalt (MORB). Gephysical Monogr. Geophys. Union 71, 281–310. https://doi.org/10.1029/GM071p0281

Hartley, M.E., Bali, E., Maclennan, J., Neave, D.A., Halldórsson, S.A., 2018. Melt inclusion constraints on petrogenesis of the 2014–2015 Holuhraun eruption, Iceland. Contrib. to Mineral. Petrol. 173, 10. https://doi.org/10.1007/s00410-017-1435-0

Hill, E., Blundy, J.D., Wood, B.J., 2011. Clinopyroxene-melt trace element partitioning and the development of a predictive model for HFSE and Sc. Contrib. to Mineral. Petrol. 161, 423–438. https://doi.org/10.1007/s00410-010-0540-0

Neave, D.A., Hartley, M.E., Maclennan, J., Edmonds, M., Thordarson, T., 2017. Volatile and light lithophile elements in high-anorthite plagioclase-hosted melt inclusions from Iceland. Geochim. Cosmochim. Acta 205, 100–118. https://doi.org/10.1016/j.gca.2017.02.009

Neave, D.A., Putirka, K.D., 2017. A new clinopyroxene-liquid barometer , and implications for magma storage pressures under Icelandic rift zones. Am. Mineral. 102, 777–794. https://doi.org/http://dx.doi.org/10.2138/am-2017-5968

Óladóttir, B.A., Larsen, G., Sigmarsson, O., 2011. Holocene volcanic activity at Grímsvötn, Bárdarbunga and Kverkfjöll subglacial centres beneath Vatnajökull, Iceland. Bull. Volcanol. 73, 1187–1208. https://doi.org/10.1007/s00445-011-0461-4

Putirka, K.D., 2008. Thermometers and Barometers for Volcanic Systems 69, 61–120. https://doi.org/10.2138/rmg.2008.69.3

Putirka, K.D., Mikaelian, H., Ryerson, F., Shaw, H., 2003. New clinopyroxene-liquid thermobarometers for mafic, evolved, and volatile-bearing lava compositions, with applications to lavas from Tibet and the Snake River Plain, Idaho. Am. Minerol. 88, 1542–1554.

Roedder, E., Emslie, R.F., 1970. Olivine-liquid equilibrium. Contrib. to Mineral. Petrol. 29, 275–289. https://doi.org/10.1007/BF00371276

Sobolev, A. V, Hofmann, A.W., Kuzmin, D. V, Yaxley, G.M., Arndt, N.T., Chung, S., Danyushevsky, L. V, Elliott, T., Frederick, A., Garcia, M.O., Gurenko, A.A., Kamenetsky, V.S., Kerr, A.C., Krivolutskaya, N.A., Matvienkov, V. V, Nikogosian, I.K., Sigurdsson, I.A., Sushchevskaya, N.M., Teklay, M., 2007. The Amount of Recycled Crust in Sources of Mantle-Derived Melts - Supplementary Information. Science 2, 412–418. https://doi.org/10.1126/science.1138113

Yang, H.J., Kinzler, R.J., Grove, T.L., 1996. Experiments and models of anhydrous, basaltic olivine-plagioclase-augite saturated melts from 0.001 to 10 kbar. Contrib. to Mineral. Petrol. 124, 1–18. https://doi.org/10.1007/s004100050169

10 Paper II

Timescales of crystal mush mobilization in the Bárðarbunga-Veiðivötn volcanic system based on olivine diffusion chronometry

Alberto Caracciolo, Maren Kahl, Enikő Bali, Guðmundur H. Guðfinnsson, Sæmundur A. Halldórsson, Margaret E. Hartley

Manuscript published in American Mineralogist, In press. DOI : 10.2138/am-2021-7670

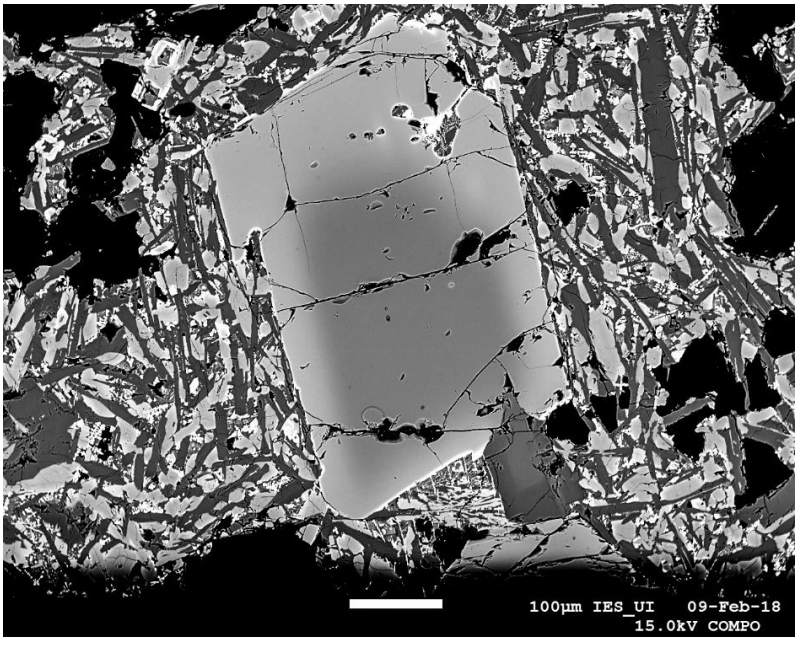

Timescales of crystal mush mobilization in the Bárðarbunga-Veiðivötn volcanic system based on olivine diffusion chronometry

Alberto Caracciolo[1,2], Maren Kahl[3], Enikő Bali[1,2], Guðmundur H. Guðfinnsson[1], Sæmundur A. Halldórsson[1], Margaret E. Hartley[4]

[1]*Nordic Volcanological Center, Institute of Earth Sciences, University of Iceland, Sturlugata 7, 101 Reykjavík, Iceland.*
[2]*Faculty of Earth Sciences, University of Iceland, Sturlugata 7, 101 Reykjavík, Iceland.*
[3]*Institut für Geowissenschaften, Universität Heidelberg, Heidelberg, Germany*
[4]*Department of Earth and Environmental Sciences, University of Manchester, Manchester, UK*

Manuscript accepted by American Mineralogist, In press. DOI : 10.2138/am-2021-7670

Abstract
The timescales of magmatic processes within a volcanic system may be variable over a volcano's geological history. Crystals reflect environmental perturbations under which they grew, and compositional gradients quenched inside crystals on eruption can be exploited to extract timescales of magmatic processes. Here, we use multi-element diffusion chronometry in olivine macrocrysts to recover their residence time in a melt which ultimately erupted at the surface. The macrocrysts were mobilized by the carrier melt from mushy layers in the magma reservoir, and diffusion timescales likely reflect the time interval between mush disaggregation, ascent and eruption. To unravel the evolution of mush disaggregation timescales with time, we target early-Holocene, middle-Holocene and historical magmatic units erupted in the Bárðarbunga-Veiðivötn volcanic system in Iceland's Eastern Volcanic Zone. Macrocryst contents vary between samples; early-Holocene samples are highly phyric (10-45 vol% macrocrysts) and contain gabbroic nodules, whereas middle-Holocene (5-15 vol%) and historical units (5-10 vol%) tend to be generally less phyric. Early-Holocene olivine macrocrysts have core compositions in the range Fo_{84-87}, whilst middle-Holocene and historical samples record a wider range in core compositions from Fo_{80} to $Fo_{86.5}$. Olivine rims are in chemical equilibrium with their carrier liquid, and are slightly more evolved in early-Holocene units (Fo_{76-81}) compared to middle-Holocene (Fo_{78-80}) and historical (Fo_{81-83}) units. Diffusion chronometry reveals that the timescale between mush disaggregation and eruption has changed over time, with timescales getting shorter approaching recent times. Early-Holocene olivine macrocrysts dominantly record Fe-Mg diffusion timescales between 200-400 days, whilst middle-Holocene and historical units typically record timescales of about 70 and 60 days, respectively. Barometric studies suggest that melts and crystals are likely stored and gradually transferred throughout an interconnected multi-tiered system that ultimately culminate in a mid-crustal reservoir(s) at about 6.8-7.5 ± 2.5 km depth, where final disaggregation by the carrier liquid took place. We argue that, as a result of extensional processes enhanced by rifting events, well-mixed melts got drawn into mid-crustal reservoir(s) causing crystal mush loosening and mobilization. In addition, we propose that more energy in the form of heat and/or melt supply was required in the early Holocene to break up the dense mush fabric and convert it into an eruptible magma. Conversely, as evidenced by the diverse macrocryst content of the historical units and by the lack of gabbroic nodules, the system has become characterized by a less compact mush fabric

since at least the middle-Holocene, such that fresh injection of melt would easily loosen and mobilize the mush, resulting in an eruption within a couple of months. This study provides evidence that along axial rift settings, rifting-related processes can help to "pull the mush apart" with no requirement for primitive magma injection as an eruption trigger. Furthermore, we provide evidence that in the Bárðarbunga-Veiðivötn volcanic system specifically, the time between mush disaggregation and eruption has decreased considerably with time, indicating shorter warning times before imminent eruptions.

1. INTRODUCTION

Understanding the time and duration of magmatic processes has been a central topic in volcanology, as time is a critical parameter to assess volcanic risk (Sparks and Sigurdsson, 1977). Great strides have been made over the past decades in developing diffusion chronometry as a fundamental tool to retrieve time information of magmatic processes recorded in minerals (Martin et al. 2008; Costa and Morgan 2010; Kahl et al. 2011, 2013, 2015, 2017; Ruprecht and Plank 2013; Cooper and Kent 2014; Viccaro et al. 2016; Hartley et al. 2016; Dohmen et al. 2017; Mutch et al. 2019a, 2019b).
The chemistry of igneous minerals reflects the environment(s) under which they grew, and any perturbation of pressure, temperature, melt composition or oxygen fugacity might be recorded by their composition (Blundy and Cashman, 2008; Ginibre et al., 2007; Streck, 2008). Changing growth conditions result in chemical zoning in minerals. At magmatic temperatures, compositional gradients tend to be smoothed out via diffusion as long as the system stays above the closure temperature. Diffusion chronometry is used to model the re-equilibration of different elements across compositionally distinct zones in crystals to derive the time that elapsed between the onset of the perturbation in growth conditions (e.g. magma injection) and the point at which diffusion effectively ceased to play a significant role (e.g. volcanic eruption) (Costa et al., 2008; Costa and Morgan, 2010; Dohmen et al., 2017; Turner and Costa, 2007). Diffusion chronometry in plagioclase, olivine and pyroxene crystals has been widely applied to estimate timescales of mixing processes and recharge events (Chamberlain et al., 2014; Costa and Chakraborty, 2004; Kahl et al., 2015, 2011; Rae et al., 2016; Rasmussen et al., 2018; Ruprecht and Cooper, 2012; Viccaro et al., 2016), magma ascent rates (Demouchy et al., 2006; Hartley et al., 2018; Mutch et al., 2019a; Ruprecht and Plank, 2013), cooling rates (Coogan et al., 2005; Faak et al., 2013; Newcombe et al., 2014; Sio et al., 2013) and crystal mush disaggregation timescales (Cooper and Kent, 2014; Costa et al., 2010; Hartley et al., 2016; Moore et al., 2014; Mutch et al., 2020; Nikkola et al., 2019; Pankhurst et al., 2018).

In Iceland, magma storage bodies occur over a large range of depths (Caracciolo et al., 2020; Haddadi et al., 2017; Hartley et al., 2018; Neave et al., 2013; Neave and Putirka, 2017) and understanding the rate of magma transfer between the different active storage zones in such active magmatic systems is vital for the interpretation of signals of volcanic unrest. The 2010 Eyjafjallajökull eruption provided a significant step forward in linking petrological and geophysical data: pre-eruptive geophysical signals (e.g. ground displacement and earthquake frequency) (Sigmundsson et al., 2010) registered between November 2009 and March 2010 are consistent with the onset of magma injection in the Eyjafjallajökull system obtained through diffusion chronometry on zoned olivine crystals (Pankhurst et al., 2018).

Diffusion chronometry applied to recent Icelandic eruptions indicates very short timescales of magma mixing (Viccaro et al., 2016) and crystal mush disaggregation

(Hartley et al., 2016; Nikkola et al., 2019; Pankhurst et al., 2018) beneath Icelandic volcanoes. However, these studies mainly focus on recent and single eruptions in different volcanic systems and it is still unknown whether timescales of magmatic processes are uniform within the lifespan of a single volcanic system. Here we employ diffusion chronometry by modeling the diffusive relaxation of Fe-Mg, Mn and Ni in olivine macrocrysts to retrieve timescales of crystal mush disaggregation beneath the Bárðarbunga-Veiðivötn volcanic system in central Iceland. Secondly, we merge diffusion modeling results with prior geobarometric constraints in order to reconstruct magmatic processes in the Bárðarbunga-Veiðivötn volcanic system throughout the Holocene. To do this, we have targeted well-characterized magmatic units of different age (early-Holocene to historical) within the same volcanic system. We determine the time that has elapsed between magma injection into the crystal mush reservoirs and the subsequent eruption, and importantly, we discuss how these timescales have changed over the Holocene period.

2. GEOLOGICAL BACKGROUND, SAMPLE LOCALITIES AND PREVIOUS WORK

Iceland is the only place in the world where a mid-ocean ridge intersects a mantle plume directly. The on-land manifestation of the Mid-Atlantic Ridge is split into four main neovolcanic rift zones (Fig. 1a), the Reykjanes Volcanic Belt (RVB), the Western Volcanic Zone (WVZ), the Eastern Volcanic Zone (EVZ) and the Northern Volcanic Zone (NVZ). The Bárðarbunga volcanic system is the largest volcanic system of the EVZ and it rises above the current presumed centre of the mantle plume (Bjarnason, 2008) (Fig. 1a). The southwesternmost segment of the Bárðarbunga volcanic system is commonly referred to as the Bárðarbunga-Veiðivötn volcanic system and it consists of a fissure swarm that fades out towards the south into the Torfajökull volcanic system (Larsen and Guðmundsson, 2014; Thordarson and Larsen, 2007). The volcanic units in the Bárðarbunga-Veiðivötn volcanic system considered in this study are represented by a suite of well-characterized samples, which have previously been studied by Caracciolo et al. (2020). Here we summarize key findings of that study and we guide the reader to this work for further details on these units and the geology of the area. The sampled units are: Brandur, Fontur and Saxi (early Holocene), Þjórsárdalshraun and Drekahraun (middle Holocene) and Veiðivötn 1477 (historical) (Fig. 1b). Brandur, Fontur and Saxi are three early-Holocene tephra cones and the samples consist of fresh, macrocryst-rich, glassy tephra material and highly crystalline gabbroic nodules. Þjórsárdalshraun and Drekahraun are dated as middle-Holocene units (3-4 ka, Pinton et al. 2018) and the samples come from lava and fresh vesicular scoria, respectively. Veiðivötn 1477 was produced in a 65 km long fissure eruption that occurred in 1477 AD (Fig. 1b).

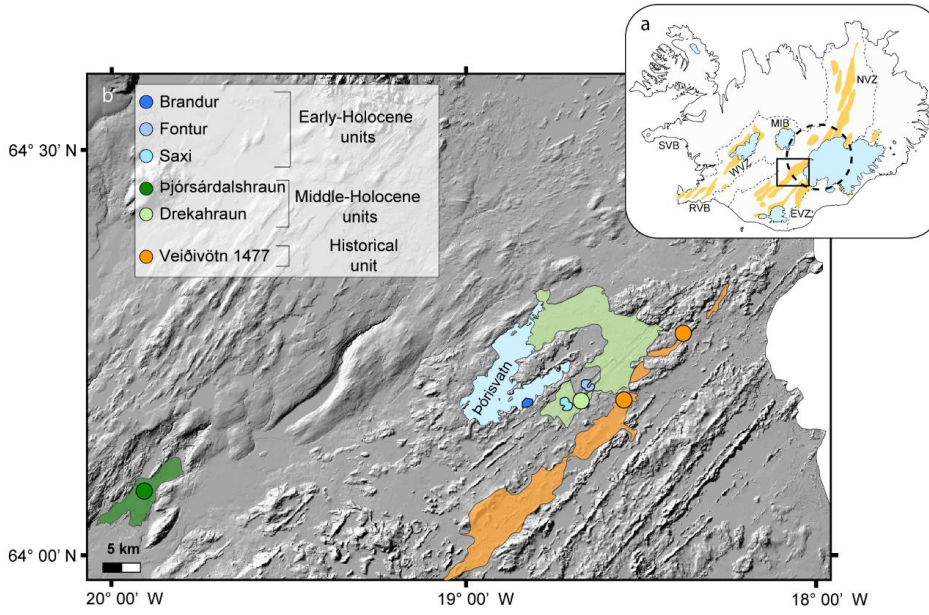

Fig. 1 *a) Map of Iceland showing the neovolcanic rift zones outlined with dashed lines, individual volcanic systems in yellow (subglacial parts not shown) and the inferred location of the mantle plume is shown as a dotted circle. b) Hillshade map of the southernmost part of the Bárðarbunga volcanic system with sample localities and eruptive units indicated with different colors. SVB: Snæfellsnes Volcanic Belt; RVB: Reykjanes Volcanic Belt; WVZ: Western Volcanic Zone; MIB: Mid-Iceland Belt; EVZ: Eastern Volcanic Zone; NVZ: Northern Volcanic Zone.*

Caracciolo et al. (2020) found that all samples contain macrocrysts and polymineralic clots, indicative of a crystal mush origin. The compositions of the macrocrysts vary with time, with early-Holocene magmatic units containing more primitive compositions compared to middle-Holocene and historical magmatic units. Application of different thermobarometers to crystals, groundmass glasses and melt inclusions (MIs) revealed temporally invariant crystallization conditions in the middle crust, at about 1.9-2.2 kbar (6.8-7.8 km), along with the occurrence of deep-seated storage reservoir(s) during the time covered by the oldest magmatic units. This deep crystallization record has been linked to a different crustal response associated with post-glacial isostasy rebound (Gee et al., 1998; Le Breton et al., 2016; Sinton et al., 2005).

3. SAMPLE PREPARATION AND ANALYTICAL METHODS

Unaltered olivine macrocysts in the size range 0.5-2.4 mm were hand-picked from crushed tephra and lava samples and mounted in epoxy resin to expose a flat surface. High-contrast backscattered electron (BSE) images were taken of olivines using the JEOL JXA-8230 SuperProbe electron probe microanalyzer (EPMA) at the Institute of Earth Sciences,

University of Iceland. ImageJ software was used to process the BSE images to identify crystals with zoning patterns and to select traverses suitable for diffusion modeling.

3.1. Electron microprobe analyses (EMPA)

Olivine concentration profiles of major and minor elements (Si, Ti, Al, Cr, Fe, Mn, Ni, Mg, Ca) were acquired using the EPMA at the University of Iceland. Chemical transects were measured using a focused beam with an accelerating voltage of 15 kV and a probe current of 20 nA. A counting time of 30 s at the peak and background was used for Ti, Al, Mn, Cr and Ni. Si, Fe, Mg and Ca were analyzed using a counting time of 30 s at peak and 15 s at the background. Chemical profiles with point spacing between 3-6 µm (25 to 100 points) were measured perpendicular to macrocryst margins along different directions in a total of 121 olivine grains from all studied eruptive units. Multiple standard samples were analyzed prior to and after each session. Error bars reported in the chemical diagrams indicate 2σ of multiple standard analyses (2σFo=0.34 mol%, 2σMn=0.038 wt%, 2σNi=0.018 wt%). In order to test for equilibrium conditions, groundmass glasses immediately around olivine macrocrysts were analyzed with the EPMA. In this study, we include some olivine-hosted MIs (n=8) analyzed by Caracciolo et al. (2020), along with new MI data (n=13) (supplementary material S1). See Caracciolo et al. (2020) for analytical details about MI analyses and post-entrapment process correction.

3.2. Electron backscatter diffraction (EBSD)

Crystallographic orientations of olivine macrocrysts were obtained using electron backscatter diffraction (EBSD; Prior et al., 1999; Costa and Chakraborty, 2004) on the FEI Quanta 650 FEG-SEM at the University of Leeds Electron Microscopy and Spectroscopy Centre (LEMAS). Characterizing the crystallographic directions in olivine with respect to the micro-analytical traverses is essential for accurate diffusion modeling, as the diffusivity of different elements (e.g. Fe–Mg or Ni) in olivine is strongly anisotropic, with diffusion along the c-axis being six times faster than that along the a- and b-axes (e.g. Clark and Long 1971; Dohmen et al. 2007).

To minimize uncertainty in the determination of the orientation data, orientation maps consisting of hundreds of EBSD point determinations were conducted for each macrocryst (Kahl et al., 2017). Maps were acquired using an accelerating voltage of 20 kV and a spot size of 5.5 µm. EBSD maps over crystal areas of interest were generated and processed using the HKL CHANNEL5 EBSD post-processing software, enabling the extraction of hundreds to thousands of orientation measurements. Measured Euler angles were converted into trends and plunges of the olivine crystallographic a-, b- and c-axes using Stereo32 software developed at the Ruhr-Universität Bochum. Using this software, it is possible to calculate the angles between the measured electron microprobe traverses and the crystallographic a-, b- and c-axes in olivine (Supplementary material S2) (Costa and Chakraborty 2004; Kahl et al. 2011).

4. KINETIC MODELING

At high temperatures, compositional heterogeneities in magmatic crystals will homogenize due to diffusive relaxation. Following the modeling approach outlined in Kahl et al. (2011, 2013) and Costa and Chakraborty (2004), we modeled the diffusive relaxation of Fe-Mg, Ni and Mn zoning in olivine macrocrysts from all studied localities. Details of

the methods and the criteria for the choice of concentration profiles for modeling, including tests for robustness, have been reported in full detail by Costa et al. (2008) and Kahl et al. (2011, 2013).

Among 121 olivine grains representing all eruptive units (Table 1), 21 grains show dipping plateaux (Shea et al., 2015) or zoning patterns probably related to crystal growth (Costa et al., 2008). These grains are not suitable for olivine diffusion modeling and were excluded from further consideration. For the diffusion models, the spacing was set to 5µm, which is a good compromise between calculation speed and EMPA resolution of the analyzed diffusion profiles. For each crystal, the modelling curves were calculated by manually changing the number of time steps until a best-fit curve for a given Fe-Mg diffusion profile was observed. Therefore, depending on the zonation pattern, the number of time steps was different for each crystal. Subsequently, we used the same number of time steps and the identical initial conditions to model diffusion profiles of Mn and Ni (Fig. S1.4). In most of the cases, best-fit curves (and comparable timescales) were observed for Fe-Mg, Mn and Ni (Fig. S1.4), suggesting that zoning profiles are likely to be controlled by diffusion.

4.1. Modeling approach

We used the composition-dependent, one-dimensional expression of the diffusion equation (i.e. Fick's second law):

$$\frac{\partial C_i(x,t)}{\partial t} = \frac{\partial}{\partial x}\left(D_i \frac{\partial C_i(x,t)}{\partial x}\right)$$

where C_i is the concentration of element i, x denotes the distance, D_i is the diffusion coefficient of element i, and t is time. The evolution of the concentration with time (t) at different spatial coordinates (x), $C_i(x,t)$, is obtained numerically using a one-dimensional finite difference scheme (see Costa et al. 2008). In this study, we mainly focused on Fe-Mg but also on Ni and Mn zoning when possible, to increase the robustness of the calculated timescales. Diffusion coefficients are functions of pressure, temperature, composition, oxygen fugacity and crystallographic orientation, and were taken from experimentally determined data (Fe–Mg and Mn: Dohmen et al., 2007; Ni: Petry et al., 2004 and Holzapfel et al., 2007).

4.2. Modeling parameters and error propagation

4.2.1. Initial and boundary conditions

The initial condition refers to the shape of the zoning pattern before diffusive modification. The strategies outlined in Kahl et al. (2011) were adopted to identify initial conditions for each profile. In most cases, we assumed a homogeneous initial profile (Fig. S1.1a), guided by the occurrence of extended compositional core plateaux. Only in a few cases, plateaux at the rims (Fig. S1.1b) were observed. These were interpreted as stranded diffusion profiles and a stepped initial profile shape was invoked.

In our modeling, we assume that macrocrysts re-equilibrated with their host liquid (i.e. open boundary conditions) and that the composition of the liquid is constant with time within a specific magmatic unit.

4.2.2. Input parameters

Clinopyroxene-liquid, OPAM and liquid-only thermobarometry constraints suggest that the final equilibration depth of the carrier liquids before eruption and olivine rim

crystallization occurred in the mid-crust at about 1.1-2.7 kbar pressure, at temperatures of 1160-1175 °C (Caracciolo et al. 2020). Therefore, we have modeled the chemical zoning with temperature and pressure set according to the magmatic unit under consideration (Caracciolo et al. 2020). A summary of input temperature and pressure conditions is reported in Table 1. Oxygen fugacity was set to the FMQ (Fayalite-Magnetite-Quartz) buffer based on spinel-olivine oxybarometry.

4.2.3. Error propagation

Timescale uncertainties have been calculated following the method described by Kahl et al. (2015), with temperature showing the largest effect on the propagated error. For instance, a 1σ temperature uncertainty of ± 5 °C yields errors of ± 134 days for a calculated diffusion timescale of 1000 days, ± 13.4 days for a timescale of 100 days and ± 1.4 days for a timescale of 10 days.

5. RESULTS

5.1. Petrography of the samples

Among all studied samples, plagioclase is the principal macrocryst (>0.5 mm) phase, followed by olivine and clinopyroxene. Early-Holocene units consist of tephra and high-crystallinity gabbroic nodules. Tephra are slightly vesicular (~15-20 %) and contain between ~15 and ~45 vol% macrocrysts (Fig. 2a). Nodules (Fig. 2b) consist of pseudo-spherical olivine gabbros (up to 10 cm in diameter) with a crystallinity between ~80-95%, and they are made of a network of plagioclase macrocrysts (~80-85%), interspersed with olivine macrocrysts (~5-10%), clinopyroxene (~5%) and interstitial glass (~5-10%) (Fig. 2 b-c). Olivine crystals found in the gabbroic nodules are morphologically and texturally similar to those found in the tephra samples. Lava and scoria samples from middle-Holocene units show variable vesicularity (50-80 %) and a low abundance of macro- and microcrysts (Fig. 2d). The macrocryst content ranges between ~5-15 %, with plagioclase macrocrysts being more abundant than olivine and clinopyroxene (Fig. 2d). Historical samples consist of fresh, highly vesicular (~70-90 %), crystal-poor scoria with the most crystalline samples having ~5-10 % macrocrysts. Detailed sample petrography is provided by Caracciolo et al. (2020).

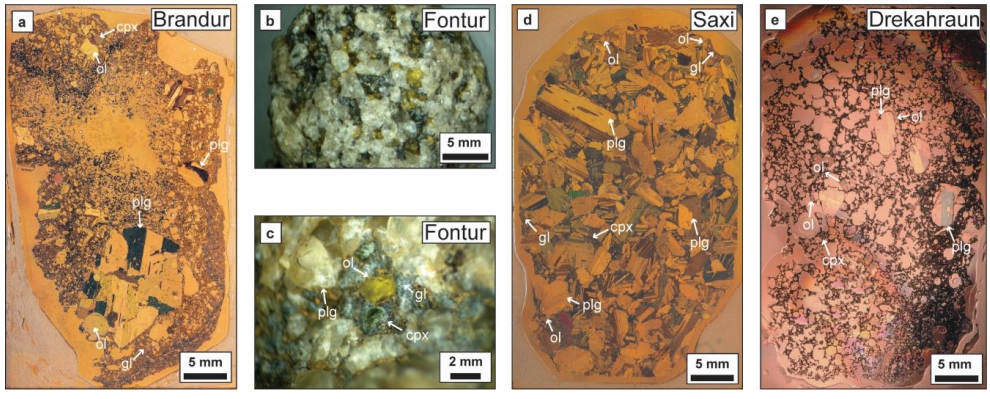

Fig. 2. *Macroscopic features of studied samples. a) Thin section image of a lava sample from Brandur tephra cone. Note the occurrence of a nodule-like aggregate made of a large plagioclase (~1 cm) and olivine grains. Macrocrysts are found in a glassy, light brown groundmass. b-c) Macroscopic photo of a crystalline olivine gabbro nodule from Fontur tephra cone. This gabbroic nodule contains around ~90 vol% macrocrysts, most of which are plagioclase (white greasy macrocrysts), followed by olivines (yellow-green macrocrysts) and clinopyroxene (dark green macrocrysts). The crystal framework is permeated by interstitial glass (dark areas). d) Thin section image of a gabbroic nodule from Saxi. The framework comprises plagioclase macrocrysts with minor olivine macrocrysts. Clinopyroxene crystals are mostly found in glomerophyric clots in interstitial positions. e) Thin section image from Drekahraun. Note the lower abundance of macrocrysts compared to Brandur samples. Thin section images were acquired with the use of a high-resolution scanner and the thin sections placed between two polarizing sheets to display the interference colors of different phases. plg: plagioclase; ol: olivine; cpx: clinopyroxene. gl: glass*

5.2. Olivine - chemistry and zoning

We have measured a total of 173 chemical profiles in 121 olivine macrocrysts from all localities (Table 1). The olivine core and rim compositions range between Fo_{76-87} and Fo_{74-84} [Fo=100*Mg/(Mg + Fe), in mol%], respectively, although we find systematic compositional differences between eruptions (Fig. 3).

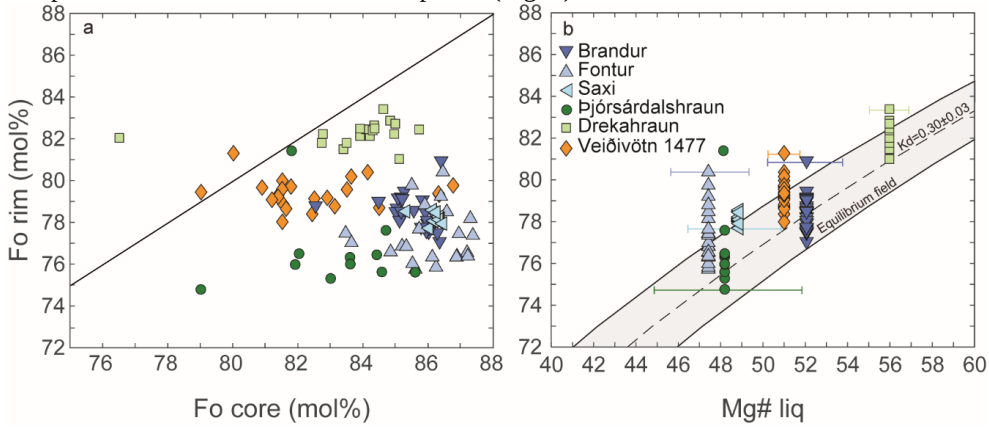

Fig. 3. *a) Core versus rim compositions of modeled olivine macrocrysts from all studied magmatic units. Brandur, Fontur and Saxi olivines have similar and narrow core compositions and more variable rim compositions. Þjórsárdalshraun, Drekahraun and Veiðivötn record distinct rim compositions with a narrow range, whereas olivine cores show a larger compositional range. Most macrocrysts plot below the black 1:1 line, meaning that they are normally zoned. b) Rhodes diagram to test for olivine-liquid equilibrium. Olivine in equilibrium with coexisting liquid compositions should fall in the grey field indicative of a* $Kd_{(Fe\text{-}Mg)}^{ol\text{-}liq} = 0.30 \pm 0.03$ *(Roeder and Emslie, 1970). Rim compositions of the studied olivine macrocrysts are close to being in equilibrium with the carrier liquid. Colored bars depict 1σ compositional variability uncertainty of the carrier liquid of each sample, where the glass composition is taken as representative of the carrier liquid. The large variation of the Þjórsárdalshraun carrier liquid is due to its microcrystalline nature.*

Brandur, Fontur and Saxi olivine macrocryst cores record the smallest compositional variation, whilst rims show the largest range among all magmatic units (Fig. 3a). Olivine cores from Brandur are in the range $Fo_{84.5-86.5}$ and rims in the range Fo_{77-81}. Fontur olivines have core and rim compositions of $Fo_{83.5-87.5}$ and $Fo_{76-80.5}$, respectively. Saxi olivine macrocrysts preserve cores of $Fo_{85-86.5}$ and rims of $Fo_{77.5-79}$. Olivine cores from Fontur and Saxi gabbroic nodule samples display a larger Fo range ($Fo_{80-87.5}$) than olivine cores in tephra samples (Fo_{85-87}) (Fig. S1.2). Brandur olivines record remarkably homogeneous core compositions within gabbroic nodule and tephra samples, with 1 mol% difference between the two. Most of the tephra olivines from Brandur are slightly more primitive ($Fo_{\sim 86}$) than nodule olivines ($Fo_{\sim 85}$) (Fig. S1.2), although this difference is not observed in Fontur and Saxi. Drekahraun and Þjórsárdalshraun record similar olivine core composition range ($Fo_{80-85.5}$), while olivine rims are in the range Fo_{75-81} and Fo_{81-83}, respectively (Fig. 3a). Olivine macrocrysts from the Veiðivötn 1477 eruption display core compositions in the range $Fo_{80-86.5}$ and rims in the range Fo_{78-81}. The majority of olivine macrocrysts display normal zoning (Fig. 3a and Fig. S1.1a), with forsterite-rich cores surrounded by less forsteritic rims. Two macrocrysts from Veiðivötn 1477 and one macrocryst from Drekahraun display reverse zonation (Fig. 3a and Fig. S1.1b), with the latter showing a strong compositional gradient between core (Fo_{76}) and rim (Fo_{82}). Some olivine macrocrysts from Drekahraun (n=4), Þjórsárdalshraun (n=3) and Veiðivötn 1477 (n=9) show complex zoning patterns with reversely zoned macrocryst interiors followed by normally zoned outermost rims (Fig. S1.1c). The difference in Fo content between the core and the intermediate zone is always lower than 1 mol% but still above the analytical uncertainty ($2\sigma_{Fo}$= 0.34). This intermediate pattern is not recorded by other elements. Finally, we do not observe any unzoned olivine macrocrysts in the magmatic units discussed in this work (Fig. 3a).

At any given Fo content, olivine cores from early-Holocene, middle-Holocene and historical units do not show any difference in terms of Mn and Ni. Primitive olivine cores (Fo85-87) from early-Holocene samples have Mn contents in the range 1400-1700 ppm and Ni contents in the range 1200-1700 ppm. Less primitive (Fo78-82) olivine cores are found in the historical samples and they record Mn contents between 2000-2500 ppm and Ni contents between 800-1300 ppm. The measured Mn and Ni contents overlap with those of olivine macrocrysts from the 2014-15 Holuhraun eruption (Halldórsson et al., 2018) (Fig. S1.3).

Table 1. Number of olivine crystals, chemical profiles and timescale (days) result for each magmatic unit.

Unit	Age	Olivine grains	Chemical profiles	Modelled olivines	Timescale		Temperature*		Pressure*	
		n	*n*	*n*	*average*	*st.dev.*	*Mean*	*σ*	*Mean*	*σ*
Brandur	Early-Holocene	31	44	29	300	158	1170	4	2.2	0.7
Fontur	Early-Holocene	21	31	16	332	241	1161	7	2.2	0.6
Saxi	Early-Holocene	13	13	11	419	339	1163	5	2.3	0.7
Þjórsárdalshraun	Middle-Holocene	11	16	7	40	32	1160	9	1.9	0.7
Drekahraun	Middle-Holocene	19	27	14	70	24	1174	2	2.6	0.8
Veiðivötn 1477	1477 AD	26	42	23	58	41	1167	3	1.9	0.6

*Modelling input pressure (kbar) and temperature (°C) data from Caracciolo et al. (2020)

5.3. Relation to the carrier liquid

Each eruptive unit is characterized by a specific range in groundmass glass compositions (Fig. 3b), which is assumed to represent the carrier liquid composition. Early-Holocene groundmass glasses have the largest chemical variability (MgO 5.5-7.5 wt%, TiO_2 1.0-2.5 wt%), whereas recent units are more homogeneous (Caracciolo et al.,

2020). Middle-Holocene carrier liquids have MgO and TiO_2 contents in the range 7.0-7.5 wt% and 1.6-1.8 wt% respectively, while historical carrier liquids are in the range 6.3-6.9 wt% for MgO and 1.6-2.0 wt% for TiO_2. The melt Mg# (Mg#= 100*Mg/(Mg+Fe^{2+})) of the carrier liquid was obtained by calculating Fe^{2+} and Fe^{3+} contents following the model of Kress and Carmichael (1991) at the FMQ buffer. Following this procedure, 91% of olivine macrocryst rims are in chemical equilibrium with the carrier liquid (Fig. 3b).

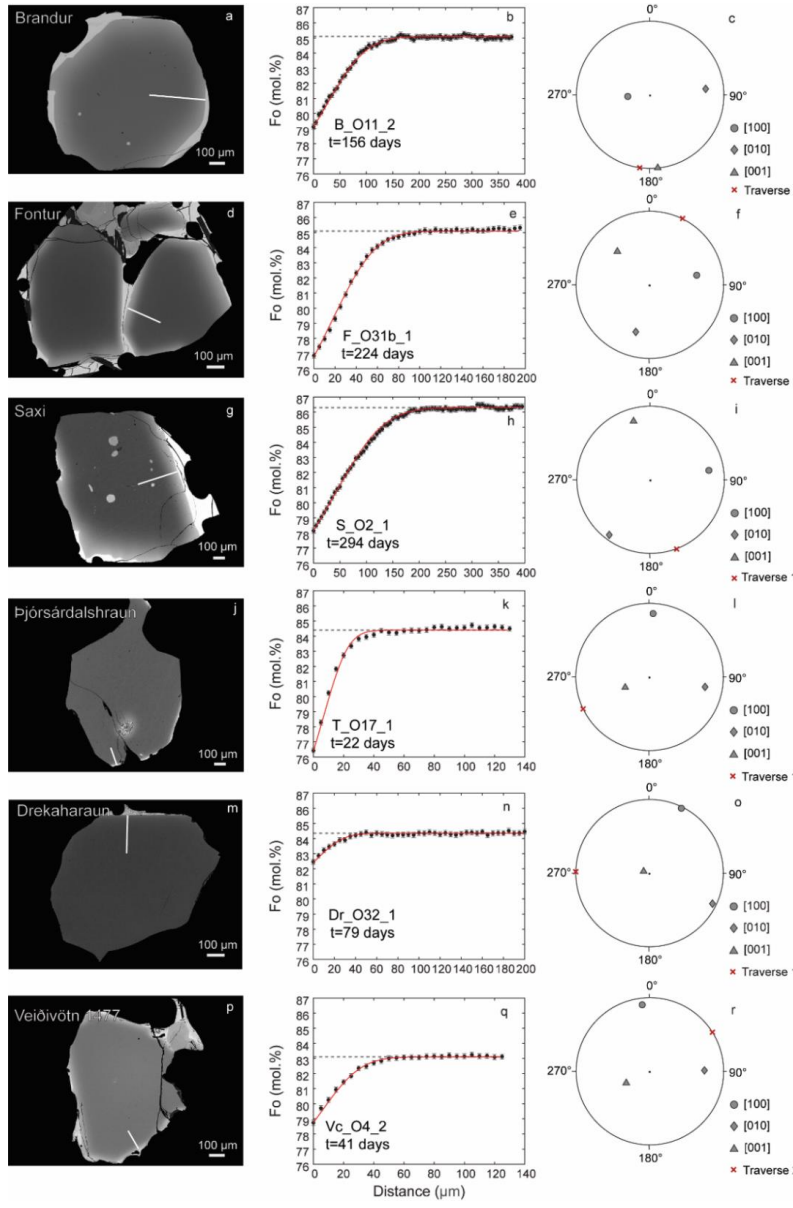

Fig. 4. *Representative backscattered electron (BSE) images (a,d,g,j,m,p), concentration profiles with model fits (b, e, h, k, n, q) and stereographic plots (c, f, i, l, o, r) of studied olivine macrocrysts from all localities. White arrows in the BSE photos indicate the*

position of the analytical traverse. Black dashed lines indicate the assumed initial profile. Red lines are best fit models for the measured compositional gradient. For each macrocryst the calculated timescale (days) is also reported. The orientation of crystallographic axes with respect to the direction of the EPMA traverse (red cross) is shown in the stereographic plots. Analytical error of EPMA data is based on 2σ for multiple standard analyses.

5.4. Diffusion modeling results

We modeled 100 olivine crystals with zoning patters related to diffusive relaxation of Fe and Mg and well-suited for diffusion modelling (Fig. 4). Independent Fe-Mg timescale results for each locality are reported in Fig. 5 and in S1, while a summary is listed in Table 1. Kernel density estimate (KDE) distribution curves are shown in Fig. 6.

5.4.1. Brandur, Fontur and Saxi (early-Holocene)

Olivine macrocrysts from the three tephra cones, Brandur, Fontur and Saxi, record a large range of timescales, varying from 20 to 1330 days (Fig. 5a-c and Fig. 6a). The large range of timescales is observed both, in olivines found in gabbroic nodules and in tephra samples (Fig. 5a-b). KDE distribution curves largely overlap (Fig. 6a), with the majority of olivines (63%) recording timescales between 150 and 400 days (0.4-1.1 years). Only 17% of the olivines give timescales shorter than 150 days and 20% longer than 400 days. Brandur olivines (n=29) show a narrowly focused major peak at 340 days. Fontur olivines (n=16) display the widest timescale distribution, with a major peak located at 444 days and a large shoulder with timescales between ~100 and ~230 days (n=5). The shortest timescale of 19 days is recorded by one macrocryst from Fontur (Fig. 5b). Finally, Saxi olivines (n=11) show most probable timescales of 210-350 days (Fig. 6a), with a main peak at 220 days, and a minor band located at a timescale >800 days (n=2).

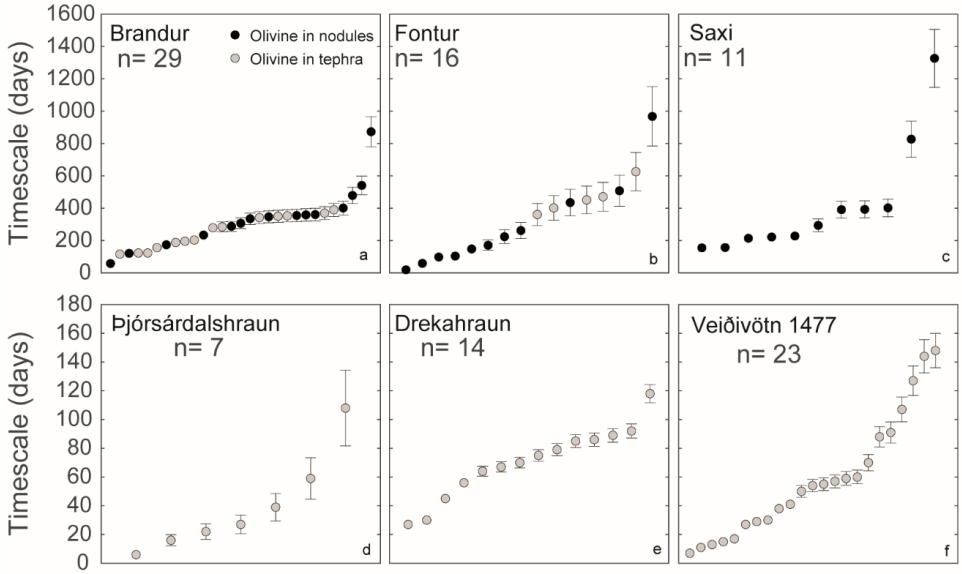

Fig. 5. *Fe-Mg diffusion modeling timescale results for a) Brandur, b) Fontur, c) Saxi, d) Þjórsárdalshraun, e) Drekahraun and f) Veiðivötn 1477. Early-Holocene units (Brandur, Fontur and Saxi tephra cones) record longer and more variable timescales up to 1300*

days, compared to other magmatic units. Timescale uncertainties have been calculated following the procedure described by Kahl et al. (2015). Olivines found in the gabbroic nodules and in the tephra samples are shown with different markers. n=number of modeled olivine macrocrysts for each locality.

5.4.2. Þjórsárdalshraun and Drekahraun (middle-Holocene)

Diffusion timescales calculated for Þjórsárdalshraun olivines show a scattered KDE distribution (Fig. 6b). Timescales are all below 110 days (Fig. 4d), with a major peak at 24 days. However, the Þjórsárdalshraun samples come from a section of the lava that had flowed about 50-60 km before ultimately forming a rootless cone field. For this reason, olivines from this unit are likely affected by post-eruptive diffusion and/or crystallization processes and timescale results are treated with caution. Indeed, only a few macrocrysts (n=7) suitable for diffusion measurements were found within the Þjórsárdalshraun samples and sample bias might affect the distribution. In contrast, samples from the Drekahraun unit consist of fresh scoria. KDE timescale distribution for Drekahraun olivines show a prominent peak at 78 days and a minor peak at 30 days (Fig. 5e and Fig. 6b). Only one macrocryst records a timescale above 100 days (118 days). Intermediate zoning patterns observed in some middle-Holocene macrocrysts were modeled sequentially and return diffusion timescales between 2-29 days.

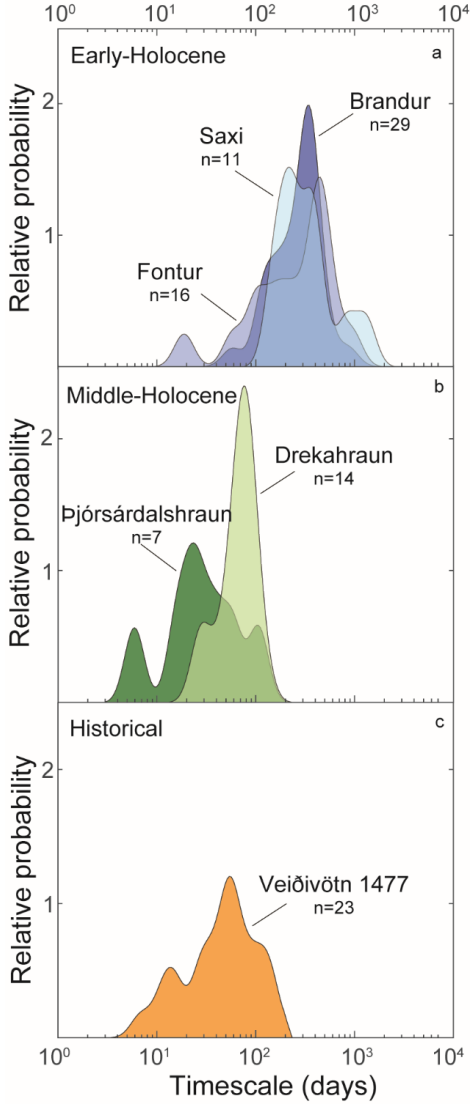

5.4.3. Veiðivötn 1477 (historical)

83% of olivine macrocrysts from Veiðivötn 1477 register diffusion timescales shorter than 100 days (Fig. 5f), with a main peak in the KDE distribution at 55 days (Fig. 6c). A minor peak is observed at 15 days, while only 4 macrocrysts out of 22 record timescales longer than 100 days (Fig. 5f). Finally, the intermediate chemical zoning found in some macrocrysts gives an average timescale of 25 days.

***Fig. 6**. Kernel density estimate plots with bandwidth 0.1, showing calculated timescales for a) early-Holocene units, b) middle-Holocene units and c) historical unit. Early-Holocene units record the largest timescale variation among all localities, with a main distribution peak between 200-400 days. n=number of olivine macrocrysts modeled for each locality.*

6. DISCUSSION

6.1. Relationship between melt composition, magma depth and timescales

Barometry constraints show that the carrier liquid last equilibrated with the crystal cargo in a reservoir(s) located in the middle-crust (7-11 km depth), before being erupted (Caracciolo et al. 2020). The cores of 21 olivine macrocrysts contain large (up to 120 µm in diameter), naturally quenched melt inclusions (e.g. Fig. 4g and Fig. S1.4i), which are mostly hosted in early-Holocene units (Fig. 7a). These melt inclusions have MgO contents between 7.6 and 9.2 wt% and TiO_2 in the range 0.8-1.8 wt% (Mg#55-65). We estimated MI equilibration pressures within the Bárðarbunga-Veiðivötn plumbing system by applying the Olivine-Plagioclase-Augite-Melt (OPAM) barometer (Hartley et al., 2018; Yang et al., 1996) with the goal to locate the macrocrysts within the crust. MI equilibration pressures (n=3) of middle-Holocene and historical samples range between 1.8 and 1.9 kbar (Fig. 7a) and they are hosted in olivine cores with compositions in the range Fo81.6-84.6. However, MIs hosted in plagioclase macrocrysts record pressures down to 4 kbar (Caracciolo et al. 2020). Early-Holocene units register a much larger pressure variation, between 1.5 and 6 kbar, with a clear positive relationship between olivine composition, MI composition and MI equilibration pressure (Fig. 7a). The olivine crystals become more evolved as MI equilibration pressures decrease, with primitive olivines (Fo>86) recording the highest pressures (4-6 kbar) and the most primitive MI compositions (Mg# 64-65) (Fig. 7a). These findings, which are in good agreement with the data of Caracciolo et al. (2020), support a stacked-sills model (Kelemen et al. 1997; Maclennan 2019) in which olivine macrocrysts are exposed to slightly more evolved environments as they move shallower in the crust (Fig. 8).

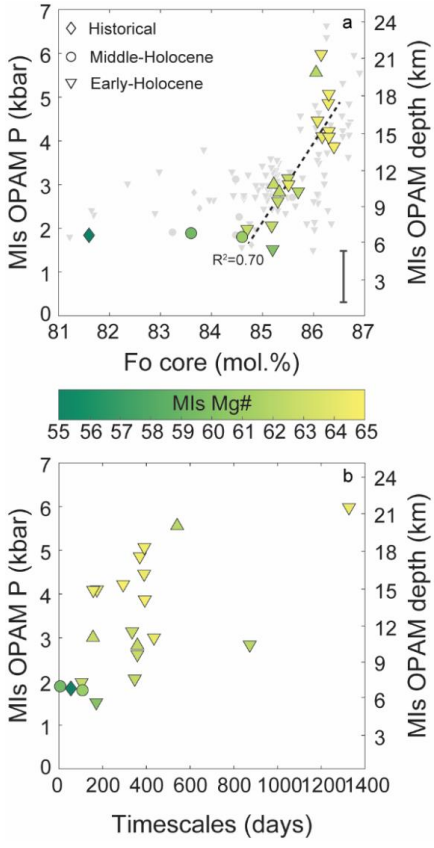

Fig. 7. *a) Olivine core compositions plotted versus melt inclusion (MI) OPAM equilibration pressures. Early-Holocene macrocrysts are separated into olivines from tephra samples (upwards-pointing triangles) and olivines from gabbroic nodule samples (inverted triangles). Most of the MIs are hosted in olivine macrocrysts from Brandur (n=10), Fontur (n=3) and Saxi (n=5). A statistically significant linear correlation (R^2=0.70) between MI OPAM pressure, MI composition and olivine Fo is observed among macrocrysts from early-Holocene units. As they move upwards in the crust, the composition of crystals and melts becomes more evolved, suggesting storage and evolution across a stacked-sills system. Error bar refers to the OPAM standard error of estimate (SSE=1.3 kbar). Grey symbols are olivine-hosted MIs from Caracciolo et al. (2020). b) Olivine diffusion timescales vs MI OPAM pressures within the same macrocrysts. Olivines that have crystallized in deep-seated regions record similar timescales to olivines formed at mid-crustal levels. Symbols colored according to melt inclusion Mg#.*

The shortest diffusion timescales (6-108 days) are recorded by macrocrysts from middle-Holocene and historical units, which likely crystallized at mid-crustal (7-11 km) levels (Fig. 7b and Caracciolo et al. 2020). In contrast, early-Holocene olivines cluster at timescales between 200-400 days (Fig. 7b) and they most likely crystallized throughout the crustal section. Although there is a positive correlation between early-Holocene olivine depths and their compositions (Fig. 7a), we do not observe any clear relationship between MI equilibration pressure and olivine diffusion timescales (Fig. 7b) nor between olivine Fo content and diffusion timescales (Fig. S1.5). This suggests that olivine macrocrysts are likely to have been transported up to mid-crustal (7-11 km) mush piles during earlier remobilization events throughout a multi-tiered system of interconnected stacked sills in which crystals are gradually transported to higher levels until they accumulate in the main mid-crustal reservoir at about 7-11 km. Indeed, the absence of intermediate zoning sectors may indicate that these macrocrysts resided in the mid-crust for a period sufficiently long to erase any chemical gradient previously formed. Eventually, at some point in the early-Holocene, injection of melts with variable composition (Caracciolo et al. 2020) into the mid-crustal reservoir(s) caused remobilization of these deep-origin olivines and their incorporation in the carrier melt.

6.2. Timing of crystal mush disaggregation and triggering mechanism

Gabbroic nodules found in early-Holocene magmatic units are unique samples whose mineralogical and textural characteristics indicate that they represent exhumed pieces of the crystal mush (Hansen and Grönvold 2000; Caracciolo et al. 2020). The lack of notable chemical differences between olivines in the gabbroic nodules and in the tephra samples (Fig. S1.2) support their common origin. Except for Brandur samples (Fig. S1.2), no notable differences in composition are observed between olivines coming from the mush and olivines carried in the melt as a result of disaggregation processes (Fig. 5a-c). While the majority of olivine rim compositions are found to be in chemical equilibrium with the carrier liquid (Fig. 3b), olivine cores are not. They most likely crystallized from a set of compositionally diverse primitive melts, as supported by MI data (Caracciolo et al. 2020). In most cases, olivine cores are homogenous, forming long compositional plateaux, which can extend up to 200 µm within the largest grains (Fig. 4b, h). This observation suggests long residence time whereby olivine cores have either been re-equilibrated completely through diffusion or they have grown in a reservoir(s) under steady chemical and physical conditions before rim crystallization occurred. In contrast, some olivine cores in the more recent samples (middle-Holocene and historical) record more complex zoning patterns, with Fo variations of ~1 mol% (Fig. S1.1c). These jumps likely relate to changes in the intensive thermodynamic variables (composition, pressure, temperature and/or oxygen fugacity) of the magmatic environment (e.g. Kahl et al. 2017), so that the next increment of olivine that grew had a slightly different composition.

The decrease in the Fo content at the rims is an evidence for changes in the chemical and/or physical conditions of the reservoir. We infer that the outermost normal zoning is related to interaction of a relatively evolved melt (e.g. the final carrier liquid) within an undisturbed crystal mush reservoir(s); the evolved liquids got injected into the reservoir and permeated the mush, thereby starting the diffusion clock after efficient mixing was achieved (Fig. 8). This process most likely caused disaggregation of mush clots and addition of mush crystals (Sigmundsson et al., 2020b) into the carrier melt. If this is the case, then diffusion timescales correspond to the time elapsed between the disaggregation of crystal mush following magma injection, when chemical re-equilibration

with the carrier liquid started, and the eruption, when diffusion ceased to play a role (Fig. 8). Specifically, the composition of the tholeiitic basalt magma being injected into the mush reservoir has not remained constant over the Holocene period (see 5.2 above and Fig. 1. in Caracciolo et al. 2020).

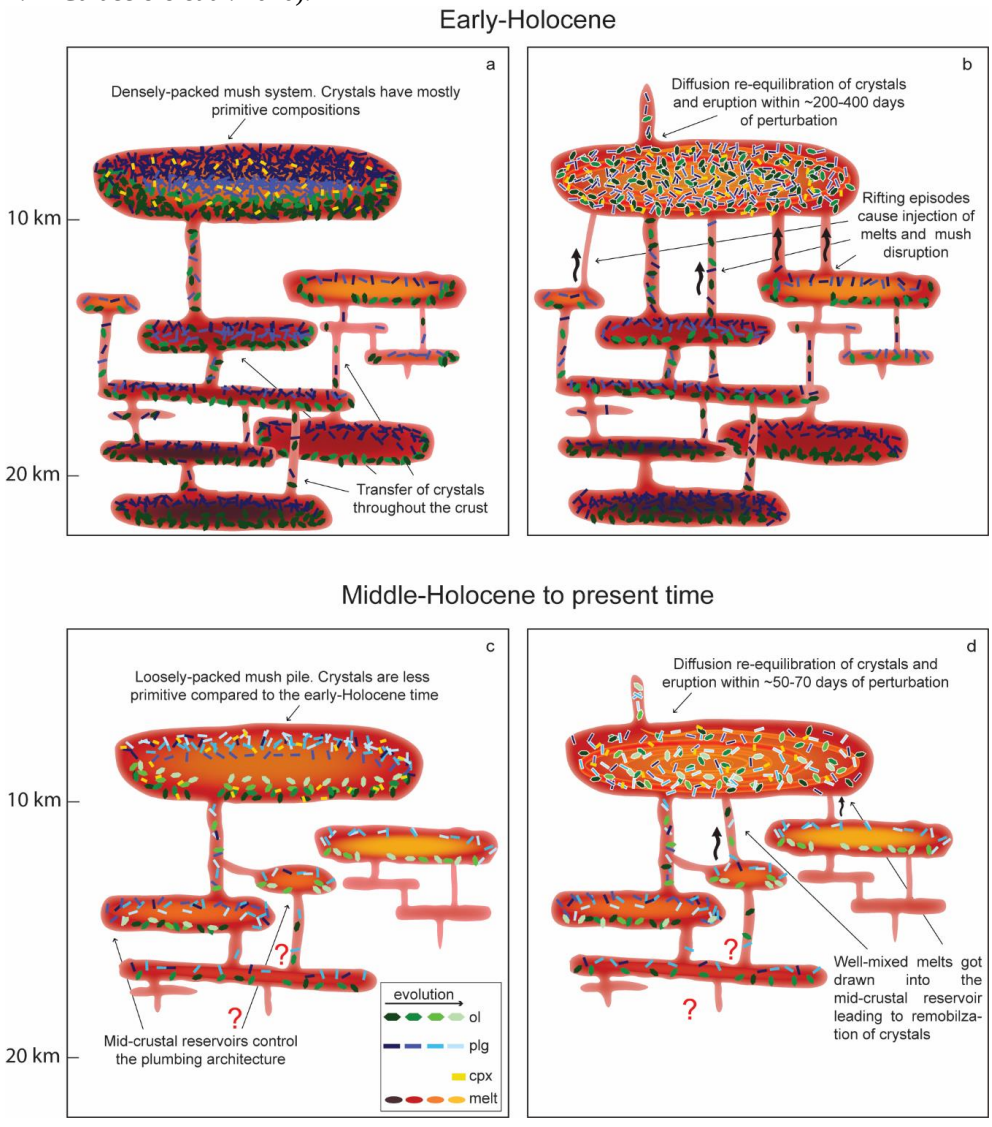

Fig. 8. *Schematic cartoon (not to scale) summarizing processes operating underneath the Bárðarbunga-Veiðivötn volcanic system in the early-Holocene (a-b) and in the middle-Holocene to present time (c-d). Our observations suggest the presence of a multi-tiered magmatic system in which crystals are gradually transported to shallower levels and exposed to more evolved compositions. The main storage reservoir(s) is located at 7-10 km depth (Caracciolo et al. 2020). a) In the early-Holocene, the mid-crustal storage zone is composed of a packed and compact mush fabric, containing predominantly primitive crystals which are transferred throughout stacked-sills at different depths. b) Around 200-*

400 days before the eruption, relatively evolved melts located in the middle-crust intruded into the mushy reservoir(s), marking the onset of olivine equilibration. This intense melt injection, possibly triggered by rifting events and/or enhanced by increased early-postglacial melt production rates, caused loosening and mobilization of the packed mush pile(s). The incorporation of macrocrysts and crystalline gabbroic nodules in the carrier liquid and subsequent vertical transport occurred over long and variable timescales (~200-400 days). c) Macrocrysts are more evolved in composition and they are more likely to have formed at mid-crustal levels (1-4 kbar), with no evidence of deep-seated storage reservoirs (Caracciolo et al. 2020). Since the middle-Holocene, the mid-crustal storage reservoir(s) is composed of a less rigid mush fabric with relatively evolved crystals being more abundant compared to the early Holocene. d) Once evolved melt pocket(s) intruded the reservoir, the mush was quickly remobilized and macrocrysts ascended to the surface within short timescales (days up to a few months). Different color gradients of crystals and melt layers point out a variation of composition with time and throughout the crust. However, different colors do not reflect real crystal or melt populations. ol: olivine; plg: plagioclase; cpx: clinopyroxene.

Olivine macrocrysts with complex and reverse zoning patterns are widespread in off-rift Icelandic settings and their zoning features have been associated with late mafic magma replenishment events (e.g. Mattsson and Oskarsson 2005; Pankhurst et al. 2014; Viccaro et al. 2016), which could have triggered the eruptions. In contrast, rift-related olivine macrocrysts commonly preserve normal zoning patterns (e.g. Neave et al. 2013, 2015; Thomson and Maclennan 2013; Hartley et al. 2016; Halldórsson et al. 2018), which could indicate a different triggering mechanism. In fact, about 95% of the olivine macrocrysts studied in this work do not preserve direct evidence for late mafic recharge events. It is possible that slightly deeper, well-mixed and relatively evolved melts pockets could get remobilized and intrude the mid-crustal reservoir as a result of rift-related events that would "pull the mush apart", promoting mush disaggregation and the vertical rearrangement of crystal and melt layers within the crust. If so, rifting-related events can play a fundamental role on eruption triggering mechanisms along axial rift zones.

6.3. Temporal variation of crystal mush disaggregation timescales in the Bárðarbunga-Veiðivötn volcanic system

The older Holocene macrocrysts appear to have resided longer in their carrier liquid than the younger macrocrysts (Fig. 6 and S1.5). One noteworthy observation is that early-Holocene units contain mush nodules and a larger macrocryst load than the younger units (Fig. 2 and Fig. 9). The gabbroic nodules contain up to 90 vol% macrocrysts and confirm the existence of a crystal-rich mush fabric. In Fig. 9 we show diffusion modeling timescales yielded by olivine macrocrysts in relation to the estimated macrocryst content of the samples for each studied time period. We also report diffusion durations for the subglacial Skuggafjöll eruption (Mutch et al., 2020) that occurred in the Bárðarbunga-Veiðivötn volcanic system and which shares many features with our samples. The Skuggafjöll products consist of a highly phyric (6-45% by volume), plagioclase-rich basalts (Neave et al., 2014) that crystallized at about 11 ± 4 km (Neave and Putirka, 2017). Subglacial and early-Holocene units record the largest timescale spread and the most abundant crystal content (up to 45 vol%). On the other hand, middle-Holocene and historical units preserve a smaller macrocryst content (5-15 vol %) than early-Holocene and subglacial units, which is coupled with much shorter timescales and narrower

timescale ranges (Fig. 9). Therefore, we suggest that during subglacial and early-Holocene times the mid-crustal mush network required more time to be converted into an eruptible magma (Cashman et al., 2017) because of the occurrence of a more compact mush fabric. It is possible that multiple injections of melt fractions were needed to eventually mobilize the rigid network of the mush reservoir(s) (Fig. 8a-b), causing long residence times of macrocrysts in the reservoir(s). Furthermore, we find important to highlight that crystals found in the gabbroic nodules and crystals found in the tephra samples reveal the same timescales (Fig. 5). Those units were sourced from packed mush piles, which required more heat or a larger volume of intruding magma to be weakened and mobilized compared to the present. The larger volume of magma or energy (i.e. heat) supply is consistent with the increase of magma production rates observed in Iceland during the early Holocene that were likely caused by glacio-isostacy effects (Caracciolo et al., 2020; Le Breton et al., 2016; Sinton et al., 2005). In contrast, the present-day system is most likely characterized by a less dense mush fabric and a larger melt-mineral ratio (Fig. 8c-d). If this is true, then since the middle-Holocene, injections of smaller melt fractions would be enough to mobilize the mush network almost instantly (Fig. 8d), with magma flowing towards the surface within short timescales. The shortening of timescales approaching the present day is consistent with magma transport durations of about 1-12 days (Fig. 10), estimated for the 2014-15 Holuhraun lava (Hartley et al., 2018) that was emplaced in the northern segment of the Bárðarbunga volcanic system.

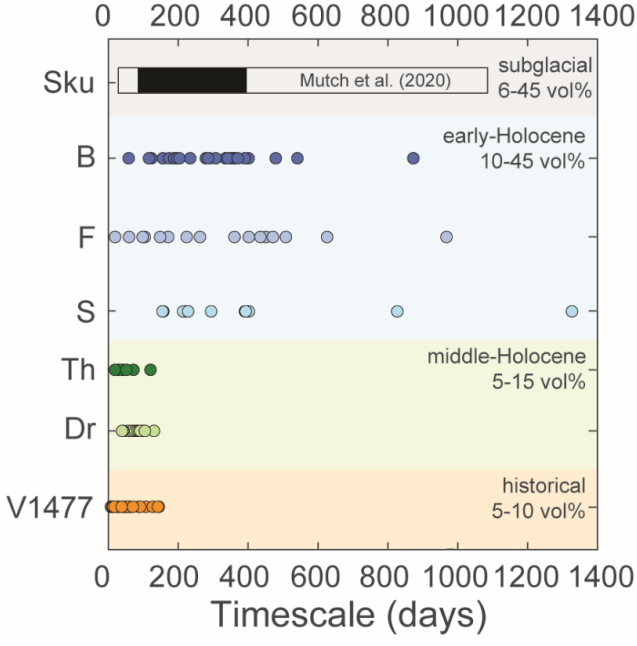

Fig. 9. *Estimated timescales in the Bárðarbunga-Veiðivötn volcanic system for different eruptions as a function of time and macrocryst cargo. Subglacial and early-Holocene units record highly variable crystal mush disaggregation timescales with the most probable estimates on the order of a few months to one year. Subglacial and early-Holocene units have the largest macrocryst content (up to 45 vol %) among all studied localities. Middle-Holocene and historical units record narrow timescale variations in the range of a few months at most. These more recent magmatic units are associated with relatively small macrocryst load. The denser mush fabric associated with subglacial and early-Holocene units could be responsible for the observed longer timescales between melt injection, mush mobilization and eruption. Most probable timescales for the Skuggafjöll eruption are between 50 and 400 days. Data for Skuggafjöll are taken from Mutch et al. (2020) and Neave et al. (2014). Sku= Skuggafjöll, B=Brandur, F=Fontur, S=Saxi, Th= Þjórsárdalshraun, Dr= Drekahraun, V1477= Veiðivötn 1477.*

6.4. Timescales of magmatic processes in Iceland and MOR settings

Our study is the first to obtain diffusion timescales for a temporally diverse magmatic suite erupted within the same volcanic system (Fig. 10). Our results can be combined with diffusion timescales estimated for the subglacial Skuggafjöll eruption (Mutch et al., 2020) to evaluate the temporal evolution of crystal mush disaggregation from the subglacial period until historical time within the Bárðarbunga-Veiðivötn volcanic system. Diffusion modeling of plagioclase and olivine macrocrysts from Skuggafjöll yield most probable timescales in the range 50-400 days (Mutch et al., 2020), suggesting that mush disaggregation processes started about a year or less prior to the eruption. These estimates are in good agreement with the early-Holocene timescales calculated in this study and consistently longer than middle-Holocene and historical mush disaggregation times (Fig. 10).

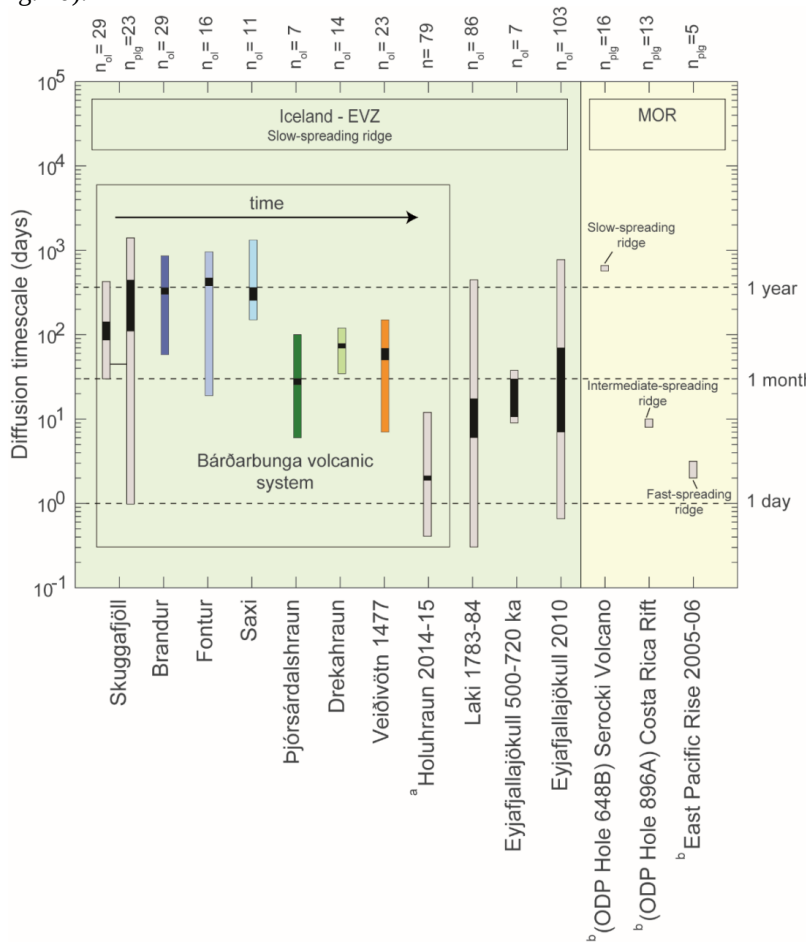

Fig. 10. *Compilation of crystal mush disaggregation to eruption timescales derived from modeling diffusive re-equilibration of compositional zoning in magmatic macrocrysts. We report all crystal mush disaggregation timescale ranges from Iceland (light green field) along with available literature data for mid-ocean ridge settings (light yellow field). In each case, the light-shaded bar represents the full range of calculated diffusion times while*

the inner black bar indicates the location of the most probable band in a KDE distribution within the time interval. Diffusion timescales modeled in this work are indicated with colored bars. Eruptions within the Bárðarbunga volcanic system are outlined by the black square and ordered according to time from subglacial to historical units. The volcanic eruptions are listed below the horizontal axis. Note that the timescale on the vertical axis is logarithmic. From left to right: Skuggafjöll (Mutch et al., 2020); Brandur, Fontur, Saxi, Þjórsárdalshraun, Drekahraun and Veiðivötn 1477 (this study); Holuhraun 2014-2015 (Hartley et al., 2018); Laki 1783-84 (Hartley et al., 2016); Eyjafjallajökull 500-720 ka (Nikkola et al., 2019); Eyjafjallajökull 2010 (Pankhurst et al. 2018); Serocki Volcano (Costa et al., 2010); Cost Rica Rift (Costa et al., 2010); East Pacific Rise 2005-06 (Moore et al., 2014). nol = number of olivine crystals modeled for diffusion kinetics; nplg = number of plagioclase crystals modeled for diffusion kinetics. a Diffusion chronometry calculated with a different method: timescales are based on H+ re-equilibration between plagioclase (n=70) and olivine-hosted (n=9) melt inclusions with a more hydrous melt. b Authors do not specify timescale ranges. For those eruptions, the interval between crystal mush disaggregation and eruption is ≤ 1.5 years (Serocki Volcano), <10 days (Costa Rica Rift) and <2 days (East Pacific Rise).

To our knowledge, published diffusion chronometry data for Icelandic volcanoes ascribed to crystal mush disaggregation processes only concern single eruptions that occurred in the EVZ. Diffusion kinetic data are available for a subglacial unit erupted in the Bárðarbunga-Veiðivötn volcanic system (Mutch et al., 2020), for the 2014-15 Holuhraun lava flow emplaced in the northern segment of the Bárðarbunga volcanic system (Hartley et al., 2018), for the 1783-84 Laki eruption of the Grímsvötn volcanic system (Hartley et al., 2016) and for the 2010 (Pankhurst et al., 2018) and middle-Pleistocene (Nikkola et al., 2019) Eyjafjallajökull eruptions in the southernmost section of the EVZ. With the exception of Skuggafjöll (Mutch et al., 2020), these studies reveal short diffusion times between mush disaggregation and entrainment prior to eruption, on the order of days up to 1-2 months (Fig. 10). These estimates overlap and are consistent with timescales calculated for middle-Holocene and historical units from the Bárðarbunga-Veiðivötn system (Fig. 10). Eyjafjallajökull is the only system studied so far for which there are timescale estimates available for eruptions of different ages. Timescales between mobilization of mush macrocrysts and eruption of about 10-30 days were calculated for the 2010 Eyjafjallajökull eruption (Pankhurst et al., 2018), in good agreement with mush mobilization times of about 9-37 days estimated for the middle-Pleistocene Eyjafjallajökull units (Nikkola et al., 2019).

At the present, Iceland is the only place above a slow-spreading ridge where numerous timescales of mush crystal entrainment to eruption are available and only very few data exist at fast-, intermediate- and slow-spreading MOR settings (Fig. 10). Timescales between mush disruption and eruption are on the order of few days for the East Pacific Rise (fast-spreading ridge) (Moore et al., 2014) and for the Costa Rica Rift (intermediate-spreading ridge) (Costa et al., 2010), while mush disruption beneath Serocki Volcano (slow-spreading ridge) occurred about 1.5 years before an eruption on the seafloor (Costa et al. 2010). Mush disruption to eruption timescales estimated for slow-spreading MOR settings are consistent with timescales obtained from the oldest units from this work. Overall, most timescales calculated at slow-spreading ridges (Fig. 10) tend to be longer (months to years) than the ones obtained at intermediate and fast spreading ridges (days). The fact that the time between mush disintegration and eruption increases with decreasing spreading rates (Zellmer et al., 2012) is consistent with thickening of the lithosphere and

increase in the depth of melt levels at slow-spreading ridges (Wanless and Shaw, 2012). However, further geospeedometric work on intermediate- and fast-spreading ridges is required to elucidate whether or not there is spreading-rate control of the mush disaggregation-to-eruption timescales along MOR settings.

7. IMPLICATIONS

Samples studied in this work include crystalline gabbroic nodules that most likely preserve the physical and mineralogical features of the mush itself. We modeled Fe-Mg, Mn and Ni diffusion in olivine crystals from Holocene samples of the Bárðarbunga-Veiðivötn volcanic system in central Iceland to reconstruct crystal residence time in the carrier melt, which we link to the time elapsed between melt injection (i.e. mush disaggregation) and eruption.

One important implication highlighted by our study is that not every magma replenishment event results in an eruption. In the early Holocene, a year or more may have elapsed between initial perturbation of the shallow reservoir(s) and final eruption, but the timescale between perturbation and eruption appears to get shorter approaching the present day. This difference in crystal residence times in the carrier liquid appears to be associated with the occurrence of a much denser and more rigid mush fabric in the early Holocene, which required more energy to be loosened, disaggregated and mobilized. In terms of hazard assessment, this study highlights that the Bárðarbunga-Veiðivötn volcanic system has been responding faster to melt injection as time proceeds, providing less warning between magma injection and eruption. This could possibly indicate the recent establishment of dominant magma transfer routes along which magma can quickly migrate towards the surface. More studies on the temporal evolution of magma transport timescales underneath single volcanic systems are needed to better constrain the behavior of volcanic systems through time, with a direct implication for volcanic hazard assessment, especially in regions where the last known eruption occurred long before the installation of modern volcano monitoring networks.

The crystal cargos in our samples do not record any evidence of late-stage primitive magma replenishment that could have triggered the eruption. This feature is observed also in crystals from other rift settings in Iceland. Primitive melts with different compositions have been supplied to the Bárðarbunga-Veiðivötn system during earlier stages of its magmatic history (Caracciolo et al. 2020), but these magmas are typically homogenized by concurrent mixing and crystallization (Caracciolo et al., 2020; Maclennan, 2008) before being injected into the shallow crystal mush reservoir. These processes likely take place in a multi-tiered magmatic system made up of stacked sills in which macrocrysts are gradually transported upwards and exposed to melts that become more evolved as they move toward the mid-crustal reservoir(s). A plausible eruption trigger mechanism is that rifting-associated events can enable the vertical rearrangement of crystal and melt horizons and facilitate ascent of relatively evolved and mixed melt pockets stored a at mid-crustal levels, with no requirement to supply hot and primitive magmas. Our findings have broad implications for the dynamics of magmatic processes operating in axial ridge settings, since we emphasize the possibility that rifting events can significantly control the vertical arrangement of crystal and melt layers.

Acknowledgments

EPMA and EBSD data collection was financed by Landsvirkjun energy company (NÝR-18 – 2018). This research work was financially supported by the University of Iceland Research Fund (Nr: HI17060092). We would like to thank Duncan Hedges, Richard Walshaw and Geoffrey E. Lloyd (University of Leeds) for their help with EBSD analyses and data processing. We are grateful to Sylvie Demouchy for editorial handling, and Thomas Shea and Cliff Shaw for their valuable reviews that significantly improved the quality of the manuscript. The involvement of S. A. Halldórsson was partly in relation to the H2020 project EUROVOLC, funded by the European Commission (Grant 731070). M. Kahl acknowledges support from IRF postdoctoral fellowship grant 152726–051 and funding from the Deutsche Forschungsgemeinschaft (DFG, German Research Foundation) - KA 3532/2-1. M. E. Hartley acknowledges support from Natural Environment Research Council (NERC) grant NE/P002331/1. A MATLAB® code for Fe-Mg, Ni and Mn diffusion can be requested from the authors.

References

Bjarnason, I. (2008) An Iceland hotspot saga. Jökull, 3–16.

Blundy, J., and Cashman, K. (2008) Petrologic reconstruction of magmatic system variables and processes. Reviews in Mineralogy and Geochemistry, 69, 179–239.

Caracciolo, A., Bali, E., Guðfinnsson, G.H., Kahl, M., Halldórsson, S.A., Hartley, M.E., and Gunnarsson, H. (2020) Temporal evolution of magma and crystal mush storage conditions in the Bárðarbunga-Veiðivötn volcanic system, Iceland. Lithos, 352–353.

Cashman, K. V., Sparks, R.S.J., and Blundy, J.D. (2017) Vertically extensive and unstable magmatic systems: A unified view of igneous processes. Science, 355, 1–9.

Chamberlain, K.J., Morgan, D.J., and Wilson, C.J.N. (2014) Timescales of mixing and mobilisation in the Bishop Tuff magma body: Perspectives from diffusion chronometry. Contributions to Mineralogy and Petrology, 168, 1–24.

Clark, A.M., and Long, J.V.P. (1971) Anisotropic diffusion of nickel in olivine. In Thomas Graham Memorial Symposium on Diffusion Proceses,Volume 2 pp. 511–521.

Coogan, L.A., Hain, A., Stahl, S., and Chakraborty, S. (2005) Experimental determination of the diffusion coefficient for calcium in olivine between 900°C and 1500°C. Geochimica et Cosmochimica Acta, 69, 3683–3694.

Cooper, K.M., and Kent, A.J.R. (2014) Rapid remobilization of magmatic crystals kept in cold storage. Nature, 506, 480–483.

Costa, F., and Chakraborty, S. (2004) Decadal time gaps between mafic intrusion and silicic eruption obtained from chemical zoning patterns in olivine. Earth and Planetary Science Letters, 227, 517–530.

Costa, F., and Morgan, D. (2010) Time Constraints from Chemical Equilibration in Magmatic Crystals, 125–159 p. Timescales of Magmatic Processes: From Core to Atmosphere.

Costa, F., Dohmen, R., and Chakraborty, S. (2008) Time Scales of Magmatic Processes from Modeling the Zoning Patterns of Crystals. Reviews in Mineralogy and Geochemistry, 69, 545–594.

Costa, F., Coogan, L.A., and Chakraborty, S. (2010) The time scales of magma mixing and mingling involving primitive melts and melt-mush interaction at mid-ocean ridges. Contributions to Mineralogy and Petrology, 159, 371–387.

Demouchy, S., Jacobsen, S.D., Gaillard, F., and Stem, C.R. (2006) Rapid magma ascent recorded by water diffusion profiles in mantle olivine. Geology, 34, 429–432.

Dohmen, R., Becker, H.W., and Chakraborty, S. (2007) Fe-Mg diffusion in olivine I: Experimental determination between 700 and 1,200°C as a function of composition, crystal orientation and oxygen fugacity. Physics and Chemistry of Minerals, 34, 389–407.

Dohmen, R., Faak, K., and Blundy, J.D. (2017) Chronometry and Speedometry of Magmatic Processes using Chemical Diffusion in Olivine, Plagioclase and Pyroxenes. Reviews in Mineralogy and Geochemistry, 83, 535–575.

Faak, K., Chakraborty, S., and Coogan, L.A. (2013) Mg in plagioclase: Experimental calibration of a new geothermometer and diffusion coefficients. Geochimica et Cosmochimica Acta, 123, 195–217.

Gee, M.A.M., Taylor, R.N., Thirlwall, M.F., and Murton, B.J. (1998) Glacioisostacy controls chemical and isotopic characteristics of tholeiites from the Reykjanes Peninsula , SW Iceland. Earth and Planetary Science Letters, 164, 1–5.

Ginibre, C., Wörner, G., and Kronz, A. (2007) Crystal Zoning as an Archive for Magma Evolution. Elements, 3, 261–266.

Haddadi, B., Sigmarsson, O., and Larsen, G. (2017) Magma storage beneath Grímsvötn volcano, Iceland, constrained by clinopyroxene-melt thermobarometry and volatiles in melt inclusions and groundmass glass. Journal of Geophysical Research: Solid Earth, 122, 6984–6997.

Halldórsson, S.A., Bali, E., Hartley, M.E., Neave, D.A., Peate, D.W., Guðfinnsson, G.H., Bindeman, I., Whitehouse, M.J., Riishuus, M.S., Pedersen, G.B.M., and others (2018) Petrology and geochemistry of the 2014–2015 Holuhraun eruption, central Iceland: compositional and mineralogical characteristics, temporal variability and magma storage. Contributions to Mineralogy and Petrology, 173, 1–25.

Hansen, H., Grönvold, K., 2000. Plagioclase ultraphyric basalts in Iceland : the mush of the rift. Journal of Volcanology and Geothermal Research 98, 1-32.

Hartley, M.E., Morgan, D.J., Maclennan, J., Edmonds, M., and Thordarson, T. (2016) Tracking timescales of short-term precursors to large basaltic fissure eruptions through Fe-Mg diffusion in olivine. Earth and Planetary Science Letters, 439, 58–70.

Hartley, M.E., Bali, E., Maclennan, J., Neave, D.A., and Halldórsson, S.A. (2018) Melt inclusion constraints on petrogenesis of the 2014–2015 Holuhraun eruption, Iceland. Contributions to Mineralogy and Petrology, 173, 1–23.

Holzapfel, C., Chakraborty, S., Rubie, D.C., and Frost, D.J. (2007) Effect of pressure on Fe-Mg, Ni and Mn diffusion in (FexMg1-x)2SiO4olivine. Physics of the Earth and Planetary Interiors, 162, 186–198.

Kahl, M., Chakraborty, S., Costa, F., and Pompilio, M. (2011) Dynamic plumbing system beneath volcanoes revealed by kinetic modeling, and the connection to monitoring data: An example from Mt. Etna. Earth and Planetary Science Letters, 308, 11–22.

Kahl, M., Chakraborty, S., Costa, F., Pompilio, M., Liuzzo, M., and Viccaro, M. (2013) Compositionally zoned crystals and real-time degassing data reveal changes in magma transfer dynamics during the 2006 summit eruptive episodes of Mt. Etna. Bulletin of Volcanology, 75, 1–14.

Kahl, M., Chakraborty, S., Pompilio, M., and Costa, F. (2015) Constraints on the nature and evolution of the magma plumbing system of Mt. Etna volcano (1991-2008) from a combined thermodynamic and kinetic modelling of the compositional record of minerals. Journal of Petrology, 56, 2025–2068.

Kahl, M., Viccaro, M., Ubide, T., Morgan, D.J., and Dingwell, D.B. (2017) A branched magma feeder system during the 1669 eruption of Mt Etna: Evidence from a time-integrated study of zoned olivine phenocryst populations. Journal of Petrology, 58, 443–472.

Kelemen, P.B., Koga, K., Shimizu, N., 1997. Geochemistry of gabbro sills in the crust–mantle transition zone of the Oman ophiolite: implications for the origin of the oceanic lower crust. Earth and Planetary Science Letters 146, 1–31. https://doi.org/https://doi.org/10.1016/S0012-821X(96)00235-X

Kress, V.C., and Carmichael, I.S.E. (1991) The compressibility of silicate liquids containing Fe_2O_3 and the effect of composition, temperature, oxygen fugacity and pressure on their redox states. Contributions to Mineralogy and Petrology, 108, 82–92.

Larsen, G., and Guðmundsson, M.T. (2014) Volcanic system : Bárðarbunga system. Catalogue of Icelandic Volcanoes, 1–11.

Le Breton, E., Dauteuil, O., and Biessy, G. (2016) Post-glacial rebound of Iceland during the Holocene. Journal of the Geological Society, London, 167, 417–432.

Maclennan, J. (2008) Concurrent mixing and cooling of melts under Iceland. Journal of Petrology, 49, 1931–1953.

Maclennan, J. (2019) Mafic tiers and transient mushes: evidence from Iceland. Philosophical Transactions of the Royal Society A, 377, 1–20.

Martin, V.M., Morgan, D.J., Jerram, D.A., Caddick, M.J., Prior, D.J., and Davidson, J.P. (2008) Bang! Month-scale eruption triggering at santorini volcano. Science, 321, 1178.

Mattsson, H.B., and Oskarsson, N. (2005) Petrogenesis of alkaline basalts at the tip of a propagating rift: Evidence from the Heimaey volcanic centre, south Iceland. Journal of Volcanology and Geothermal Research, 147, 245–267.

Moore, A., Coogan, L.A., Costa, F., and Perfit, M.R. (2014) Primitive melt replenishment and crystal-mush disaggregation in the weeks preceding the 2005-2006 eruption 9°50' N, EPR. Earth and Planetary Science Letters, 403, 15–26.

Mutch, E., Maclennan, J., Shorttle, O., Rudge, J., and Neave, D. (2020) DFENS: Diffusion chronometry using Finite Elements and Nested Sampling. Earth and Space Science Open Archive.

Mutch, Euan J F, Maclennan, J., Holland, T.J.B., and Buisman, I. (2019b) Millennial storage of near-Moho magma. Science, 264, 260–264.

Mutch, Euan J. F., Maclennan, J., Shorttle, O., Edmonds, M., and Rudge, J.F. (2019a) Rapid transcrustal magma movement under Iceland. Nature Geoscience.

Neave, D.A., and Putirka, K.D. (2017) A new clinopyroxene-liquid barometer , and implications for magma storage pressures under Icelandic rift zones. American Mineralogist, 102, 777–794.

Neave, D.A., Passmore, E., Maclennan, J., Fitton, G., and Thordarson, T. (2013) Crystal-melt relationships and the record of deep mixing and crystallization in the AD 1783 Laki eruption, Iceland. Journal of Petrology, 54, 1661–1690.

Neave, D.A., Maclennan, J., Hartley, M.E., Edmonds, M., and Thordarson, T. (2014) Crystal storage and transfer in basaltic systems: The skuggafjoll eruption, Iceland. Journal of Petrology, 55, 2311_2346.

Neave, D.A., Maclennan, J., Thordarson, T., and Hartley, M.E. (2015) The evolution and storage of primitive melts in the Eastern Volcanic Zone of Iceland: the 10 ka Grímsvötn tephra series (i.e. the Saksunarvatn ash). Contributions to Mineralogy and Petrology, 170, 1–23.

Newcombe, M.E., Fabbrizio, A., Zhang, Y., Ma, C., Le Voyer, M., Guan, Y., Eiler, J.M., Saal, A.E., and Stolper, E.M. (2014) Chemical zonation in olivine-hosted melt inclusions. Contributions to Mineralogy and Petrology, 168, 1–26.

Nikkola, P., Bali, E., Kahl, M., van der Meer, Q.H.A., Rämö, O.T., Guðfinnsson, G.H., and Thordarson, T. (2019) Mid-crustal storage and crystallization of Eyjafjallajökull. Jökull, 69, 77–96.

Pankhurst, M.J., Dobson, K.J., Morgan, D.J., Loughlin, S.C., Thordarson, T.H., Lee, P.D., and Courtois, L. (2014) Technical note monitoring the magmas fuellingvolcanic eruptions in near-real-time using x-ray micro-computed tomography. Journal of Petrology, 55, 671–684.

Pankhurst, M.J., Morgan, D.J., Thordarson, T., and Loughlin, S.C. (2018) Magmatic crystal records in time, space, and process, causatively linked with volcanic unrest. Earth and Planetary Science Letters, 493, 231–241.

Petry, C., Chakraborty, S., and Palme, H. (2004) Experimental determination of Ni diffusion coefficients in olivine and their dependence on temperature, composition, oxygen fugacity, and crystallographic orientation. Geochimica et Cosmochimica Acta, 68, 4179–4188.

Pinton, A., Giordano, G., Speranza, F., and Thordarson, T. (2018) Paleomagnetism of Holocene lava flows from the Reykjanes Peninsula and the Tungnaá lava sequence (Iceland): implications for flow correlation and ages. Bulletin of Volcanology, 80, 1–19.

Rae, A.S.P., Edmonds, M., Maclennan, J., Morgan, D., Houghton, B., Hartley, M.E., and Sides, I. (2016) Time scales of magma transport and mixing at Kīlauea Volcano, Hawai'i. Geology, 44, 463–466.

Rasmussen, D.J., Plank, T.A., Roman, D.C., Power, J.A., Bodnar, R.J., and Hauri, E.H. (2018) When does eruption run-up begin? Multidisciplinary insight from the 1999 eruption of Shishaldin volcano. Earth and Planetary Science Letters, 486, 1–14.

Roeder, P.L., and Emslie, R.F. (1970) Olivine-liquid equilibrium. Contribution to MIneralogy and Petrology, 29, 275–289.

Ruprecht, P., and Cooper, K.M. (2012) Integrating the uranium-series and elemental diffusion geochronometers in mixed magmas from Volcán Quizapu, Central Chile. Journal of Petrology, 53, 841–871.

Ruprecht, P., and Plank, T. (2013) Feeding andesitic eruptions with a high-speed connection from the mantle. Nature, 500, 68–72.

Shea, T., Costa, F., D. Krimer, and Hammer, J.E. (2015) Accuracy of timescales retrieved from diffusion modeling in olivine : A 3D perspective †, 100, 2026–2042.

Sigmundsson, F., Hreinsdóttir, S., Hooper, A., Árnadóttir, T., Pedersen, R., Roberts, M.J., Óskarsson, N., Auriac, A., Decriem, J., Einarsson, P., and others (2010) Intrusion triggering of the 2010 Eyjafjallajökull explosive eruption. Nature, 468, 426–432.

Sigmundsson, F., Pinel, V., Grapenthin, R., Hooper, A., Halldórsson, S.A., Einarsson, P., Ófeigsson, B.G., Heimisson, E.R., Jónsdóttir, K., Gudmundsson, M.T., and others (2020) Unexpected large eruptions from buoyant magma bodies within viscoelastic crust. Nature Communications, 11, 1–11.

Sinton, J., Grönvold, K., and Sæmundsson, K. (2005) Postglacial eruptive history of the Western Volcanic Zone, Iceland. Geochemistry, Geophysics, Geosystems, 6, 1–34.

Sio, C.K.I., Dauphas, N., Teng, F.Z., Chaussidon, M., Helz, R.T., and Roskosz, M. (2013) Discerning crystal growth from diffusion profiles in zoned olivine by in situ Mg-Fe isotopic analyses. Geochimica et Cosmochimica Acta, 123, 302–321.

Sparks, R.S.J., and Sigurdsson, H. (1977) Magma mixing: a mechanism for triggering acid explosive eruptions. Nature, 267, 315–318.

Streck, M.J. (2008) Mineral textures and zoning as evidence for open system processes. Reviews in Mineralogy and Geochemistry, 69, 595–622.

Thomson, A., and Maclennan, J. (2013) The distribution of olivine compositions in icelandic basalts and picrites. Journal of Petrology, 54, 745–768.

Thordarson, T., and Larsen, G. (2007) Volcanism in Iceland in historical time: Volcano types, eruption styles and eruptive history. Journal of Geodynamics, 43, 118–152.

Turner, S., and Costa, F. (2007) Measuring timescales of magmatic evolution. Elements, 3, 267–272.

Viccaro, M., Giuffrida, M., Nicotra, E., and Cristofolini, R. (2016) Timescales of magma storage and migration recorded by olivine crystals in basalts of the March-April 2010 eruption at Eyjafjallajökull volcano, Iceland. American Mineralogist, 101, 222–230.

Wanless, V.D., and Shaw, A.M. (2012) Lower crustal crystallization and melt evolution at mid-ocean ridges. Nature Geoscience, 5, 651–655.

Yang, H.-J., Kinzler, R.J., and Grove, T.L. (1996) Experiments and models of anhydrous, basaltic olivine-plagioclase-augite saturated melts from 0.001 to 10 kbar. Contributions to Mineralogy and Petrology, 124, 1–18.

Zellmer, G.F., Dulski, P., Iizuka, Y., and Perfit, M.R. (2012) Rates and processes of crystallization in on-axis and off-axis MOR basaltic melts. Lithos, 154, 1–15.

10.1 Supplementary information and figures attached to Paper II

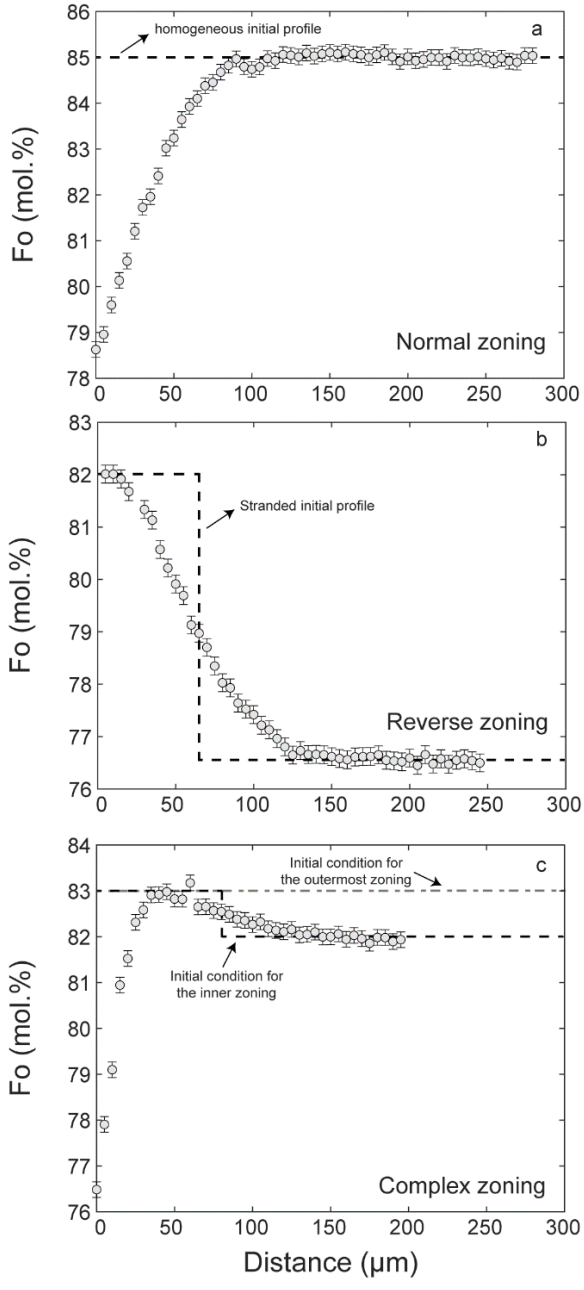

Fig. S1.1. *The types of olivine zoning patterns identified in the magmatic units. a) Normal zoning: the majority of olivine macrocrysts (n=82) are normally zoned, with homogeneous, high forsterite core plateaux, followed by decreasing forsterite contents towards the rim. b) Reverse zoning: only 3 olivine macrocrysts are reversely zoned with forsterite increasing from core to rim. c) Macrocrysts with complexly zoned patterns, with reversely zoned interiors followed by normally zoned outermost rims (n=15). Dotted lines indicate inferred initial profiles. Error bars indicate 2σ uncertainty.*

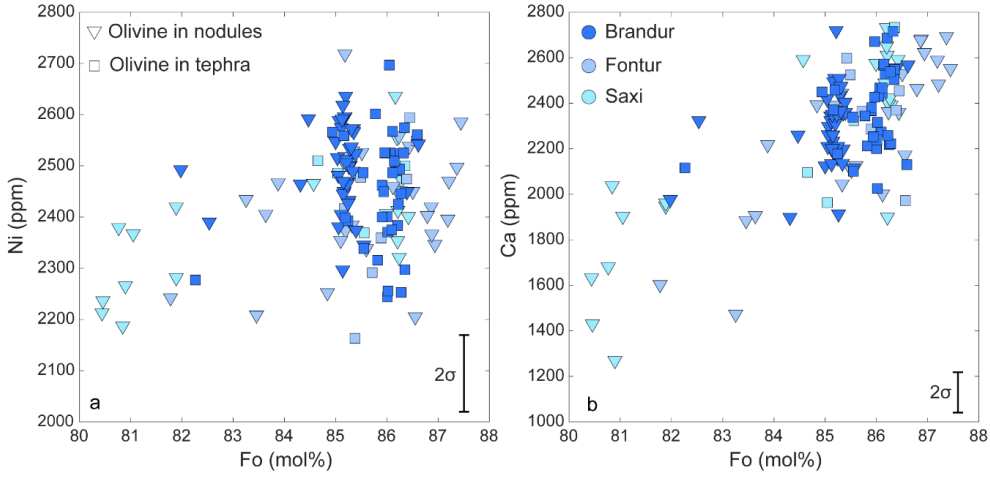

Fig. S1.2. *Olivine variation diagrams showing a) Ni content and b) Ca content as a function of Fo in olivine macrocrysts from early-Holocene units only. In this figure, we distinguish between olivine crystals found in the nodules and olivine crystals found in the tephra using different symbols (inverted triangles and squares respectively). No significant differences are observed between the two groups, except that olivine macrocrysts from Brandur nodules plot at lower Fo content (Fo ~85) compared to olivine macrocrysts from Brandur tephra samples (Fo ~86). Analytical errors are representative of 2σ for multiple standard analyses.*

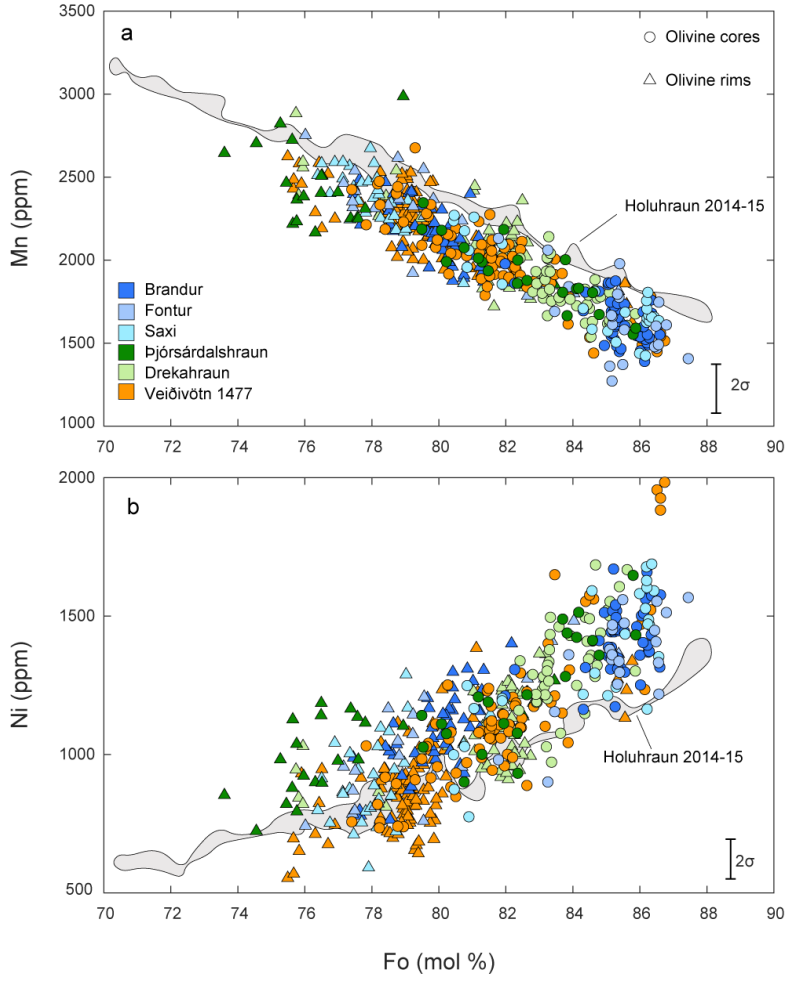

Fig. S1.3. *Variation diagrams showing a) Mn content and b) Ni content as a function of Fo in olivine macrocrysts from all studied magmatic units. Circles represent olivine cores and triangles are olivine rims. High current analyses of 2014-15 Holuhraun olivines are reported for comparison (Halldórsson et al., 2018). Olivine macrocryst cores from historical units are more evolved with higher contents of Mn and lower contents of Ni compared to early-Holocene units. Analytical errors are representative of 2σ for multiple standard analyses.*

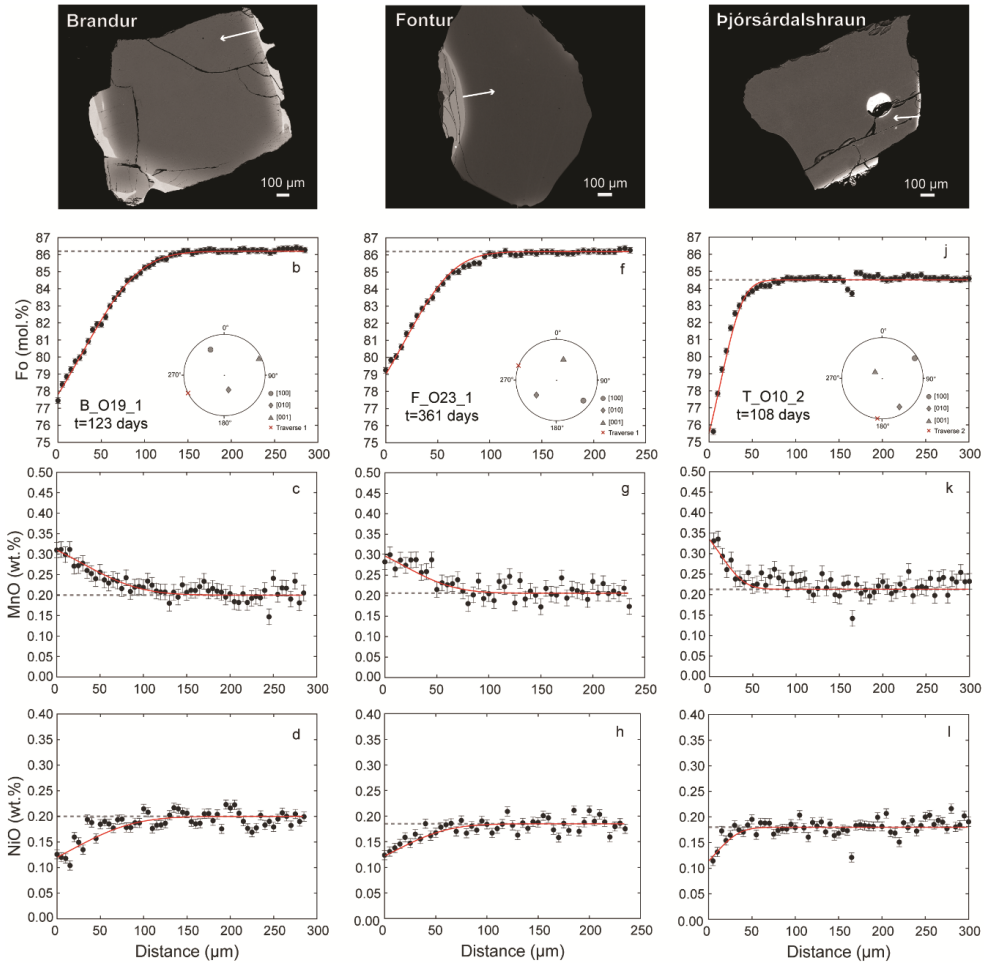

Fig. S1.4*. Selected macrocrysts suitable for multi-element (Fe-Mg, Mn, Ni) diffusion modeling along the same EMP traverse (white line). a-d) Olivine macrocryst from Brandur, e-h) olivine macrocryst from Fontur, and i-l) olivine macrocryst from Þjórsárdalshraun. Red lines are best fit curves obtained for Fe-Mg, Mn and Ni diffusion modeling. Black dashed lines show inferred initial conditions. Analytical errors of the EMP data based on 2σ for multiple standard analyses.*

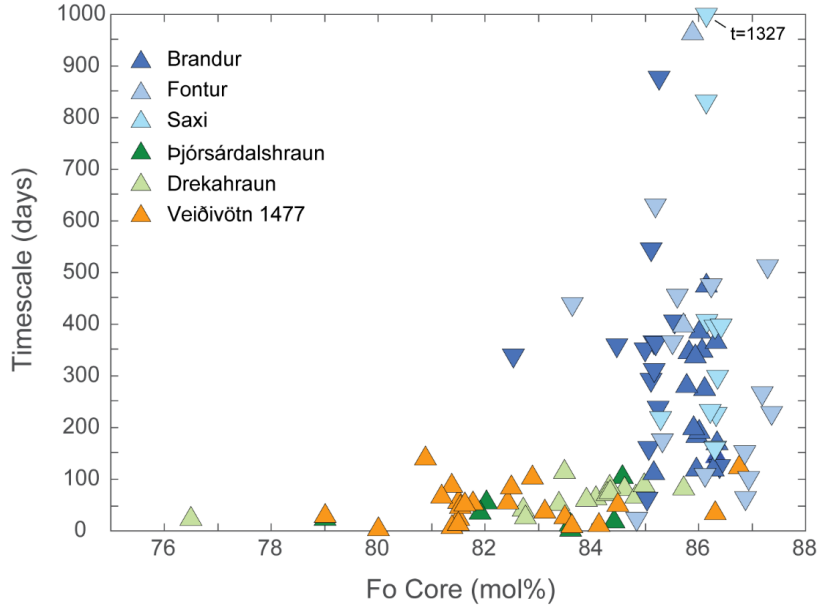

Fig. S1.5*. Relationship between olivine Fo cores and calculated diffusion timescales. At any given Fo content, early-Holocene olivines register longer and more variable timescales compared to middle-Holocene and historical olivines. Furthermore, early-Holocene olivine cores are more primitive than middle-Holocene and historical olivine cores. Olivine crystals from tephra/lava and nodule samples are indicated with upwards pointing triangles and inverted triangles, respectively.*

11 Paper III

Oxygen isotope evidence for progressively assimilating trans-crustal magma plumbing systems in Iceland

Alberto Caracciolo, Sæmundur A. Halldórsson, Enikő Bali, Edward W. Marshall, Heejin Jeon, Martin J. Whitehouse, Jaime D. Barnes, Guðmundur H. Guðfinnsson, Maren Kahl, Margaret E. Hartley

Manuscript to be submitted to Geology (or a similar journal)

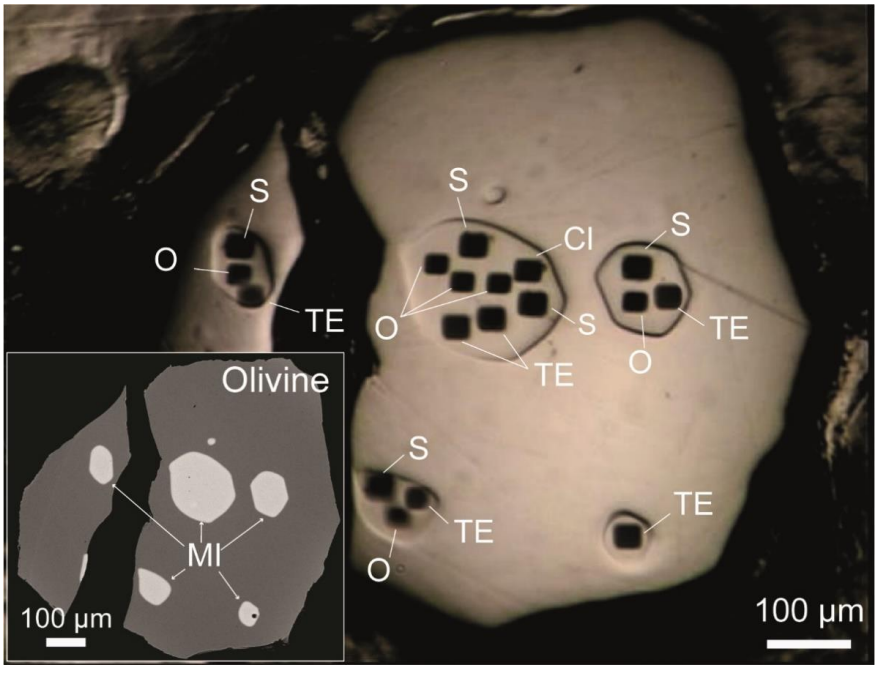

Oxygen isotope evidence for progressively assimilating trans-crustal magma plumbing systems in Iceland

Alberto Caracciolo[1], Sæmundur A. Halldórsson[1], Enikő Bali[1], Edward W. Marshall1[1], Heejin Jeon[2], Martin J. Whitehouse[2], Jaime D. Barnes[3], Guðmundur H. Guðfinnsson[1], Maren Kahl[4], Margaret E. Hartley[5]

[1]*Nordic Volcanological Center, Institute of Earth Sciences, University of Iceland, Sturlugata 7, 101 Reykjavík, Iceland.*
[2]*Department of Geosciences, Swedish Museum of Natural History, Stockholm, Sweden*
[3]*Department of Geological Sciences, University of Texas, Austin, Texas 78712, USA*
[4]*Institut für Geowissenschaften, Universität Heidelberg, Heidelberg, Germany*
[5]*Department of Earth and Environmental Sciences, University of Manchester, Manchester, UK*

Corresponding author

Alberto Caracciolo (alberto@hi.is)

ABSTRACT

The oxygen isotope composition of mantle-derived melts can place important constraints on how magmas are processed as they navigate through the crustal section. Indeed, assimilation of crustal material is a crucial aspect of basalt petrogenesis as it affects the chemical and rheological behaviour of eruptive magmas at active volcanoes. Here, we report oxygen isotope and trace element data from a large number of well characterised melt inclusions and groundmass glasses from the Bárðarbunga volcanic system (BVS), the most extensive volcanic system of Iceland, with the goal to assess how and where in the plumbing system crustal rocks interact with ascending magmas. While both melt inclusions and groundmass glasses record a large range in $\delta^{18}O$ values, form +3.2‰ to +6.4‰ and +2.6‰ and +5.5 ‰, respectively, groundmass glasses reveal, on average, lower values. Relationships between incompatible trace element ratios (e.g. Zr/Nb, La/Sm) and oxygen isotopes are best explained with three-component mixing, where primary melts derived from depleted and enriched mantle components with distinct $\delta^{18}O$ values, mix and acquire a low-$\delta^{18}O$ character upon progressive contamination with altered Icelandic crust. We show in the most extreme cases, mantle-derived melts have exchanged up to 50% of their primary oxygen with a low- $\delta^{18}O$ Icelandic crust, but the majority (60%) of melt inclusions require 10-30% oxygen isotope exchange to explain their oxygen isotope signatures. In addition, we observe a correlation between melt equilibration depth and the extent of oxygen isotope exchange. We therefore propose that progressively assimilating multi-tiered plumbing system represent a characteristics feature of the BVS and that modifications resulting from interaction with the crust systematically increase as melts migrate through higher crustal levels. We also demonstrate the importance of similar processes for other parts other active rift zone in Iceland.

INTRODUCTION

There is consensus that magma batches underneath active basaltic volcanoes are processed over a large range of depths in so-called trans-crustal magmatic systems (Maclennan, 2019 and reference therein). Mantle-derived mafic magmas can assimilate the overlying crust during their ascent, overprinting their original chemical compositions. Magma interaction with crustal rocks is best followed by observing changes in isotopic composition. Oxygen isotope ratios ($\delta^{18}O$, see definition in the supplement) of Icelandic crustal rocks, for example, deviate significantly from mantle values, likely due to the combined effects of surface weathering and water-rock interaction (Gautason and Muehlenbachs, 1998). As a result, oxygen isotopes have been widely used to study the role of crustal rocks in Iceland's basalt petrogenesis, either in the form of crustal material subducted into the mantle (source contamination) and/or as contaminants throughout the magmatic column (crustal contamination) (Gee et al., 1998; Eiler et al., 2000; Skovgaard et al., 2001; Kokfelt et al., 2006; Thirlwall et al., 2006; Bindeman et al., 2008; Hartley et al., 2013).

Fresh mid-ocean ridge basalt (MORB) glasses typically have $\delta^{18}O$ values between +5.3 and +6.2 ‰, with most falling within the range 5.7 ± 0.2 ‰ (Eiler, 2001; Bindeman, 2008). In contrast, glasses and melt inclusions (MIs) from Iceland's rift zones are typically ^{18}O-depleted (down to 2.5 ‰) compared to MORB (Breddam, 2002; Burnard and Harrison, 2005; Peate et al., 2010; Hartley et al., 2013; Halldórsson et al., 2016). Although the origin of this shift towards ^{18}O-depleted values is still a matter of debate, secondary crustal contamination appears to control oxygen isotope variations of Icelandic glasses (Gee et al., 1998; Eiler et al., 2000; Hartley et al., 2013). The hypothesis is that Icelandic melts inherit their ^{18}O-depleted character by passing through and assimilating anomalously thick crust that has extensively interacted with ^{18}O-depleted high-latitude waters ($\delta^{18}O$ from -6.5 to -14.5 ‰, Sveinbjörnsdóttir et al., 2020). However, at present, our understanding of how and where melts are affected by crustal contamination in trans-crustal magmatic systems across Iceland is limited, primarily as the identification of $\delta^{18}O$ components which truly are mantle-derived, has proven to be challenging.

Our objectives here are (1) to pinpoint the depths in the Icelandic crust at which assimilation processes affect $\delta^{18}O$ values of Icelandic basalts, and (2) to quantify the extent of crustal contamination as melts migrate through the Icelandic crust. We target a well-characterized subglacial and Holocene sample suite (Caracciolo et al., 2020; Caracciolo et al. in press) from the BVS, including samples from the 2014-15 Holuhraun event. Located in the Eastern Rift Zone (ERZ), the BVS is one of the most productive systems of Iceland (Larsen and Guðmundsson, 2014) and it is situated above the inferred location of the Iceland mantle plume (Harðardóttir et al., 2018). The BVS is an ideal candidate to evaluate the effects of crustal contamination, since the crust is up to 35-40 km thick (Jenkins et al., 2018) and the plumbing architecture is likely controlled by multi-level stacked reservoirs in which melts are processed over a large range of depths (Hansen and Grönvold, 2000; Caracciolo et al., 2020; Caracciolo et al. in press). We therefore present new oxygen isotope analyses and trace element data on well-characterized melt inclusions and groundmass glasses to better assess these processes. We supplement this dataset with new LF $\delta^{18}O$ values from a set of subglacial glasses from the active rift zones in Iceland (see supplement). Our data suggest that the BVS is a progressively assimilating multi-level magmatic system and that systems operating in similar manner, are likely to be found in other parts of the active rifts in Iceland.

RESULTS

Trace element and oxygen isotope analyses were performed via SIMS and laser fluorination at the NordSim facility in Stockholm and at the University of Texas, respectively (see the supplementary text for more details on the analytical methods). Ion probe analyses show that melt inclusion $\delta^{18}O$ values vary between +3.2‰ and +6.4‰, whereas corresponding groundmass glasses have $\delta^{18}O$ values between +2.6‰ and +5.5‰, on average lower than melt inclusions (Fig. 1 and Table S1-S2). In contrast, laser fluorination (LF) data on groundmass glasses, which are generally in good agreement with SIMS data Fig. S5, highlight a narrower range of $\delta^{18}O$ values, between +3.70 ‰ and +4.21 ‰ (Fig. 1a and Fig. S4). Oxygen isotope ratios of MIs and groundmass glasses correlate with melt MgO and trace element ratios. MIs with the most primitive compositions (MgO>8 wt%) record the largest spread in $\delta^{18}O$ values (from +3.4‰ to +6.4‰) and in trace element ratios, whereas the variation of oxygen isotopes and trace element ratios becomes narrower as MgO decreases (Fig. 1 and Fig. S6). Incompatible trace element enriched (Zr/Nb <7, La/Yb>2.2) and depleted (Zr/Nb>15, La/Yb<1.3) MIs preserve a primitive character (Fig. 1b and Fig. DR6b), while the most evolved MIs and glasses record low $\delta^{18}O$ values and intermediate trace element ratios. Finally, we note the largest variation in $\delta^{18}O$ values and incompatible trace element ratios is observed in melts with high MgO contents, and the variation decreases with melt evolution (Fig. 1 and Fig. DR6).

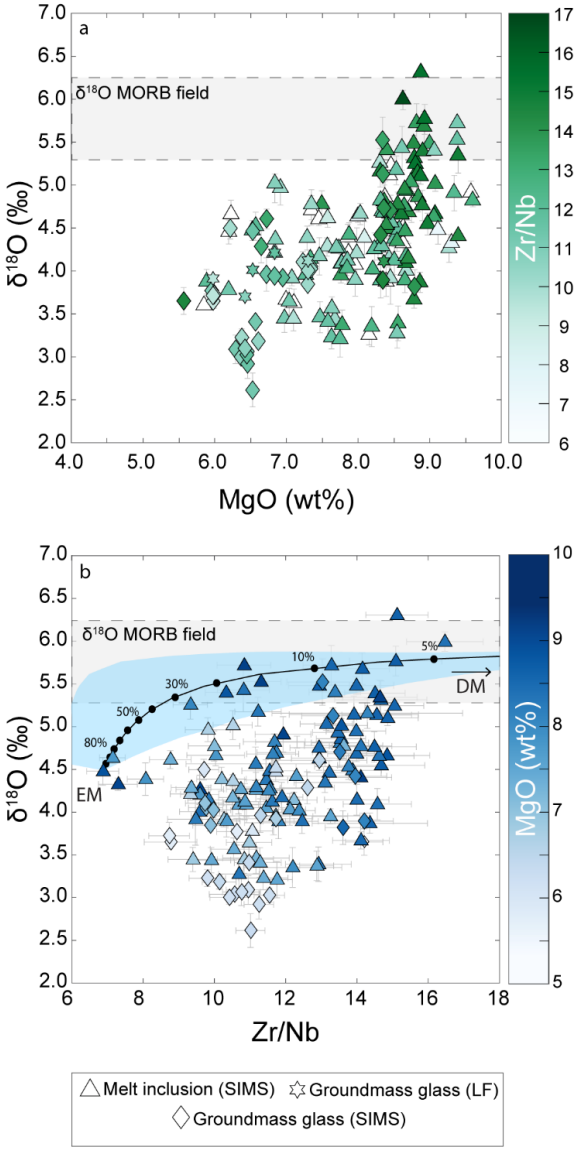

Figure 1. *a) MgO content versus $\delta^{18}O$ for Bárðarbunga melt inclusions and groundmass glasses. Samples are coloured according to their Zr/Nb ratio (see scale on the right). The grey field indicates the $\delta^{18}O$ range of MORBs. The largest variation in $\delta^{18}O$ is observed in the most primitive compositions. b) Zr/Nb versus $\delta^{18}O$ values for the same samples. The black curve indicates binary mixing between the depleted mantle (DM) and the inferred*

enriched mantle (EM) sources. The mantle array (light blue field) is modelled assuming different degrees of partial melting of DM (15%) and EM (5%). Most of the samples have lower $\delta^{18}O$ values than MORB. LF: laser fluorination data; SIMS: ion microprobe data. Error bars reflect 1σ external precision calculated as standard error of the mean.

DISCUSSION

The role of the crust in masking mantle heterogeneities

Abundant evidence suggests that the Icelandic mantle is heterogeneous. Many studies have demonstrated that the mantle underneath Iceland contains an enriched, ^{18}O-depleted component (Skovgaard et al., 2001; Burnard and Harrison, 2005; Macpherson et al., 2005; Kokfelt et al., 2006; Thirlwall et al., 2006). Thirlwall et al. (2006) demonstrated that a strong relationship exists between the Icelandic Pb-Nd-Sr-He isotope signatures and low $\delta^{18}O$ values found in lavas from Reykjanes Peninsula. This relationship indicates that a geochemically enriched low-$\delta^{18}O$ domain exists in the mantle underneath the Reykjanes Peninsula. A comparable, low $\delta^{18}O$ component has also been found in samples from north, south and central Iceland (Breddam, 2002; Maclennan et al., 2003; Burnard and Harrison, 2005; Macpherson et al., 2005). The geochemical features of this enriched component likely reflect a mantle source containing recycled subducted oceanic lithosphere (Skovgaard et al., 2001; Breddam, 2002; Gurenko and Chaussidon, 2002; Stracke et al., 2003; Macpherson et al., 2005; Kokfelt et al., 2006; Thirlwall et al., 2006; Peate et al., 2010).

Collectively, melt inclusions and groundmass glasses from the Bárðarbunga volcanic system as well as the subglacial glasses from Iceland's neovolcanic rift zones, exhibit a large variation of $\delta^{18}O$ values (Fig. 2). Melts with $\delta^{18}O$ values similar to MORB are only observed in some depleted to moderately enriched primitive melt inclusions, whereas primitive enriched melt inclusions have low $\delta^{18}O$ values (Fig. 1b and DR6b). Assuming that depleted (DM) and enriched (EM) mantle components are present underneath Bárðarbunga volcano as elsewhere in Iceland (Thirlwall et al., 2004, 2006; Macpherson et al., 2005), and that variations in trace elemental ratios, such as Zr/Nb (e.g., Fitton et al., 1997), reflect such source heterogeneity, we tested if end-members evident in oxygen isotope and trace elemental characteristics of the most primitive melt inclusions can be reproduced by binary mixing between the DM and EM domains (Fig. 1b). Our modelling shows that by taking into account high degree of partial melting of DM (15%) and small degree of partial melting for EM (5%) (Stracke and Bourdon, 2009), we are only able to reproduce a small subset of the melt inclusions, with most of the data falling underneath the modelled envelope in a diagram with $\delta^{18}O$ plotted against Zr/Nb (blue field in Fig. 1b).

We observe decreasing $\delta^{18}O$ with decreasing MgO (Fig. 1a), which is consistent with previous studies (Hemond et al., 1988; Nicholson et al., 1991; Hartley et al., 2013), and is likely to indicate that crustal assimilation processes play a fundamental role in controlling melt oxygen isotope ratios. Similarly, the variability in trace element ratios decreases with decreasing $\delta^{18}O$ (Fig. 1b and Fig. DR6b). The relationship between trace element ratios, $\delta^{18}O$ and MgO contents suggests that as melt evolution proceeds and MgO decreases, melts acquire a low-$\delta^{18}O$ character (Fig. 1b) and the trace element compositional variability collapses to narrower ranges as a result of concurrent mixing and crystallization (Maclennan, 2008) coupled with assimilation of hydrothermally altered, ^{18}O-depleted, Icelandic crust. We observe decreasing $\delta^{18}O$ with decreasing MgO (Fig. 1a), which is

consistent with previous studies (Hemond et al., 1988; Nicholson et al., 1991; Hartley et al., 2013), and is likely to indicate that crustal assimilation processes play a fundamental role in controlling melt oxygen isotope ratios. Similarly, the variability in trace element ratios decreases with decreasing $\delta^{18}O$ (Fig. 1b and Fig. DR6b). The relationship between trace element ratios, $\delta^{18}O$ and MgO contents suggests that as melt evolution proceeds and MgO decreases, melts acquire a low-$\delta^{18}O$ character (Fig. 1b) and the trace element compositional variability collapses to narrower range as a result of concurrent mixing and crystallization (Maclennan, 2008) coupled with assimilation of hydrothermally altered, ^{18}O-depleted, Icelandic crust.

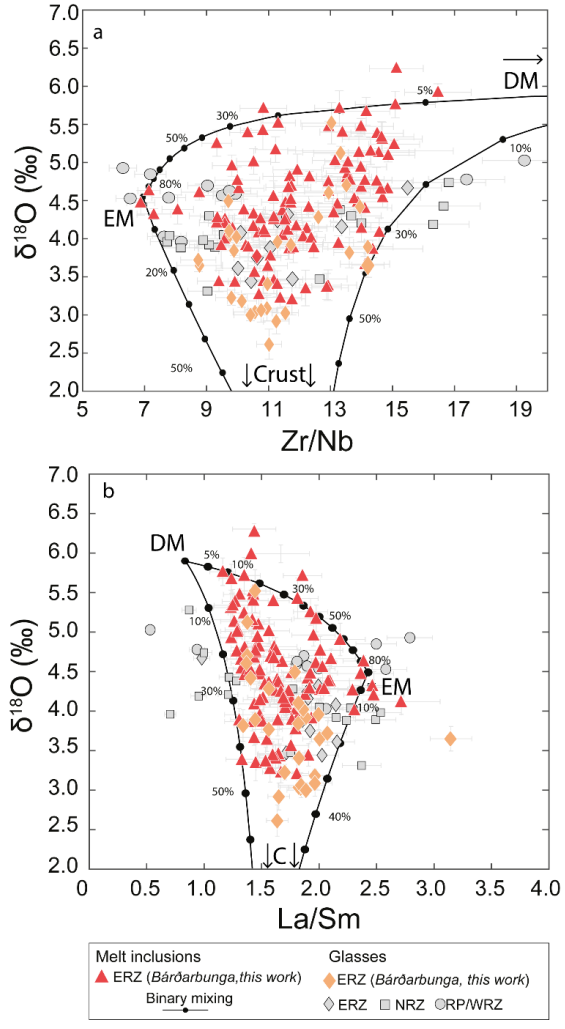

Figure 2. *a) Zr/Nb vs $\delta^{18}O$ and b) La/Sm vs $\delta^{18}O$ for Bárðarbunga melt inclusions and glasses. The enriched mantle (EM) domain produces melts with $\delta^{18}O$ = 4.5 ‰ and Zr/Nb = 6.9. As the degree of partial melting increases, enriched melts become diluted with melts derived from a depleted mantle (DM) domain, with $\delta^{18}O$ = 5.9 ‰ and Zr/Nb = 26.2. Black lines show binary mixing models between EM, DM and a crustal endmember with d18O=0*

‰ and Nb/Zr=12.6. The most depleted MIs sampled by our dataset contain a small fraction (~5%) of the enriched component. Also, around 90% of the Bárðarbunga data derive from primary mixtures which contain between 5-50% of DM component. Melt inclusions from this study are shown with red triangles, and groundmass glasses with orange diamonds. The subglacial glass dataset from Reykjanes Peninsula and Western Rift Zone (RP/WRZ), Eastern Rift Zone (ERZ) and Northern Rift Zone (NRZ) is indicated with grey symbols (see supplementary dataset).

We test the idea of three distinct endmember components (EM, DM and the crust) by modelling bulk digestion of low-$\delta^{18}O$ basaltic crust into the mantle-derived melts. We modelled binary mixing processes between the different pairs of the endmembers for different trace element ratios (Fig. 2). The modelling was carried out assuming a crust with $\delta^{18}O$ value of 0 ‰, in agreement with $\delta^{18}O$ values observed in drill core samples from Southwest and Eastern Iceland (Hattori and Muehlenbachs, 1982), and trace element ratios of 11.8 for Zr/Nb and 1.5 for La/Sm (see Table 1 and data repository for the definition of the endmembers).

Overall, the model show that the distribution of magma compositions from Iceland's rift zones are consistent with the inferred existence of a DM and EM components. Particularly, we note that low-$\delta^{18}O$ values (down to ~4.5‰) are more readily sampled in regions of the mantle that have undergone small degrees of partial melting (EM). As the degree of melting increases, melts derived from this enriched domain become diluted with melts from the DM domain (Fig. 2). The $\delta^{18}O$ values of mixtures lying along the mantle array (blue field in Fig. 1b) are then progressively shifted towards even lower $\delta^{18}O$ values upon assimilation. Therefore, any melt composition associated with the BVS is circumscribed within the binary mixing lines according to a three-step process: 1) Enriched and depleted mantle domains undergo differing degrees of partial melting, producing enriched and depleted primary melts. 2) Primary enriched and depleted melts mix together in different proportions. 3) The mixed melts ascend throughout the crust. Their initial mantle-like $\delta^{18}O$ is lowered as they progressively assimilate low-$\delta^{18}O$ crustal material when rising toward higher levels in the crust. This three-step process is capable of explaining the full diversity of $\delta^{18}O$ -trace element data not only in the BVS but also in melts erupted across Iceland's neovolcanic rift zones (Fig. 2).

Table 1. Compositional data of end member melts that have been estimated in this study (EM=enriched mantle component, DM=depleted mantle component).

	EM		DM[a]		Crust[b]		
	n=8	1σ		1σ		1σ	n
Ni	56	±13	242		88	±55	(662)
Sr	183	±106	80		197	±72	(698)
Y	24	±5	16		30	±11	(672)
Zr	88	±60	24		118	±62	(698)
Nb	12.7	±9	0.9		12.3	±6.8	(633)
La	8	±7	1.0		9.7	±6.0	(650)
Ce	19.8	±16	3.4		25	±14	(636)
Nd	12.6	±10	3.1		16.5	±8.7	(636)
Sm	3.3	±1.5	1.2		4.5	±2.2	(468)
Eu	1.2	±0.5	0.5		1.6	±0.7	(465)
Gd	3.7	±1.0	1.8		5.3	±2.3	(416)
Dy	4.3	±0.7	2.3		5.6	±2.1	(395)
Er	2.5	±0.4	1.5		3.1	±1.0	(416)
Yb	2.4	±0.3	1.5		2.9	±0.9	(489)
$\delta^{18}O$	+4.5	0.15	+5.9	0.17	0.0		
Zr/Nb	6.9		26.2		9.5	±7.2	
Ce/Nb	1.6		3.60		2.0	±1.6	
La/Sm	2.4		0.83		2.2	±1.7	

[a] Trace element composition from Shorttle and Maclennan (2011).
[b] The composition of the crust used in our modelling in Fig. 2 is ~20-30% more depleted, in terms of trace element ratios, compared to the estimated composition, with Zr/Nb = 12.5, La/Sm=1.5 and Ce/Nb=2.7.

Quantification of crustal contamination throughout the Bárðarbunga volcanic system

Following the mixing equation outlined in Sohn (2013) (see 3.3 in the supplement), we have quantitatively derived the extent of oxygen isotope exchange required to explain the observed $\delta^{18}O$ values and trace element contents (Fig. 2) in each of the BVS melt inclusion and groundmass glass. We note that the majority of the glasses and melt inclusions in the BVS require between 10-35 % of oxygen isotope exchange to explain their low-$\delta^{18}O$ character (Fig. 3a), with a main peak in the probability distribution at 20-30% (Fig. S7). The model shows that up to 55% of oxygen isotope exchange is required to explain the lowest $\delta^{18}O$ values recorded by groundmass glasses. It should be noted, however, that the extent of oxygen isotope exchange is strongly dependent on the chosen $\delta^{18}O$ composition of the assimilant, which is difficult to constrain. For example, if melts were to assimilate crust with $\delta^{18}O$ = -2 ‰, we can reproduce the lowest $\delta^{18}O$ values (~2.6‰) with 35-40% of oxygen isotope exchange.

Having constrained the extent of oxygen isotope exchange, which is commonly adopted as a proxy for amount of crustal materials assimilated, we next seek to establish where this process occurs within the Bárðarbunga magmatic system. The equilibration pressure of glasses and MIs can be estimated by applying the Olivine-Plagioclase-Augite-Melt (OPAM) barometer (Yang et al., 1996; Hartley et al., 2018). OPAM equilibration pressures for the Bárðarbunga samples are between 1-6.3 kbar (3.5-22.5 km), with ~60% of the samples being in the range 2-4 kbar (7.1-14.3 km) (Caracciolo et al., 2020; Caracciolo et al., in press). The distribution of equilibration pressures (Fig. 3a) is consistent with a multi-tiered, trans-crustal magmatic system in which melts are stored and transferred throughout interconnected stacked sills (Maclennan et al. 2019; Caracciolo et al., 2020, In press). Our data show that equilibration pressures correlate with the extent of oxygen isotope exchange (Fig. 3a). The most contaminated melts, which record the lowest $\delta^{18}O$ values (Fig. 1b) and the lowest MgO (Fig. 3a), register the lowest equilibration pressures in the range 1-2 kbar (3.5-7.1 km). Regardless of the extent of oxygen isotope exchange, the running average plotted in Fig. 3a indicates that the shallower a melt equilibrated in the crust, the higher the extent of oxygen exchange. Specifically, melts which stored and equilibrated at ~4 kbar (14.3 km), have experienced on average 15% of crustal contamination, but melts equilibrated at 1.5 kbar (5.4 km) have experienced on average 35% contamination. Therefore, we argue that as melts are transferred upwards throughout the Bárðarbunga plumbing system, their $\delta^{18}O$ becomes lower as they get more crustally-contaminated (Fig. 3b). We note that most of the oxygen isotope exchange that affects $\delta^{18}O$ values of melts supplied to the BVS occurs in the upper and middle crust, between 3.5 and 10 km. Although the scarcity of data below ~4-4.5 kbar (~14-16 km) does not allow us to provide reliable estimates of the extent of oxygen isotope exchange in the deep crust, there is evidence that lower crustal material has little effect on $\delta^{18}O$ values, due to its intrusive nature and therefore, the lack of altered, low-$\delta^{18}O$ rocks in this region of the crust (e.g. Pálmason, 1986).

This study shows that melts supplied to the BVS during the Holocene period and in recent times, have undergone different degrees of crustal assimilation that influenced their $\delta^{18}O$ character. We demonstrate that as melts ascend through the crust and approach shallow levels at around 3.5-10 km depth, they acquire lower $\delta^{18}O$ values because they assimilate more crustal material. We therefore envision the BVS as progressively assimilating multi-tiered systems in which magmas are processed through a large range of depths (3.5-22.5 km) within stacked-sills reservoirs.

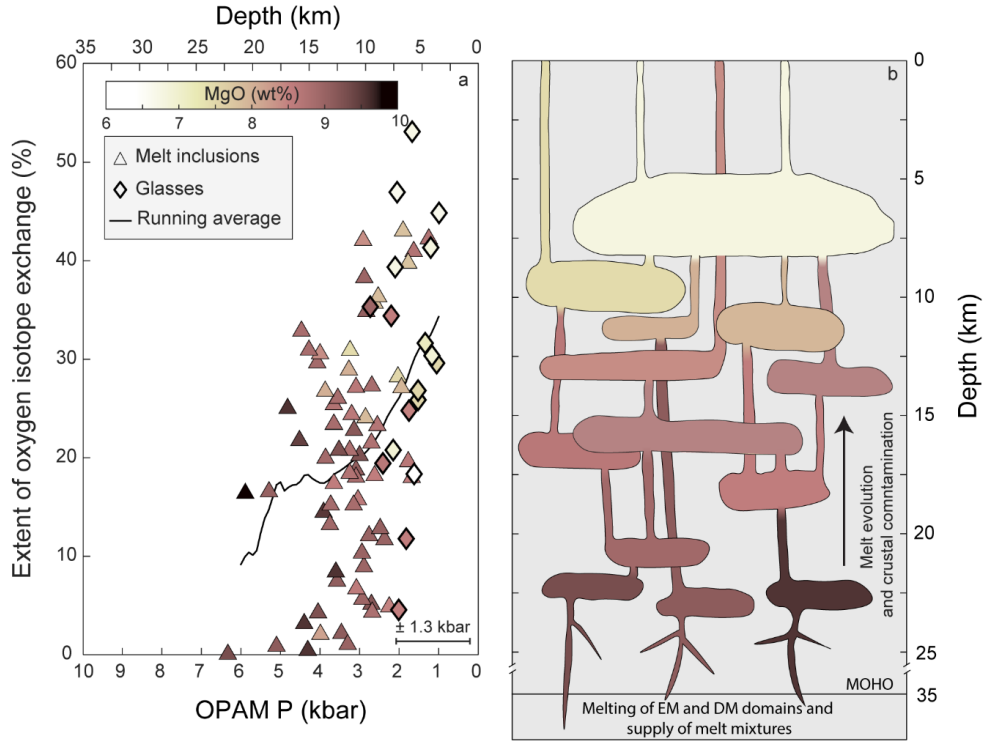

Figure 3. *a) Relationship between pressures derived by OPAM barometry for melt inclusions and groundmass glasses and the extent of oxygen isotope exchange. Symbols are coloured according to their MgO content. We only plotted samples from the Bárðarbunga volcanic system that return a probability of being three-phase saturated > 0.8 (this work, n=89). The black curve indicates the running average, calculated using a boxcar equal to the 1σ uncertainty of the OPAM barometer (1.3 kbar). b) Schematic cartoon illustrating the plumbing architecture of the Bárðarbunga volcanic system. The system is envisioned as a multi-tiered trans-crustal system in which melts are progressively assimilating crustal material as they move up towards the surface. Melt compositions evolve throughout the crustal section and the most contaminated melts are located in the upper and middle crust between 3.5-10 km depth.*

ACKNOWLEDGMENTS

This research was supported by the University of Iceland Research Fund (Nr: HI17060092). SAH acknowledges support from the Icelandic Research Fund (Grant #196139-051). We thank Kerstin Lindén for laboratory assistance in Stockholm and Robert Sohn for the help with mathematical equations.

REFERENCES

Bindeman, I., 2008, Oxygen Isotopes in Mantle and Crustal Magmas as Revealed by Single Crystal Analysis: Reviews in Mineralogy and Geochemistry, v. 69, p. 445–478, doi:10.2138/rmg.2008.69.12.

Bindeman, I., Gurenko, A., Sigmarsson, O., and Chaussidon, M., 2008, Oxygen isotope heterogeneity and disequilibria of olivine crystals in large volume Holocene basalts from Iceland: Evidence for magmatic digestion and erosion of Pleistocene hyaloclastites: Geochimica et Cosmochimica Acta, v. 72, p. 4397–4420, doi:10.1016/j.gca.2008.06.010.

Breddam, K., 2002, Kistufell: Primitive Melt from the Iceland Mantle Plume: Journal of Petrology, v. 43, p. 345–373, doi:10.1093/petrology/43.2.345.

Burnard, P., and Harrison, D., 2005, Argon isotope constraints on modification of oxygen isotopes in Iceland Basalts by surficial processes: Chemical Geology, v. 216, p. 143–156, doi:10.1016/j.chemgeo.2004.11.001.

Caracciolo, A., Bali, E., Guðfinnsson, G.H., Kahl, M., Halldórsson, S.A., Hartley, M.E., and Gunnarsson, H., 2020, Temporal evolution of magma and crystal mush storage conditions in the Bárðarbunga-Veiðivötn volcanic system, Iceland: Lithos, v. 352–353, doi:10.1016/j.lithos.2019.105234.

Caracciolo, A., Kahl, M., Bali, E., Guðfinnsson, G.H., Halldórsson, S.A., and Hartley, M.E. Timescales of crystal mush mobilization in the Bárðarbunga-Veiðivötn volcanic system based on olivine diffusion chronometry: American Mineralogist, doi:doi.org/10.2138/am-2021-7670.

Eiler, J.M., 2001, Oxygen Isotope Variations of Basaltic Lavas and Upper Mantle Rocks: Reviews in Mineralogy and Geochemistry, v. 43, p. 319–364, doi:10.2138/gsrmg.43.1.319.

Eiler, J.M., Grönvold, K., and Kitchen, N., 2000, Oxygen isotope evidence for the origin of chemical variations in lavas from Theistareykir volcano in iceland's northern volcanic zone: Earth and Planetary Science Letters, v. 184, p. 269–286, doi:10.1016/S0012-821X(00)00318-6.

Gautason, B., and Muehlenbachs, K., 1998, Oxygen isotopic fluxes associated with high-temperature processes in the rift zones of Iceland: Chemical Geology, v. 145, p. 275–286, doi:10.1016/S0009-2541(97)00148-4.

Gee, M.A.M., Thirlwall, M.F., Taylor, R.N., Lowry, D., and Murton, B.J., 1998, Crustal processes: major controls on Reykjanes Peninsula lava chemistry, SW Iceland: Journal of Petrology, v. 39, p. 819–839, doi:10.1093/petroj/39.5.819.

Genske, F.S., Beier, C., Haase, K.M., Turner, S.P., Krumm, S., and Brandl, P.A., 2013, Oxygen isotopes in the Azores islands: Crustal assimilation recorded in olivine: Geology, v. 41, p. 491–494, doi:10.1130/G33911.1.

Gurenko, A.A., and Chaussidon, M., 2002, Oxygen isotope variations in primitive tholeiites of Iceland: evidence from a SIMS study of glass inclusions, olivine phenocrysts and pillow rim glasses: Earth and Planetary Science Letters, v. 205, p. 63–79, doi:10.1016/S0012-821X(02)01005-1.

Halldórsson, S.A., Barnes, J.D., Stefánsson, A., Hilton, D.R., Hauri, E.H., and Marshall, E.W., 2016, Subducted lithosphere controls halogen enrichments in the Iceland mantle plume source: Geology, v. 44, p. 679–682, doi:10.1130/G37924.1.

Hansen, H., and Grönvold, K., 2000, Plagioclase ultraphyric basalts in Iceland : the mush of the rift: Journal of Volcanology and Geothermal Research, v. 98, p. 1–32.

Harðardóttir, S., Halldórsson, S.A., and Hilton, D.R., 2018, Spatial distribution of helium isotopes in Icelandic geothermal fluids and volcanic materials with implications for location, upwelling and evolution of the Icelandic mantle plume: Chemical Geology, v. 480, p. 12–27, doi:10.1016/j.chemgeo.2017.05.012.

Hartley, M.E., Bali, E., Maclennan, J., Neave, D.A., and Halldórsson, S.A., 2018, Melt inclusion constraints on petrogenesis of the 2014–2015 Holuhraun eruption, Iceland: Contributions to Mineralogy and Petrology, v. 173, p. 1–23, doi:10.1007/s00410-017-1435-0.

Hartley, M.E., Thordarson, T., and Fitton, J.G., 2013, Oxygen isotopes in melt inclusions and glasses from the Askja volcanic system, North Iceland: Geochimica et Cosmochimica Acta, v. 123, p. 55–73, doi:10.1016/j.gca.2013.09.008.

Hattori, K., and Muehlenbachs, K., 1982, Oxygen isotope ratios of the Icelandic crust: Journal of Geophysical Research, v. 87, p. 6559–6565, doi:10.1029/JB087iB08p06559.

Hemond, C., Condomines, M., Fourcade, S., Allègre, C.J., Oskarsson, N., and Javoy, M., 1988, Thorium, strontium and oxygen isotopic geochemistry in recent tholeiites from Iceland: crustal influence on mantle-derived magmas: Earth and Planetary Science Letters, v. 87, p. 273–285, doi:10.1016/0012-821X(88)90015-5.

Jenkins, J., Maclennan, J., Green, R.G., Cottaar, S., Deuss, A.F., and White, R.S., 2018, Crustal Formation on a Spreading Ridge Above a Mantle Plume: Receiver Function Imaging of the Icelandic Crust: Journal of Geophysical Research: Solid Earth, v. 123, p. 5190–5208, doi:10.1029/2017JB015121.

Kokfelt, T.F., Hoernle, K., Hauff, F., Fiebig, J., Werner, R., and Garbe-Schönberg, D., 2006, Combined trace element and Pb-Nd-Sr-O isotope evidence for recycled oceanic crust (upper and lower) in the Iceland mantle plume: Journal of Petrology, v. 47, p. 1705–1749, doi:10.1093/petrology/egl025.

Larsen, G., and Guðmundsson, M.T., 2014, Volcanic system : Bárðarbunga system: Catalogue of Icelandic Volcanoes, p. 1–11.

Maclennan, J., 2008, Concurrent mixing and cooling of melts under Iceland: Journal of Petrology, v. 49, p. 1931–1953, doi:10.1093/petrology/egn052.

Maclennan, J., 2019, Mafic tiers and transient mushes: evidence from Iceland: Philosophical Transactions of the Royal Society A, v. 377, p. 1–20, doi:10.1098/rsta.2018.0021.

Maclennan, J., McKenzie, D., Hilton, F., Gronvöld, K., and Shimizu, N., 2003, Geochemical variability in a single flow from northern Iceland: Journal of Geophysical Research: Solid Earth, v. 108, p. ECV 4-1-ECV 4-21, doi:10.1029/2000JB000142.

Macpherson, C.G., Hilton, D.R., Day, J.M.D., Lowry, D., and Grönvold, K., 2005, High-3He/4He, depleted mantle and low-δ 18O, recycled oceanic lithosphere in the source of central Iceland magmatism: Earth and Planetary Science Letters, v. 233, p. 411–427, doi:10.1016/j.epsl.2005.02.037.

Mattey, D., Lowry, D., and Macpherson, C., 1994, Oxygen isotope composition of mantle peridotite: Earth and Planetary Science Letters, v. 128, p. 231–241, doi:10.1016/0012-821X(94)90147-3.

Nicholson, H., Condomines, M., Fitton, J.G., Fallick, A.E., Grönvold, K., and Rogers, G., 1991, Geochemical and isotopic evidence for crustal assimilation beneath krafla, Iceland: Journal of Petrology, v. 32, p. 1005–1020, doi:10.1093/petrology/32.5.1005.

Pálmason, G., 1986, Model of crustal formation in Iceland, and application to submarine mid-ocean ridges (P. R. Vogt & B. E. Tucholke, Eds.): The Western North Atlantic Region, v. M, p. 0, doi:10.1130/DNAG-GNA-M.87.

Peate, D.W., Breddam, K., Baker, J.A., Kurz, M.D., Barker, A.K., Prestvik, T., Grassineau, N., and Skovgaard, A.C., 2010, Compositional characteristics and spatial distribution of enriched Icelandic mantle components: Journal of Petrology, v. 51, p. 1447–1475, doi:10.1093/petrology/egq025.

Skovgaard, A.C., Storey, M., Baker, J., Blusztajn, J., and Hart, S.R., 2001, Osmium-oxygen isotopic evidence for a recycled and strongly depleted component in the Iceland mantle plume: Earth and Planetary Science Letters, v. 194, p. 259–275, doi:10.1016/S0012-821X(01)00549-0.

Sohn, R.A., 2013, A method for inverting ratio-ratio data to estimate end-member compositions in mixing problems: Chemical Geology, v. 352, p. 63–69, doi:10.1016/j.chemgeo.2013.06.002.

Stracke, A., and Bourdon, B., 2009, The importance of melt extraction for tracing mantle heterogeneity: Geochimica et Cosmochimica Acta, v. 73, p. 218–238, doi:10.1016/j.gca.2008.10.015.

Stracke, A., Zindler, A., Salters, V.J.M., McKenzie, D., Janne, B.T., Albarède, F., and Grönvold, K., 2003, Theistareykir revisited: Geochemistry, Geophysics, Geosystems, v. 4, doi:10.1029/2001GC000201.

Sveinbjörnsdóttir, Á.E., Stefánsson, A., Heinemeier, J., Arnórsson, S., Eiríksdóttir, E.S., and Ólafsdóttir, R., 2020, Assessing the sources of inorganic carbon in surface-, soil-

and non-thermal groundwater in Iceland by δ13C and 14C: Geochimica et Cosmochimica Acta, v. 279, p. 165–188, doi:10.1016/j.gca.2020.03.021.

Thirlwall, M.F., Gee, M.A.M., Lowry, D., Mattey, D.P., Murton, B.J., and Taylor, R.N., 2006, Low δ 18 O in the Icelandic mantle and its origins: Evidence from Reykjanes Ridge and Icelandic lavas: Geochimica et Cosmochimica Acta, v. 70, p. 993–1019, doi:10.1016/j.gca.2005.09.008.

Thirlwall, M.F., Gee, M.A.M., Taylor, R.N., and Murton, B.J., 2004, Mantle components in Iceland and adjacent ridges investigated using double-spike Pb isotope ratios: Geochimica et Cosmochimica Acta, v. 68, p. 361–386, doi:10.1016/S0016-7037(03)00424-1.

Yang, H.-J., Kinzler, R.J., and Grove, T.L., 1996, Experiments and models of anhydrous, basaltic olivine-plagioclase-augite saturated melts from 0.001 to 10 kbar: Contributions to Mineralogy and Petrology, v. 124, p. 1–18, doi:10.1007/s004100050169.

11.1 Supplementary information and figures attached to paper III

1. GEOLOGICAL SETTING AND SAMPLE PREPARATIONS

Samples used in this study are from a subglacial to Holocene magmatic suite which has been previously studied by Caracciolo et al. (2020a) and Caracciolo et al. (in press). In addition, we include new oxygen isotope data of samples from the 2014-15 Holuhraun eruption, which in terms of major and trace elements were characterized by Hartley et al. (2018). All magmatic units are located in the Bárðarbunga volcanic system (BVS), the most extensive volcanic system of Iceland. This system is situated in central Iceland, in the Eastern Rift Zone (ERZ) (red triangles, Fig. S1) Samples consist of fresh scoria and lavas and we guide the reader to Caracciolo et al. (2020) for further information on the units and on the geology of the area. In the discussion, we also include a set of subglacial glasses from Iceland's rift zones for which oxygen isotope and trace element data have been acquired (grey symbols, Fig. S1). See Excel table S1, S2 and S3 attached to the thesis for more information about the dataset.

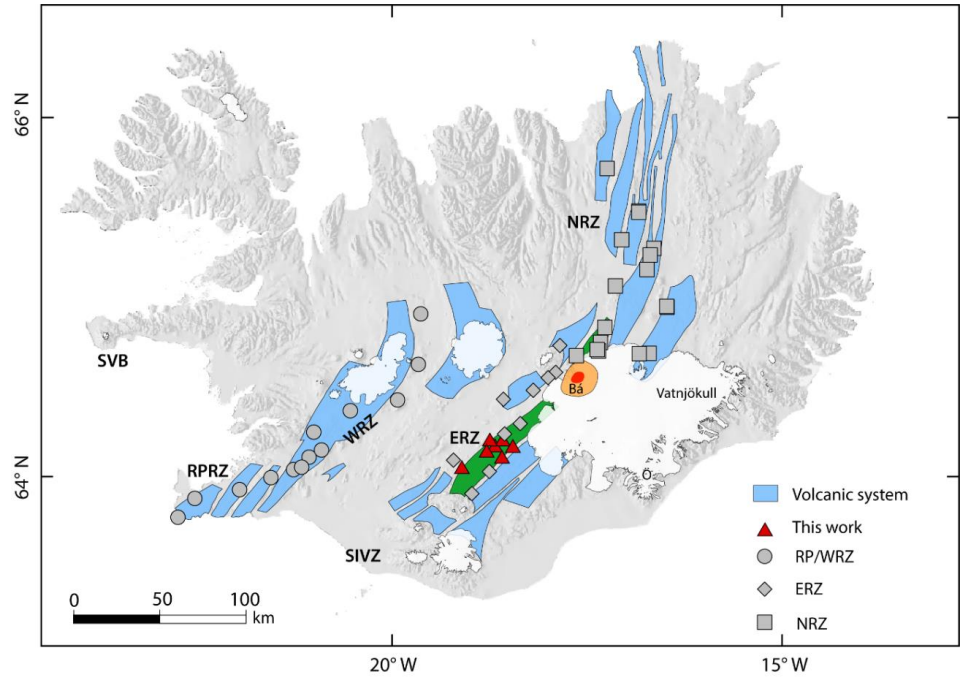

Figure S1. *Map of Iceland showing the location of samples used in this study from the Bárðarbunga volcanic system (red symbols). Samples from the subglacial glass dataset are indicated with grey symbols. RPRZ: Reykjanes Peninsula Rift Zone; WRZ: Western Rift Zone; SIVZ: South Iceland Volcanic Zone; ERZ: Eastern Rift Zone; NRZ: Northern Rift Zone; SVB: Snæfellsnes Volcanic Belt. The Bárðarbunga volcanic system is indicated in green and the location of the Bárðarbunga central volcano is shown in orange.*

We hand-picked glass, plagioclase and olivine crystals from crushed scoria and we selected crystals containing melt inclusions (MIs). Chosen crystals were mounted in epoxy resin and polished to expose MIs (Fig. S2). In most of the localities, olivine crystals contain large (up to 150 µm in size) and naturally quenched MIs (n=102) (Fig. S2). Crystals containing devitrified MIs (n=63) were homogenized in a high-temperature furnace (see Caracciolo et al. 2020).

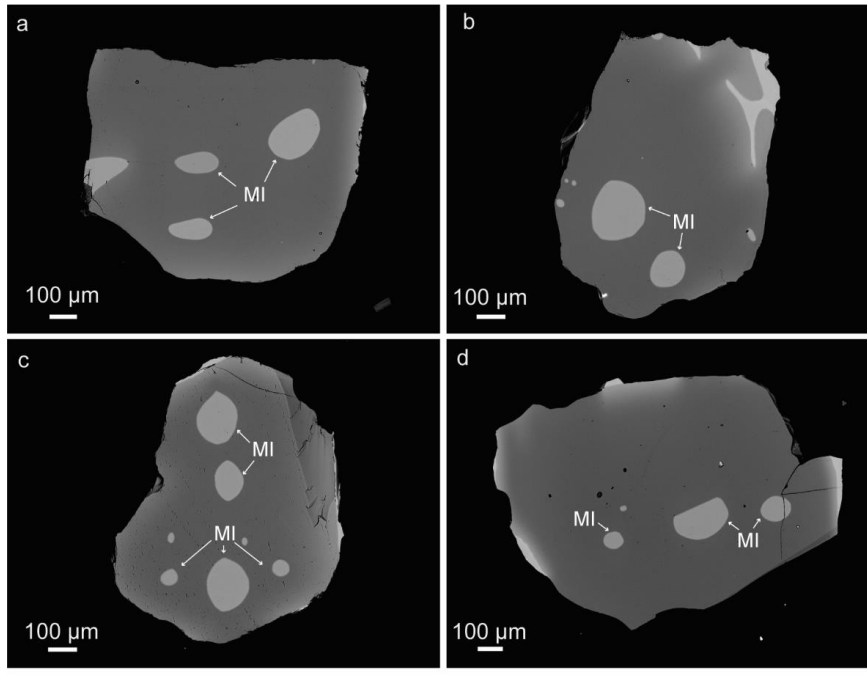

Figure S2. *Backscattered electron (BSE) images of olivine crystals with melt inclusions from early-Holocene magmatic units. Large and naturally quenched melt inclusions are widespread in these magmatic units. MI: melt inclusion.*

2. ANALYTICAL METHODS

We carried out trace element and $\delta^{18}O$ measurements on MIs hosted in olivine (n=46) and plagioclase (n=117) crystals using Secondary Ion Mass Spectrometry (SIMS). Additionally, we analyzed groundmass glass chips (n=30). We prepared four resin mounts with MI-bearing crystals and groundmass glasses from the different magmatic units. When feasible, multiple analyses of trace elements and isotopes were carried out within the same MI (Fig. S3). Small melt inclusions required fine polishing between trace element and $\delta^{18}O$ analysis sessions to remove the SIMS ablation pit. Groundmass glass chips from same localities were also analysed by laser fluorination to provide an external test of the SIMS analyses. The full dataset is presented in the supplementary excel table(S1-S2).

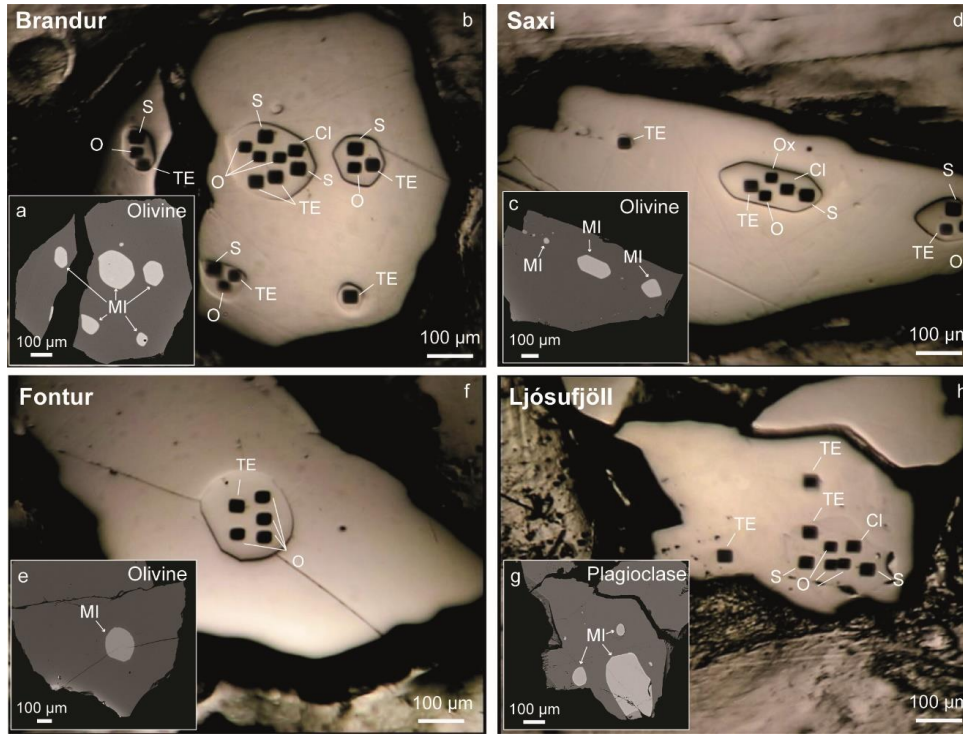

Figure S3. *Backscattered electron (BSE) images of crystals containing melt inclusions (a,c,e,g) and images of the same crystal taken using the microscope with reflected light after SIMS analyses (b,d,f,h). Black rectangles inside the melt inclusions are SIMS craters for different analyses. Note that given the large dimensions of MIs, it has been possible to measure oxygen (O), sulphur (S) and chlorine (Cl) isotopes along with trace elements (TE) within the same melt inclusion. MI: melt inclusion. Chlorine and sulphur isotope analyses are not presented in this work.*

2.1 Secondary-Ion Mass Spectrometry (SIMS) analyses

2.1.1 Trace elements

The trace elements Ni, Sr, Y, Zr, Nb, La, Ce, Nd, Sm, Eu, Gd, Dy, Er, and Yb were measured in melt inclusions using a CAMECA IMS1280 SIMS instrument at the NordSIM facility, Swedish Museum of Natural History, Stockholm. An Oregon Physics H201 Hyperion RF Plasma source attached to the IMS1280 was used to generate a critically focussed 6 nA O^{2-} oxygen beam, which was used to sputter melt inclusions with an impact energy of 23 kV (-13 kV primary, + 10 kV secondary). Following removal of the 30 nm Au coating over a 25 x 25 µm rastered area, the analytical beam was set to a 5 x 5 µm raster to homogenise the Gaussian focussed beam and the secondary ion beam centered in the field aperture (field of view 18 µm at high transmission mode), optimised for maximum energy in the 22 eV energy slit, and the mass using the SiO_2^+ species at nominal 60 Da. Potential molecular interferences on species of interest were filtered out using a combination of a high mass resolution (M/ΔM) of 10000 (common to all species measured) and, where needed, moderate amounts of energy filtering. The peak hopping

data acquisition sequence comprised six cycles through the following species (energy offset if applied and integration time in parentheses): $^{48}Ti^{+}$ (-25 eV, 2 s), $^{60}Ni^{+}$ (4 s), $^{28}Si^{16}O_2^{+}$ (1 s), $^{88}Sr^{+}$ (-25 eV, 4 s) , $^{89}Y^{+}$ (-25 eV, 4 s) , $^{90}Zr^{+}$ (-25 eV, 4 s), $^{93}Nb^{+}$ (-45 eV, 6 s), $^{139}La^{+}$ (-25 eV, 4 s), $^{140}Ce^{+}$ (-25 eV, 4 s), $^{143}Nd^{+}$ (-25 eV, 4 s), $^{149}Sm^{+}$ (-25 eV, 4 s), $^{153}Eu^{+}$ (-25 eV, 4 s), $^{157}Gd^{+}$ (-25 eV, 4 s), $^{163}Dy^{+}$ (-25 eV, 4 s), $^{166}Er^{+}$ (-45 eV, 6 s), $^{173}Yb^{+}$ (-45 eV, 6 s), the total integration time being ca. 500 s. All species were detected in a low noise ion-counting electron multiplier. Several measurements were performed during the session on each of the reference materials ATHO-G (n = 5), GOR-128G (n = 5), GOR-132G (n = 4), KL2-G (n = 2), ML3B-G (n = 3), StHs6/80-G (n = 5) and T1-G (n = 3) and the measured $M^{+}/^{28}Si^{16}O_2^{+}$ ratios converted to raw concentration assuming the values given by Jochum et al. (2005). Selecting ML3B-G for the primary calibration as it is closest in SiO_2 content to the target melt inclusions, the averages of the measured $M^{+}/^{28}Si^{16}O_2^{+}$ ratios from the reference materials define a negative linear correlation with increasing SiO_2, which was used to define a second-order relative sensitivity factor correction of ca. -0.02 per wt. % SiO_2, which was applied to all raw concentrations using the EPMA-determined SiO_2. Uncertainties in concentration (Table S1) were estimated using the within-run uncertainty on $M^{+}/^{28}Si^{16}O_2^{+}$, which is highly dependent on analyte concentration, propagated together with the primary reference material repeatability.

Table S1. *Uncertainties in trace element concentrations*

Element	Uncertainty	1σ
	%	%
TiO_2	5.9	1.4
Ni	1.5	1.2
Sr	3.5	0.9
Y	4.6	2.0
Zr	3.9	1.9
Nb	5.6	1.8
La	4.5	2.0
Ce	3.8	2.2
Nd	6.5	2.4
Sm	9.2	2.4
Eu	8.1	1.6
Gd	8.3	2.4
Dy	8.0	1.9
Er	16.1	2.4
Yb	15.2	3.6

2.1.2 Oxygen isotopes

Oxygen isotope analyses were performed in five separate analytical sessions using a CAMECA IMS1280 large geometry SIMS at the NordSIM facility in Stockholm, Sweden. In all sessions, a critically focused Cs^{+} primary beam with 20 keV impact was used to sputter the sample, and a low-energy electron flooding gun was used for charge compensation. The primary beam current was ca. 2.5 – 3 nA, which yielded ca. 15 µm analytical spots, including a 10 µm raster to homogenize the beam. Each analysis consisted of an initial pre-sputter over a rastered 20 µm area to remove the gold coating, followed by centering of the secondary beam in the field aperture (field of view on the sample of 30 µm with 90x magnification transmission ion optics). The ^{16}O (ca. 3 x 109 cps) and ^{18}O ion beams were mass filtered at a mass resolution of ca. 2500 ($M/\Delta M$) and analysed simultaneously using two Faraday detectors with amplifiers housed in an evacuated, temperature stabilized chamber. The secondary magnet field was locked at high stability using an NMR field sensor operating in regulation mode. All pre-sputter, beam centering and data acquisition steps were automated in the run definition. Typical internal precision obtained for individual run $^{18}O/^{16}O$ ratios determined from 12 4-second integrations was ca. 0.15 ‰ (SE). The oxygen isotopic values presented in this study are reported relative to VSMOW (Vienna Standard Mean Ocean Water) in standard delta notation (δ) following this equation:

$$\delta^{18}O = \left(\frac{\left(\frac{^{18}O}{^{16}O}\right)_{sample}}{\left(\frac{^{18}O}{^{16}O}\right)_{standard}} - 1 \right) \times 1000 \quad \text{(Eq. 1)}$$

Fully automated sequences comprised regular measurements of the reference materials, bracketing measurements of unknown targets. Reference materials were mounted alongside the unknown samples (Bárðarbunga melt inclusions and glasses). Chosen standards consist of a set of natural glasses (STAP-1, A35, StHs6/80-G) spanning a compositional range between basalt and andesite (Excel table S5). Their major element and $\delta^{18}O$ compositions are given in Table S2. All standard repetitions are reported in Figure S4c. In the majority of the cases, multiple oxygen isotope analyses were carried out within the same MI and groundmass chip. See excel table S4 for individual $\delta^{18}O$ analyses. External precision on $\delta^{18}O$ was <0.17 ‰ (1SD). Error bars reported in the figures refer to the standard error of the mean at 1σ level. Instrumental drift was monitored through the session and it was negligible.

***Table S2**. Composition of the standards used in this study for oxygen isotope analyses. Variation at 1σ level is given in parentheses.*

Sample	SiO_2	TiO_2	Al_2O_3	*FeO*	*MnO*	MgO	CaO	Na_2O	K_2O	P_2O_5	Total	$\delta^{18}O^b$
A35	49.56 (0.26)	1.64 (0.03)	13.97 (0.08)	12.40 (0.12)	0.21 (0.02)	7.01 (0.07)	12.07 (0.17)	2.31 (0.06)	0.19 (0.01)	0.15 (0.02)	99.80	3.88
(n=20)												
STAP-1	48.29 (0.17)	1.75 (0.03)	15.27 (0.11)	11.00 (0.07)	0.19 (0.02)	8.22 (0.05)	12.54 (0.08)	2.02 (0.05)	0.27 (0.01)	0.21 (0.02)	99.91	4.66
(n=15)												
StHs6/80-G[a]	63.70 (0.50)	2.56 (0.02)	17.80 (0.20)	4.37 (0.07)	0.08 (0.004)	1.97 (0.04)	5.28 (0.09)	4.44 (0.14)	1.29 (0.02)	0.16 (0.02)	99.79	6.12

[a] *From Jochum et al. (2005)*

[b] *Laser fluorination data (in ‰). See table S3.*

Instrumental mass fractionation (IMF) was corrected following the procedure described in Hartley et al. (2012). For each session, a linear regression of IMF vs SiO_2 was used to correct for matrix effects (Fig. S4a-d). Since the variation of SiO2 in our melt inclusions and glasses is very narrow (48-52 wt%), the IMF correction was very small, on average 0.10 ± 0.11 ‰ (1σ).

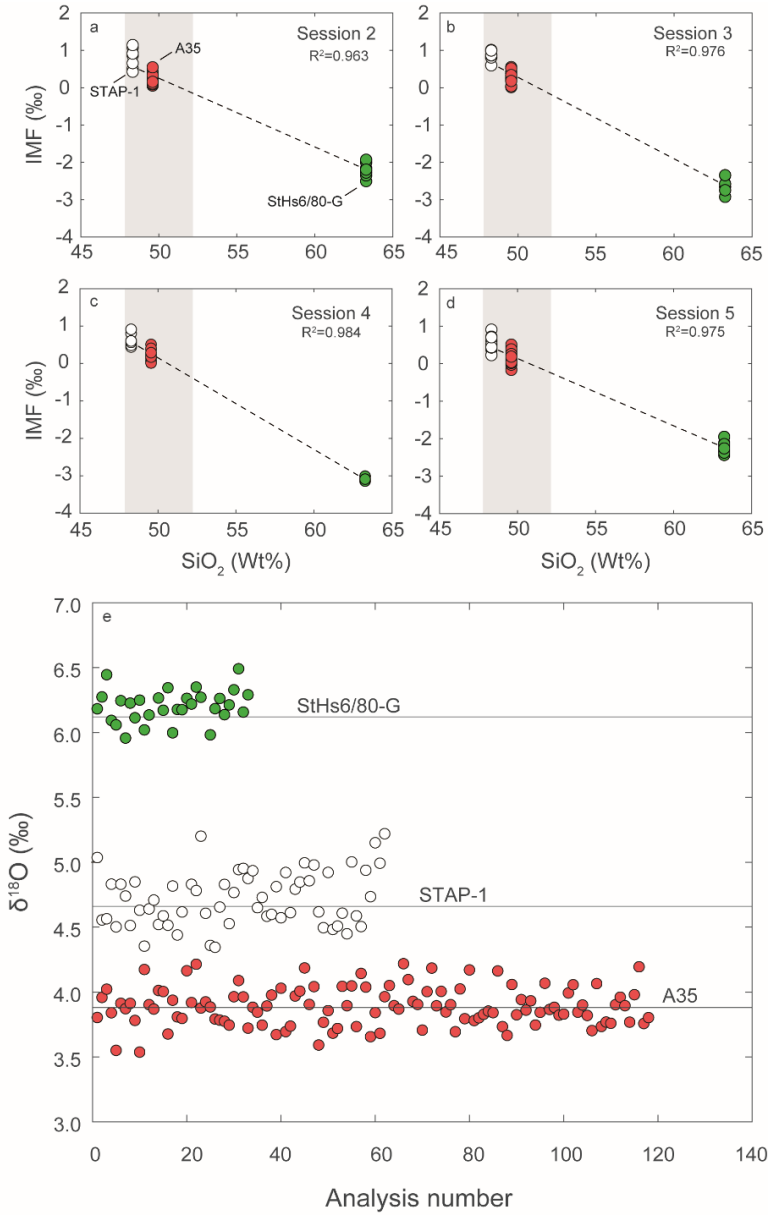

Figure S4. *Instrumental mass fractionation (a-d) and primary and secondary standard measurements (e). (a-d) Correlations between measured IMF vs SiO_2 of standards during each session. These correlations have been used to generate correction schemes to correct the instrumental mass fractionation for compositional matrix effects (Hartley et al., 2012). The grey area indicates the compositional range of the Bárðarbunga melt inclusions and groundmass glasses analysed in this work. (e) SiO_2-corrected $\delta^{18}O$ values for the primary (A35) and secondary standards (STAP-1 and* StHs6/80-G*) measured during all sessions. Straight lines indicate the accepted values for those standards.* StHs6/80-G *$\delta^{18}O$ accepted value (6.12 ± 0.07 ‰) is from Jochum et al. (2006). STAP-1 (4.66 ± 0.15 ‰) and A35 (3.88 ± 0.05 ‰) $\delta^{18}O$ have been constrained by laser fluorination methods in this work.*

2.1.3 Laser fluorination (LF)

Oxygen isotope analyses were conducted at the University of Texas at Austin on a ThermoElectron MAT 253 mass spectrometer using the laser fluorination method of Sharp (1990). Glass chips were crushed, rinsed in deionized water, and hand-picked under a binocular microscope to ensure sample homogeneity (e.g., free of alteration and crystals). Approximately 2.0 mg of material was used per analysis. Garnet standard UWG-2 ($\delta^{18}O$ = +5.8‰; Valley et al., 1995) and in-house quartz standard Lausanne-1 ($\delta^{18}O$ = +18.1‰) were analyzed along with samples to ensure precision and accuracy. $\delta^{18}O$ values are reported relative to SMOW. Precision is < ± 0.1‰ (1SD) based on long-term reproducibility of standards. In-run standards had a precision of ± 0.04‰ (1SD). LF analyses were carried out on standards (A35 and STAP-1) employed in the SIMS analyses and on picked groundmass glasses from the Bárðarbunga-Veiðivötn volcanic system (Table S3 and Fig. S4).

Table S3. *Comparison of $\delta^{18}O$ values obtained by SIMS and LF methods for the standards employed in SIMS analyses. We also report SIMS and LF data measured on groundmass glasses from the Bárðarbunga magmatic suite (see Fig. S5). The number of analyses is given in parentheses. $\delta^{18}O$ and 1σ are in ‰.*

Sample	$\delta^{18}O$ *LF*	1σ *LF*	$\delta^{18}O$ *SIMS*	1σ *SIMS*
	Standards			
A35	3.88	0.05 (n=4)	3.89	0.15 (n=118)
STAP-1	4.66	0.15 (n=11)	4.71	0.22 (n=62)
StHs6/80-G	6.12[a]	0.07[a]	6.20	0.12 (n=31)
	Bárðarbunga-Veiðivötn glasses[b]			
Ljósufjöll	4.11[c]	-	4.73	0.56 (n=5)
Brandur	4.01[c]	-	4.46	0.13 (n=3)
Fontur	3.91[c]	-	3.71	0.05 (n=3)
Saxi	4.21[c]	-	3.94	0.02 (n=2)
Drekahraun	4.12[c]	-	4.00	0.10 (n=4)
Veiðivötn 1477	3.70[c]	-	3.10	0.08 (n=6)

[a] Data for StHd6/80-G are from Jochum et al. (2006)

[b] See Caracciolo et al. (2020) for further information on these magmatic units

[c] one single analysis

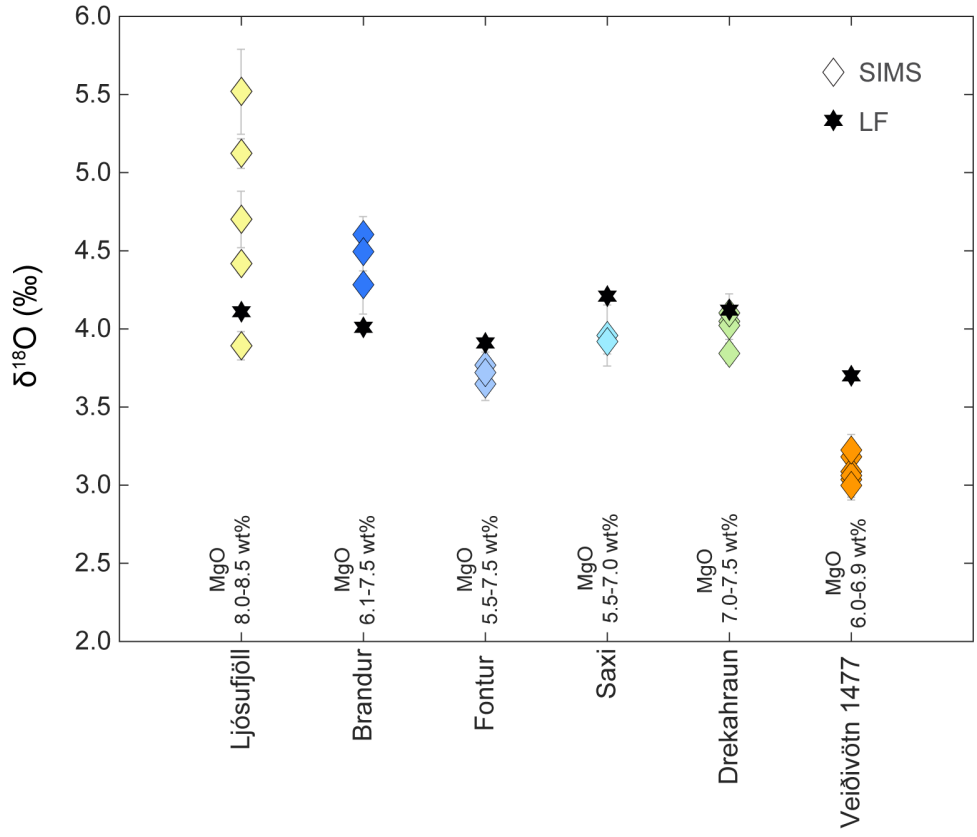

Fig. S5. *Comparison of $\delta^{18}O$ values measured by SIMS and by LF for groundmass glasses from the Bárðarbunga sample set. SIMS data have been corrected for instrumental mass fractionation following the method described by Hartley et al. (2012). We have carried out one LF repetition for each sampling locality. The largest difference between LF and SIMS analyses is observed for Ljósufjöll and Veiðivötn 1477 samples. Four out of five SIMS data points on Ljósufjöll glass are higher than the LF data. However, SIMS data show a large variability of $\delta^{18}O$ values in Ljósufjöll glass, of about 1.5‰. This could be indicative of $\delta^{18}O$ heterogeneities in glassy fragments from Ljósufjöll samples that will be further investigated with multiple LF bulk analyses. For all other studied samples, LF analyses reproduced the SIMS data within uncertainty. This external test of the SIMS analyses reinforces the confidence in the SIMS analytical technique and data correction procedure. See Caracciolo et al. (2020) for further details regarding the individual eruptive units. Error bars indicate the standard error of the mean at 1σ level.*

3. BINARY MIXING AND ASSIMILATION MODELLING

3.1 Definition of the end members

We modelled the distribution of the data in the trace element – $\delta^{18}O$ space assuming the existence of two chemically and isotopically different mantle components, along with a crustal component. The components were defined as followed:

- **Depleted mantle (DM).** The depleted mantle component is most likely not recorded by our dataset. The most depleted melts sampled by our dataset have Zr/Nb ~16, a value that is far away from the most depleted melts (Zr/Nb ~30-40) recorded for Icelandic samples (Thirlwall et al., 2004; Shorttle and Maclennan, 2011). Shorttle and Maclennan (2011) have estimated depleted endmember compositions for the NRZ and WRZ. We combined and averaged those compositions to estimate the trace element content of the depleted component to use in our modelling. The resulting depleted composition has Zr/Nb =26.2 (Table 1). In terms of oxygen isotopes, the three most 18O-enriched melt inclusions have δ18O in the range 5.7-6.3‰, with an average δ18O value of 5.9 ‰. These high-δ18O values have been reported for fresh basalts from Iceland (Hemond et al., 1993; Harmon and Hoefs, 1995). In our modelling we selected a δ18ODM value of 5.9 ‰, in agreement with the highest values estimated for fresh MORB glasses (5.5 to 5.9‰).

- **Enriched mantle (EM).** The presence of a low-δ18O, chemically enriched component in the sub-Iceland mantle has been demonstrated by isotopic studies on lavas from different parts of Iceland (Skovgaard et al., 2001; Macpherson et al., 2005; Kokfelt et al., 2006; Thirlwall et al., 2006; Winpenny and Maclennan, 2014). Here, we assume that the mantle underneath the Bárðarbunga volcanic system has the same geochemical features as observed elsewhere in Iceland. We calculated the composition of the enriched component by averaging primitive (MgO>8.0 wt%) glasses (n=1) and melt inclusions (n=3) with the most enriched trace element characteristics (Fig. 2a). The resulting composition has δ18O = +4.5‰ and Zr/Nb = 6.9. Melts defining the enriched component are from the RP/WRZ (Halldórsson et al., 2016) and ERZ (this work). The $\delta^{18}O$ composition of the enriched melt component calculated in this work is within the range of the estimated 4.5-4.8 ‰ in the literature (Breddam, 2002; Maclennan et al., 2003; Burnard and Harrison, 2005; Macpherson et al., 2005), and its trace element composition is in good agreement with the enriched compositions calculated by Shorttle and Maclennan (2011).

- **The crust.** A great uncertainty in our modelling arises from the determination of the chemical composition of the contaminant, namely the Icelandic crust. Two different contaminants are commonly invoked when assimilating low-δ18O crust: 1) rhyolitic melts, thought to originate by partial melting of hydrothermally altered basaltic crust; 2) altered basaltic rocks, with a low δ18O character. For primitive basalt and, in our case, primitive melt compositions, assimilation of basaltic crust is more likely to take place, as assimilation of rhyolitic melts would significantly skew the major and trace element compositions of the crystallizing melts.
  Due to its location at high latitudes, Iceland receives precipitation that is strongly depleted in 18O(Sveinbjörnsdóttir et al., 2020). Surface waters easily penetrate into

the crust, causing hydrothermal alteration of crustal rocks by low-δ18O fluids that ultimately deplete the 18O of the crust relative to the mantle (Gautason and Muehlenbachs, 1998). Magmas rising through the Icelandic crust assimilate crustal rocks, inheriting their 18O-depleted character. Hattori and Muehlenbachs (1982) studied drill cuttings from the uppermost 3 km of the Icelandic crust and showed that crustal rocks at active geothermal sites exhibit a large range of δ18O values, from +6 ‰ to -11‰. Although the δ18O of the contaminant likely depends upon where in the crust assimilation occurs, for our modelling we assumed that the crust has a δ18O value of 0‰. We selected this value because it agrees with field observations (Hattori and Muehlenbachs, 1982), and is thought to be representative of significant portions of the Icelandic crust (Eiler et al., 2000; Skovgaard et al., 2001; Macpherson et al., 2005; Bindeman et al., 2008), although it is somewhat lower than the most contaminated melts recorded in our dataset (+2.5‰).

The trace element composition of the crust is more challenging to constrain. Its composition is likely to be highly variable in space and time, with different sections of the crust having different compositions and therefore different influence on the contamination process. In our modelling, we neglected the silicic portion of the Icelandic crust, given that silicic rocks make up less than 10% of the crust, with basaltic and intermediate rocks accounting for about 90% of the volume (Jónasson, 2007; Jakobsson et al., 2008). In order to calculate a robust mean crustal composition, we gathered whole-rock data of basaltic rocks for which major and trace elements are available from the IVID database (Harðardóttir et al., 2018). This database compiles a large collection of isotopic ratios, along with major and trace elements, measured in Icelandic volcanic rocks. We rejected compositions with MgO <2 wt% and >13wt %, and we selected rocks with SiO2<53 wt%. Depending on the trace element under consideration, we averaged from 400 to 700 compositions from whole-rock analyses of Tertiary rocks and from Iceland's neovolcanic zones. The estimated mean trace element composition of the Icelandic crust is given in Table 1, along with its standard deviation. The standard deviation highlights the natural trace element compositional variation of Icelandic rocks. A variation in Zr of 118 ± 62 and Nb of 12.3 ± 6.8 ppm results in a propagated variability in Zr/Nb of 9.5 ± 7.2. However, in order to reproduce the compositional variation described by our data in Fig. 2, we require a crust that, with respect to trace element ratios, is about 20-30 % more depleted than the estimated composition reported in Table 1. The required composition, which lies well within the uncertainty of the estimated mean composition, has Zr/Nb = 12.5, Ce/Nb = 2.8 and La/Sm = 1.5. This difference might arise from the fact that most of the extrusives erupted at the surface represent rocks residing in the uppermost crust, which are likely to be more more enriched in incompatible trace elements compared to mid-crustal rocks, where most of the contamination is likely to occur. Therefore, it is reasonable that the required crustal contaminant composition is slightly more depleted than the bulk mean composition of the Icelandic upper crust.

3.2 Assimilation fractional crystallization (AFC) modelling

In Fig. S6 we plot AFC modelling curves with the goal to demonstrate that primitive melts with the most enriched character are inconsistent with contamination during fractional crystallization of a single parental melt with a depleted, MORB-like

composition. Therefore, with this section, we want to prove that the assumption on the existence of an isotopically light, enriched endmember is consistent with our observations.
The AFC modelling is based upon the equations of DePaolo (1981). Input parameters are the concentration of a certain element and of $\delta^{18}O$ in the magma and in the contaminant, the mass of magma remaining with respect to the initial mass of magma (F), the bulk partition coefficient (D) for each element, the oxygen isotope fractionation factor (Δ) and the ratio of mass assimilation rate to fractional crystallization rate (r). Partition coefficients between minerals and melt are from White (2013) and O'Neill and Jenner (2012). We calculated the bulk partition coefficient assuming a phase assemblage made of 55% clinopyroxene, 39% plagioclase and 6% olivine crystals. The proportions of crystallizing phases were estimated by modelling forward crystallization with Petrolog3 (Danyushevsky and Plechov, 2011), using a primitive melt inclusion as a starting composition. Despite oxygen isotope fractionation between crystallizing phases and magma being small at magmatic temperatures (Eiler, 2001; Bindeman, 2008), we evaluated $\Delta_{min\text{-}melt}$ by employing the SiO_2-dependent linear relationship of Bindeman et al. (2004). We calculated Δ for clinopyroxene-, olivine- and plagioclase-melt for all analysed MIs and groundmass glasses. Afterwards, we averaged each $\Delta_{min\text{-}melt}$ and we calculated the weighted average of each $\Delta_{min\text{-}melt}$ using the same mineral assemblage outlined above, obtaining $\Delta_{min\text{-}melt}$ =0.2‰.

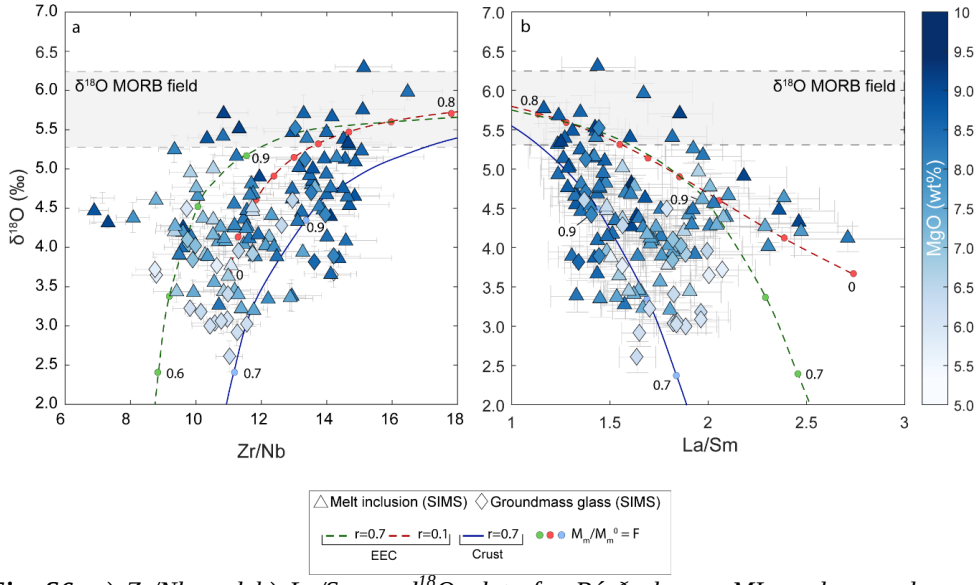

***Fig. S6**. a) Zr/Nb and b) La/Sm vs $d^{18}O$ plots for Bárðarbunga MIs and groundmass glasses. Samples are coloured according to their MgO content. Glasses with enriched compositions (La/Sm>2.2) have MgO contents above 8.0 wt% and their $\delta^{18}O$ is lower than MORB. MIs and glasses with low $\delta^{18}O$ (and low MgO) contents record intermediate La/Sm ratios, between 1.5-2. AFC modelling curves are calculated between a DM component and two different assimilant compositions. Solid curves: AFC model (r=0.7) calculated using the composition of the assimilant (Crust) reported in Table 1. Dashed curves: AFC models (r=0.1 and 0.7) calculated assuming an extremely enriched composition (EEC, see main text). Circles represent fractions of liquid remaining (F) at intervals of 0.1; some circles are labelled with the value of F. None of the modelling curves is able to reproduce the most enriched compositions recorded by our dataset.*

AFC curves were calculated at r=0.1 and r=0.7 using DM melt composition as initial composition (see Section 3.1). We have accounted for two different compositions of the crust: (1) The composition of the crust listed in Table 1 and described in Section 3.1 (solid line in Fig. S6b); (2) An extremely enriched composition (EEC), derived by averaging the most enriched (Nb>30) whole-rock analyses (n=12) found in the IVID database (Harðardóttir et al., 2018). The calculated enriched crustal composition contains 36 ppm Nb and 298 ppm Zr (La=28, Sm=11). We do not believe that this extremely enriched crustal composition is representative of any significant portion of the Icelandic crust. In fact, it is far beyond the composition of the crust estimated in Table 1. However, even assuming that an extremely enriched basalt undergoes contamination with an enriched assimilant, we are not able to reproduce the most enriched primitive melts recorded by our dataset. Therefore, we can confidently rule out that crystallization and assimilation could be responsible for the primitive, incompatible trace element-enriched, low-$\delta^{18}O$ melts observed in Fig. 2 and S6.

3.3 Binary mixing modelling

We have modelled the extent of oxygen isotope exchange between mantle-derived melts and low-$\delta^{18}O$ crust by binary mixing processes to explain the broad variation of $\delta^{18}O$ values in melt inclusions and groundmass glasses and the role of the crust in magma evolution. In addition to new MI and glass data (see supplementary excel spreadsheet), we have included glass data from other volcanic systems along Iceland's active rift zones. This dataset consists of a set of well-characterized subglacial glasses from the RP/WRZ, ERZ and NRZ (Macpherson et al., 2005; Halldórsson et al., 2016). These glasses have $\delta^{18}O$ values between +3.3‰ and +5.3‰. We refer the reader to the supplementary table for detailed information on the dataset.

We calculated binary mixing models between pairs of endmembers (EM, DM and the crust) for different trace element ratios (Fig. 2). We also tested the effect of different degrees of partial melting of the two mantle components, assuming 15% of partial melting of the depleted component and 5 % of the enriched component (Fig. 1b).

For each data point falling inside the envelope defined by the binary mixing trends, we have estimated the relative contributions of the three endmembers with the goal to quantify the contribution of the crust to the measured $\delta^{18}O$. To do this, we have used the ratio-ratio mixing equation from Sohn (2013):

$$\sum_{q=1}^{n} \phi_q a_q^j \left(x^j - X_q^j\right) = 0 \quad (Eq.2)$$

where X_q^j is the composition of the endmember q for the ratio j, a_q^j is the concentration of the denominator of ratio j in the endmember q, ϕ_q is the mixing proportion of endmember i and x^j is the composition of the mixture (sample) for ratio j.

In our ternary system, conservation of the mass requires that:

$$\phi_{DM} + \phi_{EM} + \phi_C = 1 \quad (Eq.3)$$

where ϕ_{DM}, ϕ_{EM} and ϕ_C are the proportions of the depleted endmember (DM), enriched endmember (EM) and the crust (C), respectively. Solving Eq. 2 for $\delta^{18}O$ and trace element ratios (e.g. Zr/Nb) we obtain:

$$\phi_{DM}\left(x^{\delta^{18}O} - X_{DM}^{\delta^{18}O}\right) + \phi_{EM}\left(x^{\delta^{18}O} - X_{EM}^{\delta^{18}O}\right) + \phi_C\left(x^{\delta^{18}O} - X_C^{\delta^{18}O}\right) = 0 \quad (Eq.4)$$

$$\phi_{DM} a_{DM}^{Nb}(x^{Zr/Nb} - X_{DM}^{Zr/Nb}) + \phi_{EM} a_{EM}^{Nb}(x^{Zr/Nb} - X_{EM}^{Zr/Nb}) + \phi_C a_C^{Nb}(x^{Zr/Nb} - X_C^{Zr/Nb}) = 0 \quad (Eq.5)$$

The percentage of the three components ϕ in each sample can be quantitatively calculated by solving the three-by-three system (eq. 3, 4 and 5).

We have calculated the extent of oxygen isotope exchange for different trace element ratios (Zr/Nb, La/Sm and Ce/Nb) (Fig. S7). Our modelling shows that the majority of the glasses and melt inclusions require between 20 and 30 % of oxygen isotope exchange before being erupted at the surface. Furthermore, up to 50% exchange is needed to explain the lowest $\delta^{18}O$ values recorded by some groundmass glasses from the ERZ. The extent of oxygen isotope exchange is commonly linked to the amount of crustal contamination. However, this quantification is strongly influenced by the chosen $\delta^{18}O$ value of the crust (Fig. S7). A crust with $\delta^{18}O$ of -2‰ would yield maximum crustal assimilation estimates of 35-40%. Previous studies have estimated up to 50% of assimilation for the Askja volcanic system (Hartley et al., 2013) and ~30-35% assimilation for the Laki volcanic system (Bindeman et al., 2006).

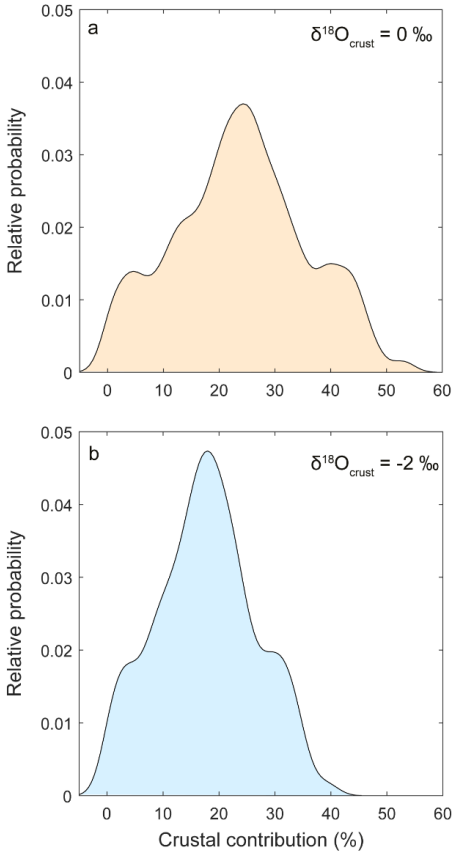

Fig. S7. *Kernel density estimate (KDE) distributions, with bandwidth of 2, showing the relative probability of crustal contamination percentages assuming a crust with a)* $\delta^{18}O$ = 0‰ and b) $\delta^{18}O$ = -2 ‰.

Supplementary references

Bindeman, I., 2008, Oxygen Isotopes in Mantle and Crustal Magmas as Revealed by Single Crystal Analysis: Reviews in Mineralogy and Geochemistry, v. 69, p. 445–478, doi:10.2138/rmg.2008.69.12.

Bindeman, I., Gurenko, A., Sigmarsson, O., and Chaussidon, M., 2008, Oxygen isotope heterogeneity and disequilibria of olivine crystals in large volume Holocene basalts from Iceland: Evidence for magmatic digestion and erosion of Pleistocene hyaloclastites: Geochimica et Cosmochimica Acta, v. 72, p. 4397–4420, doi:10.1016/j.gca.2008.06.010.

Bindeman, I.N., Ponomareva, V. V., Bailey, J.C., and Valley, J.W., 2004, Volcanic arc of Kamchatka: A province with high-δ18O magma sources and large-scale 18O/16O depletion of the upper crust: Geochimica et Cosmochimica Acta, v. 68, p. 841–865, doi:10.1016/j.gca.2003.07.009.

Bindeman, I.N., Sigmarsson, O., and Eiler, J., 2006, Time constraints on the origin of large volume basalts derived from O-isotope and trace element mineral zoning and U-series disequilibria in the Laki and Grímsvötn volcanic system: Earth and Planetary Science Letters, v. 245, p. 245–259, doi:10.1016/j.epsl.2006.02.029.

Breddam, K., 2002, Kistufell: Primitive Melt from the Iceland Mantle Plume: Journal of Petrology, v. 43, p. 345–373, doi:10.1093/petrology/43.2.345.

Burnard, P., and Harrison, D., 2005, Argon isotope constraints on modification of oxygen isotopes in Iceland Basalts by surficial processes: Chemical Geology, v. 216, p. 143–156, doi:10.1016/j.chemgeo.2004.11.001.

Caracciolo, A., Bali, E., Guðfinnsson, G.H., Kahl, M., Halldórsson, S.A., Hartley, M.E., and Gunnarsson, H., 2020, Temporal evolution of magma and crystal mush storage conditions in the Bárðarbunga-Veiðivötn volcanic system, Iceland: Lithos, v. 352–353, doi:10.1016/j.lithos.2019.105234.

Caracciolo, A., Kahl, M., Bali, E., Guðfinnsson, G.H., Halldórsson, S.A., and Hartley, M.E. Timescales of crystal mush mobilization in the Bárðarbunga-Veiðivötn volcanic system based on olivine diffusion chronometry: American Mineralogist, doi:doi.org/10.2138/am-2021-7670.

Danyushevsky, L. V., and Plechov, P., 2011, Petrolog3: Integrated software for modeling crystallization processes: Geochemistry, Geophysics, Geosystems, v. 12, p. 1–32, doi:10.1029/2011GC003516.

DePaolo, D.J., 1981, Trace element and isotopic effects of combined wallrock assimilation and fractional crystallization: Earth and Planetary Science Letters, v. 53, p. 189–202.

Eiler, J.M., 2001, Oxygen Isotope Variations of Basaltic Lavas and Upper Mantle Rocks: Reviews in Mineralogy and Geochemistry, v. 43, p. 319–364, doi:10.2138/gsrmg.43.1.319.

Eiler, J.M., Grönvold, K., and Kitchen, N., 2000, Oxygen isotope evidence for the origin of chemical variations in lavas from Theistareykir volcano in iceland's northern volcanic zone: Earth and Planetary Science Letters, v. 184, p. 269–286, doi:10.1016/S0012-821X(00)00318-6.

Gautason, B., and Muehlenbachs, K., 1998, Oxygen isotopic fluxes associated with high-temperature processes in the rift zones of Iceland: Chemical Geology, v. 145, p. 275–286, doi:10.1016/S0009-2541(97)00148-4.

Halldórsson, S.A., Barnes, J.D., Stefánsson, A., Hilton, D.R., Hauri, E.H., and Marshall, E.W., 2016, Subducted lithosphere controls halogen enrichments in the Iceland mantle plume source: Geology, v. 44, p. 679–682, doi:10.1130/G37924.1.

Harðardóttir, S., Halldórsson, S.A., and Hilton, D.R., 2018, Spatial distribution of helium isotopes in Icelandic geothermal fluids and volcanic materials with implications for location, upwelling and evolution of the Icelandic mantle plume: Chemical Geology, v. 480, p. 12–27, doi:10.1016/j.chemgeo.2017.05.012.

Harmon, R.S., and Hoefs, J., 1995, Oxygen isotope heterogeneity of the mantle deduced from global 18O systematics of basalts from different geotectonic settings: Contributions to Mineralogy and Petrology, v. 120, p. 95–114, doi:10.1007/BF00311010.

Hartley, M.E., Bali, E., Maclennan, J., Neave, D.A., and Halldórsson, S.A., 2018, Melt inclusion constraints on petrogenesis of the 2014–2015 Holuhraun eruption, Iceland: Contributions to Mineralogy and Petrology, v. 173, p. 1–23, doi:10.1007/s00410-017-1435-0.

Hartley, M.E., Thordarson, T., and Fitton, J.G., 2013, Oxygen isotopes in melt inclusions and glasses from the Askja volcanic system, North Iceland: Geochimica et Cosmochimica Acta, v. 123, p. 55–73, doi:10.1016/j.gca.2013.09.008.

Hartley, M.E., Thordarson, T., Taylor, C., Fitton, J.G., and EIMF, 2012, Evaluation of the effects of composition on instrumental mass fractionation during SIMS oxygen isotope analyses of glasses: Chemical Geology, v. 334, p. 312–323, doi:10.1016/j.chemgeo.2012.10.027.

Hattori, K., and Muehlenbachs, K., 1982, Oxygen isotope ratios of the Icelandic crust: Journal of Geophysical Research, v. 87, p. 6559–6565, doi:10.1029/JB087iB08p06559.

Hemond, C., Arndt, N.T., Lichtenstein, U., Hofmann, A.W., Oskarsson, N., and Steinthorsson, S., 1993, The heterogeneous Iceland plume: Nd-Sr-O isotopes and trace element constraints: Journal of Geophysical Research, v. 98, doi:10.1029/93jb01093.

Jakobsson, S.P., Jònasson, K., and Sigurdsson, A., 2008, The three igneous rock series of Iceland: Jökull, v. 58, p. 117–138.

Jochum, K.P. et al., 2006, MPI-DING reference glasses for in situ microanalysis: New reference values for element concentrations and isotope ratios: Geochemistry, Geophysics, Geosystems, v. 7, doi:10.1029/2005GC001060.

Jónasson, K., 2007, Silicic volcanism in Iceland: Composition and distribution within the active volcanic zones: Journal of Geodynamics, v. 43, p. 101–117, doi:10.1016/j.jog.2006.09.004.

Kokfelt, T.F., Hoernle, K., Hauff, F., Fiebig, J., Werner, R., and Garbe-Schönberg, D., 2006, Combined trace element and Pb-Nd-Sr-O isotope evidence for recycled oceanic crust (upper and lower) in the Iceland mantle plume: Journal of Petrology, v. 47, p. 1705–1749, doi:10.1093/petrology/egl025.

Maclennan, J., McKenzie, D., Grönvold, K., Shimizu, N., Eiler, J.M., and Kitchen, N., 2003, Melt mixing and crystallization under Theistareykir, northeast Iceland: Geochemistry, Geophysics, Geosystems, v. 4, p. 1–40, doi:10.1029/2003GC000558.

Macpherson, C.G., Hilton, D.R., Day, J.M.D., Lowry, D., and Grönvold, K., 2005, High-3He/4He, depleted mantle and low-δ 18O, recycled oceanic lithosphere in the source of central Iceland magmatism: Earth and Planetary Science Letters, v. 233, p. 411–427, doi:10.1016/j.epsl.2005.02.037.

O'Neill, H.S.C., and Jenner, F.E., 2012, The global pattern of trace-element distributions in ocean floor basalts: Nature, v. 491, p. 698–704, doi:10.1038/nature11678.

Sharp, Z.D., 1990, A laser-based microanalytical method for the in situ determination of oxygen isotope ratios of silicates and oxides: Geochimica et Cosmochimica Acta, v. 54, p. 1353–1357, doi:10.1016/0016-7037(90)90160-M.

Shorttle, O., and Maclennan, J., 2011, Compositional trends of Icelandic basalts: Implications for short-length scale lithological heterogeneity in mantle plumes: Geochemistry, Geophysics, Geosystems, v. 12, p. 1–32, doi:10.1029/2011GC003748.

Skovgaard, A.C., Storey, M., Baker, J., Blusztajn, J., and Hart, S.R., 2001, Osmium-oxygen isotopic evidence for a recycled and strongly depleted component in the Iceland mantle plume: Earth and Planetary Science Letters, v. 194, p. 259–275, doi:10.1016/S0012-821X(01)00549-0.

Sohn, R.A., 2013, A method for inverting ratio-ratio data to estimate end-member compositions in mixing problems: Chemical Geology, v. 352, p. 63–69, doi:10.1016/j.chemgeo.2013.06.002.

Sveinbjörnsdóttir, Á.E., Stefánsson, A., Heinemeier, J., Arnórsson, S., Eiríksdóttir, E.S., and Ólafsdóttir, R., 2020, Assessing the sources of inorganic carbon in surface-, soil- and non-thermal groundwater in Iceland by δ13C and 14C: Geochimica et Cosmochimica Acta, v. 279, p. 165–188, doi:10.1016/j.gca.2020.03.021.

Thirlwall, M.F., Gee, M.A.M., Lowry, D., Mattey, D.P., Murton, B.J., and Taylor, R.N., 2006, Low δ 18 O in the Icelandic mantle and its origins: Evidence from Reykjanes

Ridge and Icelandic lavas: Geochimica et Cosmochimica Acta, v. 70, p. 993–1019, doi:10.1016/j.gca.2005.09.008.

Thirlwall, M.F., Gee, M.A.M., Taylor, R.N., and Murton, B.J., 2004, Mantle components in Iceland and adjacent ridges investigated using double-spike Pb isotope ratios: Geochimica et Cosmochimica Acta, v. 68, p. 361–386, doi:10.1016/S0016-7037(03)00424-1.

Valley, J.W., Kitchen, N., Kohn, M.J., Niendorf, C.R., and Spicuzza, M.J., 1995, UWG-2, a garnet standard for oxygen isotope ratios: Strategies for high precision and accuracy with laser heating: Geochimica et Cosmochimica Acta, v. 59, p. 5223–5231, doi:10.1016/0016-7037(95)00386-X.

White, W.M., 2013, Geochemistry: Wiley-Blackwell, 668 p.

Winpenny, B., and Maclennan, A.J., 2014, Short length scale oxygen isotope heterogeneity in the icelandic mantle: Evidence from plagioclase compositional zones: Journal of Petrology, v. 55, p. 2537–2566, doi:10.1093/petrology/egu066.